Measurement of the W-boson mass with the ATLAS detector at the LHC

Mesure de la masse du boson W avec le détecteur ATLAS au LHC

Thèse de doctorat de l'université Paris-Saclay et de l'université Johannes-Gutenberg de Mayence

École doctorale n° 576 Particules, Hadrons, Énergie, Noyau, Instrumentation, Imagerie, Cosmos et Simulation (PHENIICS)
Spécialité de doctorat: physique des particules
Graduate School : Physique, Référent : Faculté des sciences d'Orsay

Thèse préparée dans le **Département de Physique des Particules** (Université Paris-Saclay, CEA), et l'**Institut für Physik** (Johannes Gutenberg-Universität Mainz), sous la direction de **Maarten BOONEKAMP**, Ingénieur-chercheur et la co-direction de **Matthias SCHOTT**, professeur des universités.

Thèse soutenue à Paris-Saclay, le 12 septembre 2024, par

Andres PINTO PINOARGOTE

Composition du jury
Membres du jury avec voix délibérative

Reza ANSARI	Président
Professeur des universités, Université Paris-Saclay	
Maria UBIALI	Rapporteure & Examinatrice
Professor (équiv. HDR), University of Cambridge	
Roberto SALERNO	Rapporteur & Examinateur
Professeur des universités, École Polytechnique	
Concettina SFIENTI	Examinatrice
Professor, Johannes Gutenberg-Universität Mainz	
Christoph AMELUNG	Examinateur
Chercheur, CERN	
Mika VESTERINEN	Examinateur
Associate Professor, University of Warwick	

MEASUREMENT OF THE $W-$BOSON MASS WITH THE ATLAS DETECTOR AT THE LHC

Dissertation zur Erlangung des Grades

Doktor der Naturwissenschaften

am Fachbereich Physik, Mathematik und Informatik

der Johannes Gutenberg-Universität in Mainz

Andrés PINTO

geb. in ECUADOR

Frankreich, den 12. September 2024

1. Gutachter: Prof. Dr. Matthias Schott

2. Gutachter: Prof. Dr. Maarten Boonekamp

Titre: Mesure de la masse du boson W avec le détecteur ATLAS au LHC

Mots clés: Interactions électrofaibles, Ajustement électrofaible, Masse du W

Résumé: Le présent travail montre l'état actuel de la mesure de la masse du boson W en utilisant les données du LHC en collisions proton-proton collectées par le détecteur ATLAS à 5.02, 7 et 13 TeV. Pour ce faire, des procédures de calibration dédiées du Détecteur Interne (DI) et du Spectromètre à Muons (SM) d'ATLAS ont été conçues et appliquées, et la stratégie de la mesure a été optimisée.

La procédure de calibration du DI prend en compte les biais possibles dans la flèche de la trace du muon, les déformations géométriques et les distorsions du champ magnétique. Dans le cas du SM, les résidus d'alignement entre le DI et le SM ont été étudiés, et le champ magnétique toroïdal résiduel présent dans les calorimètres a été réévalué. Une calibration dédiée de l'impulsion du muon a été mise en œuvre. Après ces corrections, l'accord entre les données et la simulation est trouvé au niveau du pour mille, et les incertitudes correspondantes sont propagées à la mesure de la masse du boson W.

Le présent travail comprend également une étude détaillée de la stratégie d'ajustement de la masse du boson W. Un ajustement de type profil de vraisemblance (profile likelihood) analytique dans la limite gaussienne a été mis en œu-

vre, permettant une décomposition adéquate des incertitudes de l'ajustement, améliorant les "impacts" habituels. Dans ce scénario, nous sommes en mesure de déterminer la contribution réelle de chaque source systématique à l'incertitude finale de la mesure. Les données de mesure résultantes peuvent alors être utilisées de manière cohérente pour d'autres combinaisons et ajustements.

L'ajustement analytique a été utilisé pour obtenir une mesure de la masse du boson W à 7 TeV avec une valeur de 80366.5 ± 15.9 MeV, en bon accord avec les ajustements numériques. Pour l'ensemble de données à faible empilement (low pile-up), la calibration améliorée et la stratégie d'ajustement optimisée aboutissent à une précision attendue de 14.3 MeV. En combinant avec les données à 7 TeV, une précision finale de 10.3 MeV est attendue.

La compatibilité et la combinaison des mesures de la masse du boson W avec la nouvelle mesure ATLAS 2024 à 7 TeV et d'autres mesures (LEP, CDF, D0, LHCb) ont été étudiées. La combinaison donne $m_W = 80388.4 \pm 10.3$ MeV avec 0.2% de compatibilité en incluant CDF, et $m_W = 80366.1 \pm 11.7$ MeV avec 92% sans CDF, différant du résultat CDF par 3.8σ.

Title: Measurement of the W-boson mass with the ATLAS detector at the LHC

Keywords: Electroweak interactions, Electroweak fit, W boson mass

Abstract: The present work shows the current status of the determination of the W boson mass, using the LHC datasets in proton-proton collisions collected by the ATLAS detector at 5.02, 7 and 13 TeV. To achieve this, dedicated calibration procedures of the ATLAS Inner Detector (ID) and Muon Spectrometer (MS) have been designed and applied, and the W boson mass measurement strategy has been optimised.

The ID calibration procedure considers possibles biases in the muon track sagitta, geometrical deformations and magnetic field distortions. In the case of the MS, the alignment residuals between the ID and MS have been investigated, and the residual toroidal magnetic field present in the calorimeters has been re-evaluated. A dedicated muon momentum calibration has been implemented. After these corrections, the data-to-simulation agreement is found to be at the per mile level, and the corresponding uncertainties are propagated to the W-boson mass measurement.

The present work also includes a detailed study of the W-boson mass fitting strategy. An analytical Profile Likelihood fit in the Gaussian limit has been implemented, allowing a proper decomposition of the fit uncertainties, improving over the usual "impacts". In this scenario, the actual contribution of each systematic source to the final measurement uncertainty can be determined. The resulting measurement data can then be used consistently for further combinations and fits.

The analytical fit was used to obtain a W mass measurement at 7 TeV with value 80366.5 ± 15.9 MeV, in good agreement with numerical fits. For the low pile-up dataset, the improved calibration and optimised fitting strategy result in an expected precision of 14.3 MeV. Combining with the 7 TeV data an ultimate precision of 10.3 MeV can be obtained.

The compatibility and combination of the world W-boson mass using the new ATLAS 2024 measurement at 7 TeV with other measurements (LEP, CDF, D0, and LHCb) was studied. The combination yields $m_W = 80388.4 \pm 10.3$ MeV with 0.2% compatibility when CDF is included, and $m_W = 80366.1 \pm 11.7$ MeV with 92% compatibility when CDF is removed, differing from the CDF result by 3.8σ.

Titel: Messung der W-boson-Masse mit dem ATLAS-Detektor am LHC

Schlüsselwörter: Elektroschwache Wechselwirkungen, Elektroschwache Anpassung, W-boson-Masse

Zusammenfassung: Die vorliegende Arbeit zeigt den aktuellen Stand der W-Boson-Masse unter Verwendung der LHC-Datensätze in Proton-Proton-Kollisionen, die vom ATLAS-Detektor bei 5.02, 7 und 13 TeV gesammelt wurden. Um dies zu erreichen, wurden spezielle Kalibrierungsverfahren für den ATLAS Inner Detector (ID) und das Muon Spectrometer (MS) entwickelt und angewendet und die Anpassungsstrategie wurde optimiert.

Das ID-Kalibrierungsverfahren berücksichtigt mögliche Verzerrungen in der Muonenspur-Sagitta, geometrische Verformungen und Magnetfeldverzerrungen. Im Fall des MS wurden die Ausrichtungsresiduen zwischen ID und MS untersucht und das verbleibende toroidale Magnetfeld in den Kalorimetern neu bewertet. Eine spezielle Kalibrierung des Muonenimpulses wurde implementiert. Nach diesen Korrekturen wird festgestellt, dass die Übereinstimmung zwischen Daten und Simulation auf Promilleebene liegt und die entsprechenden Unsicherheiten auf die W-Boson-Massenmessung übertragen werden.

Die vorliegende Arbeit enthält auch eine detaillierte Studie der W-Boson-Massenanpassungsstrategie. Eine analytische Profil-Likelihood-Anpassung im gaußschen Grenzbereich wurde implementiert, die eine ord-nungsgemäße Zerlegung der Anpassungsunsicherheiten ermöglicht und gegenüber den üblichen "Impacts" verbessert. In diesem Szenario kann der tatsächliche Beitrag jeder systematischen Quelle zur endgültigen Messunsicherheit bestimmt werden. Die resultierenden Messdaten können dann konsistent für weitere Kombinationen und Anpassungen verwendet werden.

Die analytische Anpassung wurde verwendet, um eine W-Massenmessung bei 7 TeV mit einem Wert von 80366.5 ± 15.9 MeV zu erhalten, die gut mit numerischen Anpassungen übereinstimmt. Für den Datensatz mit geringer Stapelung resultieren die verbesserte Kalibrierung und die optimierte Anpassungsstrategie in einer erwarteten Genauigkeit von 14.3 MeV. Durch Kombination mit den 7 TeV-Daten wird eine Genauigkeit von 10.3 MeV erreicht.

Die Kompatibilität und Kombination der W-Boson-Masse unter Verwendung der neuen ATLAS 2024-Messung bei 7 TeV mit anderen Messungen (LEP, CDF, D0, LHCb) wurde untersucht. Die Kombination ergibt $m_W = 80388.4 \pm 10.3$ MeV mit 0.2% Kompatibilität bei Einbeziehung von CDF und $m_W = 80366.1 \pm 11.7$ MeV mit 92% ohne CDF, abweichend vom CDF-Ergebnis um 3.8σ.

I declare that I have written this work independently and have not used any sources or aids other than those indicated, and have properly acknowledged all citations.

I certify that this dissertation has been partially published in the following journals:

- ATLAS Collaboration. "Measurement of the W-boson mass and width with the ATLAS detector using proton-proton collisions at $\sqrt{s} = 7$ TeV." arXiv:2403.15085 (2024).

- A. Pinto, Z. Wu et al., "Uncertainty components in profile likelihood fits", Eur. Phys. J. C, vol. 84, no. 6, p. 593, 2024.

However, it has not been submitted in full as part of another qualification.

I confirm that the manuscript will be hosted at Université Paris-Saclay and Johannes Gutenberg University of Mainz due to the cotutelle agreement between the two institutions.

France, September 12, 2024

Andrés Eloy Pinto Pinoargote

Institut für Physik

Johannes Gutenberg-Universität

Staudingerweg 7

D-55128 Mainz

Université Paris-Saclay

Commissariat à l'énergie atomique et aux énergies alternatives

Département de Physique des Particules

91191, Gif-sur-Yvette

Je déclare avoir rédigé ce travail de manière indépendante et n'avoir utilisé que les sources et aides indiquées, et avoir correctement mentionné toutes les citations.

Je certifie que cette thèse a été partiellement publiée dans les revues suivantes :

- ATLAS Collaboration. "Measurement of the W-boson mass and width with the ATLAS detector using proton-proton collisions at $\sqrt{s} = 7$ TeV." arXiv:2403.15085 (2024).

- A. Pinto, Z. Wu et al., "Uncertainty components in profile likelihood fits", Eur. Phys. J. C, vol. 84, no. 6, p. 593, 2024.

Cependant, elle n'a pas été soumise en intégralité dans le cadre d'une autre qualification.

Je confirme que le manuscrit sera hébergé à l'Université Paris-Saclay et à l'Université Johannes Gutenberg de Mayence en raison de l'accord de cotutelle entre les deux institutions.

France, 12 septembre 2024

Andrés Eloy Pinto Pinoargote

Institut für Physik

Johannes Gutenberg-Universität

Staudingerweg 7

D-55128 Mainz

Université Paris-Saclay

Commissariat à l'énergie atomique et aux énergies alternatives

Département de Physique des Particules

91191, Gif-sur-Yvette

Ich versichere, dass ich die Arbeit selbstständig verfasst und keine anderen als die angegebenen Quellen und Hilfsmittel benutzt sowie Zitate kenntlich gemacht habe.

Ich bestätige, dass diese Dissertation teilweise in den folgenden Zeitschriften veröffentlicht wurde:

- ATLAS Collaboration. "Measurement of the W-boson mass and width with the ATLAS detector using proton-proton collisions at $\sqrt{s} = 7$ TeV." arXiv:2403.15085 (2024).

- A. Pinto, Z. Wu et al., "Uncertainty components in profile likelihood fits", Eur. Phys. J. C, vol. 84, no. 6, p. 593, 2024.

Sie wurde jedoch nicht vollständig als Teil einer anderen Qualifikation eingereicht.

Ich bestätige, dass das Manuskript aufgrund der Cotutelle-Vereinbarung zwischen der Université Paris-Saclay und der Johannes Gutenberg-Universität Mainz an beiden Institutionen hinterlegt wird.

Frankreich, 12. September 2024

Andrés Eloy Pinto Pinoargote

Institut für Physik

Johannes Gutenberg-Universität

Staudingerweg 7

D-55128 Mainz

Université Paris-Saclay

Commissariat à l'énergie atomique et aux énergies alternatives

Département de Physique des Particules

91191, Gif-sur-Yvette

Acknowledgements

I would like to extend my sincere gratitude to my thesis jury members: Reza Ansari, Maria Ubiali, Roberto Salerno, Concettina Sfienti, Christoph Amelung, and Mika Vesterinen. I am especially thankful to Maria Ubiali and Roberto Salerno for their time and effort in reviewing my work. Your insightful feedback and valuable suggestions have greatly enhanced the quality of this thesis. I also appreciate all members for attending the defense and contributing to the evaluation of my work.

To my supervisor, Maarten, whose infinite patience helped this project finds its path. Though we couldn't spend much time together during the first year, the second and third years were incredible. Working with you has been a challenging experience, with long talks and brainstorming sessions that turned small projects into big ones. Thank you very much for all the experience I gained with you, and I hope I met your expectations. I can say that I found a good mentor and friend in you.

To my supervisor, Matthias, I am truly grateful to have such a dedicated and supportive mentor. I deeply appreciate your commitment to your students and am thankful for everything you did for me. I hope our paths will continue to cross in future projects.

To Laurent and Pierre-François, who guided me during my first year and taught me everything I needed to start in ATLAS. Both of you are probably the most encouraging and awesome supervisors anyone could ask for. I cannot express how great it was working with you, sharing ideas, and bringing out the best in myself. For every mistake I made, Laurent would tell me, "Les jeunes qui ne se trompent pas sont les jeunes qui ne travaillent pas", and I always remember this when I make mistakes.

To Frédéric, even though I was not your PhD student, you were always supportive and ready to help from the first day. Being the boss is not easy, but I sincerely thank you for being a kind

Résumé

Le Modèle Standard ("Standard Model", SM) de la physique des particules est un cadre théorique élégant pour étudier les particules élémentaires et les interactions fondamentales qui régissent l'univers, à l'exception de la gravité. Dans la nature, il existe deux types de particules : les fermions et les bosons. Les premiers ont un spin demi-entier et existent en trois générations, divisées en deux groupes : les leptons et les quarks. Il existe six types (saveurs) de leptons : électron, muon et tau, avec une charge électrique de -1, chacun étant associé à un neutrino électriquement neutre. D'autre part, il existe six saveurs de quarks : up, charm et top avec une charge électrique de $+2/3$, et down, strange et bottom avec une charge électrique de $-1/3$. Les bosons ont un spin entier : les bosons de spin non-nul sont les vecteurs des forces permettant aux particules d'interagir entre elles; enfin, il existe un boson de spin nul, le boson de Higgs, à l'origine des masses des autres particules du SM.

Le SM décrit trois interactions ou "forces" connues : l'interaction électromagnétique, l'interaction forte et l'interaction faible. L'interaction électromagnétique implique un boson jauge avec une masse nulle connu sous le nom de photon (γ), l'interaction forte comprend huit bosons jauge avec une masse nulle connus sous le nom de gluons (g), et l'interaction faible a trois bosons jauge massifs : un neutre, connu sous le nom de Z, et deux chargés électriquement, W^+ et W^-. Dans le cadre du SM, le mécanisme de Brout-Englert-Higgs (BEH) explique comment les particules acquièrent leur masse après brisure spontanée de symétrie (SSB) et prédit l'existence du boson de Higgs, dernière pièce du SM et découvert en 2012.

Le Modèle Standard comporte 25 paramètres pour décrire les masses des quarks, des leptons et des neutrinos, le boson de Higgs, ainsi que les paramètres de la matrice de mélange des quarks et les couplages entre les particules. Parmi eux, la masse du boson W (m_W) est un paramètre essentiel,

déterminé théoriquement au premier ordre à partir de la masse du boson Z, de la constante de structure fine (α) et de la constante de Fermi (G_F). Aux ordres supérieurs, les corrections radiatives impliquant d'autres particules du Modèle Standard, telles que le quark top et le boson de Higgs, affectent la valeur de m_W. Ces corrections radiatives ne se limitent pas nécessairement au SM, et peuvent impliquer de nouvelles particules ou interactions. La mesure de m_W constitue donc un test de la validité du SM, et une recherche indirecte de nouvelle physique.

Depuis sa découverte en 1983, la masse du boson W a été mesurée dans divers collisionneurs. La première mesure a été réalisée au collisionneur proton-antiproton du CERN avec une valeur de $m_W = 81 \pm 5$ GeV. Suivie par différentes expériences telles que D0, ATLAS, LHCb et CDF conduisant à une valeur moyenne mondiale combinée de $m_W = 80369 \pm 13$ MeV, soit une précision relative de moins de 0,01%. Ce niveau de précision est crucial pour tester les prédictions du SM et pour explorer les limites des prédictions théoriques ainsi que pour éclairer d'éventuels scénarios au-delà du Modèle Standard, tels que la Supersymétrie, la Matière Noire, etc.

En collisions hadroniques, la précision de mesure est limitée par la description théorique de la production et la désintégration du boson W, ainsi que par la configuration expérimentale. Au LHC, la production des bosons W dépend principalement des quarks de mer, nécessitant une connaissance précise des fonctions de structure du proton qui sont l'une des principales sources systématiques. D'autre part, la reconstruction des particules est un défi en raison du grand nombre d'interactions inélastiques simultanées, ou empilement, limitant les analyses aux désintégrations leptoniques des bosons W, $W \rightarrow \ell\nu$. Dans ces scénarios, les neutrinos ne peuvent pas être détectés directement, mais ils peuvent être identifiés par un déséquilibre de l'impulsion mesurée dans le plan transverse au faisceau. Cela introduit d'importantes incertitudes systématiques, notamment dans la modélisation du moment transverse du boson W, p_T^W.

Pour déterminer m_W, un ajustement des données aux différentes distributions cinématiques obtenues par simulation dans les canaux de désintégration (canaux muoniques et électroniques) et dans plusieurs catégories cinématiques est effectué. Ces distributions sont les distributions du moment transverse des leptons chargés, p_T^ℓ, et de la masse transverse du boson W, m_T. D'autres distributions peuvent être considérées comme des régions de contrôle telles que l'énergie transverse

manquante, E_T^{miss}, le recul hadronique, u_T ou la rapidité du lepton, η_ℓ. Ensuite, la valeur de m_W peut être obtenue directement à partir des données en utilisant la méthode des templates. Cette méthode implique la génération d'échantillons simulés pour différentes hypothèses de valeurs de m_W et la comparaison des distributions de ces échantillons avec celles observées dans les données. L'échantillon qui correspond le mieux aux données est utilisé pour déterminer la valeur mesurée de m_W.

Cette thèse discute de l'état actuel et des perspectives pour la mesure de la masse et de la largeur du boson W en utilisant les données du détecteur ATLAS au LHC. Deux lots de données, correspondant à la première prise de données Run 1 à 7 TeV, et au Run 2 (2017 et 2018) à 5,02 TeV et 13 TeV sont exploités. Le premier bénéficie d'une grande précision statistique avec un fort taux d'empilement, tandis que le second correspond à un faible empilement, offrant une meilleure résolution dans la mesure du recul hadronique au prix d'une statistique plus faible. Ceci permet une modélisation précise du moment transverse du boson W contrairement à l'approche habituelle.

Diverses calibrations expérimentales, liées aux sous-détecteurs et au champ magnétique d'ATLAS, ainsi que l'étalonnage de la mesure de l'impulsion des muons, sont discutées. Une méthode statistique, le profil de vraisemblance (PLH), est introduite pour la première fois dans l'estimation des paramètres du W, ainsi qu'une nouvelle approche pour évaluer les composantes d'incertitude dans un tel ajustement. À cela s'ajoute une nouvelle modélisation pour le moment transverse du boson W dans le faible empilement. Ces considérations contribuent de manière significative à la précision de la détermination de m_W.

Le traitement statistique de ce travail repose sur le profil de vraisemblance, qui consiste à maximiser la fonction de vraisemblance par rapport aux paramètres d'intérêt (la masse et la largeur du W) tout en profilant sur les paramètres de nuisance (les sources d'incertitude sytématique), qui ne sont pas d'intérêt direct mais affectent la mesure. L'interprétation du profil de vraisemblance est l'un des principaux défis de cette méthode statistique, ainsi que l'incertitude et ses composantes statistique et systématiques. La première est évaluée dans le contexte des ajustements de vraisemblance et une différence claire avec les ajustements purement statistiques est établie, montrant que l'incertitude d'un ajustement purement statistique n'est pas égale à la composante

statistique d'un ajustement PLH comprenant des nuisance, et est strictement inférieure. D'autre part, l'incertitude systématique et la contribution de chaque source systématique à l'incertitude systématique totale sont l'un des points centraux du présent travail.

Dans la communauté de la physique des hautes énergies, la contribution d'une source systématique est déterminée habituellement par la méthode dite "d'impact", qui consiste à calculer l'incertitude totale d'un ajustement, σ_{total}, puis à retirer la source systématique pour recalculer l'incertitude totale, $\sigma'_{\text{total}} < \sigma_{\text{total}}$. Si la contribution de cette source systématique est significative, on s'attend à ce que σ'_{total} soit plus petit que σ_{total}, et la composante "d'impact" ou systématique est déterminée comme la différence quadratique $\sqrt{\sigma_{\text{total}} - \sigma'_{\text{total}}}$. Cette approche conduit à des incertitudes qui ne récupèrent pas entièrement l'incertitude systématique totale. Cette discussion non seulement explique pourquoi le concept d'impacts est incorrect, mais propose également une méthode précise pour évaluer les composantes d'incertitude réelles en utilisant la méthode des observables décalées.

De plus, dans le contexte où toutes les incertitudes sont distribuées selon une loi normale, la solution analytique complète est discutée avec une décomposition directe de l'incertitude qui peut être utilisée dans les ajustements et combinaisons ultérieurs. Cette stratégie d'ajustement a été mise en œuvre non seulement pour les études de la masse du boson W mais aussi dans les études de calibration des muons.

Pour réaliser une mesure précise de m_W, une bonne calibration de p_T^ℓ est requise, principalement influencée par la calibration des leptons chargés. Pour obtenir une bonne calibration, des résonances connues sont utilisées pour ajuster la simulation, de sorte que les données observées soient bien reproduites. En particulier, le présent travail se concentre sur la calibration des muons en utilisant le méson J/ψ ainsi que le boson Z dans l'état final à deux muons, c'est-à-dire $J/\psi \to \mu\mu$ et $Z \to \mu\mu$. Dans le détecteur ATLAS, les candidats muons sont reconstruits indépendamment en utilisant des informations provenant du Détecteur Interne (ID) et du Spectromètre à Muons (MS). Ensuite, un candidat muon combiné (CB) est obtenu par une combinaison statistique des pistes ID et MS. Pour cette raison, garantir une bonne calibration MS/ID améliore la reconstruction CB, et donne par conséquent une meilleure modélisation de la distribution de p_T^ℓ.

La procédure de calibration commence par corriger les biais possibles liés à la flèche de la trace des muons dans les données. Il s'agit d'un effet dépendant de la charge du muon et qui affecte le moment transverse des muons et avant correction, à une valeur moyenne d'environ 0,05 TeV^{-1}, introduisant un décalage d'environ 80 MeV dans la masse de W. Pour le corriger, la flèche est évaluée dans l'espace (η, ϕ) en minimisant la variance de la distribution de masse invariante. Après correction, le biais est réduit à une valeur moyenne de 2×10^{-4} TeV^{-1}. Cela permet d'améliorer les performances du moment transverse avec un gain en résolution dans les résonances telles que le boson Z et le méson J/ψ.

L'alignement de l'ID est réalisé en utilisant une minimisation des résidus χ^2 entre les traces mesurées et les points de mesure. Cependant, certains biais systématiques peuvent échapper à cette procédure, entraînant des biais résiduels connus sous le nom de modes faibles, qui nécessitent un traitement différent. La reconstruction de p_T dans l'ID peut être affectée par différentes sources telles que la connaissance incomplète de la quantité de matière dans le détecteur, la mauvaise modélisation du champ magnétique et les déformations géométriques résiduelles après l'alignement de l'ID. Ces distorsions peuvent être soit des distorsions réelles du détecteur, soit des déformations artificielles introduites par la procédure d'alignement elle-même.

Ces biais sont présents dans les données, produisant un effet d'échelle global et des modulations dans la masse invariante du système dimuon par rapport à la simulation, avec une différence de 0,2%. Pour corriger cela, différents modèles de distorsion géométrique sont proposés. Ceux-ci prennent en compte les distorsions radiales et longitudinales possibles du détecteur ainsi que les erreurs de modélisation du champ magnétique. Le modèle radial affecte uniquement la composante transverse du moment, p_T, produisant des modulations dans la masse invariante. Le modèle de distorsion longitudinale affecte uniquement la composante longitudinale du moment, p_Z, générant une échelle globale et des modulations. Le modèle de distorsion du champ magnétique affecte les deux composantes du moment, entraînant un effet d'échelle global dans la masse invariante. Ces modèles ont été simulés pour produire des modèles à appliquer sur les données à travers un ajustement analytique dans des intervalles de rapidité. Les résultats ont montré que pour décrire les données, un modèle à deux paramètres est requis. Dans ce travail, un modèle de distorsion

magnétique-radial a été considéré dans chaque ajustement, permettant la création d'une carte de biais en fonction de la rapidité du J/ψ, menant à un biais relatif final dans la région centrale de $\langle\varepsilon_B\rangle = -1.5\times10^{-3}$ et $\langle\varepsilon_R\rangle = 1.0\times10^{-3}$ pour les distorsions magnétiques et radiales, respectivement. Après correction, un accord entre données et simulation au niveau du pourmille a été trouvé pour ces facteurs d'échelle.

Pour le Spectromètre à Muons (MS), l'alignement est effectué par un système d'alignement optique qui surveille la position des chambres à muons les unes par rapport aux autres et par rapport aux marques fiduciaires dans le détecteur. Cependant, le système d'alignement optique corrige l'alignement interne du MS mais ne voit pas de déplacement global entre le MS et l'ID. Cela introduit des résidus entre les paramètres des trace ID et MS, d'environ 1,5 millimètres dans le paramètre d'impact longitudinal, z_0, et de quelques milliradians dans l'angle polaire, θ, en plus d'un effet de charge lié au champ magnétique toroïdal. Pour l'effet dépendant de la charge, une correction de la force du champ magnétique d'environ 25% dans la région du calorimètre tile est proposée, corrigeant avec succès les asymétries de charge tandis qu'une carte de correction détaillée a également été obtenue. Pour corriger le biais associé aux secondes coordonnées, $(z_0,\ \theta)$, une carte des premières coordonnées, (d_0, ϕ), a été calculée et injectée comme fonction de correction de la trace. Après les corrections, un bon accord entre données et simulation a été trouvé.

Une fois les distorsions de l'ID traitées dans les données, une calibration dédiée du moment des muons (MMC) a été implémentée dans la simulation. Cela vise à corriger les effets d'échelle et de résolution liés aux imprécisions dans la description de l'intégrale du champ magnétique et des effets de diffusion multiple. Cela a été réalisé en classant les muons dans différents intervalles de rapidité et en effectuant un ajustement de la masse invariante des dimuons pour les paramètres d'échelle et de résolution, où le bruit de fond a été modélisé à l'aide de fonctions analytiques et considéré comme une source systématique. Les résultats de l'ajustement ont été traités par un ajustement analytique pour récupérer les paramètres de calibration finaux en fonction de la rapidité du muon. Après correction, un accord au niveau du pourmille a été trouvé entre données et simulation. Le résidu après correction entre données et simulation est considéré comme une source d'incertitude systématique.

Le présent travail présente enfin une étude détaillée de la masse du boson W, m_W, à différentes énergies de centre de masse et la première mesure de la largeur du boson W, Γ_W, réalisée par ATLAS. Les premières études à 7 TeV ré-évaluent le résultat publié en 2017 avec un ajustement de profil de vraisemblance, au lieu de la méthode utilisée initialement, ce qui donne une amélioration de la précision. Un ajustement analytique dans la limite gaussienne a été mis en œuvre, permettant une évaluation correcte des composantes d'incertitude et la décomposition des incertitudes de l'ajustement dues aux sources systématiques, une amélioration par rapport aux "impacts" habituels. La valeur de m_W a été évaluée avec différents ensembles de PDF, avec une forte dépendance. Cet effet est réduit lorsque les incertitudes pré-ajustement sont suffisamment agrandies. Pour la largeur du boson W, la même stratégie d'ajustement et de décomposition des incertitudes a été mise en œuvre ainsi qu'une étude dédiée de la dépendance PDF. Contrairement à m_W, la largeur ne montre pas une forte dépendance avec les incertitudes de PDF. La valeur finale pour m_W est cohérente avec le résultat précédemment publié par ATLAS avec une amélioration de la précision et est donnée par,

$$m_W = 80366.5 \pm 9.8(\text{stat.}) \pm 12.5(\text{syst.}) \text{ MeV} = 80366.5 \pm 15.9 \text{ MeV}. \tag{1}$$

La largeur mesurée,

$$\Gamma_W = 2202 \pm 32(\text{stat.}) \pm 34(\text{syst.}) \text{ MeV} = 2202 \pm 47 \text{ MeV}. \tag{2}$$

est en accord avec l'attente du Modèle Standard dans la limite de deux déviations standard.

Actuellement, la collaboration ATLAS travaille à améliorer la précision de m_W et les perspectives de la nouvelle mesure ont également été évaluées en utilisant les jeux de données à faible empilement à 5.02 TeV et 13 TeV. L'intérêt pour ces jeux de données réside dans les conditions expérimentales qui permettent d'optimiser la résolution sur le recul hadronique tout en maintenant un signal important. À cet effet, une campagne de simulation dédiée a été menée pour émuler les conditions à faible empilement. Différentes sources systématiques ont été évaluées, certaines extrapolées du régime à fort empilement au régime à faible empilement, et le bruit de fond multijet a été estimé par une méthode basée sur les données. Une différence remarquable dans cette analyse est la nouvelle

modélisation de p_T^W, qui représente l'une des plus grandes sources d'incertitudes. Communément, cette quantité est modélisée en extrapolant le moment transverse du boson Z, p_T^Z, ce qui introduit des incertitudes théoriques. Dans le cas à faible empilement, une mesure directe de p_T^W a été réalisée en implémentant une déconvolution itérative des effets de détecteur, améliorant cette source systématique. Deux observables, p_T^ℓ et m_T sont considérées et une stratégie d'ajustement conjointe a été mise en œuvre où les corrélations statistiques sont prises en compte par des pseudo-expériences dans leurs catégories cinématiques respectives. Le résultat conjoint final donne une précision de,

$$m_W^{5.02\ +\ 13\ \text{TeV}} = XYZ \pm 12.0(\text{stat.}) \pm 7.7(\text{syst.})\ \text{MeV} = XYZ \pm 14.3\ \text{MeV}. \tag{3}$$

où la valeur centrale est cachée par la procédure d'ajustement. La précision future a également été étudiée en exploitant tous les jeux de données ATLAS à fort et faible empilement, c'est-à-dire 5.02 + 7 + 13 TeV. Cet ajustement conjoint tient compte des corrélations systématiques possibles entre les différents jeux de données fournissant un résultat final,

$$m_W^{5.02\ +\ 7\ +\ 13\ \text{TeV}} = XYZ \pm 8.0(\text{stat.}) \pm 6.5(\text{syst.})\ \text{MeV} = XYZ \pm 10.3\ \text{MeV}. \tag{4}$$

On s'attend à ce que ce résultat soit encore amélioré une fois que le jeu de données à faible empilement prendra en compte d'autres sources systématiques et de nouvelles variables qui pourraient potentiellement aider à réduire la précision finale.

Finalement, la compatibilité et la combinaison entre le nouveau résultat d'ATLAS à 7 TeV (ce travail Eq. (1)) et les autres mesures (LHCb, CDF, D0 et LEP) ont été étudiées avec différents ensembles de PDFs, avec le PDF CT18 comme référence. Deux combinaisons de toutes les mesures, incluant CDF (w/ CDF) et sans CDF (w/o CDF), ont été réalisées. La combinaison donne les moyennes suivantes,

$$\begin{aligned} m_W^{\text{w/ CDF}} &= 80388.4 \pm 10.3\ \text{MeV}, \\ m_W^{\text{w/o CDF}} &= 80366.1 \pm 11.7\ \text{MeV}. \end{aligned} \tag{5}$$

où une compatibilité de 0.2% est obtenue lorsque CDF est inclus, et une compatibilité de 92% est obtenue lorsque CDF est retiré, avec une différence de 3.8σ par rapport à CDF.

Contents

List of Figures

xix

xxiii

List of Tables

Chapter 1

Theoretical framework

One of the main objectives of physics is to develop a theory of everything that is capable of describing the world from the sub-atomic scales to the large scales of the universe encoding the four fundamental interactions: electromagnetic, weak, strong, and gravity. However, up to now, our understanding of reality can be modelled by two remarkable theories: the General Relativity (GR) and the Quantum Physics. GR is one of the most sophisticated theories capable of describing the universe at large scales, predicting exotic objects like black holes and supernovas. The theoretical framework of GR is based on classical field theory, where space and time are combined into a single concept called space-time. Its dynamics are described by Einstein's field equations, which involve a not necessarily flat metric.

On the other hand, the subatomic world is governed by the Quantum Physics, which has evolved from Quantum Mechanics to the well-tested Quantum Field Theory (QFT). In particular, several QFT models are studied and proposed by the theoretical community. However, the most well-tested theoretical framework to date is the so-called "Standard Model (SM) of Particle Physics". The Standard Model encapsulates all the interactions seen in daily lives into three interactions between particles, resulting as perturbations of quantum fields. The SM has been tested over many years by collaborations around the world, such as LHC, LEP, Tevatron, etc., demonstrating a precision never seen before. Despite its numerous successes, intriguing questions persist, with particular emphasis on the elusive Dark Matter, which constitutes approximately a quarter of the

universe's composition.

This chapter is organized as follows, section 1.1 provides a brief review of the Standard Model theoretical framework providing insights of the latest developments in particle physics. Section 1.2 covers the the W and Z boson production in colliders such as the W boson cross section and different Parton Distribution Function (PDF) sets. Finally, section 1.3 presents the current results of the W boson mass, the prediction in the SM and physics beyond the SM.

1.1   The standard model

The Standard Model (SM) [1–4] is probably the most successful theory that describes the fundamental particles in nature and the interactions between them. The SM encapsulates three interactions, the electromagnetic and weak interactions are well understood through the electroweak theory (EW) while the flavour and colour dynamics is modelled by the quantum chromodynamics theory (QCD).

The main elements of the SM are the particles that exchange and carry the interactions that are found in two kind, the fermions and the bosons. Fermions are particles with half-integer spin values that obey Fermi-Dirac statistics, which govern their distribution in a system of particles. At the same time, they are considered the basic building blocks of matter which are divided in two types: quarks and leptons. Quarks are particles that carry two types of charges, the electric charge and the color charge, which allows them to interact via the electromagnetic, weak, and strong interactions. At the same time, they can form composite particles called hadrons, such as protons and neutrons. On the other hand, leptons are another type of fermions that can interact by electroweak interaction. Here particles like the electron, muon, neutrinos, etc., are present. Fermions consist of six quarks, six leptons, and their corresponding antiparticles, organized into three generations with different masses. Each generation includes three charged leptons (electron e, muon μ, tau τ) with neutral neutrinos (ν_e, ν_μ, ν_τ). Additionally, there are two sets of quarks: those with a positive charge ($+2/3$, namely up, charm, and top) and those with a negative charge (-1/3, namely down, strange, and bottom).

As an addition to the fermions, the SM also predicts the existence of elementary bosonic particles.

For the electromagnetic interaction there is one massless vector boson known as photon (γ) that carries a zero electric charge and with spin 1. For the strong interaction, there exist 8 massless vector bosons known as gluons with colour charge, spin 1 and they are the responsible of binding the quarks to form hadrons (mesons and baryons). Finally, for the weak interaction, several studies lead to the Glashow, Weinberg and Salam (GWS) theory that predicts the existence of three massive vector bosons known as Z^0, W^+ and W^-. One of the greatest successes of the GWS theory was its unification of the electromagnetic interaction with the weak interaction, forming the Electroweak (EW) theory. Moreover, to give mass to the bosons $W^\pm$ and Z, the inclusion of a new Gauge field was needed with a new boson of spin 0 known as the Higgs boson which arises by the Brout-Englert-Higgs mechanism known as the Spontaneous Symmetry Breaking (SSB). However, the masses predicted by the theory were so large that powerful colliders were required to study these new particles. The W and Z bosons were discovered at CERN in 1983 by the UA1 and UA2 collaborations with masses of about 80 GeV and 91 GeV, respectively. On the other hand, The Higgs boson was the last piece of the Standard Model puzzle and it was finally discovered at CERN in 2012 by the ATLAS and CMS collaborations with a mass of 125 GeV [5, 6]. The elementary particles of the SM is summarized in Fig. 1.1.
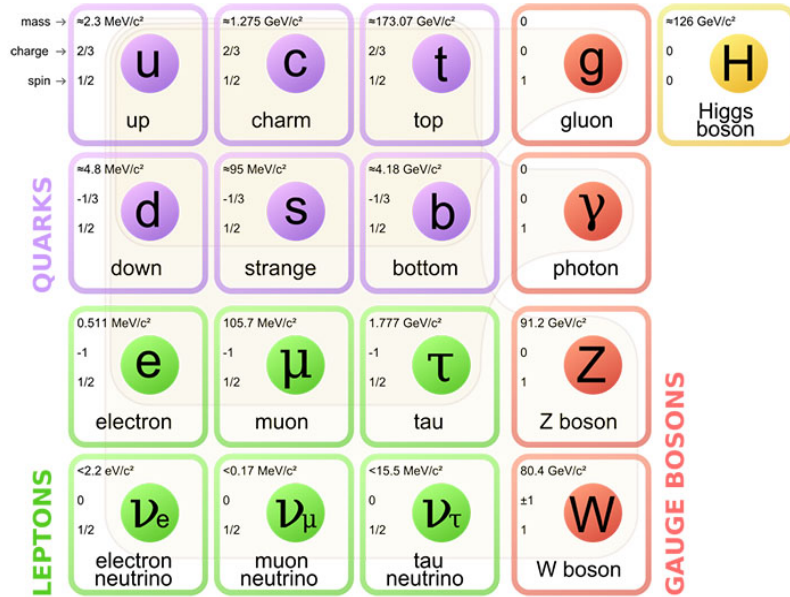
Figure 1.1: Elementary particles of the Standard Model (SM) with their respective mass, electric charge and spin [7].

1.1.1 The SM lagrangian

The SM is a Quantum Field Theory (QFT) that encompasses three symmetry groups,

$$SU(3)_C \otimes SU(2)_L \otimes U(1)_Y \tag{1.1}$$

where $SU(3)_C$ is the special unitary group that generates the Quantum ChromoDynamics (QCD) and is the responsible of the strong interactions from which the gauge fields are known as gluons that carry colour charge. On the other hand, the $SU(2)_L \otimes U(1)_Y$ is the group that generates the Electromagnetic and Weak (Electroweak, EW) interactions mediated by four gauge bosons, one massless (γ photon) and three massive ($W^\pm$, Z). In a general landscape, the SM can be summarized as the sum of the Lagrangians of each interaction, given by,

$$\mathcal{L}_{\text{SM}} = \mathcal{L}_{\text{QCD}} + \mathcal{L}_{\text{EW}} + \mathcal{L}_{\text{Higgs}}, \tag{1.2}$$

where the first two Lagrangians corresponds to the QCD and EW interactions and $\mathcal{L}_{\text{Higgs}}$ (described in subsection 1.1.2) is the Higgs boson Lagrangian. For an arbitrary symmetry group, the Lagrangian can be expressed as,

$$
\begin{aligned}
\mathcal{L} = &-\frac{1}{4} F_{\mu\nu}^a F^{a\mu\nu} \\
&+ i\bar{\psi}\gamma^\mu D_\mu \psi + h.c. \\
&+ \bar{\psi}_i y_{ij} \psi_j \phi + h.c. \\
&+ (D_\mu \phi)^\dagger (D^\mu \phi) - V(\phi),
\end{aligned}
\tag{1.3}
$$

with $F_{\mu\nu}^a$ the field strength tensor given by,

$$F_{\mu\nu}^a = \partial_\mu A_\nu^a - \partial_\nu A_\mu^a + g f^{abc} A_\mu^b A_\nu^c, \tag{1.4}$$

where A_μ^a are the gauge fields, g is the coupling constant and f^{abc} are the structure constant of the group. γ^μ are the gamma matrices and D_μ is the covariant derivative given by,

$$D_\mu = \mathbb{I}\partial_\mu - igT^a A_\mu^a, \tag{1.5}$$

where $\mathbb{I}$ and T^a are the identity matrix and the generators of the Lie group, respectively. The covariant derivative shows that Gauge bosons are coupled directly with the fermions to the so-called tree level Feynman diagram while Eq. (1.4) shows that for more than one generator of a non-abelian group the gauge field can interact with itself.

In Eq. (1.3) the first term describes the dynamic of the gauge bosons with a running over all the gauge fields, the second term is the kinematics of the fermions that encodes also the interaction between the matter(anti-matter) fields ψ ($\bar{\psi}$) and the gauge bosons. The third term is the so-called Yukawa sector that describes the interaction between the Higgs field ϕ and the fermions ψ and is the responsible to give the mass to the fermions via the SSB. Finally, the fifth term corresponds to the kinematics of the Higgs field while the last one is the potential term of the Higgs through which it acquires its mass and is given by,

$$V(\phi) = -\mu^2|\phi|^2 + \lambda|\phi|^4, \quad \mu, \lambda > 0 \tag{1.6}$$

From Eq. (1.3) all the interactions can be obtained by setting the appropriate groups. For example, the electromagnetism can be described by the abelian group $U(1)$,

$$\mathcal{L}_{\text{QED}} = -\frac{1}{4}F_{\mu\nu}F^{\mu\nu} + \bar{\psi}(i\gamma^\mu D_\mu - m)\psi. \tag{1.7}$$

with only one generator and that is invariant under a local gauge transformation,

$$\psi \to e^{i\theta(x)}\psi, \quad A_\mu \to A_\mu + \partial_\mu\theta(x), \tag{1.8}$$

that at the same time, it imposes the condition to a massless gauge boson, this is, the photon.

The QCD lagrangian can be obtained by introducing a non-abelian Lie group SU(3) leading to,

$$\mathcal{L}_{\text{QCD}} = -\frac{1}{4}G^a_{\mu\nu}G^{a\mu\nu} + \bar{\psi}_i(i\gamma^\mu(D_\mu)_{ij} - \delta_{ij}m)\psi. \tag{1.9}$$

where $\psi_i(x)$ is the quark field in the fundamental representation of the SU(3) gauge group with i running 1 to 3. In this case, the generators are given by $T^a = \lambda^a/2$ with λ^a the Gell-Mann matrices for $a = 1, 2, ..., 8$. This leads to 8 massless gauge fields A^a_μ known as gluons. Since this is a non-abelian theory the strength tensor involves the terms $A^b_\mu A^c_\nu$ which imply self-interactions between the gluons and the kinematic term also implies the triplet and quartic self-interactions. QCD also predicts the coupling to be small at short distances such that the quarks behave as free particles within hadrons. In the perturbative regime, it is possible to establish QCD Feynman rules, while for the non-perturbative regime, the lattice QCD studies are implemented.

The ElectroWeak (EW) interaction can be obtained by introducing the $SU(2)_L \times U(1)_Y$ symmetry. Here the U(1) has only one generator, Y, corresponding to the weak hypercharge while SU(2) has three generators $T_a = \sigma_a/2$ ($a = 1, 2, 3$) where σ_a are the Pauli matrices. Then, the lagrangian is given by,

$$\begin{aligned}
\mathcal{L}_{\text{EW}} = &-\frac{1}{4}W^{\mu\nu}_a W^a_{\mu\nu} - \frac{1}{4}F^{\mu\nu}F_{\mu\nu} \\
&+ \bar{\psi}_L i\gamma^\mu D_\mu \psi_L + \bar{\psi}_R i\gamma^\mu D_\mu \psi_R
\end{aligned} \tag{1.10}$$

where $W^a_{\mu\nu} = \partial_\mu A^a_\nu - \partial_\nu A^a_\mu + gf^{abc}A^b_\mu A^c_\nu$ and $F^{\mu\nu} = \partial_\mu B_\nu - \partial_\nu B_\mu$ are the field strength tensor for the SU(2) and U(1) gauge fields, respectively. Notice that $W^a_{\mu\nu}$ is non-abelian and it contains self-interaction terms between the weak gauge bosons.

Different results [8–10] have shown that the weak interaction has a chirality nature, leading to the differentiation of left-handed and right-handed particles. Then ψ_L, ψ_R are the left-handed and right-handed lepton doublet and charged lepton singlet, respectively, as follows,

$$\psi_L \rightarrow E_L = \begin{pmatrix} e \\ \nu_e \end{pmatrix}_L, \quad Q_L = \begin{pmatrix} u \\ d \end{pmatrix}_L, \tag{1.11}$$

with $Y = -1/2$ and $Y = +1/6$, respectively. While for the right-handed field there are e_R and u_R with $Y = -1$ and $Y = +2/3$, respectively. This implies that the right-handed and left-handed particles do not transform in the same way, such that the mass term $\bar{\psi}_L \psi_R + \bar{\psi}_R \bar{\psi}_L$ is no longer invariant under $SU(2)_L \times U(1)_Y$ and is necessary a new mechanism to provide mass to the fermions.

1.1.2   Spontaneously Symmetry Breaking

The described EW lagrangian works only for massless bosons which is not the case according to the experimental observations. To fix this, the electroweak symmetry should be spontaneously broken from $SU(2)_L \times U(1)_Y$ to $U(1)_{\text{EM}}$ group by the so-called Brout-Englert-Higgs mechanism [11, 12]. For this, a $SU(2)$ doublet ϕ is introduced,

$$\phi = \begin{pmatrix} \phi^+ \\ \phi^0 \end{pmatrix}, \tag{1.12}$$

where ϕ^+ and ϕ^0 are positive and neutral electric charged fields. The lagrangian for ϕ is given by,

$$\mathcal{L}_{\text{Higgs}} = (D_\mu \phi)^\dagger (D^\mu \phi) - V(\phi), \tag{1.13}$$

with

$$D_\mu = \partial_\mu - ig \frac{\sigma_a}{2} A_\mu^a - ig' \frac{Y}{2} B_\mu. \tag{1.14}$$

Where g, g' are the coupling constants to A_μ^a and B_μ, respectively. The potential $V(\phi)$ is given by Eq. (1.6) with a non-trivial minimum of value $v \approx 246\text{GeV}$ called "vaccuum expectation value (v.e.v)" such that ϕ can be expanded around the v.e.v giving place to a physical particle known as the Higgs boson with mass,

$$m_H = \sqrt{2\lambda} v. \tag{1.15}$$
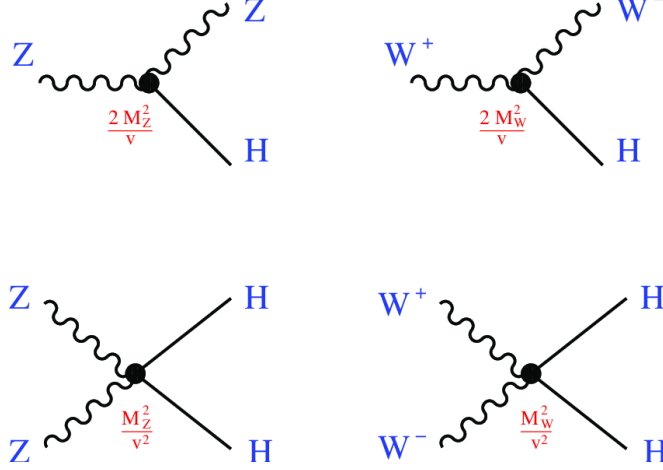
Figure 1.2: Different couplings between the Higgs boson and the EW Gauge bosons predicted by the SM [13].

From the covariant derivative, the mass of the Gauge bosons can be obtained to be,

$$m_{W^{\pm}} = \frac{vg}{2},$$
$$m_Z = \frac{v}{2}\sqrt{g^2 + g'^2}. \tag{1.16}$$
$$m_{\gamma} = 0.$$

This not only predicts the existence of the Higgs boson but also how it interacts with the electroweak gauge bosons ($W^{\pm}$, Z) and itself as shown in Fig. 1.2. To provide mass to the fermions via this mechanism, an extra term needs to be introduced, this is, the Yukawa lagrangian given by,

$$\mathcal{L}_{\text{Yuk},e} = -Y_e \bar{E}_L \cdot \phi\, e_R + h.c. \tag{1.17}$$

for the leptons while for the quarks,

$$\mathcal{L}_{\text{Yuk},q} = -Y_d \bar{Q}_L \cdot \phi\, d_R - Y_u \bar{Q}_L \cdot \tilde{\phi}\, u_R + h.c. \tag{1.18}$$

where $\tilde{\phi}$ is the conjugate of the Higgs doublet. In this way, the mass of the fermions is given by,

$$m_f = \frac{1}{\sqrt{2}} Y_f v. \tag{1.19}$$

The Higgs field, through spontaneous symmetry breaking (SSB), is the mechanism responsible for providing mass to the particles in the Standard Model (SM), and they are coupled to the Higgs boson through Yukawa couplings. These phenomena have been experimentally verified by the ATLAS and CMS collaborations, which officially announced the discovery of the Higgs boson in 2012 [5, 6]. Since its discovery, the SM has undergone extensive testing, particularly regarding the coupling of the Higgs boson to SM particles. These findings are illustrated in Fig. 1.3.

(a)   (b)
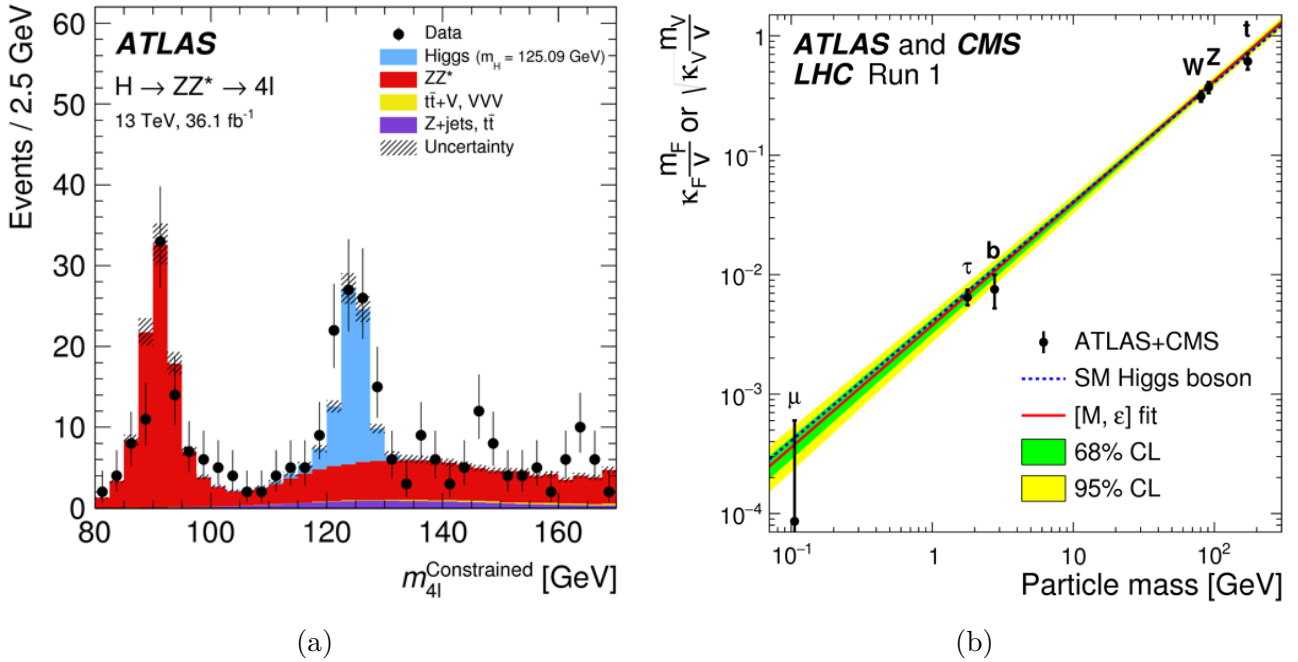
Figure 1.3: (a) Distribution of candidate Higgs events in $H \rightarrow ZZ^* \rightarrow 4\ell$ at 13 TeV. The excess of events around 125 GeV is consistent with SM predictions for the Higgs boson [14] (b) Measurements of the coupling of the Higgs-boson to fermions and vector bosons as a function of the particle mass compared to the SM expectation [15].

Despite numerous experimental tests and predictions still awaiting discovery, the Standard Model (SM) remains incomplete. Eq. (1.3) fails to explain all observed natural phenomena. For example, the mechanism detailed above do not explain why the particles have the mass they have, the origin of the neutrino mass and the order of magnitude, dark matter candidates, matter anti-matter asymmetry, etc. Furthermore, it cannot be reconciled with General Relativity.

1.1.3 The W-boson mass in the SM

The SM lagrangian predicts the massive electroweak bosons originated after Spontaneous Symmetry Breaking with a mass resulting from the Higgs sector. A simple relation among the Z and W boson is known as the custodial symmetry,

$$m_Z = m_W / \cos\theta_W, \tag{1.20}$$

where θ_W is the Weinberg angle given by $\tan\theta_W = g'/g$. The significance of custodial symmetry lies in its role in constraining the masses of the W and Z bosons relative to each other. In theories where custodial symmetry is exact, the masses of the W and Z bosons are degenerate, meaning they are equal. However, in reality, custodial symmetry is broken by quantum corrections. Nevertheless, the degree to which custodial symmetry is broken can still provide insights into physics beyond the Standard Model. Taking into account the quantum corrections, the W boson mass can be expressed as,

$$m_W^2 \left(1 - \frac{m_W^2}{m_Z^2}\right) = \frac{\pi\alpha}{\sqrt{2}G_F}(1 + \Delta r) \Rightarrow m_W^2 = m_Z^2 \left(\frac{1}{2} + \sqrt{\frac{1}{4} - \frac{\alpha\pi}{\sqrt{2}G_F m_Z^2(1 - \Delta r)}}\right) \tag{1.21}$$

where α is the fine-structure constant, G_F is the Fermi constant and Δr represents radiative corrections to the electroweak interactions. Notice that m_W at the leading order depends in well known parameters that have been measured with high precision such as $m_Z = 91.1876\pm0.0021$ GeV [16, 17], $G_F = 1.1663787(6) \times 10^{-5}$ GeV^{-2}(0.5ppm) [18] and $\alpha^{-1} = 137.035999206(11)$ [19] as shown in Fig. 1.4.

This means that the main source of uncertainty is carried in the radiative corrections Δr that accounts for quantum corrections in the SM (and extensions of it) arising from virtual particle loops in Feynman diagrams, particularly those involving the exchange of photons γ and Z bosons. These corrections can arise from the renormalization of parameters and can affect the predictions of certain observables in electroweak processes. At the one loop level, the quantum corrections
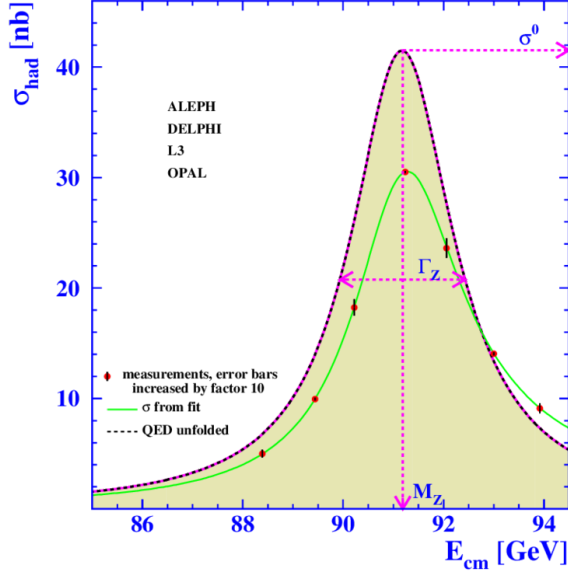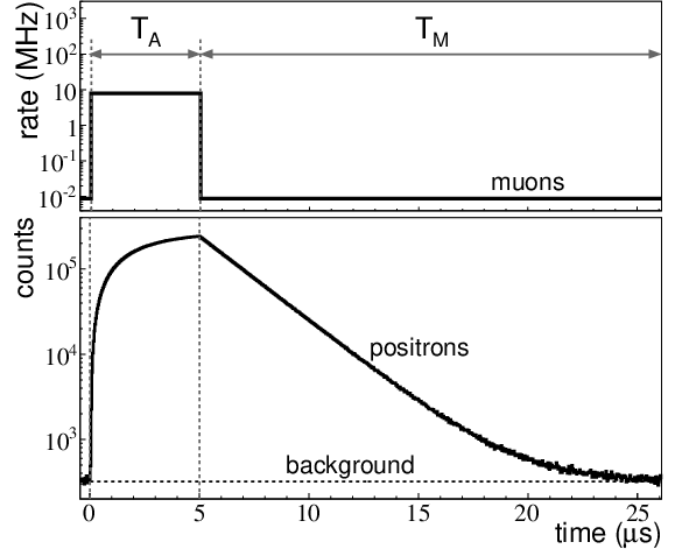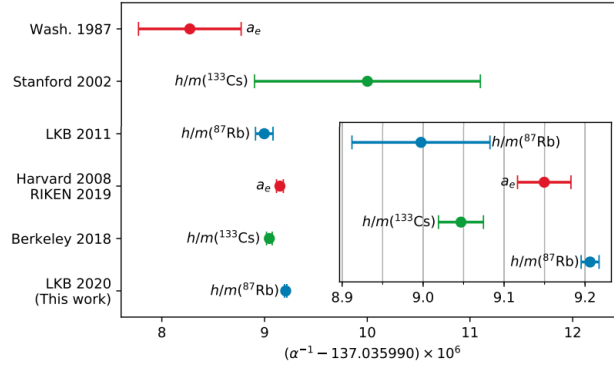
Figure 1.4: Precise measurements of m_Z, muon lifetime and fine-structure constant: (a) $Z-$ peak cross section observed by LEP in $e^+e^- \rightarrow$ hadrons and compared with the complete Standard Model prediction [17]. (b) Time dependence of the muon arrival rate (upper panel) and decay positron counts (lower panel) to determine G_F [18]. (c) Precision measurements of the fine-structure constant [19].

involving fermionic contributions in Δr allows to find the expression,

$$\Delta r = \Delta \alpha - \frac{\cos \theta_W^2}{\sin \theta_W^2} \Delta \rho + ... \tag{1.22}$$

where $\Delta \alpha \propto \log m_f$ is the shift in the fine-structure constant, $\Delta \rho$ involves contributions coming from the leading contribution to the $\rho = m_W^2/m_Z^2 \cos^2 \theta_W$ parameter, which relates to the isospin symmetry breaking in the Higgs sector of the Standard Model. It represents the difference between the measured value of $\sin^2 \theta_W$ and its tree-level prediction in the Standard Model. In other words, it accounts for quantum corrections higher order corrections (beyond the tree-level approximation) that are quadratically dependent on the top quark mass, m_t, and Higgs mass m_H effects. The leading order terms in $\Delta \rho$ for $m_W \ll m_H$ is given in Eq. (1.23) [20].

$$\Delta \rho = \frac{3 G_F m_W^2}{8\sqrt{2}\pi^2} \left[\frac{m_t^2}{m_W^2} - \frac{\sin^2 \theta_W}{\cos^2 \theta_W} \left(\ln \left(\frac{m_H^2}{m_W^2} \right) - \frac{5}{6} \right) + \dots \right] \tag{1.23}$$

However, up to date, Higher QCD corrections in $\mathcal{O}(\alpha\alpha_s)$, $\mathcal{O}(\alpha\alpha_s^2)$ and $\mathcal{O}(\alpha\alpha_s^3)$ are known [21–24]. While the full electroweak two-loop contribution in Δr has been fully calculated [25–28] and beyond the two-loop up to four-oop only fermionic contributions are known [29]. Most recent calculations for the leading three-loop contributions of $\mathcal{O}(G_F^3 m_t^6)$ and $\mathcal{O}(G_F^2 \alpha_s m_t^4)$ have been obtained for arbitrary values of the Higgs mass (expansions around $m_H = m_t$ and $m_H \ll m_t$) [30].

In this way, the calculation of $\Delta r = \Delta r(m_W, m_Z, m_H, m_t, ...)$ to obtain the W boson mass needs to be obtained by iterative procedures since it depends of m_W itself. This allows to not only obtain the W mass but also to set constraints in the Higgs boson mass that can be modified due to the uncertainties in the experiments, physics modelling, theory prediction, etc. Taking this into account, the prediction of the W boson mass has been carried out by the GFitter group [31, 32] using the least squares χ^2 method considering NNLO theoretical predictions, prospects for the LHC and ILC, new kinematic of the top quark and W boson mass measurements from the LHC, $\sin^2 \theta_{\text{eff}}^\ell$ (effective leptonic weak mixing angle) result from the Tevatron, and a new evaluation of the hadronic

contribution to $\alpha(M_Z^2)$. This leads to an updated result in 2018 of the W boson mass to be,

$$m_W = 80.3535 \pm 0.0027_{m_t} \pm 0.0030\delta_{\text{theo}m_t}$$

$$\pm 0.0026_{M_Z} \pm 0.0026\alpha_s$$

$$\pm 0.0024_{\Delta\alpha_{\text{had}}} \pm 0.0001_{M_H} \pm 0.0040\delta_{\text{theo}M_W} \text{ GeV}$$

$$= 80.354 \pm 0.007_{\text{tot}} \text{ GeV},$$

(1.24)

that corresponds to a numerical approximation of the theoretical expression with the largest uncertainties due to m_t and m_Z, respectively. Result from the `GFitter` group is shown in Fig. 1.5
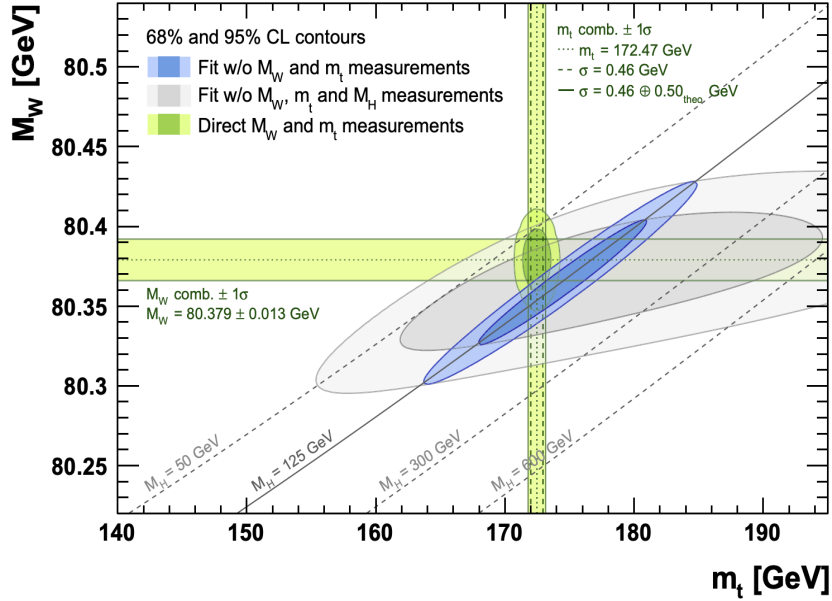
Figure 1.5: Contours at 68 and 95% CL obtained from scans of m_W versus m_t for the fit including (blue) and excluding the Higgs boson mass m_H measurement (grey), as compared to the direct measurements (green vertical and horizontal 1σ bands, and two-dimensional 1σ and 2σ ellipses) and compared to the direct measurements of m_W and m_t [31].

1.1.4 Physics Beyond the SM

Even though the W boson mass can be predicted with high precision in the SM framework, this is not fully complete since several limitations to current problems are still open like neutrino mass, matter anti-matter asymmetry, dark matter, etc. For this reason, several scenarios propose new

alternatives to the SM like Grand Unified Theories (GUTs), Loop Quantum Gravity, String Theory and Extra Dimensions, etc. While others are extensions of the SM like SUpersymmetry (SUSY), Dark Matter, Composite Higgs, etc.

In particular, SUSY is an extension of the Standard Model that proposes a symmetry between fermions and bosons, introducing supersymmetric partners to each particle in the SM. Since these new particles are out of the SM and they are so massive, they cannot be observed with the current experiments. However, in the current energy regime indirect effects of SUSY could be manifested through radiative corrections, Δr, that potentially could affect the running of the Higgs boson mass parameter affecting the W boson mass indirectly.

SUSY has been largely studied through the years with well established theoretical results. The simplest one is known as the Miniminal Super Symmetric Model (MSSM) in which each particle has a superpartner with a spin differing by $1/2$, such as electrons with selectrons and quarks with squarks. The model also includes two Higgs doublets, resulting in five physical Higgs bosons. To prevent rapid proton decay and stabilize the lightest supersymmetric particle (LSP), often the neutralino and a dark matter candidate, $R-$parity is introduced. Supersymmetry is broken through soft SUSY-breaking terms, allowing sparticles to have distinct masses. The MSSM addresses issues like the hierarchy problem and unifies forces, with potential observable signatures at particle colliders and implications for cosmology. In this framework, the radiative corrections to the m_W include contributions from sfermions, charginos, neutralinos and the Higgs bosons that enter at one-loop level. Recent study in Ref. [33] evaluates the W boson mass in the MSSM considering a full one-loop calculation, all available MSSM two-loop corrections as well as the full Standard Model result. The mass shift δm_W arising from changing Δr by the amount Δr^{SUSY} is given by,

$$\delta m_W = -\frac{m_W^{\mathrm{ref}}}{2} \frac{s_W^2}{c_W^2 - s_W^2} \Delta r^{\mathrm{SUSY}}. \tag{1.25}$$

with Δr^{SUSY} the MSSM contribution and $m_W^{\mathrm{ref}} = 80.425$ GeV. In the MSSM the higgs field and the scalar superpatners are related through the triliniear Higgs-$\tilde{t}, \tilde{b}$ coupling $A_{t,b}$ and the different Higgs are mixed through the Higgs mixing parameter μ. To these, physical phases $\phi_{A_t} + \phi_\mu$ and
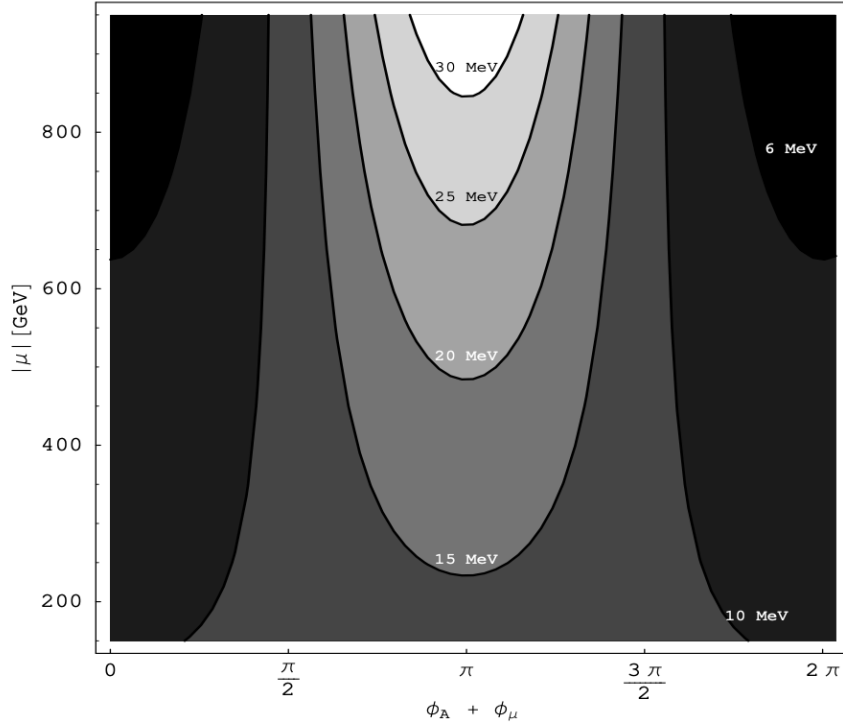
Figure 1.6: Contour lines of the squark contributions to δm_W in the plane of $(\phi_{A_b} + \phi_\mu)$ and $|\mu|$, where $\phi_A \equiv \phi_{A_t} = \phi_{A_b}$ [33].

$\phi_{A_b} + \phi_\mu$ can be associated such that the variation of $\phi_A + \phi_\mu$ can affect the shift in m_W by more than 20 MeV as shwon in Fig. 1.6. As in the SM, m_W has a dependency with the top quark mass and the MSSM can be scanned to see the values of m_W as shown in figure 1.7

SUSY is not the only BSM extension that has studied the indirect search through m_W, since other scenarios such as Dark Matter (DM), shed light on the W boson mass anomalies. One scenario is to consider the U(1) dark sector as an extension of the SM [34] in which DM candidates with mass ranging from several hundred GeV to TeV can mix up with the SM particles. These new particles are capable of producing shifts in the W mass value for at most 10 MeV while more complex extensions can easily shift m_W by 77 MeV. These extensions allow the Z boson to mix up with the DM candidates giving place to a massive Z' gauge boson that can shift m_W by,

$$\Delta m_W^2 = \frac{c_W^2 m_Z^2}{c_W^2 - s_W^2} \left(\delta^2 s_W^2 c_W^2 \right) \left(\frac{m_Z}{m_{Z'}} \right)^2, \tag{1.26}$$

with δ the kinetic mixing parameter [35]. These parameter allows to scan the DM impact in the W boson mass as shown in Fig. 1.8 in which the red region is ruled by experimental constraints while

15
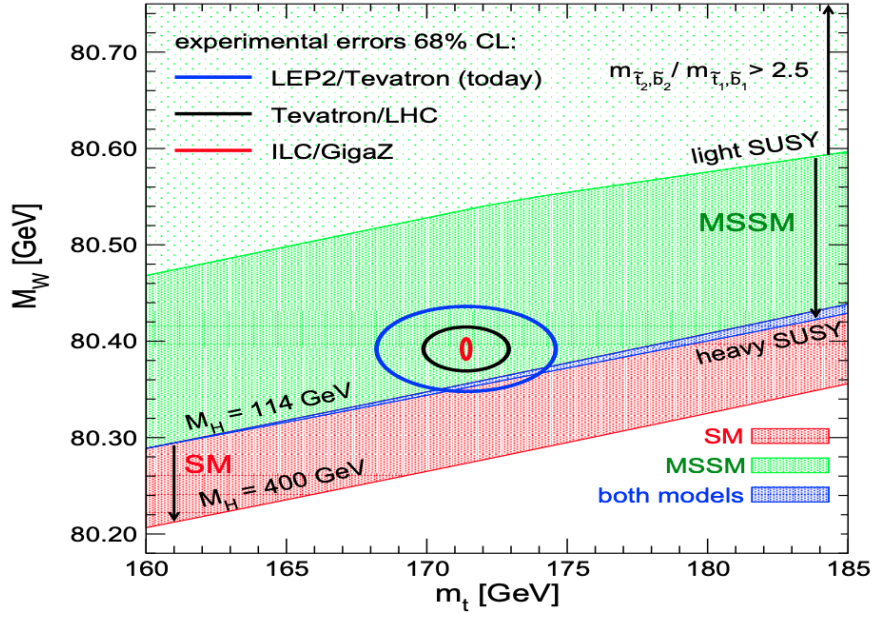
Figure 1.7: Prediction for m_W in the MSSM and the SM as a function of m_T in comparison with the experimental results for m_W and m_T for Tevatron / LHC and the ILC. [33].

for achieving $\delta m_W \sim 77$ MeV larger values of the kinetic term are required leading also to a more massive Z'.

Although the MSSM and DM are good candidates, they are not the only one. Other models that extend the SM can provide new signatures that can potentially affect m_W such as Axion-like particles, vector-like leptons, leptoquarks, etc [36–38]. These hypothetical particles could contribute into higher order loops and modify the radiative corrections in Δr that could be measured in experiments. However, many of these new candidates are currently out of the range of detection that experiments like the LHC can achieve but probably new experiments such as FCC or CEPC could potentially detect [39–41].

1.2 W and Z boson production in colliders

The SM shows that the weak vector gauge bosons couple to the fermions at the tree level such that they can be produced by quark anti-quark annihilation,

$$q\bar{q}' \to W, \quad q\bar{q} \to Z/\gamma. \tag{1.27}$$

16
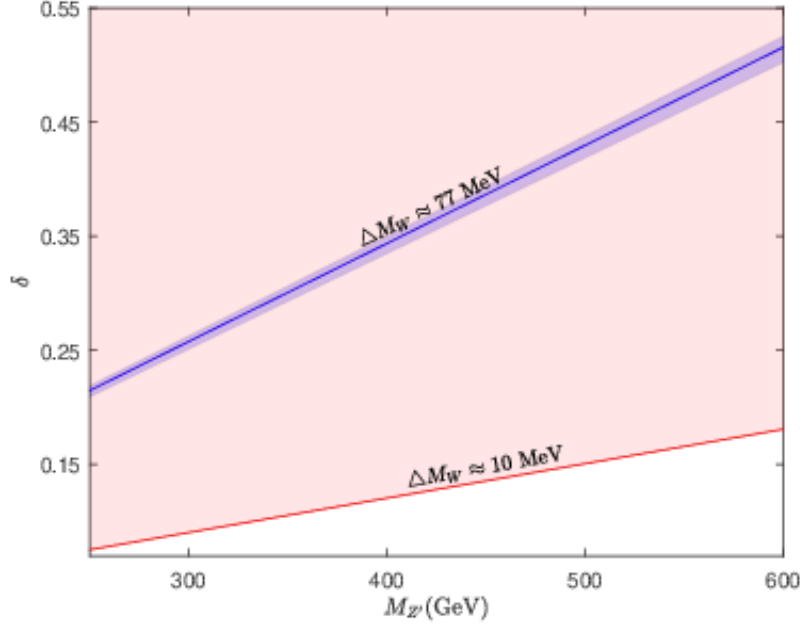
Figure 1.8: W boson mass enhancement generated by the dark U(1) extension of the SM with the Z' dark boson [35].

However, due to the QCD confinement, it is not possible to have quarks independently and for that reason is necessary to use hadrons, h, to generate the processes as in (1.27). For this, hadron colliders such as the LHC, play a crucial role by colliding proton beams at high energy leading to the production of vector bosons, V, plus several other particles, X, in the final state,

$$h_1(p_1) + h_2(p_2) \to V + X, \tag{1.28}$$

with p_1 and p_2 the momenta of the hadrons. A difficulty of the colliders is that hadrons are composite objects with quarks and gluons commonly called *partons*. In the case of the LHC, this implements protons as hadrons. Protons are composite states of two up quarks and one down quark (uud) known as the valence quarks that interact by the gluon exchange. However, the complexity of the QCD nature inside the proton leads to the gluon-gluon self-interaction producing more gluons but also the production of quarks known as sea quarks. To describe the internal structure of the proton, the so-called Parton Distribution Functions (PDFs) are used.

17

1.2.1 Parton Distribution Functions

To understand the proton-proton collisions is necessary to disentangle the dynamic inside of the composite states as a function of its partons. Several studies [42–45] have performed lepton-proton Deep Inelastic Scattering (DIS) to study the distribution of proton's momentum among the partons through the so-called DGLAP evolution equations [46–50] as a function of the energy scale Q^2. These equations are given by,

$$\frac{\partial f_i(x, Q^2)}{\partial \ln Q^2} = \sum_j \int_x^1 \frac{dz}{z} P_{ij}(z, \alpha_s(Q^2)) f_j\left(\frac{x}{z}, Q^2\right). \tag{1.29}$$

Where $f_i(x, Q^2)$ is the so-called Parton Distribution Function (PDF) that represents the probability density to find a parton i carrying momentum fraction x at energy scale Q. In Eq. (1.29), $\sum_j$ runs over all possible parton types j. It indicates that the evolution of the PDF for parton type i depends on contributions from all other parton types j. $\frac{\partial f_i(x, Q^2)}{\partial \ln Q^2}$ represents the evolution of the parton distribution function (PDF) for parton type i with respect to the logarithm of the momentum transfer scale Q^2. The integral $\int_x^1 \frac{dz}{z}$ is taken over the variable z, which represents the fraction of the parton's momentum after splitting. The integration limits are from x to 1, covering all possible values of z such that x/z remains a valid fraction (between 0 and 1). $P_{ij}(z, \alpha_s(Q^2))$ are the splitting functions (or kernels) which describe the probability of a parton of type j splitting into a parton of type i carrying a fraction z of the original parton's momentum. The splitting functions depend on the strong coupling constant $\alpha_s(Q^2)$, which varies with the scale Q^2. $f_j\left(\frac{x}{z}, Q^2\right)$ is the parton distribution function for parton type j evaluated at the scaled momentum fraction x/z and the same scale Q^2. It represents the distribution of parton j before splitting [47–50].

Due to the complexity of the problem, an exact analytical solution cannot be found to study the dependence of x as a function of Q^2. However, some perturbative analytical solutions for small values of x can be obtained in the Mellin space as shown in [51–53] that is not only useful for particular scenarios but it also allows to constrain the uncertainties analytically.

In the general case, several PDFs sets [54–62] can be generated by performing global fits to the data from a wide range of high-energy particle collisions, such as deep inelastic scattering (DIS),

inclusive jet production, vector boson production and hadron collider experiments. They aim is to directly extract the parton distributions that best describe the experimental measurements, such that the experimental uncertainties are propagated through the fitting procedures to provide the uncertainties in the PDF. For this, a function form with free parameters at the starting scale (low Q^2) is chosen and the evolution is performed using the DGLAP equations to evolve the PDFs to the scales of the data adjusting the free parameters to have an agreement with it. Examples include the NNPDF (NNPDF3.0, NNPDF3.1) PDF [61, 62] that implements neural networks to efficiently fit and interpolate PDFs from a wide range of experimental data, the CTEQ (CTEQ6, CTEQ6.1) PDF [59] which utilizes perturbative QCD calculations and parameterizations based on specific models, among others.

The PDFs fitting machinery is described in Fig. 1.9 while in Fig. 1.10 the PDFs for $Q^2 = 10$ GeV^2 and $Q^2 = 10^4$ GeV^2 are shown. These plots illustrate the behavior of parton distribution functions as a function of the momentum fraction x at different energy scales Q^2. They show how different parton species contribute to the internal structure of the proton, with gluons and sea quarks dominating at low x and valence quarks being more significant at higher x. The evolution of these distributions with Q^2 is governed by the DGLAP equations, reflecting the changing dynamics of parton interactions at different energy scales.
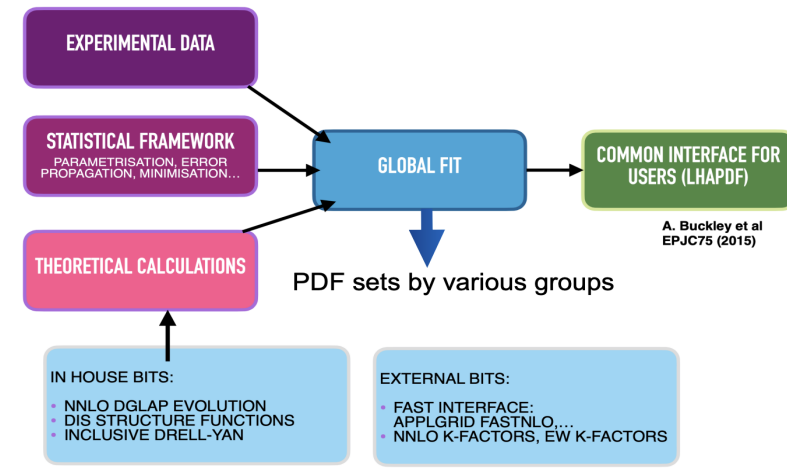
Figure 1.9: Scheme of the PDF fitting machinery scheme [63].
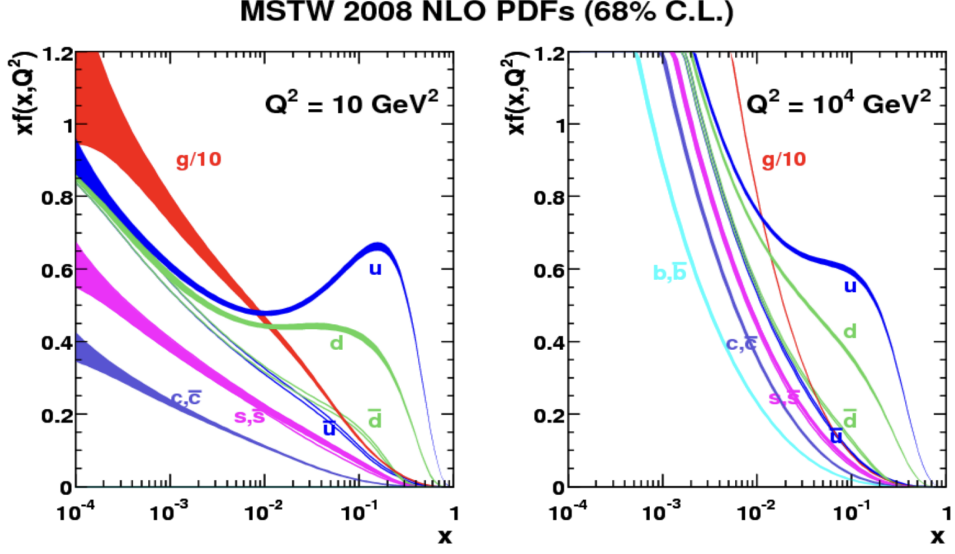
Figure 1.10: MSTW2008 parton distribution functions for $Q^2 = 2$ GeV^2 and $Q^2 = 10^4$ GeV^2 [64].

1.2.2 W and Z boson cross section

The cross section (σ) is a measure of the probability that a particular interaction will occur when two particles collide. It represents the effective area presented by a target particle for an interaction to take place. Two types of cross section are of interest: the total cross section, σ, represents the probability of any interaction happening between the colliding particles including all possible outcomes. On the other hand, the differential cross section, $d\sigma$, gives the probability of a specific outcome occurring within a certain range of angles, energies, or momenta. It provides more detailed information about the interaction process.

In hadron colliders, two QCD regimes can take place, known as hard QCD and soft QCD. The hard QCD regime typically refers to processes involving high momentum transfers or high-energy collisions. In these processes, the momentum transfer Q^2 between the initial and final-state particles is large, typically on the order of the energy scale of the process itself. For that reason, perturbative QCD (pQCD) calculations are usually applicable in the hard regime, where the strong coupling constant is small, allowing for reliable perturbative expansions.

On the other hand, the soft QCD regime, involves processes with low momentum transfers or low-energy interactions. This means, the momentum transfer is small compared to the energy scale Q^2 of the process, and particles typically have momenta comparable to or smaller than the QCD

20

scale, Λ_{QCD}. These regime often involve non-perturbative effects of QCD, where the strong coupling constant is large and perturbative methods are not applicable.

To produce vector bosons like the W boson in hadron colliders, the large momentum transfer Q^2 between the partons is needed, i.e. hard QCD. For this, the ability to separate the short distance physics and the long distance physics is the key to study the perturbartive QCD known as **factorization theorem**. This establishes that it exists a "factorization scale μ_F" (that separates the hard QCD and soft QCD regimes) for which the cross section can be factorized into separate parts containing the long distance effects in the PDFs and the hard scatter process of the partons on its sub-cross section $\sigma_{ab \to V}$. The sub-cross section $\hat{\sigma}_{ab \to V}$ is computable at a renormalisation scale μ_R. Taking this into account, the cross section of the hadron-hadron collision process in (1.28) can be written as,

$$\sigma_{h_1 h_2 \to V+X} = \sum_{ab} \int_0^1 dx_a dx_b f_{a/h1}\left(x_a, \mu_F^2\right) f_{b/h2}\left(x_b, \mu_F^2\right) \hat{\sigma}_{ab \to V}(\mu_F, \mu_R), \tag{1.30}$$

where f_{a,h_1} and f_{b,h_2} are the PDFs of the parton a in hadron h_1 and parton b in hadron h_2, respectively. Moreover, due to the factorization theorem the parton cross section can be expressed in terms of the strong coupling, μ_R. Both PDFs and the $\sigma_{ab \to V}$ can be computed at Leading-Order (LO), Next-to-Leading-Order (NLO) or Next-to-Next-to-Leading-Order (NNLO). For this, is convenient to express the partonic cross section as a series in the strong coupling constant, α_s, and choosing the factorization scale equal to the renormalization scale and equal to the vector boson mass, i.e. $\mu_F = \mu_R = m_{W/Z}$. In this way, the cross section can be express as follows,

$$\sigma_{h_1 h_2 \to V+X} = \sum_{ab} \int_0^1 dx_a dx_b f_{a/h1}\left(x_a, \mu_F^2\right) f_{b/h2}\left(x_b, \mu_F^2\right) \times \left[\hat{\sigma}_0 + \alpha_s\left(\mu_R^2\right)\hat{\sigma}_1 + \alpha_s^2\left(\mu_F^2\right)\hat{\sigma}_2 + ...\right]_{ab \to V}, \tag{1.31}$$

Several experiments have measured the cross sections of different particles and processes. The results performed by the ATLAS collaboration are shown in Fig. 1.11 while the SM cross section prediction at different centre-of-mass energy $\sqrt{s}$ is shown in Fig. 1.12.

It is convenient to express the cross section as a function of kinematic variables such as the
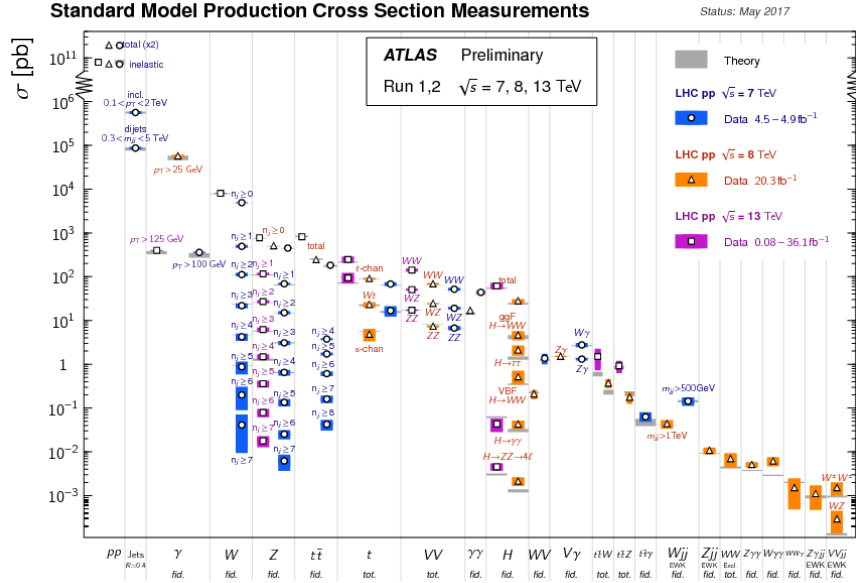
Figure 1.11: cross-section measurements in pp collisions at $\sqrt{s} = 7, 8, 13$ TeV for a variety of SM processes by the ATLAS collaboration [65].

rapidity, y, of the boson given by,

$$y = \frac{1}{2}\log\left(\frac{E + p_z}{E - p_z}\right). \tag{1.32}$$

and the parton momentum fraction,

$$x_a = \frac{M}{\sqrt{s}}e^y, \quad x_b = \frac{M}{\sqrt{s}}e^{-y}, \tag{1.33}$$

where M is the boson mass and $\sqrt{s}$ the centre-of-mass energy of the colliding hadrons. Therefore, different values of M and y probe different values of x and Q^2. Using this, the lowest order of the differential cross section in the perturbative expansion can be expressed as a function of the boson rapidity to be,

$$\frac{d\sigma}{dY} = \frac{1}{s}\sum_{ab} f_{a/h1}\left(x_a, M^2\right) f_{b/h2}\left(x_b, M^2\right) \times \hat{\sigma}_0(M)|_{ab \to V}, \tag{1.34}$$

in which the rapidity distribution at LO depends directly to the PDFs. In this way, by measuring Eq. (1.34) for $Q^2 = M^2$ the PDFs can be constrained for a given x. Similarly, using the boson rapidity distributions could also provide additional information to constrain the parton density functions. Fig. 1.13 shows the theory predictions of the rapidity distributions at LO, NLO and

22
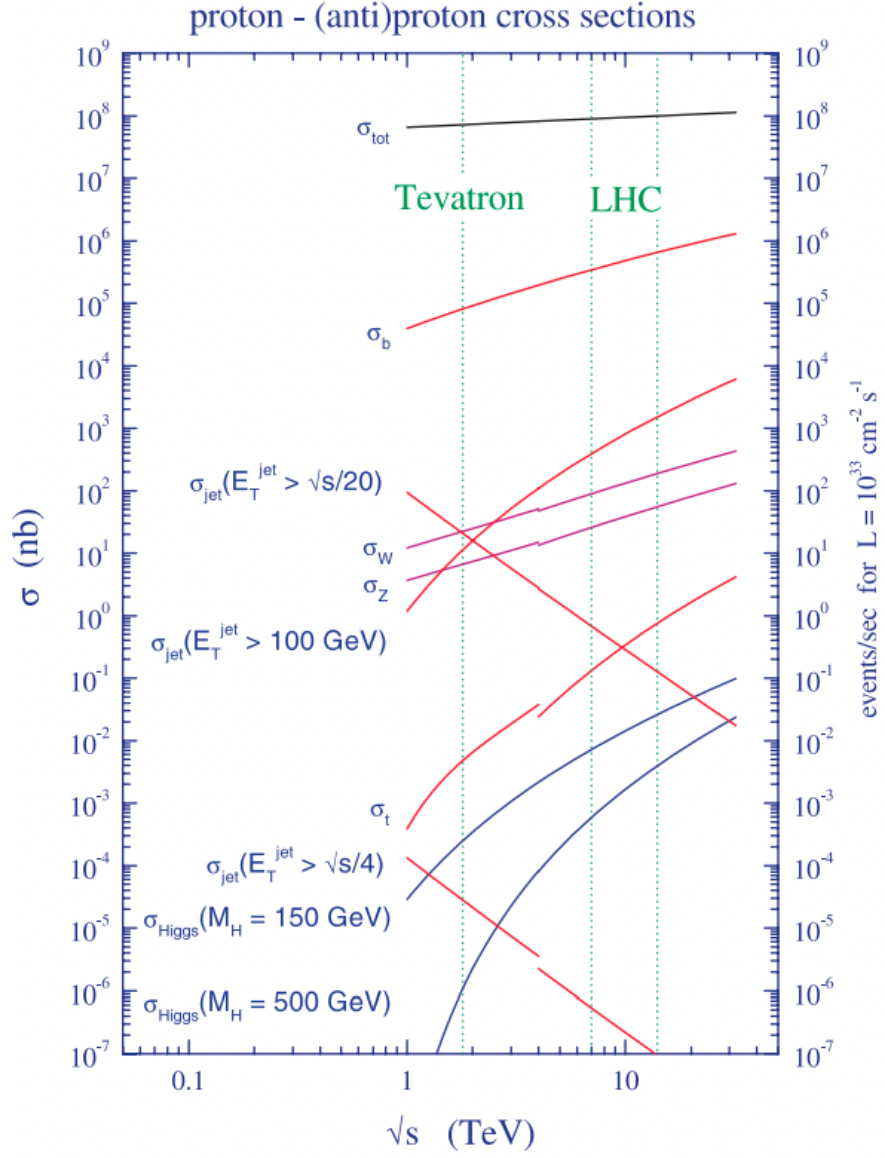
Figure 1.12: Standard Model cross sections at the Tevatron and LHC colliders as function of the centre-of-mass energy $\sqrt{s}$ [66].

NNLO for the $W^\pm$ and Z bosons at $\sqrt{s} = 14$ TeV. The significant reduction in the uncertainty bands from LO to NNLO indicates that higher-order corrections greatly enhance the precision of these predictions. This increased precision is crucial for reducing theoretical uncertainties in the cross-section measurements, thereby allowing for more accurate comparisons with experimental data.
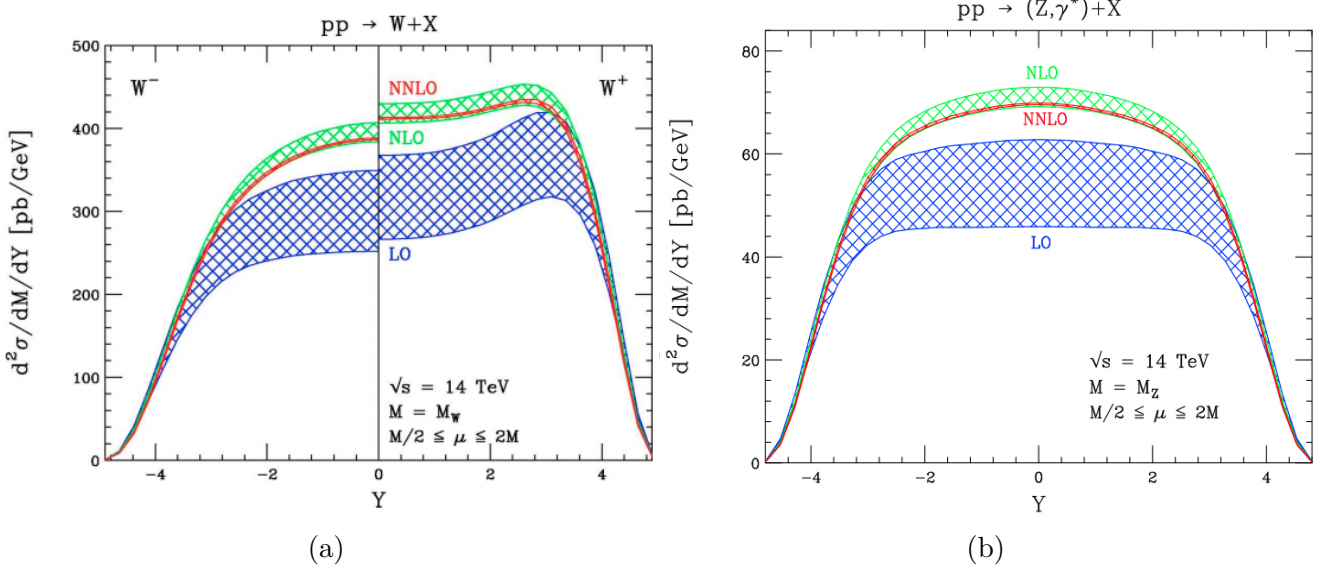
Figure 1.13: Theory predictions at LO, NLO and NNLO of the rapidity distributions for (a) W and (b) Z boson production in proton-proton collisions at $\sqrt{s} = 14$ TeV. The bands indicate the factorization and renormalization scale uncertainties, obtained by scale variations in the range $m_{W/Z}/2 \le \mu \le 2m_{W/Z}$ [67].

Next to the rapidity, one of the interesting quantities to look at is the boson transverse momentum, p_T. At the Leading Order (LO) the p_T of the boson with respect to the beam axis is expected to be zero. However, in the Next-to-Leading-Order case the partons can contribute to the p_T in two scenarios. The low p_T scenario is generated by multiple soft or almost collinear partons, while the high p_T scenario is dominated by the emission of one or multiple hard partons. The relevant NLO processes are $q\bar{q} \to Vg, qg \to Vq$, etc. Similarly, the NNLO processes like the gluon fusion can be included and convoluted with the PDFs to obtain the differential cross section as shown in [68].

In particular, for large momentum scenario $p_T \gg M$ the differential cross section can be obtained while for the low p_T case several divergences appear that can be treated in perturbation theory by the resummation formalism. In this way, an expression can be found but without including the

emission of multiple gluons.

In practice, to model the transverse momentum of the vector bosons, p_T^V, numerical approaches are required. For example, the modelling of the low p_T regime can be carried out by RESBOS [69, 70] by resumming the next-to-next-to-leading-logarithms (NNLL). Another approach is by the tunning of the parton shower Monte Carlo generators and analytical resummation free parameters to match the p_T in data through programs like DYTURBO [71], PYTHIA [72], HERWIG [73] and SHERPA [74]. Recent study in Ref. [75] developed by the ATLAS collaboration have performed the precise measurement of the transverse momentum of the W and Z bosons at $\sqrt{s} = 5$ and 13 TeV with low pile-up.

1.3 Status of W-boson mass measurements

The W boson mass, m_W, can be measured by different statistical methods and using different observables. One of the usual approaches is through the lepton transverse momentum, p_T^ℓ, as it is less sensitive to the pile-up and provides a good resolution. However, p_T^ℓ is sensitive to the modelling of the W boson transverse momentum p_T^W. An alternative observable and directly related to the W boson mass is the transverse mass, m_T, that is less sensitive to the p_T^W variations but its statistical is more sensitive to the pile-up. Other observables as the lepton rapidity, η_ℓ, and the hadronic recoil, u_T, can also be included to constrain the fits and to reduce the systematic uncertainties such as the ones related to the PDFs. Other approaches include simultaneous fits to the q/p_T distrbutions of the boson candidates. In principle, a good determination of m_W would exploit all the possible variables to reduce the systematic uncertainties that could possible bias the final result. However, it is well known that each experiment has its own limitations and it can only access to specific information. Fig. 1.14 shows the p_T^ℓ, m_T and q/p_T distributions in $W \to \mu\nu$ decay channel used by the ATLAS [76], LHCb [77] and CDF [78] collaborations, respectively to determine the most accurate values of the W boson mass.

The first experiments that measured the W boson mass were the UA1 and UA2 collaborations located at CERN's Super Proton Synchrotron (SPS) using proton anti-proton collision $p\bar{p} \to W^\pm + X$
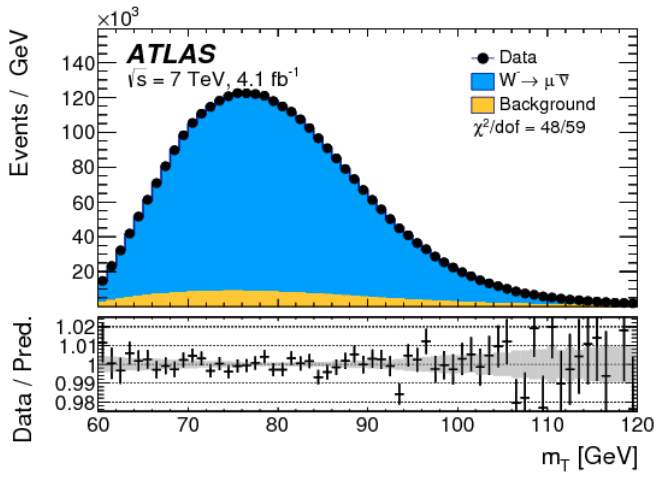
(a)
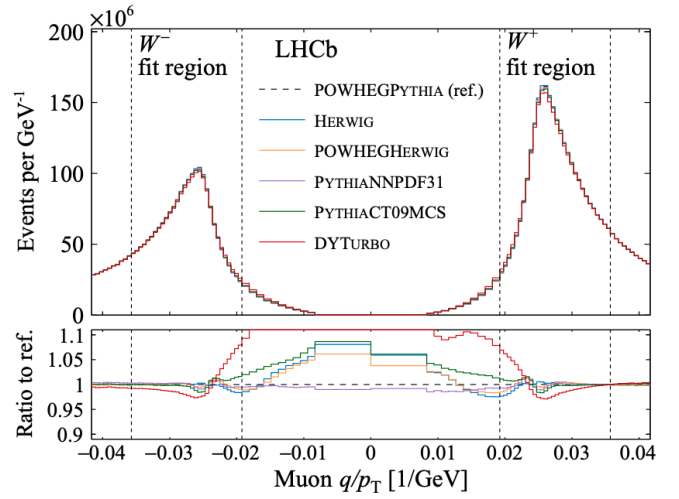
(b)
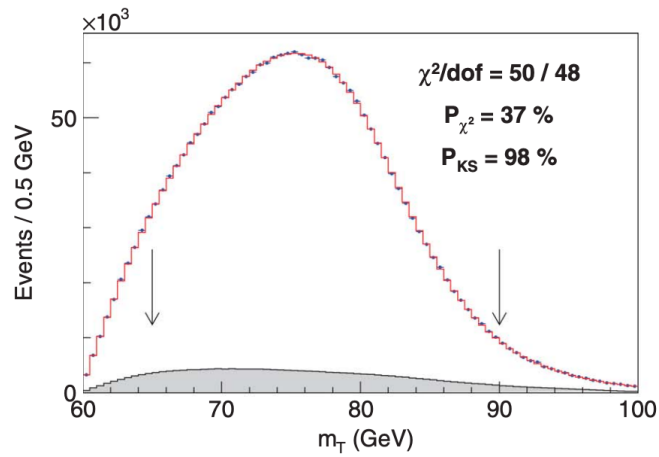
(c)

Figure 1.14: The (a) p_T^ℓ, (b) q/p_T and (c) m_T distributions for W events in the muon decay channel by the ALTAS [76], LHCb [77] and CDF [78] collaborations.

during the 1980s. These experiments were crucial in the discovery of the W and Z bosons, which confirmed the electroweak theory and led to Nobel Prizes for Carlo Rubbia and Simon van der Meer in 1984. However, while these experiments played an important role in establishing the existence of the W and Z bosons, they did not measure the W boson mass with the precision achieved by later experiments, their result was [79],

$$m_W^{\text{UA}} = 81^{+5}_{-5} \text{ GeV}. \tag{1.35}$$

After UA, The LEP (Large Electron-Positron Collider) experiments, including DELPHI, ALEPH, L3, and OPAL, were conducted at CERN from 1989 to 2000. LEP was a predecessor to the LHC and operated at energies up to 209 GeV, making it the most powerful electron-positron collider of its time. While the LEP experiments focused on a wide range of physics topics, including precision tests of the Standard Model, searches for the Higgs boson, and studies of electroweak interactions, they also made measurements of the W boson mass. The primary method LEP used to measure the properties of the W boson involved the process of "radiative return" in the production of W boson pairs. In e^+e^- collisions at high energies, the electron and positron can annihilate to produce a virtual photon (γ^*), which subsequently decays into a pair of particles, such as a $W^\pm$ boson or Z boson. This process is known as radiative return because the virtual photon is radiated off the initial e^+e^- pair. In the case of W boson studies, the aim is focused on the virtual photon decay into W^+W^- pairs that later on produce observable final states, such as charged leptons (electrons, muons, or taus) and their corresponding neutrinos, or quarks. LEP detectors, such as those in the ALEPH, DELPHI, L3, and OPAL experiments, were designed to measure the properties of the particles produced in the W^+W^- decay allowing them to reconstruct the kinematic properties of the W bosons, such as their momentum and energy. The primary type of measurement LEP performed regarding the W boson production was the measurement of its production cross section σ_{WW}. By comparing the observed production rate of W^+W^- pairs to theoretical predictions based on the Standard Model, LEP experiments could extract information about the W boson's mass, coupling strengths, and other properties. The result from LEP [80] was,

$$m_W^{\text{LEP}} = 80375 \pm 25(\text{stat.}) \pm 22(\text{syst.}) \text{ MeV} = 80376 \pm 33 \text{ MeV} \tag{1.36}$$

The next W mass measurement was carried out by the Tevatron collaboration, which consisted primarily of the CDF (Collider Detector at Fermilab) and D0 experiments that made significant contributions to the measurement of the W boson mass using proton-antiproton collisions. This collider at Fermilab accelerated protons and antiprotons to high energies and collided them head-on at the center of the CDF and D0 detectors. These collisions produced a variety of particles, including W bosons. The primary production channels for W bosons involved quark-antiquark annihilation ($q\bar{q} \rightarrow W$). The most common decay modes of the W boson are into a charged lepton (electron or muon) and a neutrino ($W \rightarrow \ell\nu$). These leptonic decay channels were particularly useful for the measurement of the W boson mass because they provided clean and well-identified final states. Since neutrinos are weakly interacting particles that escape detection, their presence was inferred indirectly from the missing transverse momentum in the detector. By balancing the momentum in the transverse plane (perpendicular to the beam direction), researchers estimated the momentum of the neutrino and thus reconstruct the full kinematics of the W boson decay. CDF and D0 employed sophisticated event reconstruction algorithms to identify and reconstruct the decay products of the W boson in their detectors. By analyzing large datasets of collision events, researchers selected candidate events consistent with the production and decay of W bosons and applied statistical techniques to extract the W boson mass. The Tevatron experiments measured the production cross section of W bosons and compared it to theoretical predictions. Additionally, they performed template fits to the observed kinematic distributions of W boson decay products, such as the transverse mass distribution, to extract the W boson mass and its uncertainty to be [81],

$$m_W^{\text{TeVatron}} = 80387 \pm 16 \text{ MeV},\tag{1.37}$$

that including measurements obtained in electron-positron collisions at LEP yields the world average

$$m_W^{\text{World Avg}} = 80385 \pm 15 \text{ MeV}.\tag{1.38}$$

In 2017 the ATLAS collaboration performed the W boson mass measurement at $\sqrt{7}$ TeV [76] to be,

$$m_W^{\text{ATLAS 2017}} = 80370 \pm 19 \text{ MeV}. \tag{1.39}$$

followed up by the LHCb m_W measurement in 2022 [77],

$$m_W^{\text{LHCb}} = 80354 \pm 32 \text{ MeV}. \tag{1.40}$$

However, the most precise m_W measurement published up to date is the CDFII 2022 [78] result,

$$m_W^{\text{CDFII}} = 80434 \pm 9 \text{ MeV}, \tag{1.41}$$

which is in tension with the SM prediction up to 7σ.

The compatibility and combination of the world W-boson mass measurements using ATLAS, LHCb, CDF, and D0 results have been largely studied in [82] where for all m_W values available up to date are combined to obtain the following m_W value,

$$m_W = 80395 \pm 12 \text{ MeV}. \tag{1.42}$$

with a 0.5% compatibility while a 91% compatibility is obtained when the CDF measurement is removed, leading to,

$$m_W = 80369 \pm 13 \text{ MeV}. \tag{1.43}$$

which differs by 3.6σ from the CDF result. The latest m_W obtained by the global analysis of electroweak data in the Standard Model [83] using state-of-the art experimental and theoretical results, including a determination of the electromagnetic coupling at the electroweak scale based on recent lattice calculations leads to a SM value of,

$$m_W^{\text{SM}} = 80355 \pm 6 \text{ MeV}. \tag{1.44}$$
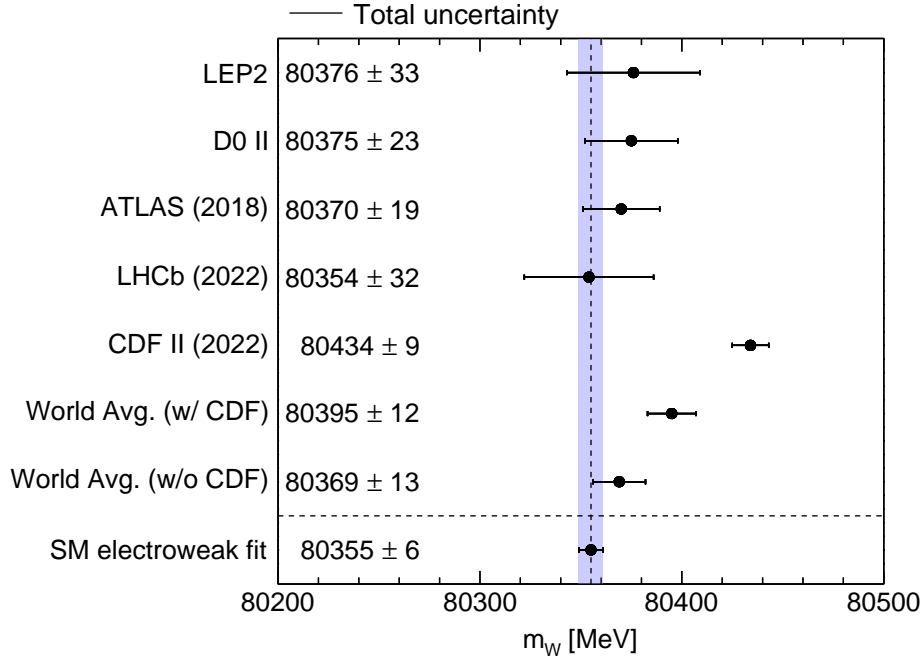
Figure 1.15: Current status of the W boson mass including the latest world average with and without CDF II (2022) result.

The current status of the W boson mass is shown in Fig. 1.15. Another parameter of the W boson that, unlike the W boson mass, has not been extensively measured by different collaborations is the W boson width, Γ_W. This can be calculated in the SM and the GFitter group computed the predicted value [31] to be,

$$\Gamma_W = 2091 \pm 1 \text{ MeV}. \tag{1.45}$$

While the latest global electroweak fit [83] provides the SM value to be,

$$\Gamma_W^{\text{SM}} = 2088 \pm 1 \text{ MeV}. \tag{1.46}$$

The value of m_W in (1.44) and Γ_W in (1.46) are taken as the SM reference value for the present work. Recently, the ATLAS collaboration has performed the measurement of both m_W and Γ_W using the $\sqrt{s} = 7$ TeV dataset [84] and the results are largely discussed in section 6.6.

Chapter 2

The ATLAS detector at the CERN LHC

The Large Hadron Collider (LHC) stands as the most advance machine of particle acceleration developed by the European Organization for Nuclear Research (CERN) and currently with a large worldwide network in several countries of the world [85]. Based near Geneva, it occupies an average depth of 100 meters within a 26.7 km circumference tunnel originally constructed for its predecessor, the Large Electron-Positron Collider (LEP). The LHC is engineered to accelerate protons to energies reaching 7 TeV and heavy ions to 2.56 TeV per nucleon. Within its structure, particles are collided at four distinct interaction points, where specialized detectors are located: the Large Ion Collider Experiment (ALICE) [86], the Large Hadron Collider beauty (LHCb) [87], the Compact Muon Solenoid (CMS) [88], and the A Toroidal LHC ApparatuS (ATLAS) [89]. ALICE's is focused on several heavy ions studies from which the quark-gluon plasma is probably one of the main core of studies. The LHCb is devoted to flavour physics such as those with $b-$quarks to unravel the matter-antimatter asymmetry, lepton flavour universality violation, etc. On the other, CMS and ATLAS are considered as multipurpose and versatile instruments, with a broad spectrum of research such as precision measurements of the standard model (SM), physics Beyond the SM (BSM), etc.

The following chapter is organized a follows, section 2.1 provides a description of the CERN accelerator complex. Section 2.2 describes the ATLAS detector and its sub-detectors such as the Inner Tracker Detector (ID), Muon Spectrometer (MS), magnetic field system, calorimeters and trigger system and data acquisition. Finally, Section 2.3 introduces the concept of luminosity, low

pile-up and a quick description of the events suitable for physics recorded by ATLAS.

2.1 CERN accelerator complex and the LHC

The CERN accelerator complex is responsible for guiding protons through a series of accelerators that will collect data for future analyses. This begins with the ionization of hydrogen atoms and the initial boost to 750 keV using Radio Frequency (RF) cavities, the protons progress through LINAC 2, reaching around 50 MeV. From there, they are guided to the Proton Synchrotron Booster (PSB), where their energy increases up to 1.4 GeV. Subsequently, they enter the Proton Synchrotron (PS) and the Super Proton Synchrotron (SPS), boosting their energy to 26 GeV and 450 GeV, respectively. Finally, they are into the LHC all this with one of the most complex magnetic fields systems and superconducting technologies that include an array of magnets, such as dipole magnets for bending the accelerated beams along curved trajectories and quadrupole magnets for precise focusing, ensuring optimal collision probabilities. Approximately 80% of the arc sections are occupied by dipole magnets, augmented by sextupole, octupole, and decapole magnets strategically positioned to correct for nonlinear beam dynamics. These superconducting systems among others, are supported by cryogenics constant supply of liquid helium to maintain its operational temperature of 1.9 K (-271.3°C), rendering it the largest cryogenic facility worldwide. The dipoles themselves, crafted from niobium-titanium (NbTi) alloys, boast a novel 2-in-1 design, accommodating two separate beam apertures within the existing tunnel infrastructure. The LHC CERN complex is shown in Fig. 2.1.

2.2 The ATLAS detector

The ATLAS (A Toroidal LHC AparatuS) detector [89] is a multipurpose particle detector with a forward–backward symmetric cylindrical geometry. It consists of an Inner Detector (ID), electromagnetic and hadronic calorimeters, and a Muon Spectrometer (MS) plus one of the most complex magnetic systems in the world.

ATLAS uses a right-handed coordinate system with its origin at the nominal interaction point
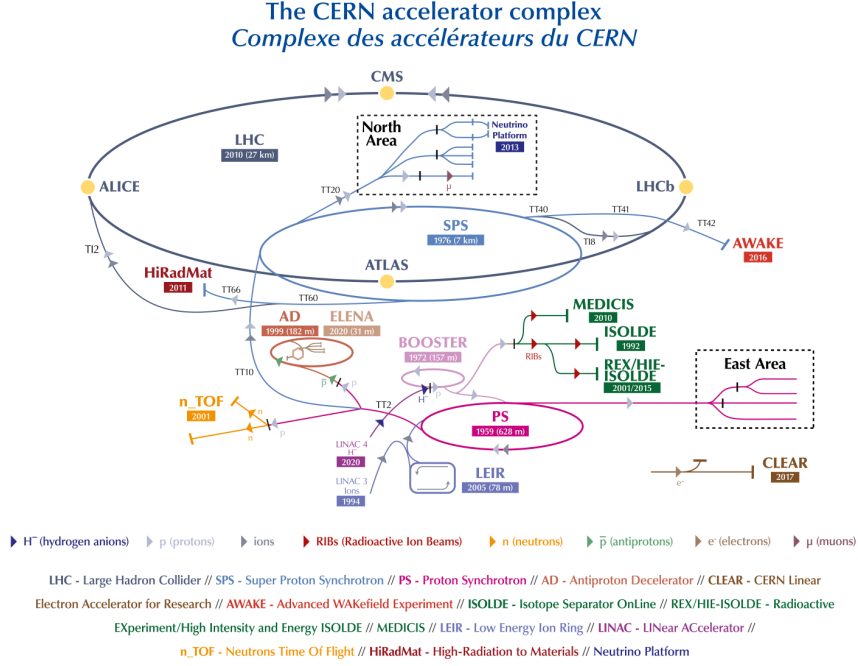
Figure 2.1: CERN accelerator complex [90]

(IP) in the centre of the detector and the $z-$axis along the beam pipe. The $x-$axis points from the IP to the centre of the LHC ring, and the $y-$axis points upwards. Cylindrical coordinates (r, ϕ) are used in the transverse plane with ϕ being the azimuthal angle around the $z-$axis. The pseudorapidity η is defined in terms of the polar angle θ as $\eta = -\ln\tan(\theta/2)$ such that the differences in pseudorapidity $\Delta\eta$ is a Lorentz invariant. Angular distance is commonly measured in units of $\Delta R = \sqrt{(\Delta\eta)^2 + (\Delta\phi)^2}$. The scheme of the ATLAS coordinate system is shown in Fig. 2.2. In the detector, three sections are considered,

- Barrel section covering the central pseudorapidity range $|\eta| < 1$

- End-Cap section covering ranges for $1 < \eta < 2.5$ name End-Cap fordward and the End-Cap backward covering $-2.5 < \eta < -1$.

For the Run 3, the ATLAS experimental setup has undergone enhancements through the replacement of the Small Wheel by the New Small Wheel (NSW) and the implementation of updates in the muon trigger systems [92].

33
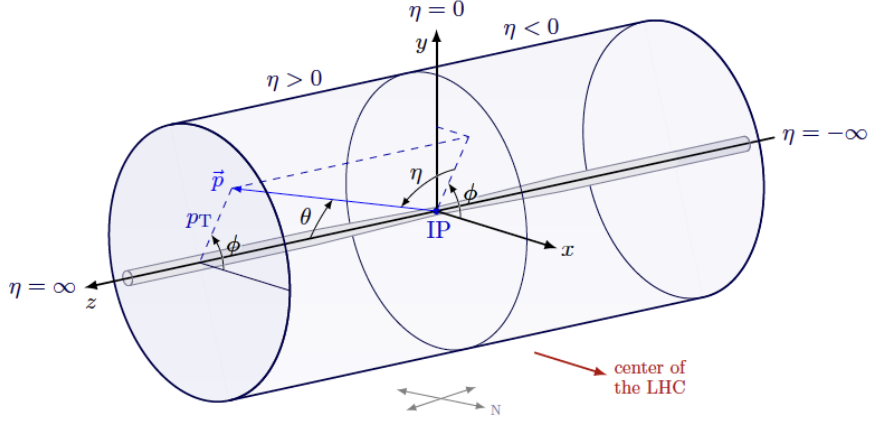
Figure 2.2: Coordinate system implemented in the ATLAS detector [91].

2.2.1 Inner detector

The ID system [93, 94] is a track charged particle detector for $|\eta| < 2.5$ with a 2 T solenoid magnetic field. It consists in 3 layers of Pixel Sensors, 4 layers of silicon strips Semi-Conductor Tracker (SCT) and 72 straw layers of Transition Radiation Tracker (TRT) modules as shown in Fig. 2.3.
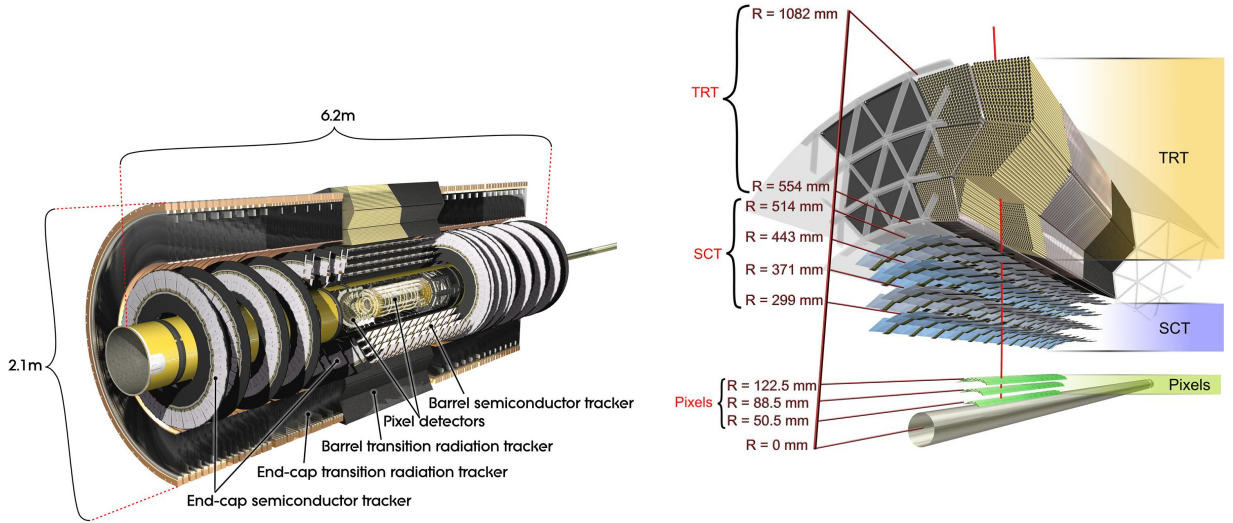
Figure 2.3: Inner tracker detector of the ATLAS detector with its subsystems [95].

Pixel detector: The Pixel Detector [96], situated at the core of the inner detector, is designed to provide the trajectory of charged particles originating from collision events with a minimum required of three data points. Its active area consists of a six disk layers of three concentric layers in the barrel section and three layers at each end. Each layer formed by modular units comprises several

elements such as silicon sensors, front-end electronics, and flex-hybrids integrated with control circuits. The spanned active surface is around $1.7m^2$ with approximately 67 million pixels in the barrel and 13 million in the endcaps. The Pixel Detector achieves a spatial resolution of 10 μm per layer in the $R - \phi$ plane perpendicular to the beam and 115 μm along the $z-$axis. To mitigate the sensitivity loss from radiation damage the Insertable B-Layer (IBL), positioned as the innermost layer, was installed during the shutdown between Run 1 and Run 2 of the LHC. Comprising 8 million pixels, the IBL enhances spatial resolution to 8 μm in the $R - \phi$ plane and 40 μm along the $z-$axis. This highly improves the impact parameter reconstruction for tracks, vertexing, and $b-$tagging performance while ensuring a robust reconstruction against pile-up effects.

Semiconductor Tracker (SCT): The Semiconductor Tracker [97] located within the midsection of the inner detector and covering a pseudorapidity region $|eta| < 2.5$, is a precision silicon microstrip detector. Its barrel region design incorporates four double layers of silicon strip sensors and nine disks in each endcap. Each layer or disk is equipped with strips arranged to provide two measurements at a stereo angle, that later are translated to space-points. Typically, the SCT furnishes eight strip measurements (equivalent to four space-points) for particles originating near the beam-interaction zone. This simplifies the trajectory reconstruction with a spatial resolution of 17 μm in the $R - \phi$ plane and 580 μm along the $z-$axis.

Transition Radiation Tracker (TRT): The Transition Radiation Tracker (TRT) [98] forms the outermost layer of the inner detector within the ATLAS system, extending its coverage to $|\eta| < 2.0$. Comprising 370,000 cylindrical drift tubes, each with a diameter of 4 mm. The TRT is filled with a mixture of Xenon (Xe), Carbon Dioxide (CO_2), and Oxygen (O_2). This unique composition enhances the drift velocity of electrons while also quenching photons.

The TRT works as a standalone component that a offers robust tracking capabilities with pattern recognition. This contributes to an improved momentum resolution by providing track measurement points up to the radius of the solenoid. Additionally, it plays an important role in the fast level-2 trigger system. Leveraging the distinctive transition radiation signature, the TRT facilitates standalone electron/pion separation, improving the detector's particle identification capabilities and overall its performance.

2.2.2 Muon spectrometer

The Muon Spectrometer (MS) [99], is a muon tracking detector with cylindrical shape detector of 22 m in diameter and 45 m in length covering the pseudorapidity range $|\eta| < 2.7$ with a 0.6 T toroidal magnetic field. The MS is equipped with a large number of precision chambers like Monitored Drift Tube (MDT) chambers and Cathode Strip Chambers (CSC). Trigger chambers like 3 layers of Resistive Plate Chambers (RPC) and 3 layers of Thin Gap Chambers (TGC) as shown in Fig. 2.4. The field integral of the toroids ranges between 2.0 and 6.0 Tm across most of the detector with one of the most complex magnet systems in the world.
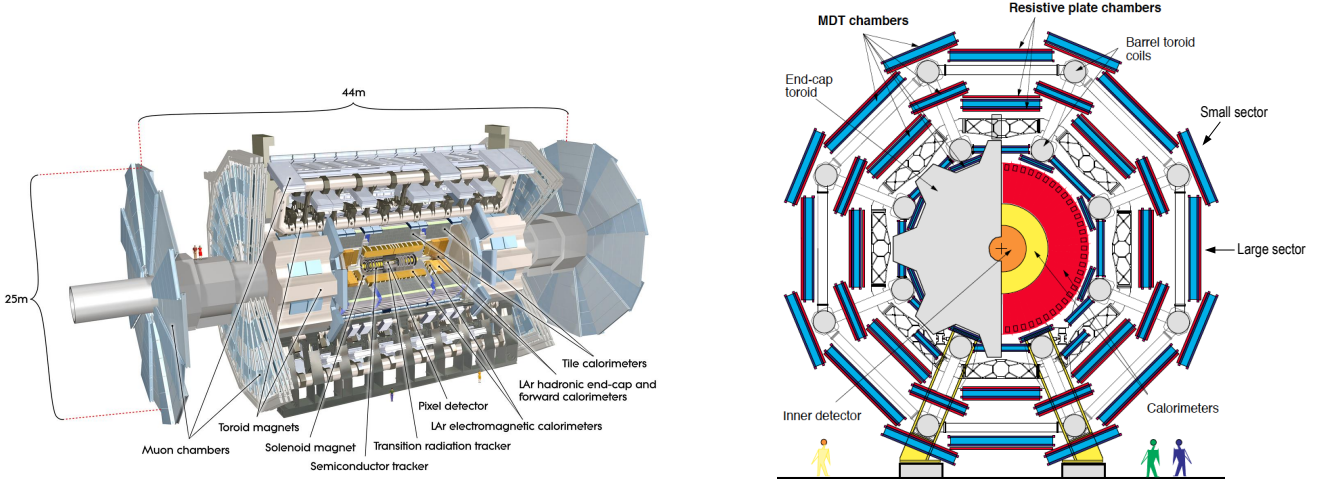
Figure 2.4: Muon Spectrometer of the ATLAS detector with its sub-components [89].

Monitored Drift Tube (MDT): The MDTs are multi-wire detectors devoted to a precise measurement of the timing of the current pulses generated by the wires. Considering the time required for ions to drift towards the nearest wire, one can deduce the distance at which a particle passed the wire. The ATLAS Monitored Drift Tube (MDT) chambers are configured with six layers of drift tubes, with three layers mounted on each side of a supporting structure. Each MDT unit consists of a 3 cm diameter drift tube housing a stretched wire within a gas-filled volume. As a muon or any charged particle traverses the volume, it ionizes the gas, generating an electric current in the wire. These MDT chambers offer precise tracking capabilities for charged particles within the plane defined by the beam axis (z) and the radial distance to the beam (r) within the pseudorapidity range $|\eta| < 2.7$. In the innermost wheel of the end-cap region, where the particle flux exceeds 100

Hz/cm^2 for $|\eta|$ ranging from 2.0 to 2.7, cathode strip chambers are deployed due to their higher granularity.

Cathode Strip Chambers (CSC): The Cathode Strip Chambers (CSCs) are complements to the MDT chambers within the region of $2.0 < |\eta| < 2.7$. They offer enhanced muon tracking capabilities in the higher-rate area with an improved timing resolution compared to the MDT chambers. This system comprises two endcaps, with 16 chambers situated in each endcap. Each chamber is equipped with four precision layers and four transverse layers, enabling a spatial resolution of 60 μm in the CSC plane and 5 mm in the non-bending direction.

Resistive Plate Chambers (RPC): Resistive Plate Chambers (RPCs) provides a rapid tracking information within the central region of $|\eta| < 1.05$. Within the ATLAS detector, RPCs are primarily tasked with first-level muon triggering and measuring coordinates in the non-bending direction within the barrel region of the muon spectrometer. In the middle station of the barrel, two RPCs are deployed to facilitate low$-p_T$ triggering, while an additional chamber is positioned in the outer barrel to support high$-p_T$ triggering. Operating on a principle akin to that of the Thin Gap Chambers (TGCs), both RPCs and TGCs contribute to muon information collection in the non-bending direction.

Thin Gap Chambers (TGC): The Thin Gap Chambers (TGCs) is one of the main components for swift tracking information within the region $|\eta| < 2.4$. Its role is crucial for triggering purposes and azimuthal coordinate determination of muons. Each TGC unit operates as a multi-wire proportional chamber, comprising two parallel cathode plates filled with a highly quenching gas mixture of CO_2 and $n-C_5H_{12}$, with wires positioned in between serving as anodes. A potential of 2.9 kV is applied across these wires. When a muon pass through the TGC, gas ionization occurs, leading to the acceleration and collection of resulting ions and electrons by the electric field towards the nearest wire. The signals generated by these interactions across different wires are used to reconstruct the trajectories of muons. Notably, TGCs offer the advantage of a high gain mode, producing large saturated signals that remain relatively insensitive to mechanical variations, thereby facilitating the construction of large, highly efficient detectors. Furthermore, TGCs exhibit a narrow time spread of signals, enabling a remarkable timing resolution of approximately 4 ns,

enhancing the precision of event reconstruction and analysis within the ATLAS detector.

Magnet systems: The ATLAS magnet systems is probably one of the most complex parts of the detector. It is designed to bend the trajectories of the particles which allows to a precise measurement of the momentum. It is composed by two parts, the first one is the Central Solenoid (CS) magnet that surrounds the inner tracker detector and the second one is a toroidal magnet system that can be separated in an air-core Barrel Toroid (BT) and two End Cap Toroids (ECT) foward and backward, as shown in Fig. 2.5. Each component consists in eight coils with an average field of 4 T in the muon spectrometer. All the magnet system has been radially and symmetrically assembled around the beam axis.
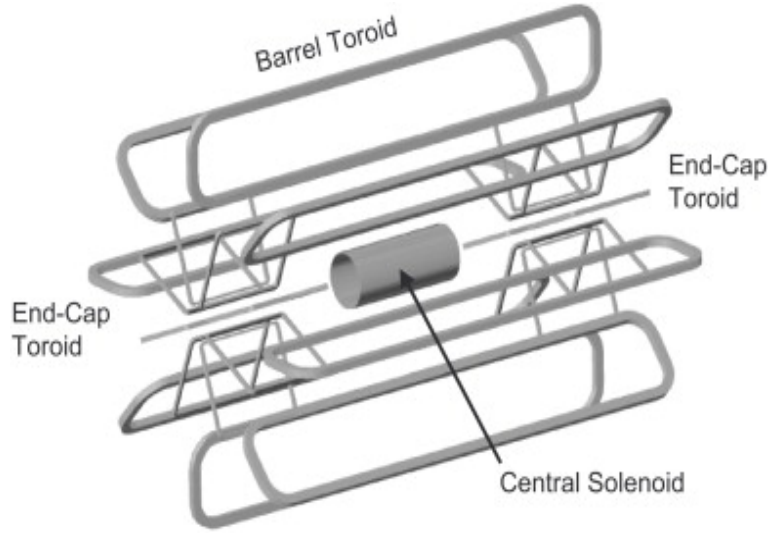
Figure 2.5: ATLAS magnet system: Central Solenoid, Barrel Toroid and End Cap Toroids [100].

2.2.3 Calorimetry

Calorimeters are designed to capture and quantify the energy carried by particles resulting from collisions. When a particle pass through a calorimeter, its interaction within the detector initiates a cascade of secondary particles, leading to the deposition of energy. This energy, deposited by charged particles within the active region of the calorimeter, is then detectable either in the form of light or charge, allowing for precise measurement of the incident particle's energy.

Two type of calorimeters are implemented in ATLAS detector: electromagnetic and hadronic. Electromagnetic calorimeters are designed to measure the energy of electrons and photons by their

electromagnetic interactions, while hadronic calorimeters specialize in quantifying the energy of hadrons through their strong interactions

In ATLAS, energy measurements are performed using a sampling calorimeter system, which consists of alternating layers of high-density absorbing material and active medium. This system is what composed the Liquid Argon (LAr) Calorimeter, designed to absorb electrons, photons, and hadrons, alongside the Tile Hadronic Calorimeter. Its designed is focused on hadrons such as protons and neutrons.

Two type of showers (electromagnetic or hadronic) can be produced depending on the nature of the incoming particle. The electromagnetic showers is primarily influenced by bremsstrahlung and electron-positron pair production. This phenomenon can be characterized by the radiation length (X_o), which is the mean length (in cm) to reduce the energy of an electron by the factor $1/e$. This distance can be described by the following equation,

$$X_0 = \frac{716.4}{Z \cdot (Z+1) \ln\left(\frac{287}{\sqrt{Z}}\right)} g \cdot cm^{-3}, \tag{2.1}$$

where Z is the atomic number of the nucleus. The relative resolution of calorimeters can be expressed as a function of the total energy E as,

$$\frac{\sigma_E}{E} = \frac{N}{E} \oplus \frac{S}{\sqrt{R}} \oplus C, \tag{2.2}$$

where N, S and C correspond to the noise of the measurements, the stochastic uncertainty and the non-uniformities of the detector, respectively.

Electromagnetic (EM) calorimeter: The electromagnetic calorimeter (ECAL) allows precise measurements of the energy of electrons and photons through their electromagnetic interactions. Positioned at the heart of the detector, the ECAL comprises layers of lead absorber plates interspersed with sensitive detecting elements, typically made of liquid argon (LAr) or lead tungstate (PbWO4) crystals. This is divided into two identical half-barrels covering $|\eta| < 1.475$ regions and two end-caps covering $1.375 < |\eta| < 2.5$ regions. The ECAL is longitudinally segmented into three layers called strip, middle and back to optimize the energy resolution and facilitate precise localiza-
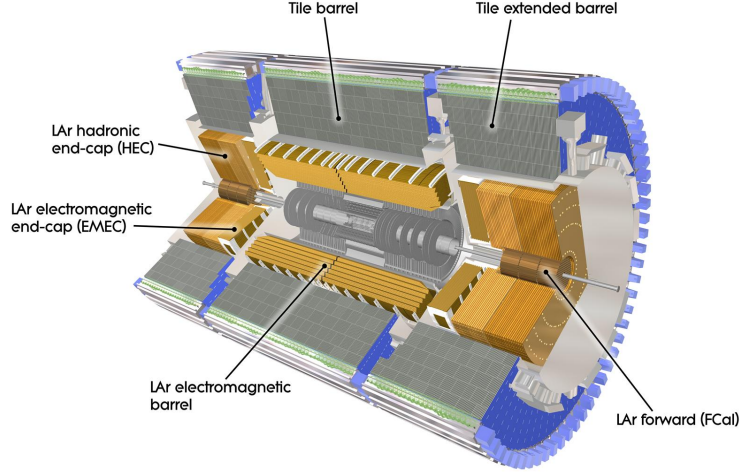
Figure 2.6: Scheme of the calorimeter at the ATLAS detector [95].

tion of energy deposits. Each layer features fine granularity, allowing for an accurate reconstruction of electromagnetic showers and discrimination against background signals. For example, the middle layer is equipped with $\Delta\eta \times \Delta\phi = 0.025 \times 0.025$ while the strip layer has 8 times finer granularity. In contrast, the back layer has a twice coarse granilarity in η adn the same ϕ segmentation as the middle layer.
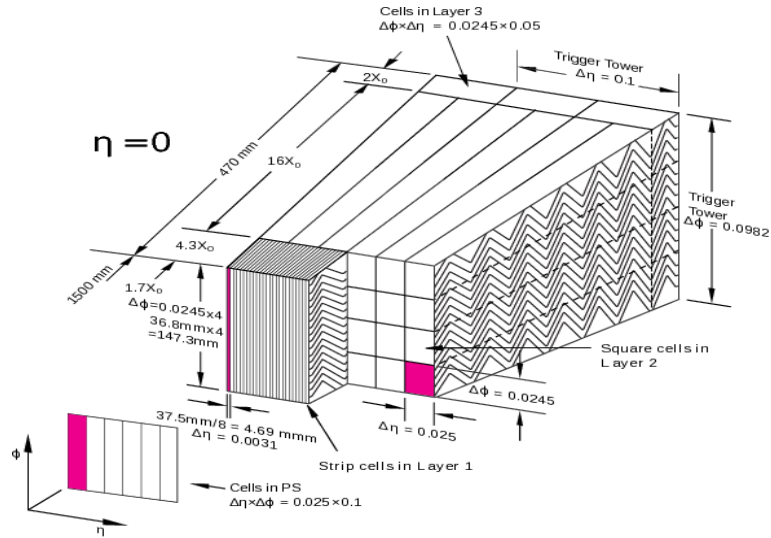
Figure 2.7: Scheme of the barrel region for the LAr calorimeter layers [89].

Hadronic calorimeter: The hadronic calorimetry within the ATLAS detector encompasses a diverse array of components constructed using various techniques and devices. Specifically, in the range of $|\eta| < 1.6$, the barrel and extended barrel Tile calorimeters use the iron-scintillating-tiles

technique, while for $1.5 < |\eta| < 3.9$, the LAr technique is employed. A critical parameter for these hadronic calorimeters is their thickness, which must be sufficiently large to contain hadronic showers and mitigate the penetration of punch-through hadrons into the muon system.

To achieve these objectives, the total thickness is carefully selected to be approximately 11 interaction lengths. This configuration ensures optimal performance in terms of resolution for high-energy jets while effectively capturing and measuring the energy of hadronic particles.

The Tile calorimeter: The Tile calorimeter [101] is positioned behind the EM barrel calorimeter, serving as the next layer for energy measurement within the ATLAS detector. Its design incorporates scintillating tiles as the active material, while iron serves as the absorber. These scintillating tiles, 3 mm thick, are arranged perpendicular to the beam-pipe. Each period of the calorimeter contains a total iron thickness of 14 mm. Comprising both barrel and extended barrel components, the Tile calorimeter features an inner radius of 2.28 m and an outer radius of 4.23 m. Longitudinally, it is sampled into three layers, with the granularity corresponding to $\Delta\eta \times \Delta\phi = 0.1 \times 0.1$ in the first two layers and $\Delta\eta \times \Delta\phi = 0.2 \times 0.1$ in the last layer. To accommodate the passage of cables from the Inner Detector (ID) and the EM calorimeter, a vertical gap, 68 cm wide, is strategically positioned between the barrel and extended barrel regions. However, it's important to note that the electronic noise in the cells of the Tile calorimeter amounts to approximately 20 MeV.
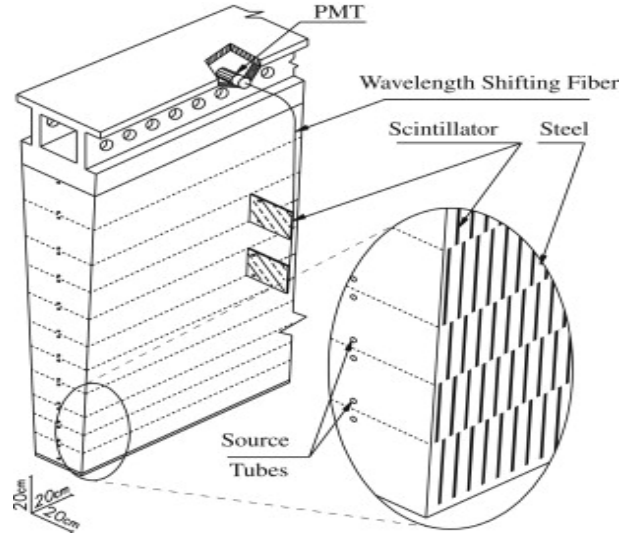
Figure 2.8: Scheme of the Tile Calorimeter readout system [89].

The Liquid Argon Calorimeter: The Liquid Argon (LAr) calorimeters [102] covers the end-

cap and forward regions, this is, $1.5 < \eta < 4.9$. It measures the energy of electrons, photons and hadrons using liquid argon as active material. The detector is structured by layers of metal that absorb the incoming particles that later on produce a particle shower. The secondary particles ionise the LAr that is located in between the metal layers that results in ionised charges that are transalated into signal in the electrodes.

Four parts can be identified in the LAr detector, The hadronic end-cap calorimeter (HEC), the forward calorimeter (FCAL), the electromagnetic barrel (EMB) and the electromagnetic endcap calorimeter (EMEC). The HEC comprises two independent wheels, each featuring absorber plates of different thickness: one wheel contains 25 mm absorber plates, while the other uses 50 mm absorber plates, with copper being the absorber material. Within the HEC, a gap equipped with three electrodes divides it into four drift spaces, each measuring 1.8 mm. Longitudinally, the HEC is segmented into front, middle, and back sections, with respective electronic noise values of approximately 250, 350, and 800 MeV. The outer radius of the copper plates in the HEC is 2.03 m, while the inner radius is 0.475 m. The Forward Calorimeter (FCAL) is positioned approximately 5 meters from the interaction point. This high-density detector comprises three longitudinal sections: the first section utilizes copper, while the subsequent two sections employ tungsten. The HEC and FCAL with the Tile caloriemter formed the ATLAS Hadronic calorimeter (HCAL) thart covers the regions $1.5 < |\eta_{\text{HEC}}| < 3.2$ and $3.1 < |\eta_{\text{FCAL}}| < 4.9$.

The EMB and the EMEC formed the elemectromagnetic calorimenter (ECal) that covers the region $|\eta| < 3.2$ and is designed with an accordion geometry alternating the lead layers as the absorber and liquid argon as the active medium. The relative resolution of the ECal in the barrel and end-cap regions are measured as,

$$\left.\frac{\sigma_E}{E}\right|_{\text{barrel}} = \frac{10.1\%}{\sqrt{E}} \oplus 0.2\%, \quad \left.\frac{\sigma_E}{E}\right|_{\text{End-Cap}} = \frac{12.1\%}{\sqrt{E}} \oplus 0.4\%. \tag{2.3}$$

LAr serves as the sensitive material within these sections, with gap sizes of 250, 375, and 500 microns in the first, second, and third sections, respectively. These gap sizes facilitate rapid signal collection in the forward region, where significant pileup effects are anticipated. In terms

of granularity, the hadronic LAr calorimeter exhibits $\Delta\eta \times \Delta\phi = 0.1 \times 0.1$ for $1.5 < \eta < 2.5$ and $\Delta\eta \times \Delta\phi = 0.2 \times 0.2$ for $2.5 < \eta < 3.2$. Conversely, the forward calorimeter features a granularity of 0.2×0.2. Notably, the forward calorimeters possess the capability to reconstruct electrons in addition to their primary function in hadronic energy measurement.

2.2.4 Trigger system and data acquisition

The ATLAS detector's trigger system [103] plays one of the most important roles in managing the large amount of data generated by proton-proton (*pp*) collisions ensuring that only events of interest are recorded for further analysis. This system is based on three levels known as L1 (hardware-based), L2 and Event Filter (software-based) that employ distinct methodologies to achieve efficient event selection.

The L1 trigger, uses information from the calorimeter and muon spectrometer. Within 2.5 microseconds of a collision, specialized electronics identify regions of interest (ROI) in the $\eta - \phi$ plane and make rapid decisions to reject background events based on hit coincidences in various subdetector layers within predefined windows. As a complement, the L1 trigger uses information from the inner detector (ID) to do the selections followed by a software-based High Level Trigger (HLT). The L1 trigger system is responsible for reducing the event rate to 100kHz and the HLT reduces the rate further down to around 1kHz.

Subsequent to L1, the second (L2) and third (Event Filter, EF) levels employ software-based systems, integrating information from all sub-detectors. These levels verify if specific trigger conditions are met for each bunch crossing, based on hundreds of predefined criteria. Triggers are established by identifying combinations of physics objects such as electrons, photons, muons, jets, and b-jets, as well as global event properties like missing transverse energy and summed transverse energy. Events selected by the EF are then directed to mass storage for further analysis, with an average processing time of approximately 4 seconds. To manage event rates effectively, "prescaled triggers" are employed when necessary, selecting only random events for storage.

In the context of data acquisition, stringent quality control measures are implemented to ensure the integrity of collected data. If mechanical or read-out issues occur during data acquisition, only

data from operational sub-detectors and magnet systems are used for analysis. The condition of the detector, referred to as data quality, is continuously monitored during data acquisition, with relevant information stored in the condition database for each data-taking period or luminosity block.

2.2.5 Sectors definition

The ATLAS detector is divided in sixteen sectors of different angular sizes that overlap between them. For that reason, there is not a unique way to define the surface covered by a sector. In this work, a sector is defined as those regions in ϕ, where the tracks are able to cross three MDT layers having their wires in the same direction. For this, sectors are considered to be centered at 22.5° with respect to the sector number,

$$\text{center} = 22.5° \cdot (n-1) \quad \text{for} \quad n = 1, 2, ..., 16.$$

Where the even $n-$values correspond to small sectors $(2, 4, ..., 16)$ and the odd $n-$values are large sectors $(1, 3, ..., 15)$. Large sectors are considered to have an angular size of $\pm 12.5°$ and the small sectors an angular size of $\pm 10°$ with respect to the center. The previous definition does not take into account the overlap between the sectors. A detailed view from the detector is shown in Fig. 2.9

2.2.6 Pseudorapidity regions and magnetic field

In the present work, three main regions were considered for the studies. The barrel region for $|\eta| \leq 1$, the intermediate region $1 < |\eta| \leq 1.7$ and the ECT $1.7 < |\eta| \leq 2.5$ forward for positive values of η and backward for negative values of η. This is showed in Fig. 2.10 and the main reason to study these three regions is due to the material influence and the role with the magnetic field. The interest in the barrel region lies in the tile calorimenter (TileCal), the intermediate due to the finger and Shielding disk and ECT for the outer part of the shielding disk. Finally, Fig. 2.11 shows the convolution between magnetic field and Detector description that implies a charge asymmetry between μ^+ and μ^-.
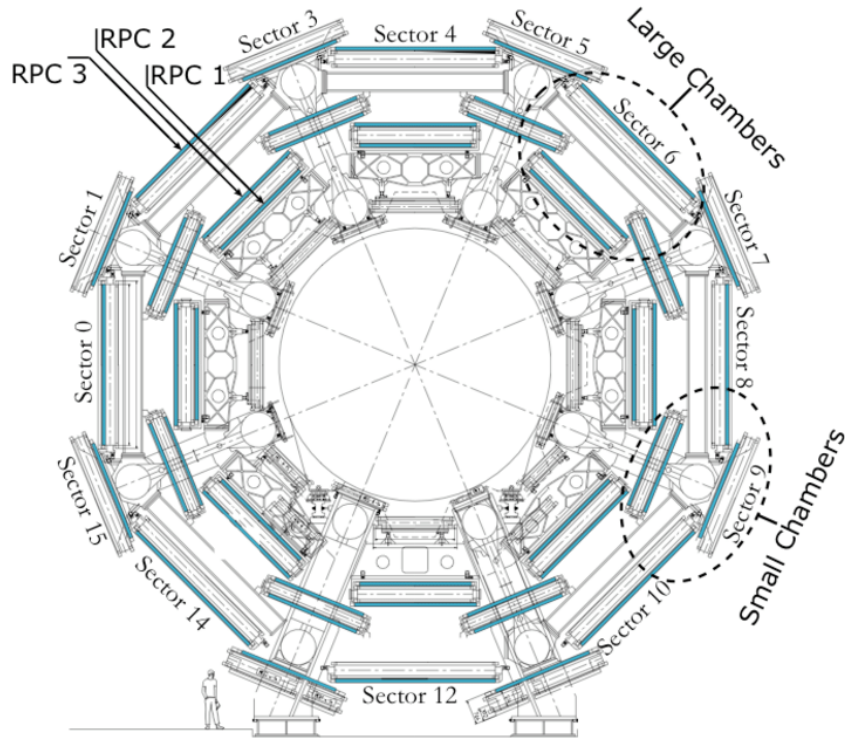
Figure 2.9: Scheme of the sixteen ATLAS detector sectors for large and small chambers [104].
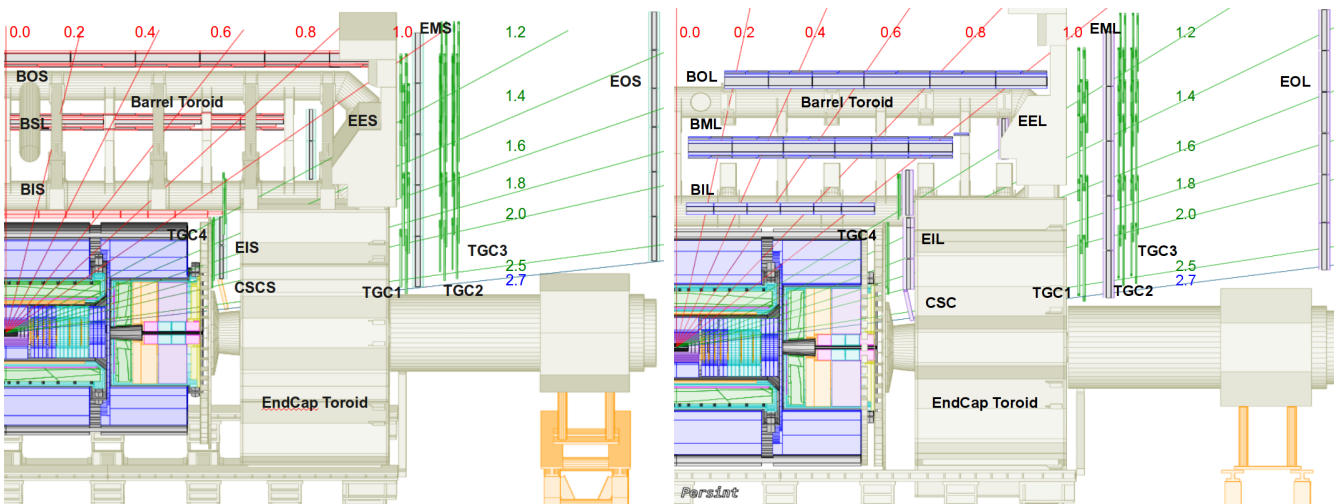
Figure 2.10: ATLAS detector scheme with different η projections [105].
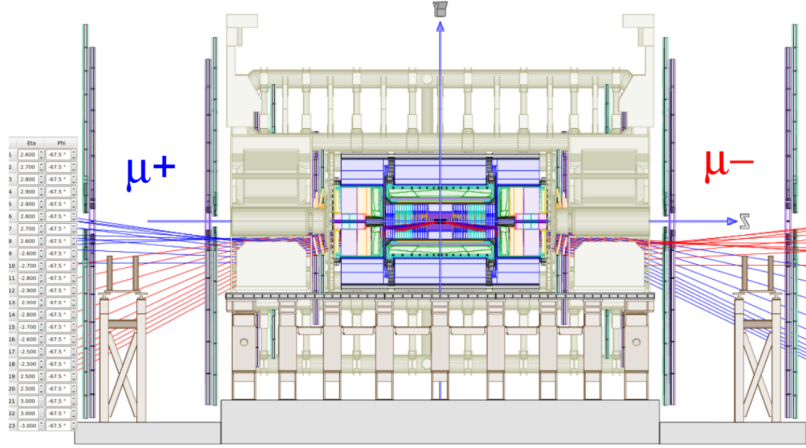
Figure 2.11: Convolution between magnetic field and detector description in ATLAS [105].

2.3 Integrated luminosity

One of the main characteristics of the particle colliders is their beam energy and the quantity that describes the ability of a particle accelerator to produce the required number of interactions is called luminosity, L. This is, the number of collisions events that can be delivered to the experiments and it stands as the proportional factor between the rate of events per time dN/dt and the cross section, σ, such that,

$$\frac{dN}{dt} = L \cdot \sigma, \tag{2.4}$$

where the total number of events can be obtained integrating in time, which results in the so-called "integrated luminosity $\mathcal{L} = \int L \, dt$". This is measured in inverse barns (1b= $10^{-24} cm^{-2}$). In the case where the protons in a beam are Gaussian-distributed an expression for L can be obtained and is given by,

$$L = \frac{N_b^2 \cdot n_b \cdot f_{rev} \cdot \gamma}{2\pi \epsilon_n \beta^*} \cdot F(\phi), \tag{2.5}$$

where N_b is the number of particles per bunch, n_b is the number of bunches per beam, f_{rev} is the revolution frequency of the accelerated protons, γ is the Lorentz factor. ϵ_n is the beam emittance defined as the smallest opening that a beam can be squeezed, β^* os the so-called amplitude function, defined by the weidth of the beam the emittance. F is a geometric factor due to the crossing angle ϕ between the beams at the interaction point (IP).

The Large Hadron Collider (LHC) is outfitted with specialized luminometers for continuous monitoring of luminosity conditions. This allows to determine the amount of integrated luminosity delivered by the LHC and the one recorded by ATLAS and deemed suitable for physics studies. ATLAS experiment employs several detectors for luminosity measurement, among these LUCID-2 is considered as the primary monitor. Due to the fact, that the LHC's is a high luminosity experiment, multiple interactions per bunch crossing occurs. These are categorized into the hard scatter (HS) process and multiple soft interactions, known as pile-up.

Consequently, when the event reconstruction is done, signals from different interactions may be captured, termed pile-up, which can be either in-time, involving soft interactions within the same bunch crossing, or out-of-time, originating from neighboring bunches. The Out-of-time pile-up correlates with the average interactions per bunch crossing, while in-time pile-up relates to the reconstructed number of primary vertices (PV).

In 2011, the LHC conducted the Run 1 data taking using proton-proton (pp) collisions at a centre-of-mass energy of $\sqrt{s} = 7$ TeV. The ATLAS detector with all relevant detector systems operational managed to collect a dataset that correspond to approximately 4.6 fb^{-1} and 4.1 fb^{-1} of integrated luminosity in the electron and muon channels, respectively [106]. The total integrated luminosity per day in 2011 and the recorded luminosity as a function of the mean number of interactions per crossing during the LHC Run 1 are shown Fig. 2.12a and Fig. 2.12b, respectively. This dataset has been implemented in section 6.6 to perform a new measurement of the W boson mass [107] and to contrast with the previous measurement released in 2018 [76].

The Run 2 of the LHC took place during 2015 to 2018 collecting data at different pile-up and centre-of-mass energy. In particular, for 2017 and 2018 the LHC carried out a low pile-up run with an average number of pp interactions, $\langle \mu \rangle$, of about two, as compared to $\langle \mu \rangle \sim 34$ for the nominal LHC Run 2. The low pile-up datasets correspond to an integrated luminosities of 254.9 ± 2.6 pb^{-1} at $\sqrt{s} = 5.02$ TeV and 338.1 ± 3.1 pb^{-1} at $\sqrt{s} = 13$ TeV [108]. The low pile-up dataset is of particular interest since it can provide a good hadronic recoil resolution for which the thresholds applied to suppress noise in the reconstruction of clusters of energy in the calorimeters were lowered [108–110]. The total integrated luminosity and the recorded luminosity as a function of the mean number of

interactions per crossing during the LHC Run 2 are shown Fig. 2.12c and Fig. 2.12d, respectively. In particular, Fig. 2.12d shows a small distribution around $\langle \mu \rangle \sim 2$ that corresponds to the low pile-up dataset. This dataset is of particular interest for the present work since it has been implemented to study the prospects of the precision physics in m_W as described in section 6.7 but it also corresponds to the one used in the most recent precision measurement of transverse momentum of the W and Z bosons in Ref. [75].

Currently the LHC is performing the Run 3 data-taking, for which several updates have been carried out such as the replacement of the small wheel by the new small wheel (NSW) [92] and the implementation of updates in the muon trigger systems. The total integrated luminosity and the recorded luminosity as a function of the mean number of interactions per crossing during the LHC Run 3 are shown Fig. 2.12e and Fig. 2.12f, respectively.
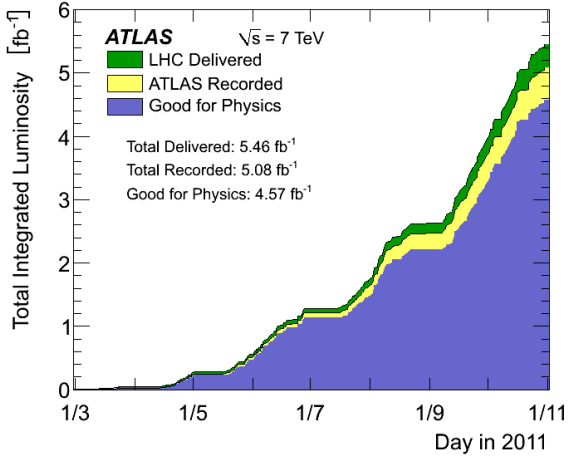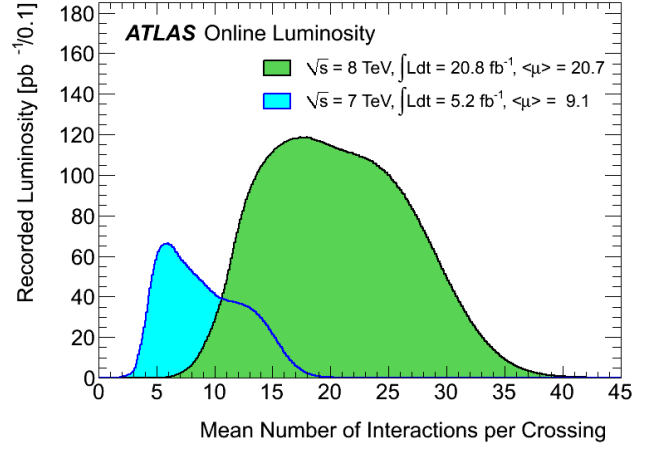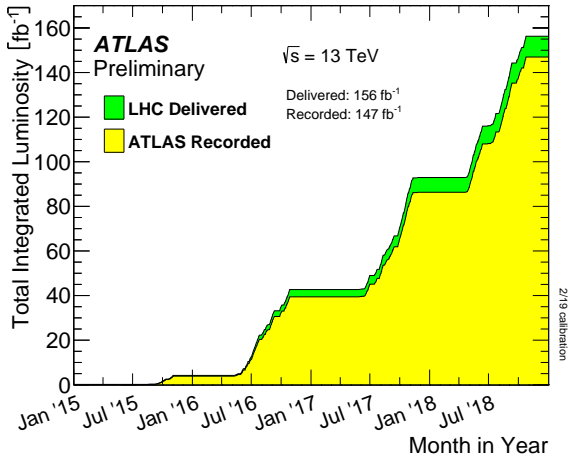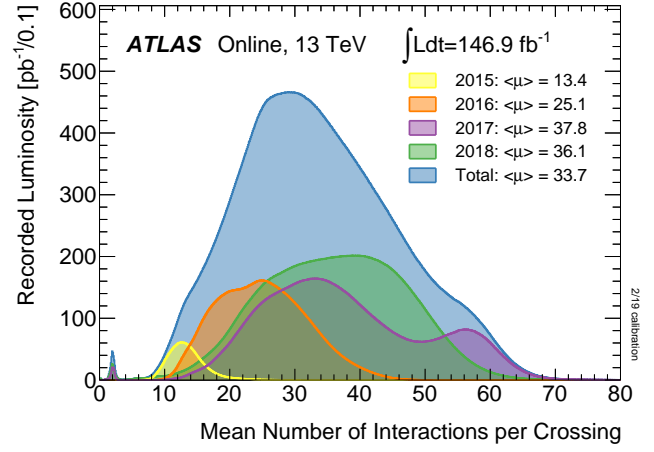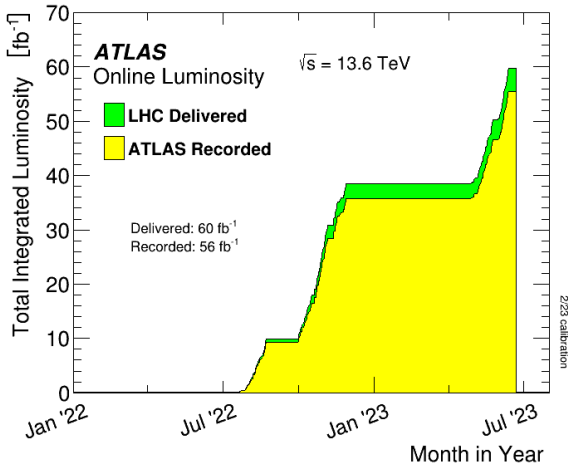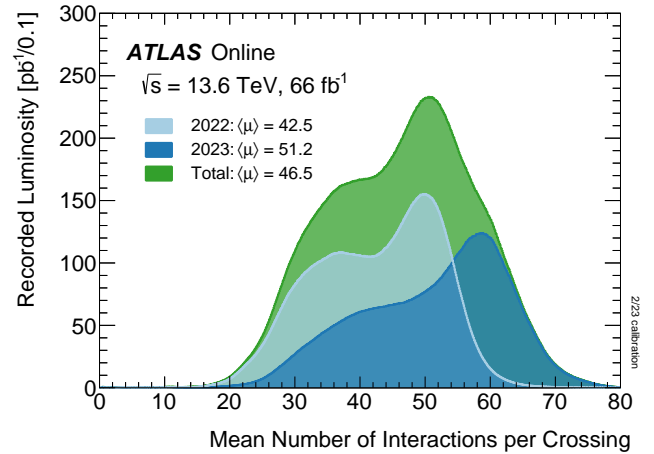
Figure 2.12: (left) Total integrated luminosity per year and (right) mean number of interactions per crossing for (top) Run 1 [111], (middle) Run 2 [112] and (bottom) Run3 [113].

Chapter 3

Event reconstruction

In the ATLAS detector, particles generated in proton-proton collisions are detected through energy deposits in the calorimeters and hits in the trackers. These signals serve as a basis for reconstructing various physics objects like jets, photons, electrons, and muons. However, some particles, such as neutrinos, escape detection, contributing to an imbalance in the total transverse momentum, which is compensated by incorporating their momenta into the missing transverse momentum.

Event reconstruction in the ATLAS detector involves combining electronic signals produced as particles traverse the detector layers. These signals are processed to discern the types of particles present in the collision. Monte Carlo simulations play a crucial role in evaluating theoretical predictions from both the Standard Model and Beyond the Standard Model physics with respect to the observed data. These simulations are essential for developing and refining the reconstruction, identification, and simulation techniques necessary for analyzing the physics objects relevant to the research presented in this thesis.

The ATLAS detector is designed with dedicated sub-detector systems tailored to exploit distinct physics properties for particle discrimination and identification. These systems enable the differentiation of particles like electrons, muons, taus, photons, and the categorization of quark or gluon decay products, known as jets. Following the measurement of all detectable objects, the energy imbalance in an event originating from imperceptible processes is quantified through the missing transverse momentum.

The reconstructed objects are divided into two types: basic objects including tracks, vertices and topological clusters (topoclusters), and composite physics objects as electrons, muons, and jets. The basic objects are used as inputs for the reconstruction of the composite objects.

This chapter summarises the ATLAS reconstruction procedure for each of these objects and is organized as follows, Section 3.1 describes the tracks and vertices reconstruction introducing the track parameters for the ID and MS and the concepts of primary and secondary vertex. Section 3.2 describes the object reconstruction related to the muon and electron reconstruction as well as their selection and working points categorized by their efficiencies for the analysis and finally a description of the Hadronic recoil reconstruction procedure.

3.1   Tracks and vertices

When a particle crosses through the detector, it leaves a signal in the components. By connecting the hits in the different layers of the Inner Detector and/or Muon Spectrometer, it is possible to reconstruct its trajectory. Specifically, tracks containing at least three hits in the ID are of interest. These tracks reconstruct the trajectories of charged primary particles using hits in the pixel detector and SCT layers as seeds for the algorithm. The silicon tracks obtained are then combined with the TRT information using what is called the "inside-out extrapolation algorithm".

For the secondary particles or photons, a similar procedure is applied but starting from the TRT information and applying the backward procedure on what is known as the "outside-in extrapolation algorithm". The ID reconstruction scheme is shown in Fig. 3.1 [114].

In the case of the Muon Spectrometer [116–119] the reconstruction is carried out taking into account the Resistive Plate Chambers (RPC), Thin Gap Chambers (TGC), and Monitored Drift Tubes (MDT) where the RPC and TGC provide fast triggering capabilities, while the MDT offers precise position measurements. Muons are triggered if at least one hit in the RPC/TGC chambers exists since muons ionize gas in the RPC and TGC, this leads to the detection of their passage with fast timing resolution. On the other hand, the MDT uses the drift of electrons in gas to determine the muon's precise trajectory. This next to the strong magnetic field within the spectrometer that
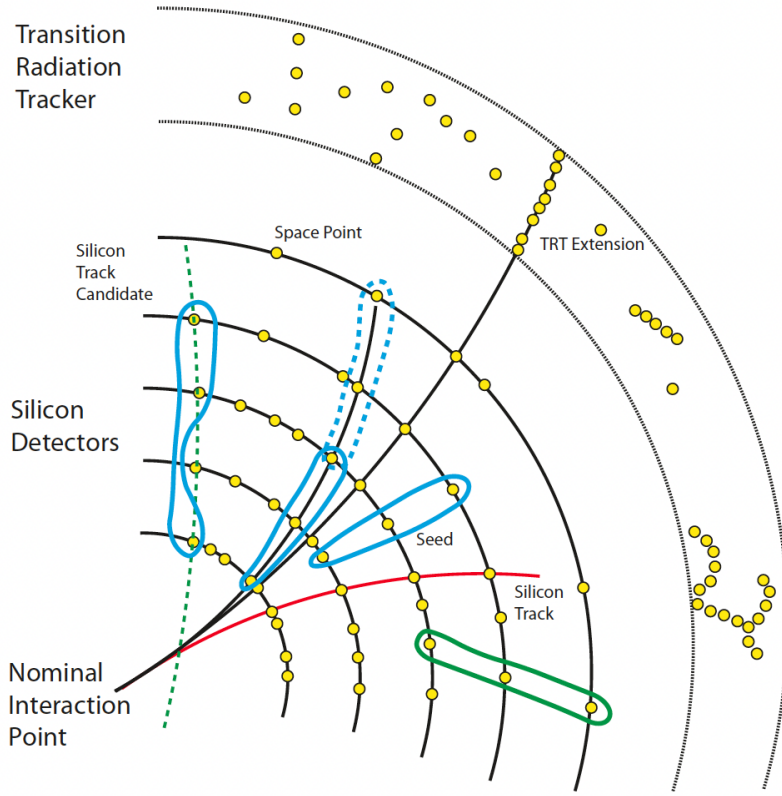
Figure 3.1: Illustration of the track reconstruction in the Inner Detector [115].

bends the trajectories of the muons, enables the determination of their momenta based on the curvature of their paths. This can be described by the relation,

$$\frac{1}{p} = \frac{8s}{BL^2},\tag{3.1}$$

where p is he momentum of the muon, B is the strength of the magnetic field through which the muon passes, L is the length of the muon's path within the magnetic field and s is known as the sagitta, which is the maximum perpendicular distance between the curved trajectory of the muon and the straight-line path it would have followed in the absence of a magnetic field. Eq. (3.1) shows direct relation between the momentum determination and the sagitta from which a good resolution is required. The final muon's trajectory is obtained by combining information from RPC, TGC and MDT through a dedicated χ^2-fit. This reconstruction allows to obtain an accurate determination of the muon's momentum and direction.

Once the tracks are obtained, they are parametrized by five parameters $(d_0, z_0, \theta, \phi, q/p)$ as shown
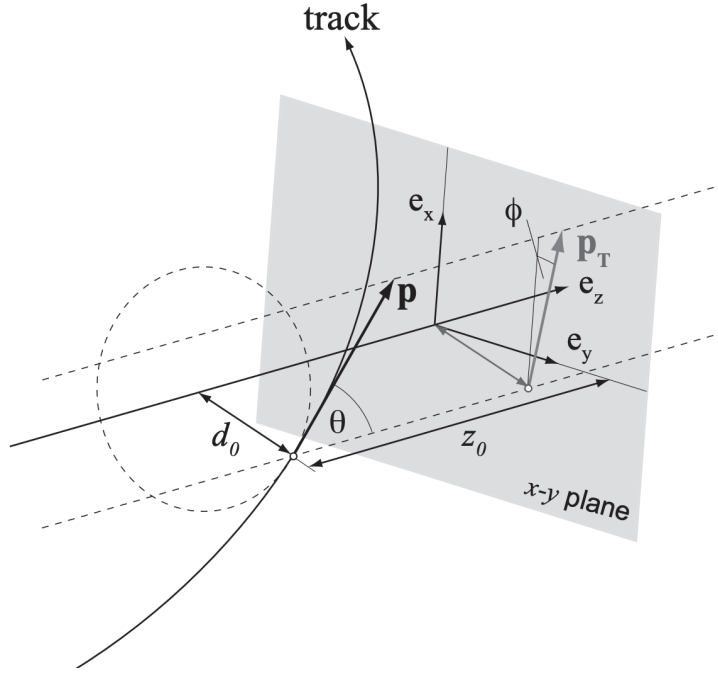
Figure 3.2: Perigee representation in the ATLAS track parameterization [120].

in Fig. 3.2 and they are required to have a transverse momentum $p_T > 400$ MeV and pseudorapidity $|\eta| < 2.5$.

Track parameters are obtained from particles originating at the interaction point, characterized by vertices. These vertices represent the positions where particles are produced or decay during collisions. Two main types of vertices are identified:

Primary Vertex: The Primary Vertex (PV) is the most important vertex in an event. It corresponds to the point where the hard collision occurred, typically the interaction point between the colliding protons. Since the protons consist of many quarks and gluons, the collision may produce several high-energy particles, each leaving behind a track in the detector. The primary vertex is reconstructed by combining these tracks, providing information about the location of the collision and allowing to study the properties of the particles produced.

Secondary Vertex: Secondary vertices are additional vertices that can be formed within the detector when particles produced in the primary collision decay or interact further. For example, heavy particles like $b-$quarks or τ leptons may travel a short distance before decaying into lighter particles, creating secondary vertices along their paths. Secondary vertices are crucial for identifying specific particle decays, such as those involving bottom or charm quarks, and for studying the

54

properties of short-lived particles.

The vertices reconstruction is done in two steps: the vertex finding and the vertex fitting. In the vertex finding, a set of vertex candidates are defined from the tracks and all vertices are required to have at least two tracks. Then, the precise z-coordinate is obtained from an iterative χ^2-fit. The vertex with the largest sum of squared transverse momenta $\sum p_T^2$ of all tracks associated is referred to as the primary vertex (PV).

3.2 Object reconstruction

3.2.1 Muon reconstruction

In the case of the muons, these are identified and reconstructed by combining the ID and MS information. About 96% of muons are reconstructed by fitting hits from ID and MS tracks. Intuitively two track types are obtained by the ID and the MS, these are the ID tracks containing only the Inner Detector information and the MS tracks using Muon Spectrometer information. In addition, the ID and MS information can be statistically combined to improve the momentum resolution and to provide a better rejection of muons from secondary interactions. The muon types are: Combined (CB) muons are obtained by performing a global refit of the ID and MS tracks through the so-called STACO algorithm. Segment-tagged (ST) muons consist of a fitted ID track and a MS segment. Calorimeter-tagged (CT) muons consist of a fitted ID track and an energy deposit in the calorimeters. Extrapolated or Muon Spectrometer Only Extrapolated (MSOE) muons consist of only MS track information. Muon track types are shown in Fig. 3.3.

After reconstruction, muon candidates are selected by a set of requirements on the number of hits in the ID sub-detectors and MS stations as well as the track fit properties and on variables that test the compatibility of the individual measurements in the two detector systems. A given set of requirements is referred to as a Working Point (WP) according to purity level and kinematics and they are defined as,

Loose muons: provide high efficiency but less purity and larger systematics. It is designed to maximise the reconstruction efficiency while providing good-quality muon tracks. All track types
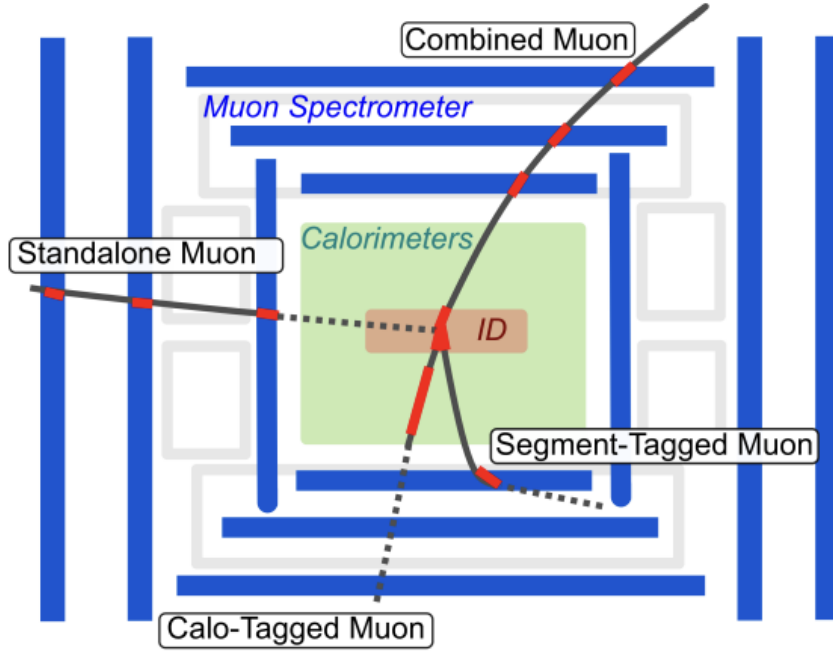
Figure 3.3: Scheme of the different muon reconstruction types using the different ATLAS sub-detectors [121].

are used but those η regions with poor MS efficiency are discarded.

Medium muons: provide a suitable efficiency and purity with low systematics. In this case, only the CB and ME tracks are used are they are used as the default Working Point. A loose requirement on the compatibility between ID and MS momentum measurements is applied to suppress the contamination due to objects misidentified as muons.

Tight muons: provide the highest purity with an improved background rejection at the cost of a few percent efficiency loss. Here, only Medium CB muons with hits in at least two stations of the MS can be defined as tight.

High$-p_T$ muons: are selected to maximise the momentum resolution of tracks with $p_T > 100$ GeV. CB muons also passing the medium selection and with at least three hits in three MS stations are selected.

Low$-p_T$ muons: are selected to optimize and to maintain high purity for $p_T \lesssim 5$ GeV

Muons from prompt decays of SM bosons or hypothetical BSM particles can be discriminated from muons from hadronic sources by measuring the amount of hadronic activity in their vicinity and therefore an isolation is required. The muon isolation is either track-based or calorimeter-based.

Track-based isolation is defined as the scalar sum of the transverse momenta of the ID tracks associated with the primary vertex in an $\eta - \phi$ cone of a given size ΔR around the muon, excluding the muon track itself. Depending on the isolation criteria, ΔR is either 0.2, labelled as p_T^{cone20}, or $\min(10 \text{ GeV}/p_T^\mu, 0.3)$, labelled as $p_T^{\mathrm{varcone30}}$.

On the other hand, Calorimeter-based isolation, labelled as E_T^{cone20} is defined as the sum of the transverse energy of cell clusters in a cone of size $\Delta R = 0.2$ around the position of the muon, extrapolated to the calorimeters after subtracting the contribution from the energy deposit of the muon.

The track-based or calorimeter-based isolation is defined as the transverse energy (or momentum if considering only tracks) reconstructed in a cone of size ΔR around a muon and divided by the muon transverse momentum (p_T). Several WPs are defined combining track-based and calorimeter-based isolation resulting in better performance. Some of these WPs use a particle-flow based algorithm to evaluate the neutral component of the energy deposit [116]. To determine the efficiency of a certain algorithm in both data and simulation the *Tag-and-Probe* method is applied to $Z \to \mu\mu$ and $J/\psi \to \mu\mu$. In this algorithm, one particle, called the "tag", is identified with high confidence using specific criteria tailored to the particle of interest. This tagged particle serves as a reference to select a sample of other particles, known as "probes", for further analysis as described in [116]. The deviation of the simulation from the detector behaviour in data is estimated by a Scale Factor (efficiencies ratio) that is used to correct the simulation.

3.2.1.1 Muon Selection

The present work implements the following selection for the di-muon resonances $Z \to \mu\mu$ and $J/\psi \to \mu\mu$,

- Both muons p_T cut (for Z only): $p_T > 25$ GeV.

- Both muons p_T cut (for J/ψ only): $p_T > 6.5$ GeV.

- Resonances mass:

  - For Z: $75 < m_Z < 105$ GeV.

– For J/ψ: $2.6 < m_{J/\psi} < 3.6$ GeV.

- Medium quality.

- Combined muons (Spectrometer + ID track).

- Vertexing cut: $|d_0|/\sigma(d_0) < 3$ and $|z_0 \sin\theta| < 0.5$ [mm].

The following triggers were applied:

- For $Z \to \mu\mu$ candidate events, the selection process implements unprescaled single-muon trigger chains with the lowest kinematic thresholds available in each data sample. Events are required to have at least one muon with p_T >20 GeV that also satisfies a loose isolation criterion based on the scalar sum of the p_T of tracks within a cone around the muon candidate track. Additionally, events are retained if they meet the criteria of a second chain, which requires at least one muon with p_T >40 GeV without any isolation requirement. [117].

- For $J/\psi \to \mu\mu$ candidate events, triggers requiring at least two muons per event are considered. These triggers also perform common vertex fits on pairs of oppositely charged muon candidates, ensuring at least one fitted vertex meets quality criteria and has an invariant mass consistent with a J/ψ resonance. Both muons must have p_T >5 GeV to satisfy the trigger requirements [117].

3.2.2   Electron reconstruction

The reconstruction of electrons and photons in the ATLAS detector involves a meticulous process designed to accurately identify and measure the properties of these particles. These process is divided in four main steps, the cluster reconstruction, track association, track refit and the final candidate reconstruction as shown in Fig. 3.4.

Initially, electrons and photons interact with the calorimeter layers, depositing energy primarily in the electromagnetic calorimeter (ECAL) for photons and both the ECAL and hadronic calorimeter (HCAL) for electrons. The energy deposited (E) by particles in the calorimeter cells forms

clusters, where neighboring cells with significant energy deposits are combined. Here, the seed cluster reconstruction is carried out in the $\eta \times \phi$ space of the EM calorimeter that is divided into a grid of 200×256 elements known as towers with a granularity of size $\Delta \eta \times \Delta \phi = 0.25 \times 0.25$. The total energy tower is then computed as the sum of the energy deposits on each element. To seed the electromagnetic-energy cluster candidates a summed transverse energy above 2.5 GeV is required by a sliding-window algorithm [122] with a windows size of 3×5 towers in $\eta \times \phi$. Finally, the duplicated seed clusters are removed. For electrons, this clustering process is crucial for identifying electromagnetic showers characteristic of electron interactions. Electromagnetic showers occur when high-energy electrons or photons interact with the material in the calorimeter, producing a cascade of secondary particles through bremsstrahlung and pair production processes. The energy (E) of the clusters is then used to determine the particle's energy. Additionally, energy calibration corrects for detector effects, ensuring precise energy measurements. This calibration involves adjusting the measured energy (E_{measured}) to account for factors such as energy loss in the detector material and non-uniformities in detector response. The calibrated energy ($E_{\text{calibrated}}$) is then used in the identification and selection of electrons and photons based on specific criteria, such as energy consistency and track association.

One the clusters are defined and the track reconstruction has been performed in the ID, the clusters are associated with at least one well-reconstructed track of the ID with the following requirements for a sucessful matching, $|\Delta \eta| < 0.05$ and $|\Delta \phi| < 0.01$. In the case that several tracks are matched with the EM cluster, the selection criteria targets the tracks with silicon hits and those with the smallest $\Delta R = \sqrt{\Delta \eta^2 + \Delta \phi^2}$ that later on are refined by taking into account the solenoid magnetic field and the energy losses due to bremsstrahlung. The track is also required to be close to the IP with $d_0/\sigma_0 < 5$ and $|z_0 \sin \theta| < 0.05$ mm to reject electrons originated from photon conversions. In the case a track cannot be matched, the cluster is classified as an unconverted photon candidate.

Once the track-association was performed successfully, the candidate reconstruction is carried out by the formation of extended clusters around the seed clusters in a window of size 3×7 and 5×5 in the $\eta - \phi$ plane for the barrel and the ECT, respectively. Then, the cluster energy is calibrated

by multivariate techniques using data and simulation. The final track parameters of the electrons are taken from the track best matched to the original seed cluster while the final energy is obtained from the calibrated energy of the extended-window cluster.

Similarly as the muon, different Working Points (WP) for the electrons are defined as loose, medium and tight.

Loose: considers electrons for $|\eta| < 2.47$ with cuts on the shower shape variables of the first and second layers of the Electromagnetic Calorimeter (ECal) and the hadronic leakage variables.

Medium: takes electrons with cuts on the track quality that verify that the hits in the Pixel Detector is larger or equal to one. The total number of hits in the pixel detector and SCT is required to be larger or equal than 7 and the transverse impact parameter $|d_0| < 5$ mm. For the track-cluster matching $\Delta\eta < 0.01$ between the cluster position in the strip layer and the extrapolated track is required. This includes also loose selection.

Tight: the cuts in the track quality are a tighter transverse impact parameter, this is, $|d_0| < 1$ mm, total number of hits in the TRT and ratio of the number of high-threshold hits to the total number of hits in the TRT. For the track cluster matching a $\Delta\phi < 0.02$ between the cluster position in the middle layer and the extrapolated track is required. For the photon conversion variables the number of hits in the b-layer are requested to be larger or equal to one and the veto electron candidates matched to reconstructed photon conversions. This includes also medium selection.

3.2.2.1 Electron selection

On what follows, electrons are required to pass the tight identification and to have $p_T > 15$ GeV and $|\eta| < 2.4$ excluding the region $1.2 < |\eta| < 1.82$. For the background rejection the requirement of absence of an activity around electron tracks is applied. To keep an isolation efficiency of 97% for track-based and 98% for calorimeter-based variables the track-based and calorimeter-based isolation cuts are considered to be p_T^{cone40} and E_T^{cone20}, respectively. Where cone40 and cone20 refers to $\Delta R < 0.4$ and $\Delta R < 0.2$ around the electron.

In the case of the low pile-up, the data was collected with unprescaled triggers that require at least one electron with transverse momentum thresholds of $p_T > 15$ GeV with Loose identification
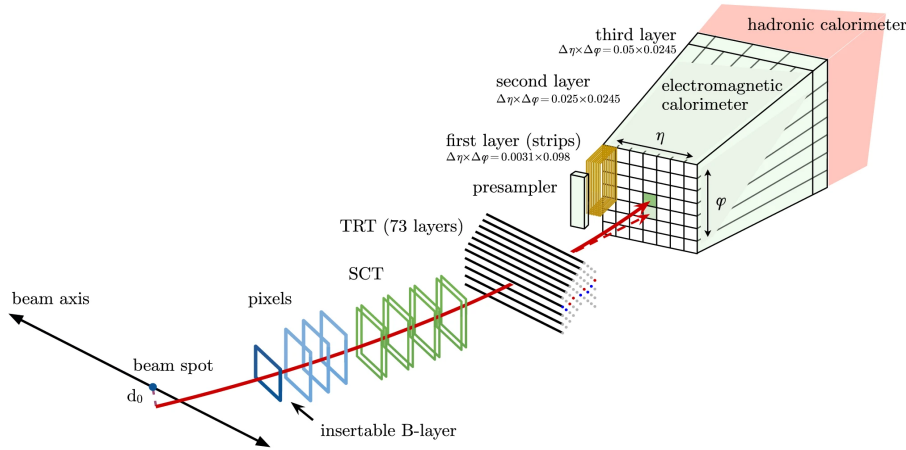
Figure 3.4: Illustration of the path of an electron through the detector. The red trajectory shows the hypothetical path of an electron, which first traverses the tracking system (pixel detectors, then siliconstrip detectors and lastly the TRT) and then enters the electromagnetic calorimeter. The dashed red trajectory indicates the path of a photon produced by the interaction of the electron with the material in the tracking system [123]

criteria and no isolation selection.

3.2.3 Hadronic Recoil

In general leptons or photons can be directly reconstructed using the procedures already described. However, this is not the general case for all particles in the ATLAS detector since some of them can escape unseen, such as, neutrinos, BSM particles, etc. However, kinematically they should produce an imbalance in the total transverse momentum of the visible particles that could be measured, e.g. the W/Z Gauge bosons. This quantity is known as missing transverse momentum, E_T^{miss}, and the neutrino transverse momentum $\vec{p}_T^{\nu}$ can be directly related to it. It can be obtained by the momentum conservation as the negative of the vector sum of the visible particle momenta,

$$\vec{p}_T^{\nu} = \vec{E}_T^{\text{miss}} = -\sum_i \vec{p}_{T,i} \tag{3.2}$$

where i runs over the visible particles. This concept is crucial in analyses as the W and Z bosons in which neutrinos are involved in their decays. At Leading Order, the transverse momentum of the bosons is expected to be zero but at higher orders, contributions for the QCD effects are expected. This, defines the Hadronic Recoil (HR), $\vec{u}_T$, as the sum of the transverse momenta of the partons

from initial state radiation,

$$\vec{u}_T = -\sum p_T^{\text{partons}}. \tag{3.3}$$

Based on this, the neutrino transverse momentum can be expressed as a function of the HR and the lepton transverse momentum $\vec{p}_T^{\ell}$,

$$\vec{p}_T^{\nu} = \vec{E}_T^{\text{miss}} = -\left(\vec{u}_T + \vec{p}_T^{\ell}\right). \tag{3.4}$$

In practice, E_T^{miss} can obtained experimentally by dividing it into two components known as the hard component, $E_T^{\text{miss, hard}}$, and the soft component, $E_T^{\text{miss, soft}}$. Where $E_T^{\text{miss, hard}}$ is defined as the vector sum of the reconstructed particles in the event while, $E_T^{\text{miss, soft}}$, is the vector sum of all the tracks that cannot be matched to a physical object. The soft term can be computed by two ways, either using the Calorimeter-based Soft Terms (CST) that correspond to the calorimeter signals that are not matched to a physical object or by the Track-based Soft Term (TST) defined as low momentum tracks that matched the PV but not a physical object.

The hadronic recoil described above is a vector quantity that can be projected along the transverse momentum vector to obtain scalar quantities known as the parallel component, $u_{\parallel}$, and the perpendicular component, $u_{\perp}$. In an ideal scenario, $u_{\parallel} = -p_T^V$ and $u_{\perp} = 0$ is expected where p_T^V is the magnitude of the vector boson momentum. In the case of the $W \to \ell\nu$ (Fig. 3.5a), the hadronic recoil relies in the direction of the charged lepton due to the neutrino in the decay product,

$$
\begin{aligned}
u_{\perp}^W &= \frac{|\vec{p}_T^{\ell} \times \vec{u}_T|}{p_T^{\ell}}, \\
u_{\parallel}^W &= \frac{\vec{p}_T^{\ell} \cdot \vec{u}_T}{p_T^{\ell}},
\end{aligned}
\tag{3.5}
$$

while for the Z boson (Fig. 3.5b), the momentum is represented by the di-lepton transverse momentum $\vec{p}_T^{\ell\ell}$ and the HR components are,

$$
\begin{aligned}
u_{\perp}^Z &= \frac{|\vec{p}_T^{\ell\ell} \times \vec{u}_T|}{p_T^{\ell\ell}}, \\
u_{\parallel}^Z &= \frac{\vec{p}_T^{\ell\ell} \cdot \vec{u}_T}{p_T^{\ell\ell}},
\end{aligned}
\tag{3.6}
$$
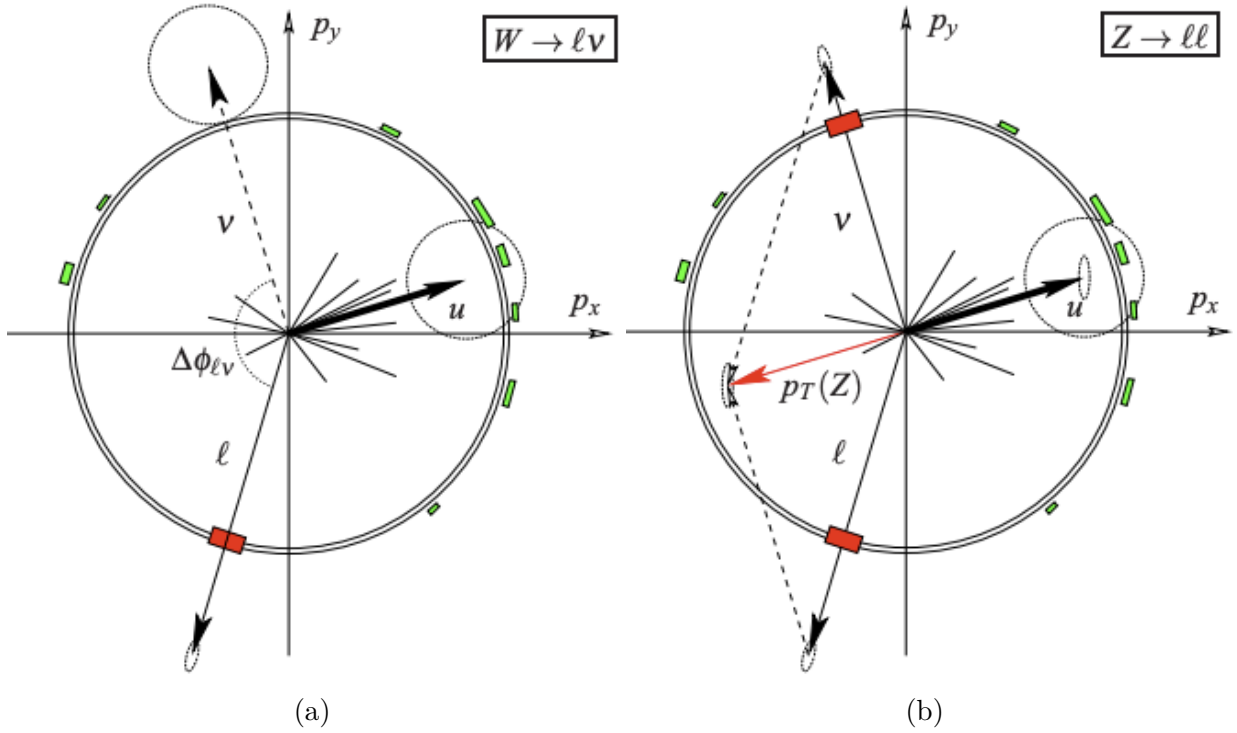
Figure 3.5: Scheme of the (a) W and (b) Z bosons decay in the transverse plane [124].

In average, $u_\perp$ is expected to compatible with zero and with an spread reflecting the hadronic recoil resolution in this direction. On the other hand, at LO the boson transverse momentum is expected to be zero implying $u_\parallel = -p_T^{\ell\ell}$. However, other effects like particles escaping detection, energy losses in dead material and the noncompensating nature of the calorimeter make difficult to reach the relation. This means, a bias "b" in the parallel component is introduced,

$$u_\parallel = b - p_T^{\ell\ell}, \tag{3.7}$$

where the average in the bias provides the parallel HR resolution.

During the reconstruction process in the ATLAS detector, it is common for objects to meet the identification requirements of multiple physical particles, resulting in an overlap. To address this, an overlap removal is employed to determine the nature of each reconstructed object and to prevent double-counting of energy, particularly in the calculation of E_T^{miss}.

3.3 Event simulation

Monte Carlo (MC) simulations are extensively used in particle physics to test the SM processes and to look for new physics scenarios. In particlar, the ATLAS collaboration uses its own simulation framework [125] and the GEANT4 [126] detector simulation toolkit. The simulation and reconstruction workflow can be summarized as,

- The simulation process in ATLAS begins with the generation of events originating from the hard-scattering of colliding partons and their immediate decay products, referred to as truth-level simulation. The choice of parton distribution functions (PDFs) is critical, providing essential parameters to compute the production cross section of the targeted physics process.

- During event generation, QCD processes and interactions resulting from parton collisions lead to multiple radiation cascades known as parton showers. Following this, hadronisation occurs where the quarks and gluons produced in these showers recombine to form new hadrons or underlying events, which subsequently decay.

- Next, the generated particles interact with the components of the detector. These interactions are simulated using the GEANT4 toolkit, which replicates the full ATLAS detector, including its geometry, realistic response, misalignments, and distortions. Single hard-scatter processes are generated individually and then overlaid to simulate additional interactions from bunch crossing (pile-up) effects. The energy deposited in the detector by the particles is converted into voltage and currents, which can then be compared with the detector readouts in a process known as digitisation.

- Finally, the simulated events are reconstructed by the detector, referred to as reco-level simulation. The same reconstruction procedure used for real observed events is applied to the Monte Carlo (MC) simulated events, leading to comparable outputs for both simulated and actual observed events.

A simplified scheme of the simulation workflow in ATLAS is shown in Fig. 3.6. The Simulation samples for muon calibration are described in Section 5.2 while for the m_W measurement, the
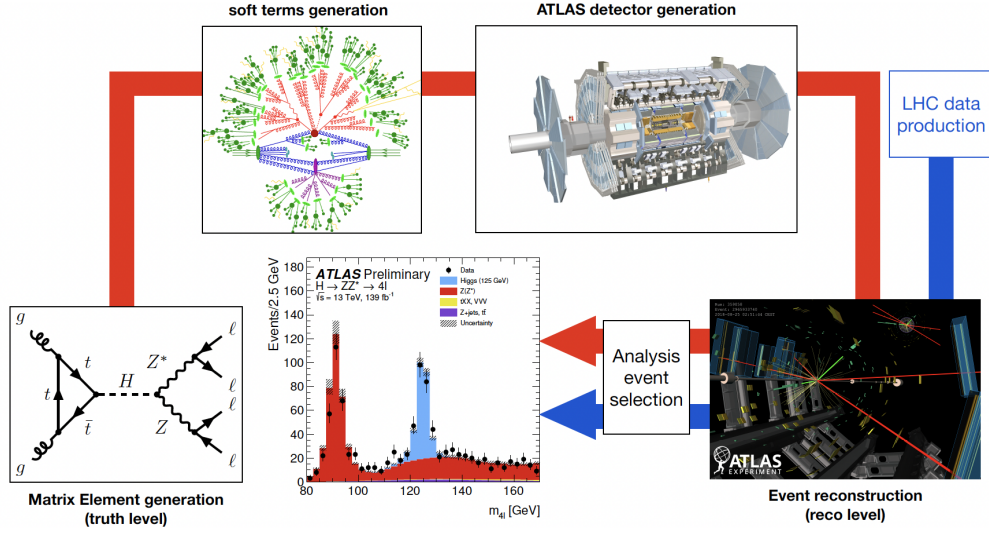
Figure 3.6: Simplified scheme of the ATLAS simulation and reconstruction infrastructure [91].

simulation samples at 7 TeV and low pile-up (5.02 TeV and 13 TeV) are detailed in Section 6.3.

Chapter 4

Parameter estimation

Parameter estimation is a fundamental aspect of statistical analysis aimed at determining the unknown parameters of a statistical model based on observed data. In statistical inference, one common approach to parameter estimation involves using methods like the chi-square (χ^2) method. This method plays significant roles in quantifying uncertainties associated with parameter estimates such as the statistical uncertainty and systematic uncertainties introduced through nuisance parameters (NPs). The statistical uncertainty refers to the inherent variability in parameter estimates due to random sampling of data. This uncertainty is quantified using statistical measures such as standard errors, confidence intervals, or likelihood-based approaches. On the other hand, the systematic uncertainty arises from potential biases or inaccuracies in the modelling assumptions or experimental setup. It represents uncertainties that persist regardless of the amount of data collected and can significantly impact parameter estimates. Systematic uncertainties are often addressed through sensitivity analyses, calibration procedures, or by incorporating additional sources of information into the estimation process.

The chi-square method is particularly valuable in scenarios where data follows a known distribution, and parameter estimation is achieved by comparing observed data with expected theoretical outcomes. This method typically involves formulating a chi-square statistic that measures the goodness-of-fit between observed data and model predictions. Minimizing these statistics allows to estimate the parameters that best describe the underlying distribution of the data. When system-

atic sources are considered in the analysis, their contribution can be obtained using the so-called "χ^2 offset method" or, more sophisticatedly, by a profile likelihood approach (PLH).

The profile likelihood approach of the χ^2 is another powerful technique used in parameter estimation, particularly in scenarios involving simultaneous estimation of multiple parameters. It involves constructing likelihood profiles by fixing certain parameters to specific values while maximizing the likelihood function with respect to the remaining parameters. The resulting profile likelihood curve provides insights into the uncertainties and correlations among the estimated parameters. Commonly, the profiling of the likelihood can takes several forms according to the data distribution and the probability models. However, in the case where the NPs and the data follows a Gaussian distribution, the likelihood can be solved analytically. This solutions allow to exploits consistent results for the POI and NPs such as a breakdown of uncertainties (uncertainty decompositon), shift induced by the NPs into the POIs, post-fit correlations among the fits, etc.

When a measurement of a physical quantity is performed, the total uncertainty can be decomposed into two components, the statistical uncertainty and the systematic uncertainty. Since different systematic sources can be considered into the analysis, the systematic uncertainty receives contributions from each source and it is important to understand the contribution of each of this source into the total systematic uncertainty. To determine this, the common approach used in high-energy physics is known as "impacts" which tends to quantify the impact of each systematic into the total uncertainty. However, this approach is not accurate since due to the post-fit correlation of the nuisance parameters the quadrature sum of the impacts does not return the total uncertainty and by consequence, these are underestimated. Here, an extensive study of profile likelihood fits and their uncertainty components was performed for a general case, as well as for the specific case when all uncertainties are Gaussian-distributed. A consistent fitting strategy is described to be used in the muon calibration in chapter 5 and for the W boson mass in chapter 6.

The following chapter is arranged as follows, Section 4.1 illustrates the statistical and systematic uncertainties via χ^2 offset method. Section 4.2 describes the Maximum Likelihood Estimator, the concept of nuisance parameters and the profile likelihood (PLH) fit approach. Section 4.3 study the PLH fit solution when the uncertainties are Gaussian-distributed exploiting the most of it and

showing a consistent uncertainty decomposition among other properties of the likelihood and the covariance matrices.

4.1 Statistical and systematic uncertainties via χ^2 offset method

Given a set of n data points (x_i, y_i) with associated uncertainties σ_i, and a model function $f(x, \theta)$ with parameters θ, the goal is to find the parameters θ that best describe the data while accounting for the uncertainties.

The chi-square function (χ^2) is defined as the sum of the squared differences between the observed data points and the model predictions, normalized by the uncertainties:

$$\chi^2(\theta) = \sum_{i=1}^{n} \left(\frac{y_i - f_i(x, \theta)}{\sigma_i} \right)^2. \tag{4.1}$$

The best-fitting parameters, θ, are obtained by minimizing the χ^2 function. In cases where f is linear in θ, an analytical expression can be found or in the case of higher orders, a perturbative approach to $|\theta| \ll 1$ can be performed. In a general approach, a Taylor expansion can be performed as follows,

$$f_i \approx f_i(\theta_0) + \left. \frac{\partial f_i}{\partial \theta} \right|_{\theta_0} (\theta - \theta_0) = f_{i,0} + h_i \cdot (\theta - \theta_0), \tag{4.2}$$

where θ_0 is the nominal value of θ[1]. This allows to expand the χ^2 to a first order in θ to fit a parabola that reaches its minimum at $\hat{\theta}$,

$$\chi^2(\theta) = \chi^2(\hat{\theta} \pm \hat{\sigma}^{\text{stat}}) = \chi^2_{min} + 1, \tag{4.3}$$

where $\hat{\sigma}^{\text{stat}}$ is the statistical uncertainty in $\hat{\theta}$. In general, a smaller value of (χ^2) indicates a better fit between the model and the observed data, with the uncertainties taken into account. Ideally, the best-fit model will have a (χ^2) close to the number of degrees of freedom (n.d.f) obtained as

---

[1]Notice that θ_0 can be set to zero without loss of generality.

n minus the number of parameters being fit, indicating that the model adequately describes the data within the uncertainties. One of the reasons why this method is largely used in data analysis is because it provides a **goodness-of-fit measure** or also called χ^2 probability $P(\chi^2, \text{n.d.f})$. A small χ^2-probability indicates that the observed data is unlikely to have occurred by chance if the model were correct, suggesting that the model provides a good fit to the data. Conversely, a large chi-square probability suggests that the model may not adequately describe the data, indicating a poor fit. In simple terms, $P(\chi^2, \text{n.d.f})$ indicates "what is the probability of getting a giving χ^2 value or something worse, assuming this is the correct fit function". Three scenarios can be distinguished,

- $\chi^2/\text{n.d.f} \approx 1 \Rightarrow 0.01 < P(\chi^2, \text{n.d.f}) < 0.99$ all is good.

- $\chi^2/\text{n.d.f} \gg 1 \Rightarrow P(\chi^2, \text{n.d.f}) < 0.01$ implies a bad fit due to a wrong hypothesis or modelling, the data is faulty, or the errors are too small.

- $\chi^2/\text{n.d.f} \ll 1 \Rightarrow 0.99 < P(\chi^2, \text{n.d.f})$ the fit modelling is too good, which could imply an overestimation of uncertainties.

The χ^2 method is a valuable statistical technique for assessing the goodness-of-fit of models to observed data. It provides a quantitative measure of the discrepancy between the observed and expected values, taking into account the uncertainties in the data. The chi-square method is particularly useful for hypothesis testing and model comparison, as it yields a chi-square statistic and associated probability ($p-$value) that indicates the likelihood of the observed data under the assumed model.

The offset method

The χ^2 in Eq. (4.1) accounts only for data in which the uncertainties are originated from statistical sources. However, in several analyses, the systematic sources play a role in the parameter estimation and by consequence they need to be accounted for to properly determine their contribution to the total uncertainty. One of the most common approaches is known as the offset method. In this, to estimate the systematic uncertainty contribution of a given source r, the data is replaced by pseudo-data accounting for the effect of the systematic source, the fit is repeated to find the minimum of the

parabola such that the offset between $\hat{\theta}_r$ and the new minimum, $\hat{\theta}$, is taken to be the uncertainty, $\hat{\sigma}_r$. The total systematic uncertainty, $\hat{\sigma}^{\text{syst}}$, is retrieved as the quadrature sum ($\oplus$) of the uncertainty components,

$$\hat{\sigma}^{\text{syst}} = \oplus_r \hat{\sigma}_r. \tag{4.4}$$

The final result is quoted as,

$$\hat{\theta} \pm \hat{\sigma}^{\text{total}} = \hat{\theta} \pm \hat{\sigma}^{\text{stat}} \oplus \hat{\sigma}^{\text{syst}}. \tag{4.5}$$

where $\hat{\sigma}^{\text{total}}$ is the quadratic sum of the statistical and systematic components. Some limitations of this approach could be related to the fact that the χ^2 offset method may not adequately capture correlations between different sources of systematic uncertainties. In practice, systematic effects can be interrelated or dependent on one another, and ignoring these correlations can lead to underestimating the true uncertainty. Also, the numerical stability can depend on the complexity of the model and the number of parameters, the minimization of the χ^2 function (particularly when including additional offset parameters) can become computationally intensive and numerically unstable. Careful optimization techniques and regularization methods may be needed to ensure reliable results.

4.2   Maximum Likelihood Estimator (MLE)

A more general and versatile technique to fit model to data is known as the Maximum Likelihood Estimator method (MLE). Given a statistical model with parameters θ and observed data $X = \{x_1, ..., x_N\}$ (statistically independent quantities), the goal is to find the values of θ that maximize the likelihood of observing the given data. To measure how likely the observed data X are under the given model and parameter values θ the likelihood function (joint probability) $\mathcal{L}(X|\theta)$ is calculated. It is often expressed as the probability density function (pdf) $f(x_i|\theta)$, conditional on the parameter values. For N trials, $\mathcal{L}$ can be expressed as,

$$\mathcal{L}(X|\theta) = \prod_{i=1}^{N} f(x_i|\theta). \tag{4.6}$$

To maximize $\mathcal{L}$ is more convenient to minimize $-2 \ln \mathcal{L}(X|\theta)$. This means, the solution to the MLE is given by,

$$\left. \frac{\partial \ln \mathcal{L}(X|\theta)}{\partial \theta} \right|_{\theta = \hat{\theta}} = 0, \qquad (4.7)$$

where $\hat{\theta}$ is the value that maximize the likelihood and the uncertainty in the MLE estimator $\sigma_{\hat{\theta}}$ is given by the inverse of the Hessian matrix of the likelihood. In the case of one single parameter θ the likelihood function expanded around $\hat{\theta}$ can be scanned around its minimum as,

$$-2 \ln \mathcal{L}(\hat{\theta} \pm \sigma_{\hat{\theta}}) = -2 \ln \mathcal{L}_{\max} + 1, \qquad (4.8)$$

where $\mathcal{L}_{\max} = \mathcal{L}(\hat{\theta})$. Sometimes the number of events n is not fixed but they are distributed as a Poisson variable with mean ν_i, then $\mathcal{L}$ can be expressed [127] as,

$$\mathcal{L}(X|\nu(\theta)) = \prod_{i=1}^{N} \frac{\nu_i^{x_i}}{x_i!} e^{-\nu_i}. \qquad (4.9)$$

Here ν_i represents the rate parameter of the Poisson distribution for the $i-$th observation. In the case where the probability density function can be expressed as a signal, S_i, and background, B_i, Eq. (4.9) is given by,

$$\mathcal{L}(X|\nu(\theta)) = \prod_{i=1}^{N} \frac{(S_i + B_i)^{x_i}}{x_i!} e^{-(S_i + B_i)}. \qquad (4.10)$$

4.2.1 Nuisance parameters

In statistical analysis, nuisance parameters (NPs) are often estimated alongside the POIs using methods such as the MLE or Bayesian inference with the Likelihood function being a function of the NPs, $\mathcal{L}(X|\theta, \alpha)$, with α the NPs. Once estimated, NPs can be "integrated out" or marginalized to obtain valid inferences about the POI. To deal with the NPs two approaches are commonly used. The first one is called the Marginalisation (Bayesian approach) that consists in integrating the likelihood $\mathcal{L}$ over the NPs with prior knowledge P, leaving a likelihood as a function of the POIs only,

$$L(\theta) = \int d\alpha P(\alpha) \mathcal{L}(\theta, \alpha). \qquad (4.11)$$

72

The second approach is known as profiling or profile likelihood (PLH) method and assumes that the likelihood can be factorized with respect to the NPs where each likelihood of the NPs is independent of the other NPs, this is,

$$\mathcal{L}(X|\theta, \alpha) = \mathcal{L}(X|\theta) \cdot \mathcal{C}(\alpha), \tag{4.12}$$

where $\mathcal{C}$ is the likelihood of the NPs known as constrain or penalty term, which takes the variation of the NPs into account. In this way, the PLH function is obtained by maximizing the likelihood function with respect to the nuisance parameters α for each fixed value of the parameters of interest θ,

$$PLH(X|\theta) = \max_{\alpha} \left\{ \mathcal{L}(X|\theta, \alpha) \right\}, \tag{4.13}$$

then the profile likelihood function $PLH(X|\theta)$ is used for inference about the POI. Often NPs are considered as univariate Gaussian random variables which simplifies considerably the problem. Moreover, the NPs treatment is totally an election that can vary according to the model approach. However, the profiling technique is largely implemented when there is more than one floating parameter involved. In the χ^2 approach the NPs can be introduced into the χ^2-function as "penalty terms" that account deviations from the expected values based on the estimated nuisance parameters, adjusting the chi-square statistic to reflect the additional uncertainty in the model providing a more accurate result compared to the χ^2-offset method in the NPs treatment.

4.2.2   Profile likelihood fit

The following study is focused on the case where the NPs are Gaussian-distributed such that the likelihood is given by Eq. (4.12) with $\mathcal{C}$,

$$\mathcal{C}(\alpha) = \prod_r \text{Gauss}(\alpha_r|a_r) = \prod_r \frac{1}{\sqrt{2\pi}\sigma_r} \exp\left(-\frac{(\alpha_r - a_r)^2}{2\sigma_r^2}\right) \tag{4.14}$$

where α_r is the $r-$th nuisance parameter, a_r and σ_r are the mean value and standard deviation of the $r-$th NP, respectively. Considering a set of data $\vec{m} = m_1, ..., m_N$, then the likelihood can be

expressed as,

$$\mathcal{L}(\vec{m}|\vec{\theta},\vec{\alpha}) = \prod_i \text{Poisson}(m_i|\nu_i(\vec{\theta},\vec{\alpha})) \cdot \prod_r \text{Gauss}(\alpha_r|a_r), \tag{4.15}$$

where m_i is the event observed in data in bin i. Here, ν_i represents the total prediction (signal modelling) in the bin i that depends on the NPs and $\vec{\theta}$ that corresponds to the vector of parameter of interest (POIs). Assuming a linear dependence of the probability model with respect to the POI and NPs, $\nu_i(\vec{\theta},\vec{\alpha})$ be parametrized as follows,

$$\nu_i(\vec{\theta},\vec{\alpha}) = t_{0,i} + \sum_p h_{ip}(\theta_p - \theta_{0,p}) + \sum_r \Gamma_{ir}(\alpha_r - a_r), \tag{4.16}$$

Where $\vec{\theta}_0$ are the reference values of the POI, $\vec{t}_0 = \nu(\vec{\theta}_0, \vec{a})$ is the nominal prediction of the POIs and NPs reference values and h and Γ are the sensitivity matrices of the prediction with respect to the POI and the NPs, this is,

$$h_{ip} = \frac{\partial \nu_i(\vec{\theta},\vec{\alpha})}{\partial \theta_p}, \quad \Gamma_{ir} = \frac{\partial \nu_i(\vec{\theta},\vec{\alpha})}{\partial \alpha_r}. \tag{4.17}$$

4.3 Likelihood fit in the Gaussian limit

The formalism previously described is suitable for several analysis and fit model to data. However, in most of the scenarios a numerical approach to find the solution that maximizes the likelihood is needed. For large datasets this can require a high numerical power apart from a considerably amount of time. For that reason, an analytical approach [128, 129] could provide a fast and accurate solution that could model the data [130–132]. It is important to highlight that in the scenario where all the uncertainties are Gaussian-distributed the negative logarithm of the likelihood is proportional to the χ^2 function,

$$-2\log\mathcal{L} \equiv \chi^2, \tag{4.18}$$

such that the PLH fit is just the way in which the minimum of the likelihood function is found. Moreover, this section shows that in this limit, the minimum of the parabola can be found by different ways, first profiling over the NPs while the POI is fixed and second by profiling over the
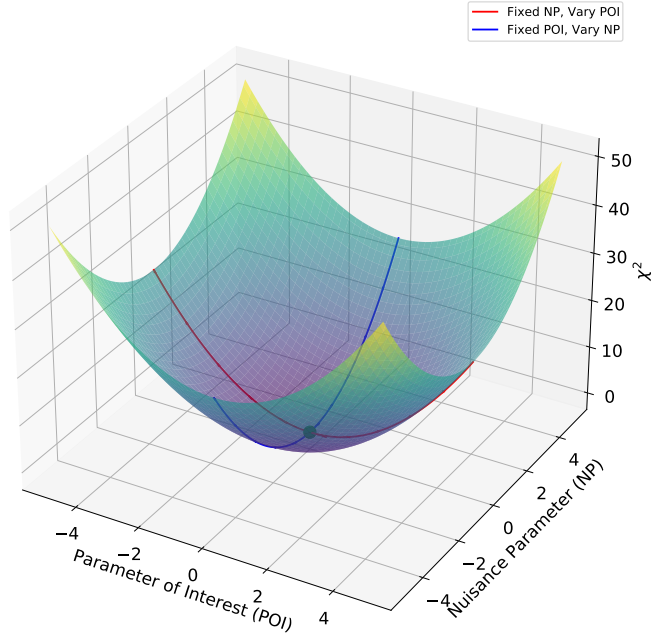
Figure 4.1: Minimization of the χ^2 (1 POI + 1 NP) by profiling over the NPs while keeping the POI fixed (blue curve) and profiling over the POI while keeping the NPs fixed (red line).

POI while the NPs are fixed as shown in Fig. 4.1. Both minimizations lead to the same result since the parabola is fully symmetric and there is no possibility of more than one minimum or plateaus in the likelihood that could deviate the minimum. This not only provides a consistent result in both cases but it also allows to exploit the analytical solution in different ways.

In the case where all the uncertainties are Gaussian and the model is linear dependent with the POI and NPs, the likelihood (4.15) admits an analytical solution [133–142] and it can be expressed as follows,

$$-2\ln\mathcal{L}(\vec{\theta},\vec{\alpha}) = \sum_{i,j}\left(m_i - t_i(\vec{\theta}) - \sum_r \Gamma_{ir}(\alpha_r - a_r)\right)V_{ij}^{-1}\left(m_j - t_j(\vec{\theta}) - \sum_s \Gamma_{js}(\alpha_s - a_s)\right) \\ + \sum_r(\alpha_r - a_r)^2. \tag{4.19}$$

where $t_i(\vec{\theta}) = \vec{t}_0 + h \cdot \vec{\theta}$ (using $\vec{\theta}_0 = \vec{0}$) and V_{ij} represents the statistical covariance matrix that in general is non-diagonal. Eq. (4.19) is solved by profiling the NPs, this is, first minimizing over $\vec{\alpha}$, for fixed $\vec{\theta}$. Then substituting the result into Eq. (4.19) (thus obtaining the *profile likelihood*

$\ln \mathcal{L}(\vec{\theta}, \hat{\vec{\alpha}}(\vec{\theta}))$; and minimizing over $\vec{\theta}$. The profiled NPs are given by,

$$\hat{\alpha}_r(\vec{\theta}) = \sum_i Q_{ri} \left(m_i - t_i(\vec{\theta}) \right) + a_r, \tag{4.20}$$

with,

$$Q_{ri} = \sum_s \left(\mathbb{I} + \Gamma^T V^{-1} \Gamma \right)_{rs}^{-1} (\Gamma^T V^{-1})_{si}. \tag{4.21}$$

The NPs covariance is given by,

$$\mathrm{cov}(\hat{\alpha}_r, \hat{\alpha}_s)(\vec{\theta}) = \left(\mathbb{I} + \Gamma^T V^{-1} \Gamma \right)_{rs}^{-1}. \tag{4.22}$$

Replacing Eq. (4.20) into Eq. (4.19), the profile likelihood can be written as

$$-2 \ln \mathcal{L} \left(\vec{\theta}, \hat{\vec{\alpha}}(\vec{\theta}) \right) = \sum_{i,j} \left(m_i - t_i(\vec{\theta}) \right) S_{ij} \left(m_j - t_j(\vec{\theta}) \right), \tag{4.23}$$

where,

$$S_{ij} = \sum_k V_{ik}^{-1} \left(\mathbb{I} - \Gamma \cdot Q \right)_{kj}, \tag{4.24}$$

Therefore Eqs. (4.23) admits a covariance representation that can be seen as the result of maximizing $\mathcal{L}(\vec{\theta}, \vec{\alpha})$ over $\vec{\alpha}$, for fixed $\vec{\theta}$: it is the profile likelihood. The solution to (4.23) is given by,

$$\hat{\theta}_p = \sum_i \lambda_{pi}(m_i - t_{0,i}), \tag{4.25}$$

$$\mathrm{cov}(\hat{\theta}_p, \hat{\theta}_q) = \sum_{i,j} \lambda_{pi} C_{ij} \lambda_{qj}. \tag{4.26}$$

or equivalently,

$$\mathrm{cov}(\hat{\theta}_p, \hat{\theta}_q) = \left(h^T \cdot S \cdot h \right)_{pq}^{-1}, \tag{4.27}$$

with $\text{cov}(\hat{\theta}_p, \hat{\theta}_q)$ the total covariance in the POIs and,

$$\lambda_{pi} = \sum_q \left(h^T \cdot S \cdot h\right)^{-1}_{pq} \cdot \left(h^T \cdot S\right)_{qi}, \tag{4.28}$$

$$C_{ij} = V_{ij} + \sum_r \Gamma_{ir}\Gamma_{jr}, \tag{4.29}$$

with C the total covariance matrix of the measurements and $C_{\text{syst.}} = \Gamma \cdot \Gamma^T$ the systematic covariance matrix. Moreover Eq. (4.24) and Eq. (4.29) verify,

$$\sum_k V_{ik}^{-1} \left(\mathbb{I} - \Gamma \cdot Q\right)_{kj} = \left(V_{ij} + \sum_r \Gamma_{ir}\Gamma_{jr}\right)^{-1} , \text{ i.e} \tag{4.30}$$

$$S_{ij} = C_{ij}^{-1}, \tag{4.31}$$

To obatin the total post-fit covariance matrix of the NPs the procedure can be repeated but this time profiling the POI, this is, first minimizing over $\vec{\theta}$ for given $\vec{\alpha}$, substituting the result into Eq. (4.19), and minimising the result over $\vec{\alpha}$ leading to,

$$\text{cov}(\hat{\alpha}_r, \hat{\alpha}_s) = \left[\mathbb{I} + (\zeta \cdot \Gamma)^T V^{-1}(\zeta \cdot \Gamma)\right]^{-1}_{rs}, \tag{4.32}$$

with

$$\zeta_{ij} = \sum_p h_{ip}\rho_{pj} - \delta_{ij}, \tag{4.33}$$

$$\rho_{pj} = \sum_q (h^T \cdot V^{-1} \cdot h)^{-1}_{pq}(h^T \cdot V^{-1})_{qj}, \tag{4.34}$$

while the "covariance" between the NPs and POI is given by

$$\text{cov}\left(\hat{\alpha}_r, \hat{\theta}_p\right) = -\sum_s \left[\mathbb{I} + (\zeta \cdot \Gamma)^T V^{-1}(\zeta \cdot \Gamma)\right]^{-1}_{rs} (\rho \cdot \Gamma)_{ps}. \tag{4.35}$$

Equations (4.26), (4.32) and (4.35) determine the full covariance matrix of the fitted parameters.

Importantly, Eq. (4.35) can be further simplified to

$$\mathrm{cov}\left(\hat{\alpha}_r, \hat{\theta}_p\right) = -\sum_i \lambda_{ip}\Gamma_{ri}, \tag{4.36}$$

The inner product of Eq. (4.36) with itself gives the systematic covariance and the statistical uncertainty can be obtained subtracting the result in quadrature from the total uncertainty in $\hat{\theta}_p$. In other words, the contribution of every systematic source to the total uncertainty is directly given by the covariance between the corresponding NP and the POI and the total covariance of the likelihood encodes the uncertainty components.

$$\mathrm{cov}\left(-2\ln\mathcal{L}\right) = \left(\begin{array}{c|c} \mathrm{cov}\left(\hat{\alpha}_r, \hat{\alpha}_s\right) & \mathrm{cov}\left(\hat{\alpha}_r, \hat{\theta}_q\right) \\ \hline \mathrm{cov}\left(\hat{\theta}_p, \hat{\alpha}_s\right) & \mathrm{cov}(\hat{\theta}_p, \hat{\theta}_q) \end{array} \right). \tag{4.37}$$

As an addition, Eq. (4.35) can be expressed in terms of the λ, h, Γ and S matrices as follows,

$$\mathrm{cov}\left(\hat{\alpha}_r, \hat{\alpha}_s\right) = \left[\mathbb{I} - 2\left(\tilde{\zeta}\cdot\Gamma\right)^T \cdot S \cdot \left(\tilde{\zeta}\cdot\Gamma\right)\right]_{rs}, \tag{4.38}$$

where,

$$\tilde{\zeta}_{ij} = \sum_p h_{ip}\lambda_{pj} - \delta_{ij}. \tag{4.39}$$

Notice that Eq. (4.38) does not involve the matrix inversion and is suitable for numerical purposes when dealing with a large number of nuisance parameters.

4.3.1 Shift induced by the NPs in the POI

When performing a fit in which the systematic sources play an important role is necessary to known which systematics are capable of deviate the POI central value with respect to the expected central value if there would not be systematic sources, i.e. the statistical only fit central value. This concept of "shift" induced by a NP into the POI is also not well understood in profile likelihood fits since commonly it is defined as the product of the pre-fit "impact" of a NP and its post-fit central value. However, as discussed in subsections 4.3.2.3 and section 4.3.3, the impact method is not fully

accurate when the post-fit NPs are correlated since the "impacts" tend to be overestimated.

Exploiting the Gaussian limit, the concept of shift induced by the NPs is straightforward and the total shift due to the systematic sources can be disentangled in the POI post-fit value as follows,

$$
\begin{aligned}
\hat{\hat{\theta}}_p(\hat{\vec{\alpha}}) &= \hat{\hat{\theta}}_p^{[\text{stat. only}]} + \hat{\hat{\theta}}_p^{[\text{syst}]}(\hat{\vec{\alpha}}), \\
&= \sum_i \rho_{pi}(m_i - t_{0,i}) - \sum_r (\rho \cdot \Gamma)_{pr}\, \hat{\alpha}_r,
\end{aligned}
\tag{4.40}
$$

where,

$$
\hat{\alpha}_r = \sum_i \tilde{Q}_{ri}\,(m_i - t_{0,i}),
\tag{4.41}
$$

and,

$$
\tilde{Q}_{ri} = -\sum_s \left[\mathbb{I} + (\zeta \cdot \Gamma)^T V^{-1}(\zeta \cdot \Gamma) \right]_{rs}^{-1} \left[(\zeta \cdot \Gamma)^T \cdot V^{-1} \right]_{si}.
\tag{4.42}
$$

In Eq. (4.40) the first component, $\hat{\hat{\theta}}_p^{[\text{stat. only}]}$, is a full statistical only contribution and the second one, $\hat{\hat{\theta}}_p^{[\text{syst}]}(\hat{\vec{\alpha}})$, is the total contribution of the NPs in the POI central value. A decomposition or shift per NP is given by,

$$
\hat{\hat{\theta}}_p^{[r]}(\hat{\vec{\alpha}}) = -(\rho \cdot \Gamma)_{pr}\hat{\alpha}_r,
\tag{4.43}
$$

where the sum over r returns the total shift. Notice that Eqs. (4.20), (4.25), (4.40) and (4.41) are totally equivalent between them and they represent the same minimum in the χ^2. However, Eq. (4.40) is more suitable to understand the contribution of each NP in the POI and in the case where no systematics are present in the fit, i.e. $\Gamma = 0$. Eq. (4.25) converges to $\hat{\hat{\theta}}_p^{[\text{stat. only}]}$.

4.3.2   Uncertainty decomposition

In the post-fit case, the measured parameters (POI and NPs) carry a total uncertainty that indicates the precision level or constraining power of the fit using the pre-fit information. The total uncertainty can be decomposed into two elements corresponding to the statistical and the systematic uncertainties. Where the first element corresponds to the uncertainty related to the statistical information from the statistical covariance matrix when the NPs are profiled (floating) and it should not be confused with the "statistical only fit uncertainty" in which the NPs are fixed. This implies

that the statistical only uncertainty has to be smaller than the statistical uncertainty component from the PLH fit. On the other hand, the systematic uncertainty receives contribution from each systematic source and is not only restricted to the POI since the NPs can have an effect among themselves. The uncertainty components in both POI and NPs and the methods to obtain them are discussed here.

4.3.2.1 Uncertainty components in the Parameter of Interest (POI)

The analytical approach allows to breakdown the components of the POI uncertainty by matrix algebra which is consistent and comes from an exact solution. From the previous equations, the statistical uncertainty and systematic uncertainty are given by,

$$\text{cov}^{[\text{stat}]}(\hat{\theta}_p, \hat{\theta}_q) = \sum_{i,j} \lambda_{pi} V_{ij} \lambda_{qj}, \tag{4.44}$$

$$\text{cov}^{[r]}(\hat{\theta}_p, \hat{\theta}_q) = \sum_{i,j} \lambda_{pi} \left(\Gamma_{ir} \Gamma_{jr} \right) \lambda_{qj}. \tag{4.45}$$

where the sum over r of Eq. (4.45) returns the total systematic uncertainty. Notice that the inner product of Eq. (4.36) with itself for a given r provide the total uncertainty in the NP r as shown in Eq. (4.45). Then, the off-diagonal elements of the total covariance matrix of the likelihood in POI-NPs representation provides the uncertainty decomposition which moreover, shows the sign of each NP. This decomposition is not only useful to understand the contributions to the total uncertainty, but also needed to propagate these contributions in subsequent analyses, such as combinations or interpretation fits including results from other measurements or experiments.

Commonly, "statistical only (stat. only)" fits are reported as the uncertainty computed solely using statistical information in the input data, or when the nuisance parameters (NPs) are fixed to a given value. However, in PLH fits, the statistical component showed in Eq. (4.44) should not be confused with the stat. only element that is strictly smaller. For example, the stat. only term can be obtained by setting all the NPs to zero and is given by,

$$\text{cov}^{[\text{stat. only}]}(\theta_p, \theta_q) = \left(h^T \cdot V^{-1} \cdot h \right)_{pq}^{-1} = \sum_{ij} \rho_{pi} V_{ij} \rho_{qj}, \tag{4.46}$$

such that,

$$\sqrt{\text{cov}^{[\text{stat}]}(\theta_p, \theta_p)} > \sqrt{\text{cov}^{[\text{stat. only}]}(\theta_p, \theta_p)} \qquad (4.47)$$

This has a strong implication in PLH fits, as subtracting only the statistical uncertainty from the total PLH uncertainty does not provide the total systematic uncertainty. Doing this provides a systematic uncertainty that is larger than what actually comes from the PLH fit.

Although the Gaussian limit admits an analytical solution this is not always case in many analysis and the uncertainty decomposition of all systematic sources is still a valuable information that needs to be retrieved from the fit. To asses this information, the usual approach is to perform the **Uncertainty decomposition from shifted observables** [143–145]. For a given probability model, the post-fit value of the POI depends on data $\vec{m}$ and the global observables $\vec{a}$ of auxiliary measurements $\hat{\theta}_p = \hat{\theta}_p(\vec{m}, \vec{a})$. Assuming no correlations between these observables, the uncertainty in $\hat{\theta}_p$ then follows from linear error propagation:

$$\text{cov}(\hat{\theta}_p, \hat{\theta}_p) = \sum_i \left(\frac{\partial \hat{\theta}_p}{\partial m_i} \Delta m_i \right)^2 + \sum_r \left(\frac{\partial \hat{\theta}_p}{\partial a_r} \Delta a_r \right)^2, \qquad (4.48)$$

where the first sum reflects the fluctuations of the data with $\Delta m_i = \sigma_i$, i.e. the statistical uncertainty (each term of the sum represents the contribution of a given m_i, measurement or bin), and the second sum collects the contributions of all systematic uncertainties where $\Delta a_r = 1$.

Similarly, the shifted observable approach can be carried out analytically. Following the error propagation, to obtain the statistical uncertainty contribution in the POI, the corresponding measurement should be varied by one standard deviation in the expression of the likelihood, and repeating the fit otherwise unchanged, this is known as varying one parameter at the time (OPAT). However, in our case the variables could be correlated and they should be varied taking into account their correlations through the Cholenksy decomposition matrix L which verify $V = L \cdot L^T$. Then

Eq. (4.49) should be solved.

$$
\begin{aligned}
-2\ln\mathcal{L}_{m_k}(\vec{\theta},\vec{\alpha}) = \sum_{i,j} & \left(m_i + L_{ik} - t_i(\vec{\theta}) - \sum_r \Gamma_{ri}(\alpha_r - a_r)\right) V_{ij}^{-1}\left(m_j + L_{jk} - t_j(\vec{\theta}) - \sum_s \Gamma_{sj}(\alpha_s - a_s)\right) \\
& + \sum_r (\alpha_r - a_r)^2,
\end{aligned}
$$

(4.49)

On the other hand, to obtain the systematic uncertainty contribution in the POI, the NP global observable is shifted by one standard deviation leading to Eq. (4.50),

$$
\begin{aligned}
-2\ln\mathcal{L}_{a_t}(\vec{\theta},\vec{\alpha}) = \sum_{i,j} & \left(m_i - t_i(\vec{\theta}) - \sum_r \Gamma_{ri}(\alpha_r - a_r)\right) V_{ij}^{-1}\left(m_j - t_j(\vec{\theta}) - \sum_s \Gamma_{sj}(\alpha_s - a_s)\right) \\
& + \sum_r (\alpha_r - a_r - \delta_{rt})^2,
\end{aligned}
$$

(4.50)

By this approach, the offsets induced in the POI due to the measurement m_k and global observable a_t shifts are given by,

$$
\Delta\hat{\theta}_p^{[m_k]} \equiv \hat{\theta}_p^{[m_k]} - \hat{\theta}_p = \sum_i \lambda_{pi} L_{ik},
$$

(4.51)

$$
\Delta\hat{\theta}_p^{[a_t]} \equiv \hat{\theta}_p^{[a_t]} - \hat{\theta}_p = -\sum_i \lambda_{pi} \Gamma_{it}.
$$

(4.52)

Where quadrature sum of these expressions recovers the total uncertainty,

$$
\begin{aligned}
\mathrm{cov}(\hat{\theta}_p, \hat{\theta}_q) &= \sum_k \Delta\hat{\theta}_p^{[m_k]}\Delta\hat{\theta}_q^{[m_k]} + \Delta\hat{\theta}_p^{[a_t]}\Delta\hat{\theta}_q^{[a_t]} \\
&= \sum_{i,j} \lambda_{pi} V_{ij} \lambda_{qj} + \sum_{i,j} \lambda_{pi}\left(\Gamma_{it}\Gamma_{jt}\right)\lambda_{qj}.
\end{aligned}
$$

(4.53)

Here, Eq. (4.52) represent the uncertainty decomposition that matches with off-diagonal block of the total covariance matrix of the likelihood given in Eq. (4.36). It is important to notice than in this case, the both POI and NPs are floating parameters in the fit and they has not been fixed. This means, that the nominal fit and the shift fits have the same dimension (POI + NPs).

4.3.2.2 Uncertainty components in the Nuisance Parameters (NPs)

Commonly, the parameter of interest is the only result that is presented with a dedicated decomposition since is more intuitive to understand. However, the nuisance parameters' total uncertainty also receives contribution from the statistics and the other nuisance parameters. To obtain this components, Eq. (4.49) and Eq. (4.50) are minimized but this time profiling the POI. For the NPs, the minimization yields,

$$\Delta\hat{\alpha}_r^{[m_k]} \equiv \hat{\alpha}_r^{[m_k]} - \hat{\alpha}_r = \sum_i \tilde{Q}_{ri}L_{ik}, \tag{4.54}$$

$$\Delta\hat{\alpha}_r^{[a_t]} \equiv \hat{\alpha}_r^{[a_t]} - \hat{\alpha}_r = \left[\mathbb{I} + (\zeta\cdot\Gamma)^T V^{-1}(\zeta\cdot\Gamma)\right]_{rt}^{-1}. \tag{4.55}$$

Summing Eqs. (4.54) and (4.55) in quadrature recovers the total NP covariance matrix in Eq. (4.32), as expected. This means that the statistical component of the NPs uncertainty is given by,

$$\text{cov}^{[\text{stat}]}(\hat{\alpha}_r, \hat{\alpha}_s) = \sum_{ij} \tilde{Q}_{ri}V_{ij}\tilde{Q}_{sj} = \text{cov}(\hat{\alpha}_r, \hat{\alpha}_s) - \sum_t \text{cov}(\hat{\alpha}_r, \hat{\alpha}_t)\text{cov}(\hat{\alpha}_t, \hat{\alpha}_s), \tag{4.56}$$

which is similar to the POI expression in Eq. (4.44) as a weighted average of the statistical covariance matrix but with the NPs weights. For the systematic components, Eq. (4.55) is the total uncertainty given in Eq. (4.32) and by consequence the systematic matrix is given by the square of this matrix,

$$\text{cov}^{[\text{syst}]}(\hat{\alpha}_r, \hat{\alpha}_s) = \sum_t \text{cov}(\hat{\alpha}_r, \hat{\alpha}_t)\text{cov}(\hat{\alpha}_t, \hat{\alpha}_s). \tag{4.57}$$

It is straightforward that the total covariance of the NPs is recovered by summing of Eq. (4.56) and Eq. (4.57). Notice that this imposes a strong condition in the NPs because only one matrix is needed to fully determine the uncertainty components of the NPs, this is, the total covariance matrix. Since the systematic is obtained by squaring the total uncertainty and the statistical can be obtained by matrix subtracting the total uncertainty matrix with the systematic uncertainty matrix.

Similarly as for the POI, the shifts correspond to the uncertainty component of each nuisance parameters, this means that $\Delta\alpha_r^{[a_t]}$ is the uncertainty component induced by the systematic t in the

NPs r and they are equal to the total covariance matrix elements. Moreover, a NP induces a shift on itself equal to the square of its total uncertainty while the other NPs induce a shift equal to the covariance. This is not only an accurate way to obtain the uncertainty decomposition but it also shows that even at the post-fit level, all the uncertainties add-up together even when correlations are presented, since they are considered by this approach.

In this way, the NPs-NPs and POI-POI covariance matrices are fully recovered. To complete the full covariance matrix of the likelihood, the covariance between the NPs and POIs can be obtained analytically by summing the products of the corresponding offsets, obtained from statistic and systematic variations, that is,

$$\sum_k \Delta\alpha_r^{[m_k]}\Delta\theta_p^{[m_k]} + \sum_t \Delta\alpha_r^{[a_t]}\Delta\theta_p^{[a_t]} = -\sum_s \left[\mathbb{I} + (\zeta \cdot \Gamma)^T V^{-1}(\zeta \cdot \Gamma)\right]_{rs} (\rho \cdot \Gamma)_{ps}, \tag{4.58}$$

which again matches the expression for $\text{cov}(\hat{\alpha}_r, \hat{\theta}_p)$ in Eq. (4.35).

4.3.2.3 Comparison with the "Impacts"

In high-energy physics analyses, contributions of systematic uncertainties are routinely quantified using "impacts". In this method a nominal fit is performed and a total uncertainty σ_{tot} is retrieved from it. To evaluate the impact of a given systematic source r into the fit result, this NP is removed from the fit and the fit is performed again retrieving an uncertainty σ'_{tot} that is strictly smaller than σ_{tot}. If σ'_{tot} is considerably smaller than σ_{tot} the systematic removed from the fit is expected to has a large impact in the final result and this can be quantified by the quadratic difference of the two uncertainties,

$$\sigma_r = \sqrt{(\sigma_{\text{tot}})^2 - (\sigma'_{\text{tot}})^2}. \tag{4.59}$$

This impact is associated as a the systematic uncertainty component σ_r of the source r. A big problem of this approach is that post-fit the NPs tend to be correlated and this do not consider those correlations into account such that the quaratic sum of the all the NPs impacts do not recover

the total systematic uncertainty coming from the real PLH fit,

$$\sum_r \sigma_r^2 \neq \sigma_{\text{syst}}^2, \tag{4.60}$$

This means Impacts do not add up to the total uncertainty, and do not match usual uncertainty decomposition formulas even when they should, i.e. when all uncertainties are genuinely Gaussian.

4.3.3 Example in m_W fits

The uncertainty decomposition discussed above is further illustrated with a toy measurement of the W-boson mass using pseudo-data, where the results obtained from the profile likelihood fit are compared with "impact" method. Since the measurement of W mass is a typical shape analysis, in which the fit to the distributions is parameterized by both POI and NPs, the conclusions drawn from this example can in principle be generalized to all kinds of shape analyses. While the effect of varying the W mass is parameterized by the POI, only one systematic source is parameterized by NPs in the probability model, this is, the p_T^W modelling uncertainty.

4.3.3.1 Simulation

The signal process under consideration is the charged-current Drell-Yan process [146] $pp \rightarrow W^- \rightarrow \mu^- \nu$ at a centre-of-mass energy of $\sqrt{s}$ =13 TeV, generated using Madgraph, with initial and final state corrections obtained using Pythia8 [147, 148]. Detailed information of the event generation is listed in Table 4.1.

Event Generator	
$pp \rightarrow W^- \rightarrow \mu^- \nu_\mu$ at $\sqrt{s}$=13 [TeV]	
Number of events	10,000,000
Matrix elements	Madgraph at LO
Input m_W	80.419 [GeV]
Input Γ_W	2.0476 [GeV]
Parton shower & QED FSR	Pythia8

Table 4.1: Madgraph+Pythia8 [147, 148] event generation for MC samples. Events with an off-shell boson are excluded in the event generation at parton level, leading to a total cross-section of 6543 pb.

Kinematic distributions for different values of the W mass are obtained in simulation via Breit-Wigner reweighting [149]. The systematic variations of p_T^W are implemented using a linear reweighting as a function of p_T^W before event selection, then taking only the shape effect on the underlying p_T^W spectrum. At reconstruction level, the p_T of the bare muon is smeared by 2% following a Gaussian distribution. The hadronic recoil $\vec{u}_T$ is taken to be the opposite of $\vec{p}_T^W$ and smeared by a constant 6 GeV in both directions of the transverse plane. The information about the W mass templates and the systematic variations is summarized in Table 4.2.

Templates and systematic variations	
W mass templates	$\pm$ 50 MeV by Breit-Wigner reweighting
p_T^W model (Reweighting)	$w(p_T^W) = 0.96 + 8 \cdot 10^{-4} \cdot p_T^W$ [GeV]

Table 4.2: W mass templates and systematic variation for the Madgraph+Pythia8 samples.

The detector smearing, as well as the event selections listed in Table 4.3, are chosen to be similar to those of a realistic W mass measurement. The reconstructed muon p_T^ℓ spectra in the fit range after the event selection is shown in Fig. 4.2, along with the relevant templates and systematic variations.

Detector smearing	
Lepton p_T resolution	2%
Nominal recoil resolutions	6 [GeV]
Event selection	
η_ℓ selection	[-2.5, 2.5]
p_T^ℓ selection	>25 [GeV]
E_T^{miss} selection	>25 [GeV]
m_T selection	>50 [GeV]
u_T selection	<25 [GeV]

Table 4.3: Detector smearing and event selection for Madgraph+Pythia8 samples. The cut-flow efficiency of the event selection is about 29%.

4.3.3.2 Uncertainty components

To study the difference between the impact method and the uncertainty decomposition described in section 4.3. An analytical profile likelihood fit is performed, the results include the fitted central values and uncertainties for all the free parameters. The uncertainty components of the systematic
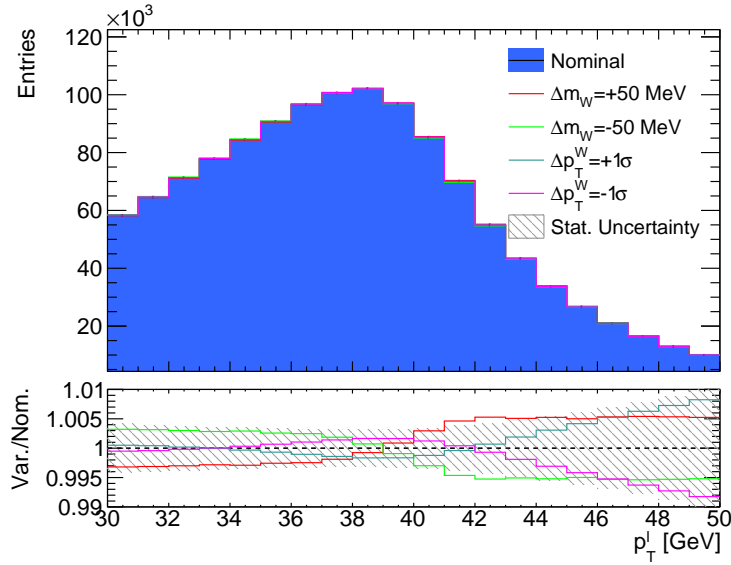
Figure 4.2: Reconstructed muon p_T^ℓ distribution of the Madgraph + Pythia8 samples. (top): Kinematic spectra. (bottom): The variation to nominal ratio with statistical uncertainty indicated by the error band.

source is also retrieved and read from the covariance matrix. However, The uncertainty components of the profile likelihood fit results are also obtained by repeating the fit to bootstrap samples obtained by resampling the pseudo data used to compute the results, or those of the central values of the auxiliary measurements, then computing the spread of offsets in the POI.

On the other hand, to evaluate the "impact" method, the PLH fit is performed using the dataset and retrieving the total uncertainty. Once this is done, the p_T^W systematic is removed and the fit is repeated such that the total uncertainty is obtained and it corresponds to the statistical only fit uncertainty. The impact of p_T^W in the final measurement is evaluated by the quadratic difference of the total uncertainty and the stat. only result.

The uncertainty decomposition is summarized in Table 4.4, where the total uncertainty is broken down into statistical and systematic components. uncertainties using the shifted observable method, and compared with the results using the conventional impact approach for PL fit. This confirms that the systematic component is not well evaluated by the usual approach since it is overestimated and both the analytical and toys method provide the same result confirming that for a general case, the correct way to obtain the uncertainty components is by fluctuating the global observable with its uncertainty. Next to it, the total covariance matrix of the likelihood proofs that the uncertainty

p_T^ℓ fit (MeV)		σ_{total}	$\sigma_{\text{stat.}}$	$\sigma_{\text{syst.}}$
Shifted	Analytical	15.49	15.13	3.31
Observable	Toys	15.49±0.01	15.13±0.01	3.31±0.00
Impact		15.49	13.81	7.00

$$\text{cov}(\mathcal{L}) = \begin{pmatrix} 0.22 & -3.31 \\ -3.31 & 239.83 \end{pmatrix}$$

Table 4.4: Left : Uncertainty decomposition for the muon p_T^ℓ fit using the shifted observable method (Analytical and toys) and the impact method for PL fit, right: post-fit covariance among the NP and the POI, for the profile-likelihood fit to p_T^ℓ distribution.

component can directly be read from the off-diagonal terms, this is, the covariance between the nuisance parameter and the parameter of interest as shown in Eq. (4.37).

4.3.4 Use of decomposed uncertainties in subsequent fits or combinations

Uncertainty decompositions obtained with the present method are meaningful only if the results can be used consistently in downstream applications, such as measurement combinations or interpretation fits in terms of specific physics models. In particular, uncertainty components that are common to several measurements generate correlations which should be evaluated properly. This happens when measurements are statistically correlated or when they are impacted by shared systematic uncertainties.

As a final validation of the presented method, the combination of profile-likelihood fits of the same observable is described. Such a combination can be performed either using the decomposed uncertainties, or in terms of the PLH fit outputs, i.e. the fitted values of the POIs and NPs and their covariance matrix.

The combination is performed starting from,

$$-2\ln\mathcal{L}_{\text{cmb}}(\vec{\theta}) = \sum_{i,j}\left(m_i - \sum_p U_{ip}\theta_p\right)C_{ij}^{-1}\left(m_j - \sum_p U_{jp}\theta_p\right), \tag{4.61}$$

that can be applied to linear measurement averaging by adapting the definition of $t(\vec{\theta})$. In case of a single combined parameter, $t_i = \theta$; for a simultaneous combination of several parameters, $t_i = \sum_p U_{ip}\theta_p$ where U_{ip} is 1 when measurement i is an estimator of POI p, and 0 otherwise [132].

Equation (4.61) can be solved by following the formalism described above.

In the case of a combination based on the uncertainty decomposition, the covariance matrix C has dimension equal to the $(n_{\text{POI}} \cdot N) \times (n_{\text{POI}} \cdot N)$ where n_{POI} is the number of POIs and N the number of fits to be combined. In the case of two fits with 1 POI and 3 NPs, C is a 2×2 matrix constructed from the decomposed uncertainties using Eq. (4.29) where the systematic sources are introduced in the sensititivy matrix Γ.

For a combination based on the PLH fit outputs, the covariance matrix C has dimension equal to $(n_{\text{POI}} + n_{\text{NPs}}) \cdot N \times (n_{\text{POI}} + n_{\text{NPs}}) \cdot N$ where n_{NPs} is the number of NPs. For example, in the two measurements case, each one with 1 POI and 3 NPs, each covariance matrix of the measurements has dimension 4×4 and C has dimension 8×8. The diagonal blocks are the post-fit covariance matrices of each fit that can be obtained by Eqs. (4.26) and (4.32). The off-diagonal blocks reflect systematic and/or statistical correlations between the fits. For two fits f_1 and f_2 the covariance matrix elements are obtained by Eq. (4.62),

$$
\begin{aligned}
\text{cov}\left(\theta_p^{f_1}, \theta_q^{f_2}\right) &= \sum_k \Delta\theta_p^{[m_k],f_1} \Delta\theta_q^{[m_k],f_2} + \sum_t \Delta\theta_p^{[a_t],f_1} \Delta\theta_q^{[a_t],f_2} \\
\text{cov}\left(\alpha_r^{f_1}, \alpha_s^{f_2}\right) &= \sum_k \Delta\alpha_r^{[m_k],f_1} \Delta\alpha_s^{[m_k],f_2} + \sum_t \Delta\alpha_r^{[a_t],f_1} \Delta\alpha_s^{[a_t],f_2} \\
\text{cov}\left(\alpha_r^{f_1}, \theta_p^{f_2}\right) &= \sum_k \Delta\alpha_r^{[m_k],f_1} \Delta\theta_p^{[m_k],f_2} + \sum_t \Delta\alpha_r^{[a_t],f_1} \Delta\theta_p^{[a_t],f_2} \\
\text{cov}\left(\theta_p^{f_1}, \alpha_r^{f_2}\right) &= \sum_k \Delta\theta_p^{[m_k],f_1} \Delta\alpha_r^{[m_k],f_2} + \sum_t \Delta\theta_p^{[a_t],f1} \Delta\alpha_r^{[a_t],f_2}
\end{aligned}
\tag{4.62}
$$

For each matrix element, the first sum is statistical and typically occurs when the fitted distributions are projections of the same data. The second sum represents shared systematic sources of uncertainty. This allows to a fast and accurate expression in the Gaussian limit that often is obtained using the Toy Monte Carlo approach.

4.4   Summary

Different approaches to obtain the uncertainty components in a given measurement have been studied. The offset method is one of the simplest approaches to retrieve the systematic uncertainties.

However, in the case of profile likelihood fits, it has been shown that the statistical uncertainty alone does not match the statistical component when systematic sources are introduced into the fit. Moreover, it has been proven that the usual impact method approach, commonly implemented in high-energy physics, not only overestimates the systematic components but also ignores possible correlations between the systematic sources. This leads to a situation where the uncertainty components do not accurately reflect the total systematic uncertainty. In this context, explicit equations were provided for obtaining each of the systematic components in the Gaussian limit, along with analytical solutions when the global observable for the parameter of interest and nuisance parameters is shifted by 1σ, including correlations. By fully exploiting the covariance matrices, it was also shown that the uncertainty decomposition can directly be derived from the total covariance of the likelihood, ensuring that all aspects of the problem are fully determined and the components of the nuisance parameters are constrained by the total post-fit covariance of the systematic sources.

Similarly, the concept of a shift in the parameter of interest (POI) due to the nuisance parameters (NPs) was introduced without relying on the impacts concept commonly implemented. This approach retrieves the statistical only result when the systematic sources are removed. These results not only aid in understanding the components in profile likelihood fits but also provide a broad framework for subsequent fits or combinations. It should be noted that the shifted global observable remains valid even for non-Gaussian limits, allowing the induced shift in the best-fit values to be implemented for combinations.

Chapter 5

Muon calibration for the Z and J/ψ resonances

5.1 Introduction

To ensure a good quality data, the ATLAS detector follows up a dedicated detector alignment [89, 150, 151]. The ID alignement is determined by a global χ^2 of the track-to-hit residuals [150] while for the MS an optical alignment system [89] monitors the position of the muon chambers relative to each other and relative to fiducial marks in the detector.

Despite the sophisticated alignment procedures in the sub-detectors, residual misalignments between the ID and the MS can introduce different biases. One of these is a charge-dependent bias in the momentum measurement and it is related to a rotation of the detector layers that can cause a sagitta bias, which has opposite effects on positively and negatively charged particles, eventually degrading the resolution in data. For the MS, due to the alignment nature this is less sensitive to charge-dependent biases, however, residual effects can still impact the data. The MS is capable of measuring the sagitta of the muon track with a precision level of tens of micrometers (μm) and up to 120–130 μm in specific detector regions. This residual manifests a potential systematic source in the reconstruction procedure that needs to be further corrected. This sagitta bias has been largely studied providing maximum values of about 0.4 TeV^{-1} that after correction it can be reduced up

to $2 \cdot 10^{-4}$ TeV^{-1} [117].

Similarly, for the ID, after the alignment procedure is performed some residual detector displacements with respect to the nominal detector geometry can still be present. These are known as the weak modes or ID geometrical distortions and they can be related to radial or longitudinal expansion of the detector layers or mismodelling in the magnetic field causing length-scale bias. These biases according to the model can impact the momentum from few parts per mille to parts per million. Combining different models can potentially improve the data-to-simulation agreement providing a per mille agreement after correction.

Correcting the data for sagitta and ID geometrical distortions are not the only effects to be considered to ensure a good reconstruction. Even though the simulation accounts for a perfect description of the ATLAS detector, the level of detail is not enough to reach an accuracy of 0.1% on the muon momentum scale and the percent level precision on the resolution measured in data. Here, the Muon Momentum Calibration (MMC) is defined as the procedure used to identify the corrections to the reconstructed muon transverse momenta in simulation to match the measurement of the same quantities in data [117]. The MMC is accounted after the charge dependent effects previously described are corrected.

The calibration of the momentum of the muons is of particular interest of the present work and part of it is fully devoted in understanding and improving the momentum and track performance, for which a dedicated calibration procedure of the Inner Detector and Muon Spectrometer have been designed and applied. After muon candidates selection, an ID calibration is carried out to correct for possible biases in the muon track sagitta, geometrical deformations and magnetic field distortions. The momentum of the muons is corrected considering charge dependent effects that can potentially degrade the resolution of the invariant mass. Once this is accounted, different models were tested (radial, longitudinal and magnetic field distortions) to model and consider possible geometrical distortions that can generate modulations or shifts in the invariant mass of the resonances. Taking these effects into account an improvement in the data-to-simulation agreement is obtained.

In the case of the MS, the alignment residuals between the ID and MS have been investigated, and the residual toroidal magnetic field present in the calorimeters has been re-evaluated. This

stage is fully based on the track parameters of the muons in the ID and MS allowing to study different extrapolation types and possible magnetic field mismodellings.

Finally, once the ID calibration has been performed, a muon momentum calibration for scale and resolution effects is carried out. The scale calibration aims to correct for inaccuracies in the description of the magnetic field integral and the dimension of the detector in the direction perpendicular to the magnetic field. On the other hand, the resolution correction accounts for multiple scattering, uncertainties related to, and inhomogeneities in, the modelling of the local magnetic field, and length-scale radial expansions of the detector layers [117]. After these corrections, the data-to-simulation agreement is found to be at the per mille level

In this chapter, Section 5.2 introduces the implemented dataset to study the muom momentum calibration. Section 5.3 describes the approach to correct the charge dependent bias associated to the muon track sagitta and how the sagitta strength is evaluated. Section 5.4 describes the ID calibration for geometrical distortion (weak modes) studies based on three models: radial, longitudinal and magnetic field distortions. Section 5.5 study the potential MS/ID misalignment residuals. Section 5.6 provides an insight into the ATLAS magnetic field and a re-evaluation of the toroidal magnetic field and possible mismodelling. Section 5.7 evaluates the MS/ID residuals in the first coordinates of the track parameters and establishes a relation with the first coordinates components. Section 5.8 provides a correction map for the track parameters based on the second coordinates results. Finally, Section 5.9 describes the muon momentum calibration strategy based on analytical fits to correct the scale and resolution of the muons and final agreement between data and simulation.

5.2 Dataset for muon calibration

The implemented samples correspond to data collected between 2015 and 2018 at 13 TeV with an integrated luminosity of 139 fb^{-1} after trigger and data-quality requirements and with an average number of pp collisions per bunch crossing of $\langle \mu \rangle = 33.7$. Only events collected in stable beam conditions and with all relevant ATLAS detector subsystems fully operational are used in the
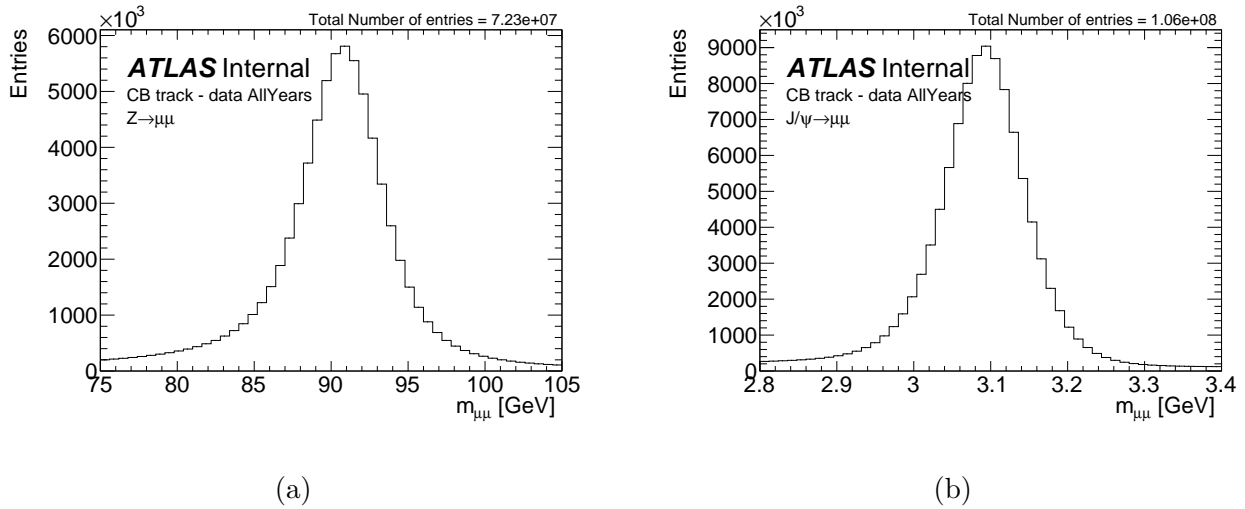
Figure 5.1: Integrated invariant mass for (a) $Z \to \mu\mu$ and (b) $J/\psi \to \mu\mu$ after selection using data taking-years (2015-2018) in CB tracks.

analysis. In particular, for $Z \to \mu\mu$ a combination of single-muon trigger algorithms is implemented while for $J/\psi \to \mu\mu$ trigger algorithms dedicated to $J/\psi \to \mu\mu$ topologies [152] were used. Muon candidates are selected by applying the cuts in section 3.2.1.1 giving a total number of Z candidates of about 7.23×10^7 and 1.06×10^8 for J/ψ. The inclusive invariant mass for the two resonances is shown Fig. 5.1.

For the Monte Carlo samples, two sets were implemented with different calibrations, release 21 (r21) known as mc16 samples and release 22 (r22) known as mc20 samples with generators POWHEG and PYTHIA8 for periods a, d and e.

The $Z \to \mu\mu$ signal process is simulated using the POWHEG-BOX v22 [153–155] generator at next-to-leading order (NLO) in QCD with the CT10 parton distribution function (PDF) [55] set for the hard-scatter process. Events were generated with a dimuon invariant mass above 40 GeV. The parton showering was simulated using PYTHIA 8.186 with the CTEQ6L1 PDF set [56] and the AZNLO set. About 210 million events were simulated for this process.

The $J/\psi \to \mu\mu$ signal process was simulated using the PYTHIA 8.186 [72] leading-order generator, with the CTEQ6L1 PDF [56] set and A14 as the underlying-event tune. In addition, PHOTOS++ v3.52 [156] was used to simulate the effect of final-state radiation. To increase the effective number
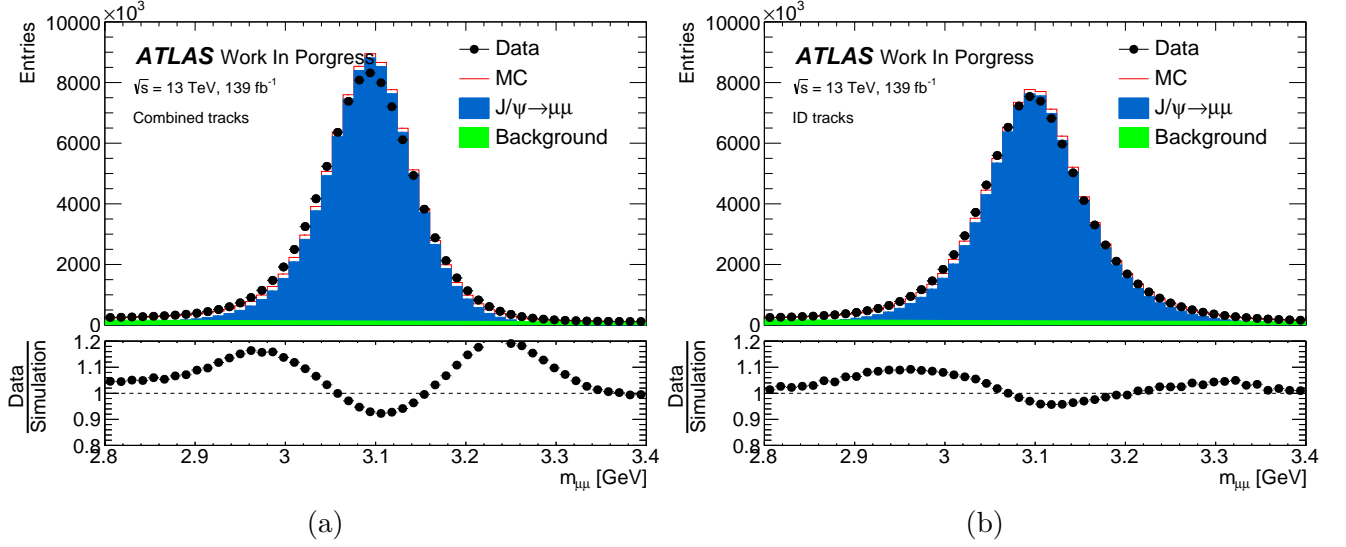
Figure 5.2: Inclusive invariant mass distribution for $J/\psi \to \mu\mu$ in (a) CB and (b) ID tracks before correction.

of events in the regions of phase space relevant to this analysis, the events were generated in a reduced phase space, requiring at least one of the two muons to have $p_T > 6$ GeV and both muons to have $|\eta| < 2.5$. About 420 million events were simulated using this configuration. After selection the total number of candidates are 8.62×10^7 for the Z and 1.03×10^7 for the J/ψ.

The agreement between data and simulation before correction is shown in Figures 5.2, 5.3 and 5.4 where the simulation integral is normalized to the data integral.

5.3 Sagitta bias correction

A dedicated calibration and alignment is performed in the ATLAS detector to reach a high precision level. Different residuals can affect the momentum measurement of the muon such as, the charge dependent bias that degrades the momentum resolution as,

$$\frac{q}{\hat{p}} = \frac{q}{p} + \delta_s, \tag{5.1}$$

where q is the electric charge, p is the unbiased momentum, $\hat{p}$ is the biased momentum and δ_s is the strength of the bias. The strength can be estimated by different methods, one of the usual approaches is under the assumption that the average p_T of the muon is half of the invariant mass
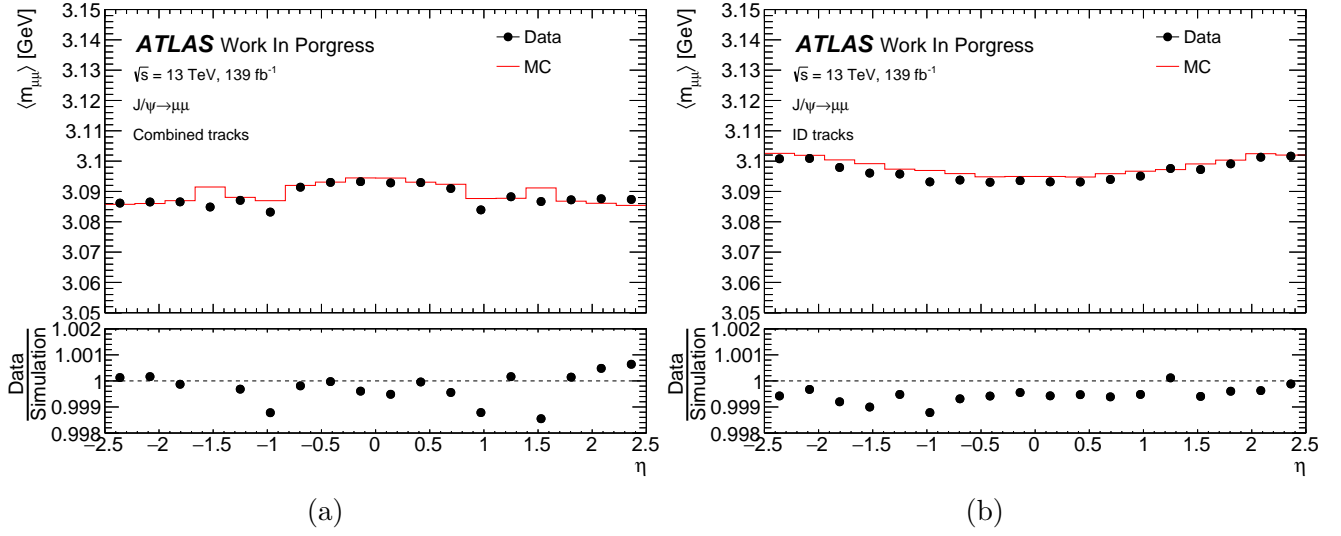
Figure 5.3: Mean mass of the dimuon system for $J/\psi \to \mu\mu$ in (a) CB and (b) ID tracks before correction.
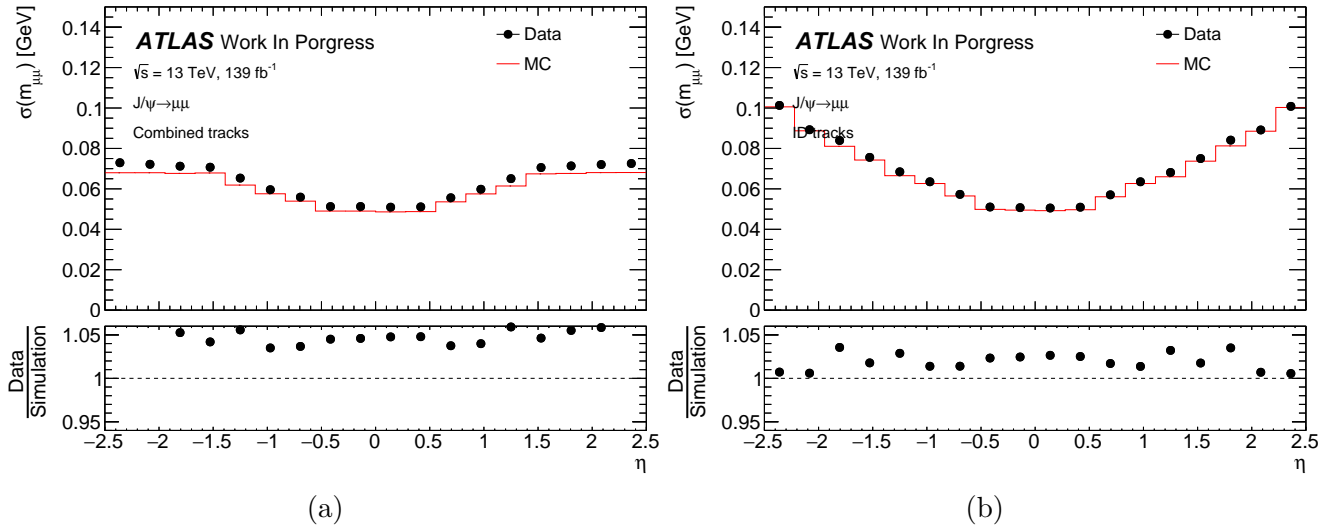
Figure 5.4: Dimuon invariant mass resolution for $J/\psi \to \mu\mu$ in (a) CB and (b) ID tracks before correction.

of the dimuon pair $m_{\mu\mu}$, then [157],

$$\delta_s(\eta, \phi) = 4 \cdot \frac{q \cdot (m_{\mu\mu}(\eta, \phi) - \langle m_{\mu\mu} \rangle)}{\langle m_{\mu\mu} \rangle^2}, \tag{5.2}$$

where $\langle m_{\mu\mu} \rangle$ is the average of the invariant mass of the dimuon pairs used to derive the correction, while $m_{\mu\mu}(\eta, \phi)$ is the average invariant mass of the dimuon pairs when the muon with the highest transverse momentum is in the given (η, ϕ) region. However, in this work, the sagitta strength, $\delta_s(\eta, \phi)$, is evaluated by minimising the variance of the invariant mass distributions [117]. The values of δ_s for different data-taking years are shown in Fig. 5.5. Once δ_s is obtained, the biased momentum of the muon, $\hat{p}_T$, is corrected using the following equation:

$$p_T = \frac{\hat{p}_T}{1 + q \cdot \delta_s(\eta, \phi) \cdot \hat{p}_T}. \tag{5.3}$$

The uncorrected and corrected invariant mass distribution for $Z \to \mu\mu$ and $J/\psi \to \mu\mu$ are shown in Fig. 5.6. After correction, an improvement in the resolution is observed at high p_T (Z boson) and a slight improvement at low p_T (J/ψ meson). Correcting sagitta bias is of particular interest in analyses such as Z and W mass measurements since in decays like $Z \to \ell\ell$ and $W \to \ell\nu$ a bias proportional to δ_s is introduced,

$$m'_Z - m_Z = (p_T^2 \delta_s^2/2) \cdot m_Z \sim (p_T \delta_s)^2, \\ m'_W - m_W = (p_T \delta_s/2) \cdot m_W \sim p_T \delta_s. \tag{5.4}$$

This means, the Z mass measurement is less affected by the sagitta correction. For the W mass, there is a first order dependency in δ_s and for that reason a good correction is needed to reduce the uncertainty associated to this source. An average value of $\langle \delta_s \rangle = 0.05$ TeV^{-1} in a $p_T = 40$ GeV track would induce a mass shift of about 80 MeV in the W boson mass and 0.1 MeV in the Z boson mass. One of the common systematics sources in the sagitta determination is the global bias with a constant value of about $\delta_s^{\text{global}} \approx 0.02$ TeV^{-1} which induces a shift of about 30 MeV in m_W and 0.01 MeV in m_Z.
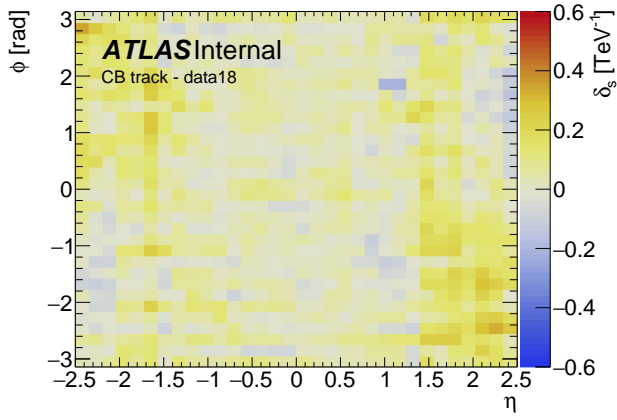
(a)
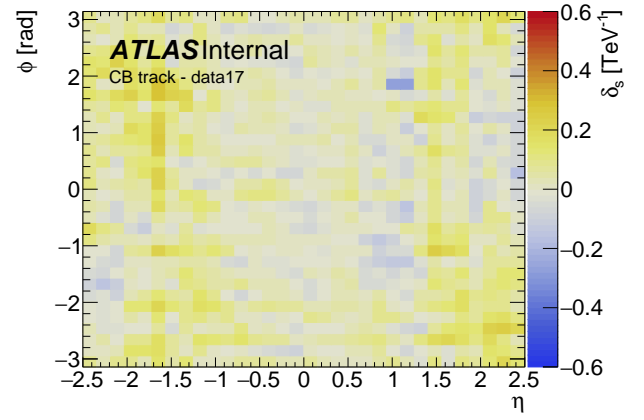
(b)
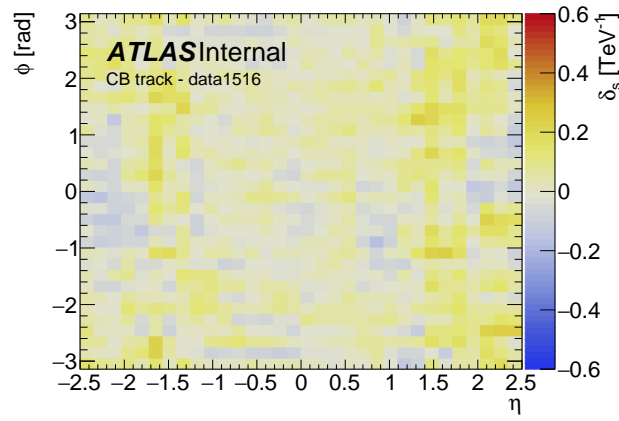
(c)

Figure 5.5: Sagitta strength δ_s maps for data-taking years (2015-2018) in CB tracks.
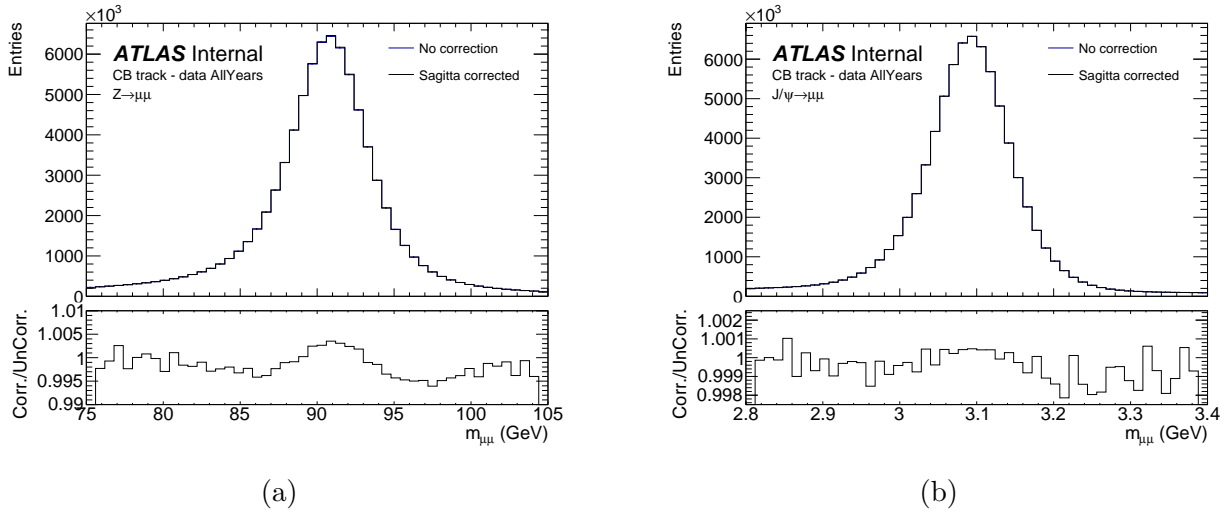
Figure 5.6: Invariant mass for (a) $Z \to \mu\mu$ and (b) $J/\psi \to \mu\mu$. The upper panel shows the distribution for the uncorrected (UnCorr.) and sagitta corrected (Corr.) distributions. Lower panel shows the ratio Corr./UnCorr.

5.4 Inner detector deformations

Achieving a good determination of the absolute scale of charged particles measured by the ATLAS ID detector is crucial for precision measurements [158–160]. The ID alignment is carried out by a global χ^2 track-to-hit residual. However, some systematic biases can escape this procedure, resulting in residual biases known as *Weak Modes*, which require a different treatment. The measurement of the track momentum provided by the ID can be affected by different sources such as incomplete knowledge of the amount of material in the detector, imperfect measurement of the direction and strength of the magnetic field, and residual geometrical deformations after the alignment of the ID. These deformations can be either real detector distortions or artificial deformations introduced by the alignment procedure itself [158]. The ATLAS ID detector is well known and the uncertainties in the measurements are derived from multiple sources, including the precision of the sensors, alignment procedures, and environmental factors such as temperature variations. For the ID components, these uncertainties are estimated in the pixel detector to be 10 μm $(R - \phi)$ and 115 μm (z) in the barrel and 10 μm $(R - \phi)$ and 115 μm (R) in the disks . For the SCT, the intrinsic accuracies per module in the barrel are 17 μm $(R - \phi)$ and 580 $(R - \phi)$ (z) and in the disks are 17 μm $(R - \phi)$ and 580 μm (R). For the TRT, approximately 130 μm in the transverse plane $(R - \phi)$ [89]. In the case of

99

the magnetic field, this is composed by two systems, the central solenoid magnet and the toroidal magnet system, each one with their uncertainties. For the solenoid one, the B field has an strength of 2T with an uncertainty ranging from 0.4mT in the center of the solenoid up to 2mT in the edges. For the toroidal magnetic field the uncertainty corresponds to 4mT [161].

Even though the ID and the magnetic field are precisely calibrated and well known, these uncertainties can produce small bias that should be corrected. One of the main deformations studied is the radial distortion. In this deformation, the measurements on a track are radially displaced by an amount proportional to their distance from the interaction point [158]. Another deformation is the longitudinal distortion which affects the transverse and longitudinal momentum components. These two, radial and longitudinal can be encompassed into a global bias that has been largely studied [159]. Similarly, possible mismodellings in the magnetic field can be accounted through a scale affecting both the transverse and longitudinal momentum components.

Notice that these models are a simplified description of the real nature of the bias, but they illustrate the degrees of freedom remaining after the standard alignment. A more accurate and more complicated model could consider time-dependent corrections, azimuthal dependence, etc. On what follows, three models are used to disentangle the effect of each weak mode into the invariant mass, these are, radial, longitudinal and magnetic field distortions. Each one is parameterized by a single parameter that corresponds to a small perturbation in the momentum components.

Radial distortion: a radial distortion of the detector implies that the measurements on a track are displaced proportionally to their radial coordinate, $\delta R(\eta, \phi) \ll r$. The transverse momentum is related to the magnetic field B, the electric charge q, the radial component R, and the sagitta s, by the expression,

$$p_T \propto q \frac{BR^2}{8s} \tag{5.5}$$

If the radial component is shifted by a small perturbation $R \rightarrow (1 + \varepsilon_R) \cdot R$ and $s \rightarrow (1 + \varepsilon_R) \cdot s$, it follows,

$$p_T' = p_T(1 + \varepsilon_R) \tag{5.6}$$

where $|\varepsilon_R| \ll 1$. At the same time, a shift in the radial component also generates a change in the

polar angle θ, that keeps unchanged the $Z-$component of the momentum,

$$\cot\theta' = \cot\theta/(1+\varepsilon_R),$$
$$p'_Z = p_Z. \tag{5.7}$$

This leads to the total momentum,

$$p' = p\left(1 + \varepsilon_R \sin^2\theta\right), \tag{5.8}$$

and invariant mass bias,

$$\frac{m'}{m} \simeq 1 + \frac{\varepsilon_R}{2}\left(\sin^2\theta_1 + \sin^2\theta_2 - \Delta_{\theta\phi}\right), \tag{5.9}$$

where $\Delta_{\theta\phi}$ is given by Eq. (A.6).

Longitudinal distortion: the tracks are displaced only in the $Z-$component affecting the longitudinal component of the momentum and the polar angle, this is,

$$\cot\theta' = (1+\varepsilon_z)\cot\theta,$$
$$p'_Z = (1+\varepsilon_z)p_Z, \tag{5.10}$$

with a total momentum,

$$p \to p\left(1 + \varepsilon_z \cos^2\theta\right), \tag{5.11}$$

and the bias in the invariant mass is given by,

$$\frac{m'}{m} \simeq 1 + \frac{\varepsilon_z}{2}\left(\cos^2\theta_1 + \cos^2\theta_2 - \Delta_{\theta\phi}\right) = 1 + \frac{\varepsilon_z}{2}\left(2 - \sin^2\theta_1 - \sin^2\theta_2 - \Delta_{\theta\phi}\right). \tag{5.12}$$

Magnetic field distortion: both components of the momentum are changed but the polar

angle remains the same,

$$p'_T = (1 + \varepsilon_B)p_T,$$

$$p'_Z = (1 + \varepsilon_B)p_Z,$$

(5.13)

therefore, the bias in the mass is given by,

$$\frac{m'}{m} = 1 + \varepsilon_B.$$

(5.14)

Notice that both radial and longitudinal distortions are functions of the angles of the two particles in the laboratory frame. These two deformations are capable of generating modulations in the reconstructed mass. In the case of the magnetic field distortion, the invariant mass is not a function of the angles and therefore is not able to generate modulations but a shift (scale) in the mass is obtained. Notice that for simplicity the parameters $\varepsilon_{R,B,z}$ are assumed to be constant but in reality they are functions of η, ϕ. This dependency is obtained by mapping the bias in rapidity bins.

The equations of the three models show that one model can be expressed as a combination of the other two. For example, a radial distortion could be parameterized as a magnetic field plus longitudinal distortion, the longitudinal distortion as a combination of the radial distortion and the magnetic field and finally the magnetic field as combination of the longitudinal distortion plus the radial distortion.

In principle, it is preferable to describe the data using only one deformation since this implies only one bias parameter, ε, but possible combinations could be considered. It is necessary to highlight that a combination of the three models (three parameters model) is ambiguous in the sense that is not possible to disentangle the effects.

5.4.1 Collins-Soper reference frame

To accurately assess geometrical deformations, it is crucial to analyze the calibration in relation to the decay angles of muons. Employing the rest frame for this analysis is particularly effective, as it ensures that the angular variables, $\cos\theta$ and ϕ, span the full theoretical ranges, $-1 < \cos\theta < 1$ and

$-\pi < \phi < \pi$, respectively. This comprehensive coverage facilitates a more thorough evaluation of potential deformations. Conversely, using the laboratory frame for these measurements results in a much more restricted angular range, especially for particles such as the J/ψ meson, which limits the effectiveness of the analysis.

In the context of Drell-Yan production in hadron collisions at the hard scattering level, it is convenient to define a reference system. This system allows the differential distributions to be well approximated by the Born-level angular dependence while remaining minimally sensitive to the amount of hard QCD radiation emitted. For a hadron collider, this reference system is known as the Collins-Soper (CS) frame [162].

The CS frame is defined as a rest-frame of the lepton-pair, with the polar and azimuthal angles constructed using proton directions in that frame. The polar axis ($z-$axis) is oriented such that it bisects the angle between the momentum of one incoming proton and the inverse momentum of the other proton. The direction of the $z-$axis is determined by the sign of the lepton-pair momentum along the $z-$axis in the laboratory frame. The $y-$axis is defined as the normal vector to the plane formed by the two incoming proton momenta, and the $x-$axis is chosen to establish a right-handed Cartesian coordinate system with the other two axes. The polar (θ) and azimuthal (ϕ) angles are calculated with respect to the outgoing lepton [163, 164]. The cosine of the polar angle can be expressed in terms of the outgoing leptons int the laboratory frame as,

$$\cos\theta_{CS} = \frac{p_z(\ell^+\ell^-)}{|p_z(\ell^+\ell^-)|} \frac{2}{m(\ell^+\ell^-)\sqrt{m^2(\ell^+\ell^-) + p_T^2(\ell^+\ell^-)}}(P_1^+ P_2^- - P_1^- P_2^+) \qquad (5.15)$$

with $p_z(\ell^+\ell^-)$ and $m(\ell^+\ell^-)$ being the longitudinal momentum and the invariant mass of the lepton system, respectively, and $P_i^\pm$ is given by,

$$P_i^\pm = \frac{1}{\sqrt{2}}(E_i \pm p_{z,i}), \qquad (5.16)$$

where E_i and $p_{z,i}$ are the energy and longitudinal momentum of the lepton ($i = 1$) and anti-lepton ($i = 2$), respectively. The ϕ angle is calculated as an angle of the lepton in the plane of the x and y axes in the Collins-Soper frame.

5.4.2 Weak modes and ID distortions

To determine if the invariant mass presents weak modes, the reconstructed invariant mass is studied as a function of the CS frame angles, $\cos\theta_{CS}$ and ϕ_{CS}. For this, the mean invariant mass of $J/\psi \to \mu\mu$ is obtained in rapidity bins, $y_{J/\psi}$, as shown in Fig. 5.7. Results indicate that modulations and shifts are present in data with respect to the simulation and these need to be corrected. To know which model describes the data, the momentum of the muons is modified in the simulation as described in the three models. Simulated results are shown in Fig. 5.8.

The models are capable to generate two effects, modulation and shift of the invariant mass. In particular, the magnetic field distortion is capable only of generating shift as showed in Eq. (5.14). For the longitudinal and radial distortions, these are capable of shifting and modulating with opposite effects as shown in Equations (5.14) and (5.12).

5.4.3 Fitting strategy

To correct the weak modes, a suitable model that generates shift and modulations is needed. For this, a template fit of the data is performed in the Collins-Soper frame where the templates correspond to the simulated samples generated in rapidity bins (i.e. Fig. 5.8). Once the fits are performed, the fitted parameters are retrieved to construct a correction map as a function of the rapidity.

Since two observables are obtained, $\cos\theta_{CS}$ and ϕ_{CS}, an analytical joint fit is performed. An unrolled distribution of two variables ($\cos\theta_{CS}$ & ϕ_{CS}) in bin number units for different rapidity bins is prepared. Then, the likelihood is minimized following the formalism described in Section 4.3.

To find the best model that describes the data, the fit is performed using the ratio data-to-simulation (data/MC) as input data and the templates correspond to model/MC while the nominal sample is the ratio equal to one, this is, MC/MC = 1. The probability model in a given $i-$bin is given by,

$$t_i(\vec{\varepsilon}) = 1_i + \sum_p h_{ip}\varepsilon_k \Rightarrow t_i(\vec{\varepsilon}) = 1 + \varepsilon_z P_{z,i} + \varepsilon_B B_i + \varepsilon_R R_i, \tag{5.17}$$

where 1_i corresponds to the nominal model in each bin, $\vec{\varepsilon} = (\varepsilon_z, \varepsilon_B, \varepsilon_R)$ is the POI vector of biases
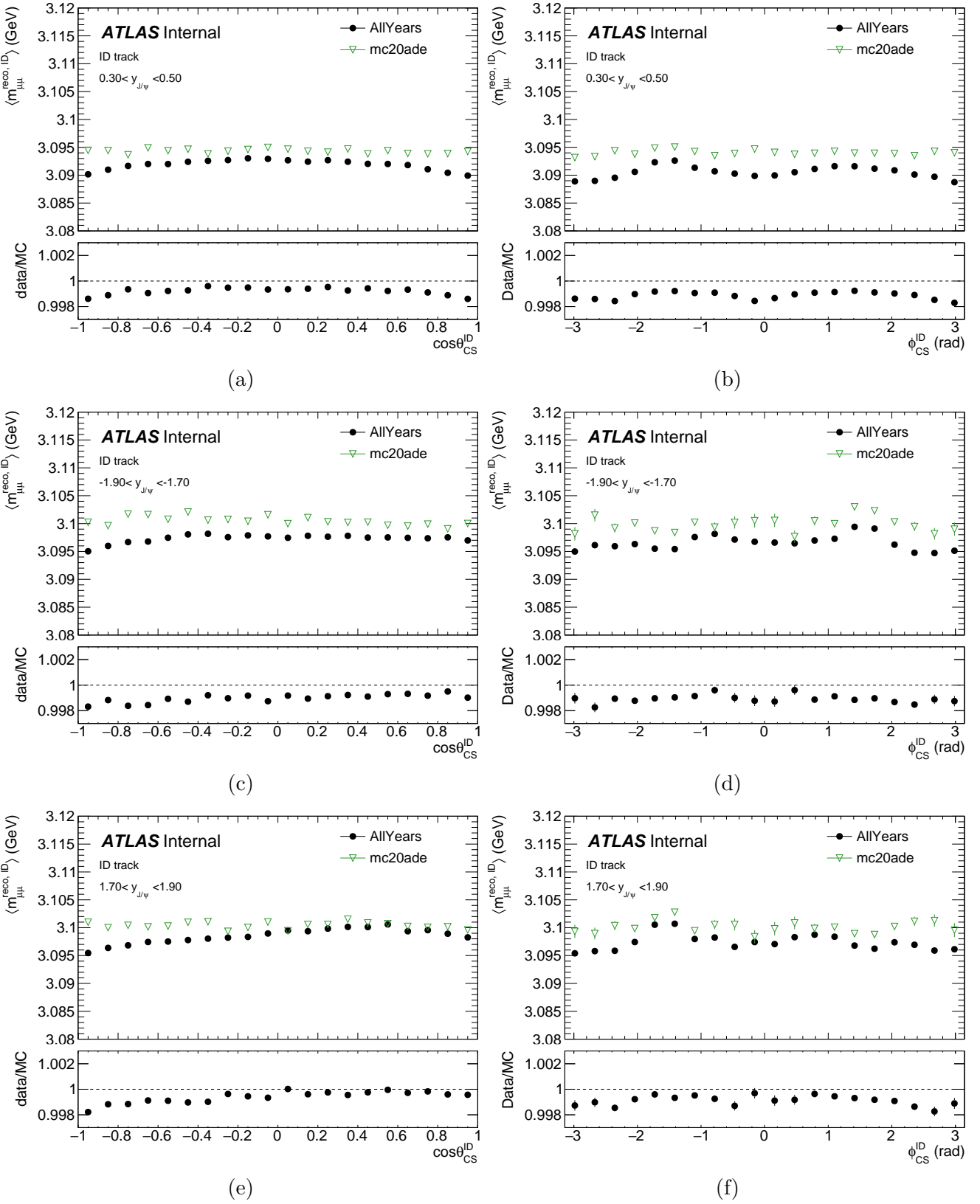
Figure 5.7: Mean invariant mass versus CS angles (left) $\cos\theta_{CS}$ and (right) ϕ_{CS} in (top) barrel, (middle) ECT backward and (bottom) ECT forward regions for ID tracks in $J/\psi \to \mu\mu$.
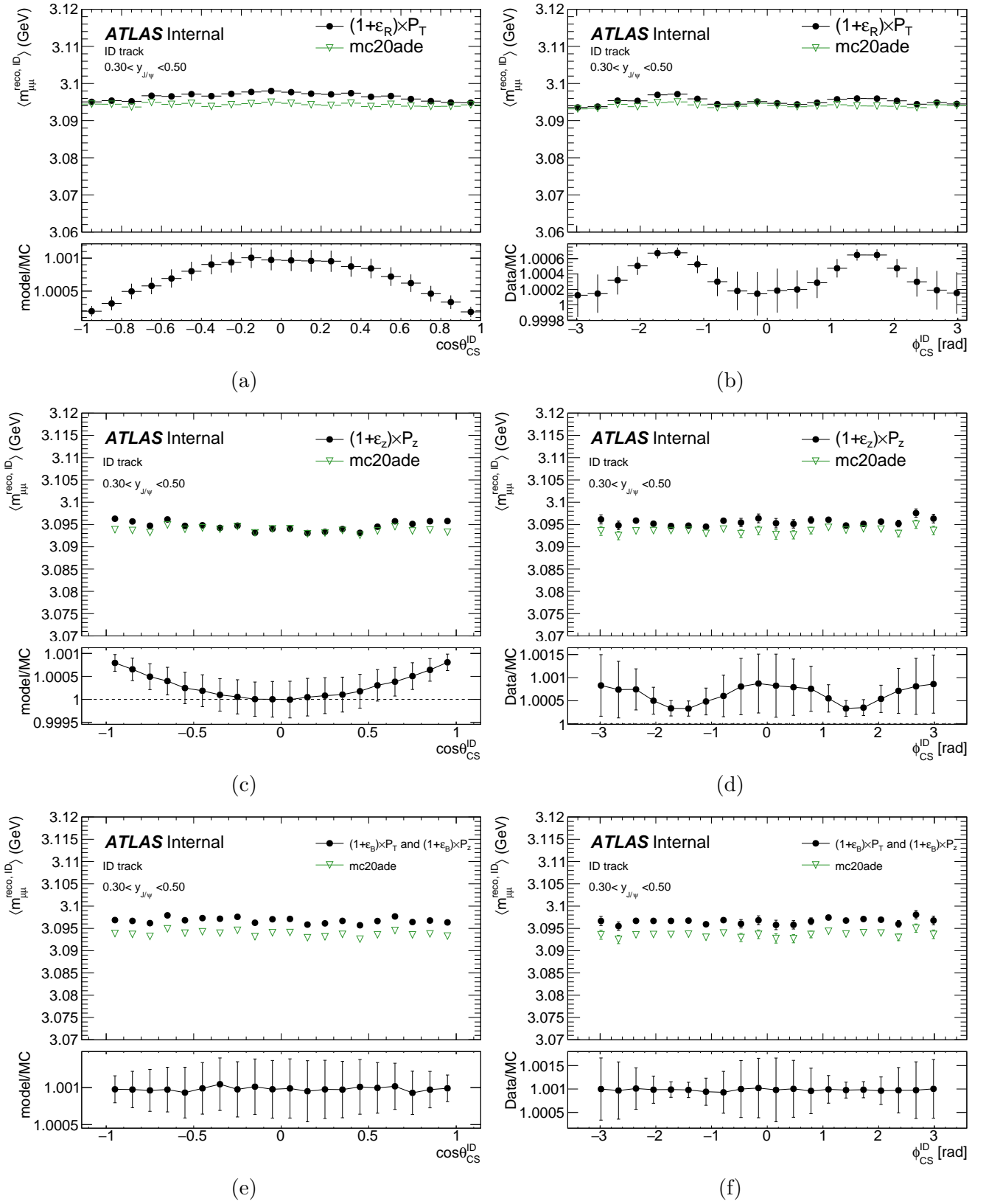
Figure 5.8: Simulated distortion models: Mean invariant mass versus CS angles (left) $\cos\theta_{CS}$ and (right) ϕ_{CS} in barrel region for (top) radial distortion, (middle) longitudinal distortion and (bottom) magnetic field distortion for ID tracks in $J/\psi \to \mu\mu$.

106

to be fitted and h is the sensitivity matrix of the POIs with respect to the model, these are, the model-to-MC ratio. Notice that for every $i-$bin there is a given $\vec{\varepsilon}$ such that a binned map in the rapidity space can be constructed.

Fits can be carried out using only one parameter model (single model fit) that implies only one bias parameter either ε_z, ε_B or ε_R as shown in Fig. 5.9. However, results show that the one-parameter model is not capable of describing the data, resulting in a high χ^2 and small χ^2-probability. For that reason a combination of models is required, i.e. two-parameter model. These are: longitudinal-magnetic field (ZB), longitudinal-radial (ZR) and magnetic field-radial (BR). Notice that a combination of the three models ZBR is degenerated, since as showed in Equations (5.9), (5.12) and (5.14), each model can be expressed as a combination of the other models and by consequence the parameters could not be disentangled. Combined model fits are shown in Fig. 5.10 where the χ^2 and the probability $\mathrm{Prob}(\chi^2)$ are improved. The three combinations provide similar results giving a "freedom" in choosing the modelling of the data. The fits are performed in all regions and a map of the biases as a function of the J/ψ meson rapidity can be obtained.

5.4.4 Correction maps and corrected dataset

After performing the fits, the biases are collected to construct the maps in J/ψ rapidity space, $y_{J/\psi}$, as shown in Figures 5.11, 5.12, 5.13. Since the three models can be expressed as combinations of the others and the three provide a similar fit quality there is a freedom in selection. An intuitive model is a radial distortion since a cylindrical detector over its own weight tends to present deformations in the radius. However, as showed in the one-parameter model results, a single deformation is not capable of describing the data. To complement the radial model, a magnetic field distortion is chosen since the residual (ε_B) generates a global scale shift in the invariant mass. This combined two-parameter model (magnetic field-radial distortion) is capable of modelling the effects in data through global shift plus modulations. Final model shows a relative bias in the barrel region of $\langle \varepsilon_B \rangle = -1.5 \times 10^{-3}$ and $\langle \varepsilon_R \rangle = 1.0 \times 10^{-3}$ for the magnetic field and radial distortions, respectively. After correction, a good agreement between the data and simulation at the per mille level is obtained as shown in Fig. 5.14.
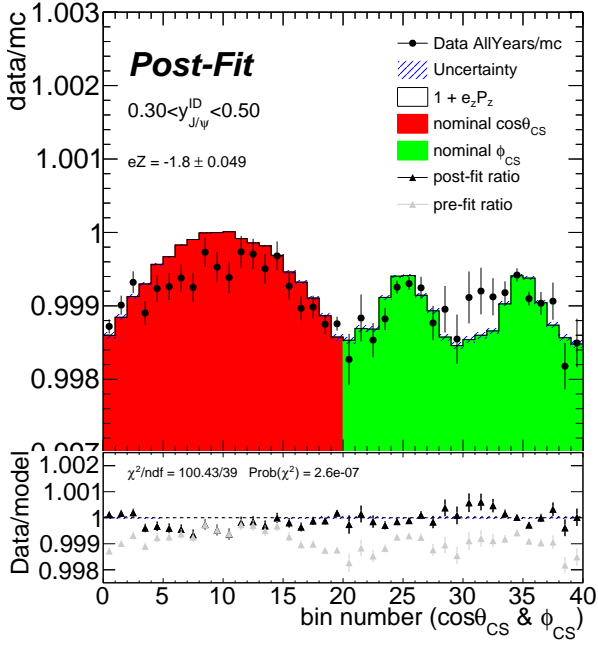
(a) Longitudinal distortion
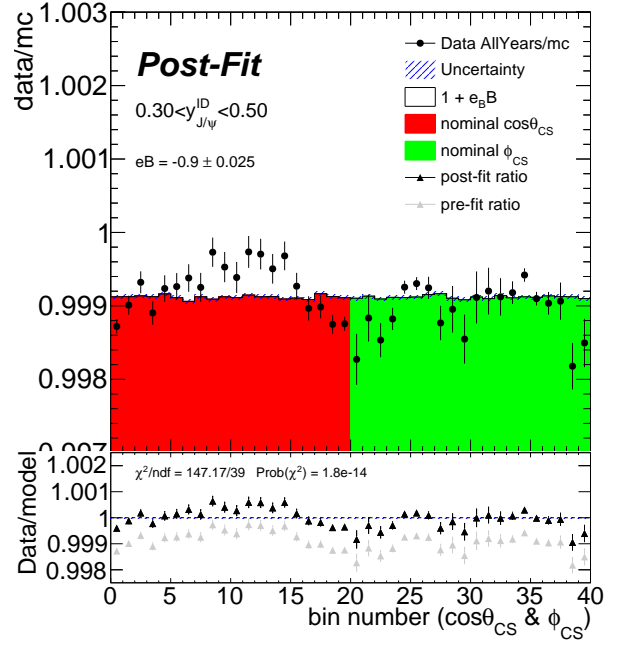
(b) Magnetic field distortion
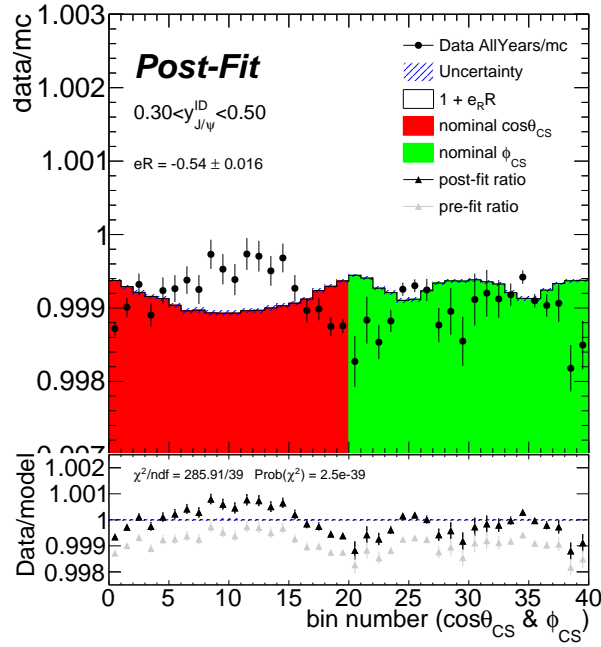
(c) Radial distortion

Figure 5.9: Analytical joint fit using single model for the barrel region.
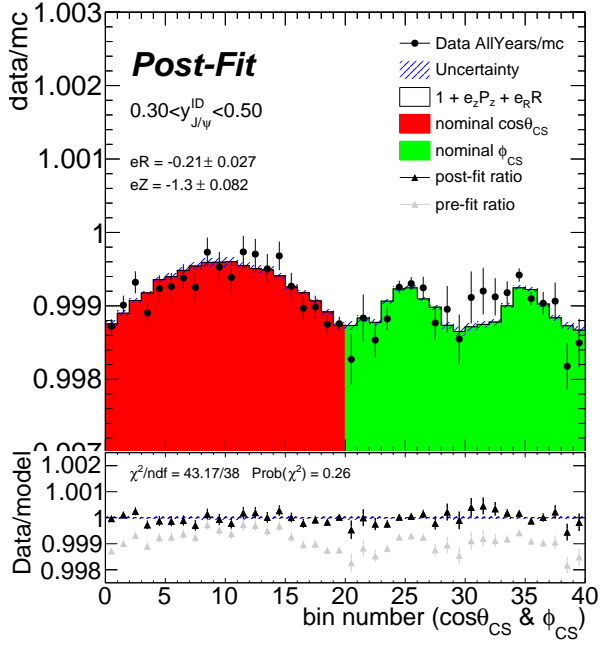
(a) Longitudinal-radial (ZR)
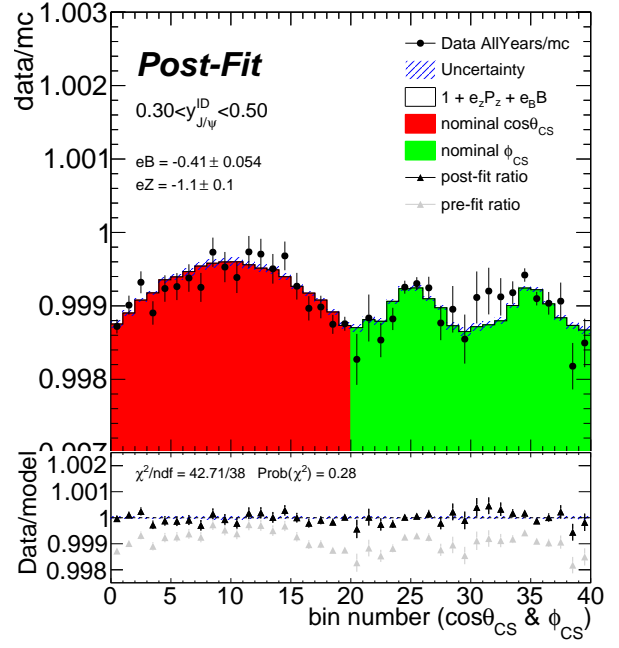
(b) Radial-magnetic field (ZB)
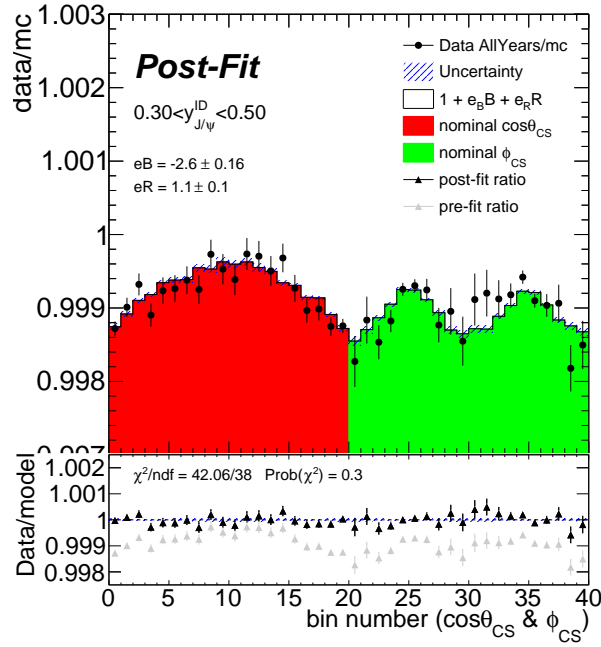
(c) Magnetic field-Radial (BR)

Figure 5.10: Analytical joint fit in combined model for the barrel region.
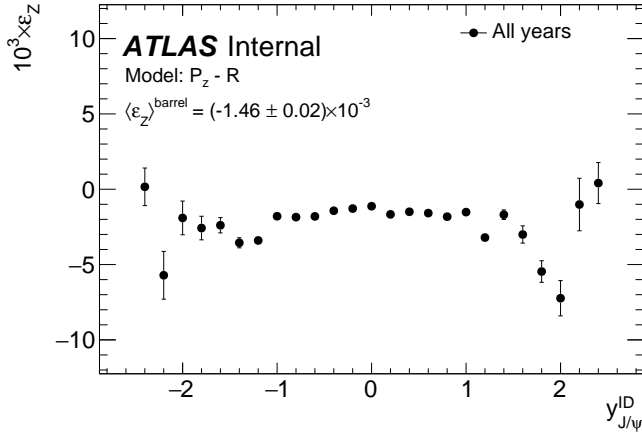
(a) Longitudinal bias ε_z.
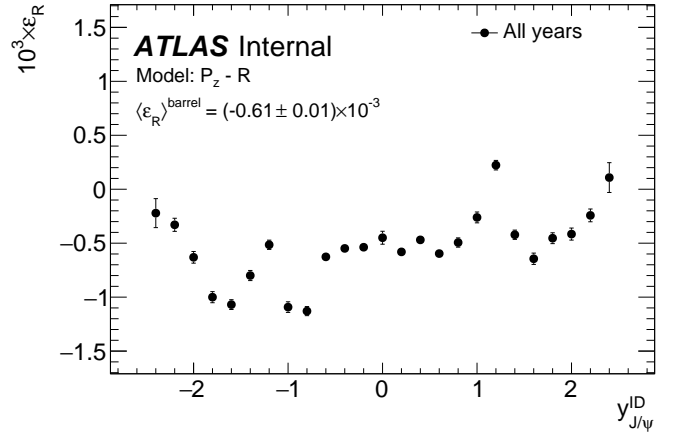
(b) Radial bias ε_R.

Figure 5.11: Bias maps for longitudinal-radial model of the ID distortions.
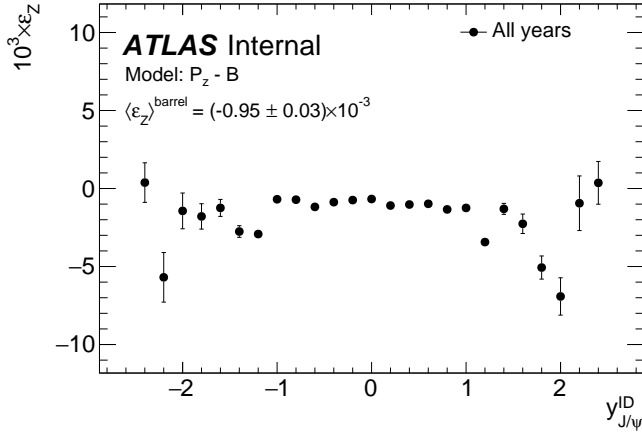
(a) Longitudinal bias ε_z.
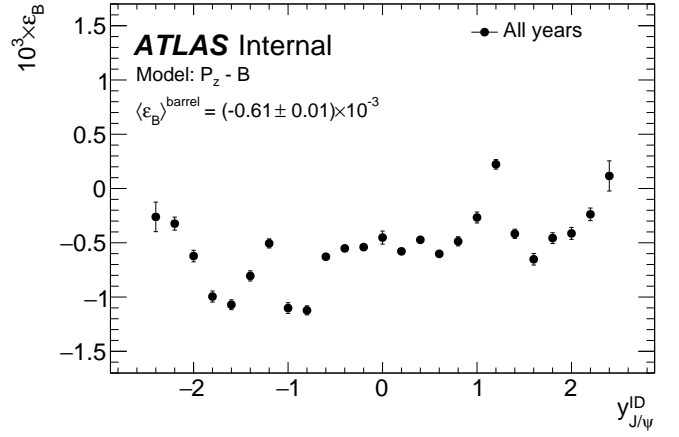
(b) Magnetic field bias ε_B.

Figure 5.12: Bias maps for longitudinal-magnetic field model of the ID distortions.
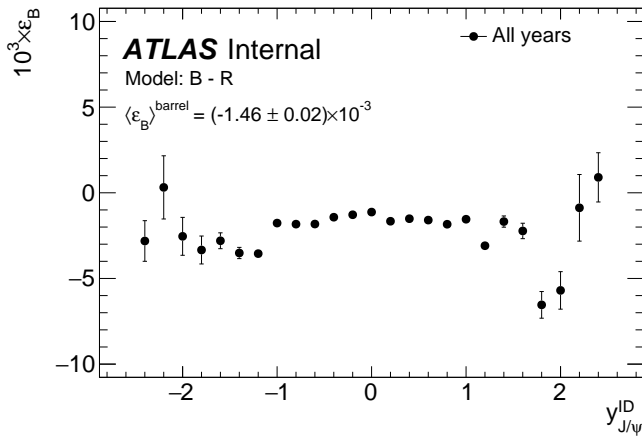
(a) Magnetic field bias ε_B.
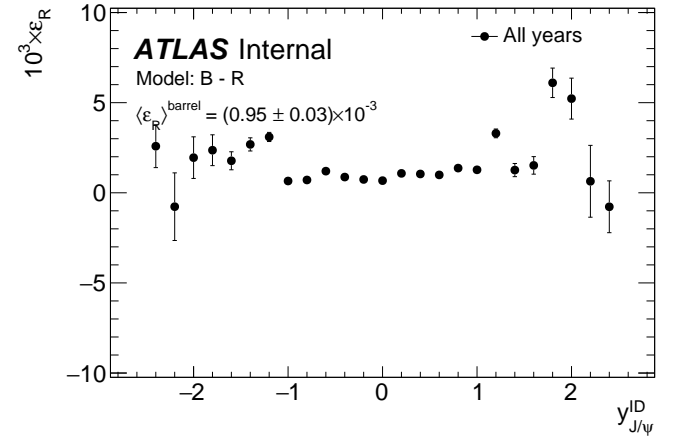
(b) Radial bias ε_R.

Figure 5.13: Bias maps for magnetic field-radial model of the ID distortions.
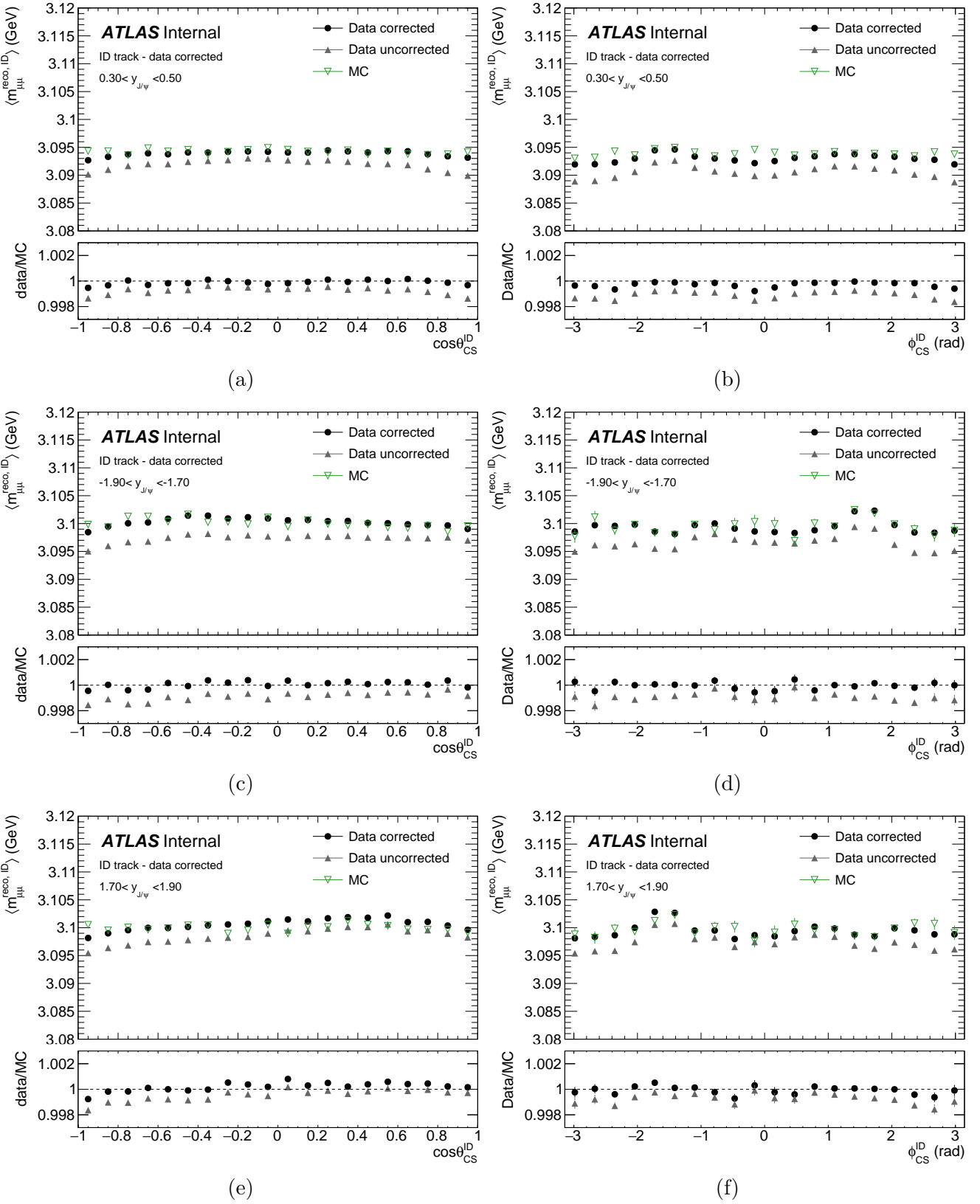
Figure 5.14: Data corrected: Mean invariant mass versus CS angles (left) $\cos\theta_{CS}$ and (right) ϕ_{CS} in (top) barrel, (middle) ECT backward and (bottom) ECT forward regions for ID tracks in $J/\psi \to \mu\mu$.
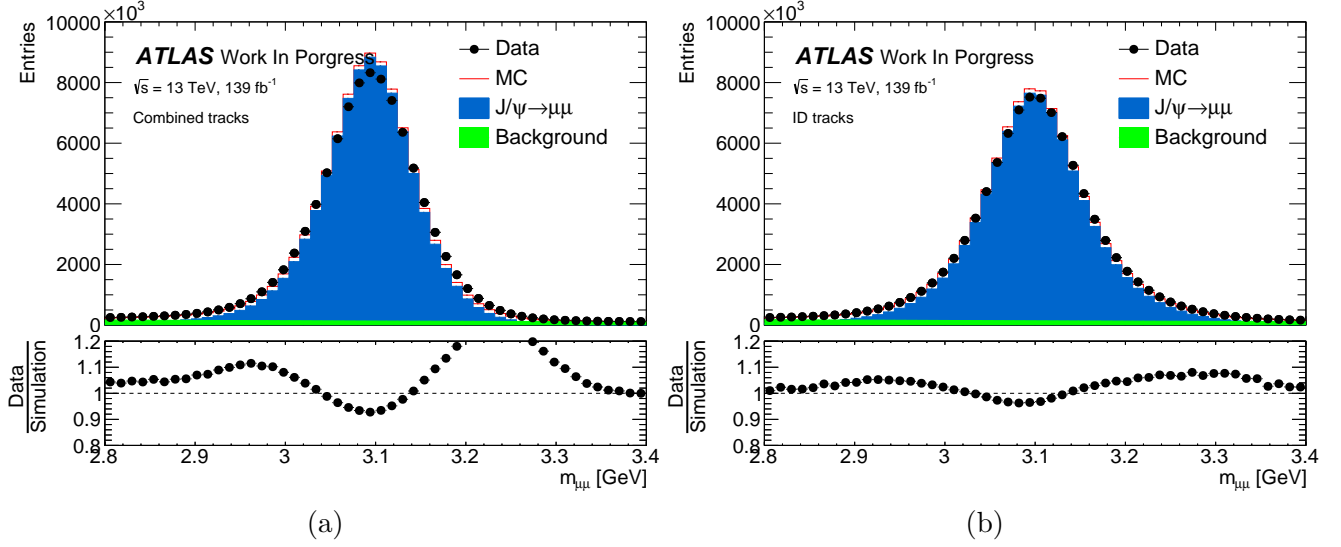
Figure 5.15: Inclusive invariant mass distribution for $J/\psi \to \mu\mu$ in (a) CB and (b) ID tracks with sagitta and ID geometrical distortion corrections applied in data.

These corrections target to improve the data-to-simulation agreement in the scales as shown in Figures 5.15 and 5.16 where a good agreement is found. However, the resolution requires another approach since the ID corrections do not improve considerably the data-to-simulation agreement as shown in Fig. 5.17.

5.5 MS/ID misalignment studies

In the ATLAS detector, the ID provides excellent resolution for low and medium momentum due to its high granularity and proximity to the interaction point. However, at momenta higher than $p_T > 40$ GeV, the MS, provides better momentum resolution, especially in the end-cap. Combining measurements from both detectors allows for optimized momentum resolution across a wide range of energies. The MS can be used to tag muons that are correctly reconstructed, helping to reject background particles that might be misidentified as muons in the ID. This is crucial for reducing contamination from non-muon tracks. Matching tracks from both systems aids in the alignment of the detectors, which is crucial for precision measurements, and ensures comprehensive coverage due to the different angular ranges and efficiencies of the ID and MS. Moreover, combining data from both detectors mitigates systematic uncertainties. For this, it is necessary to ensure a good MS/ID
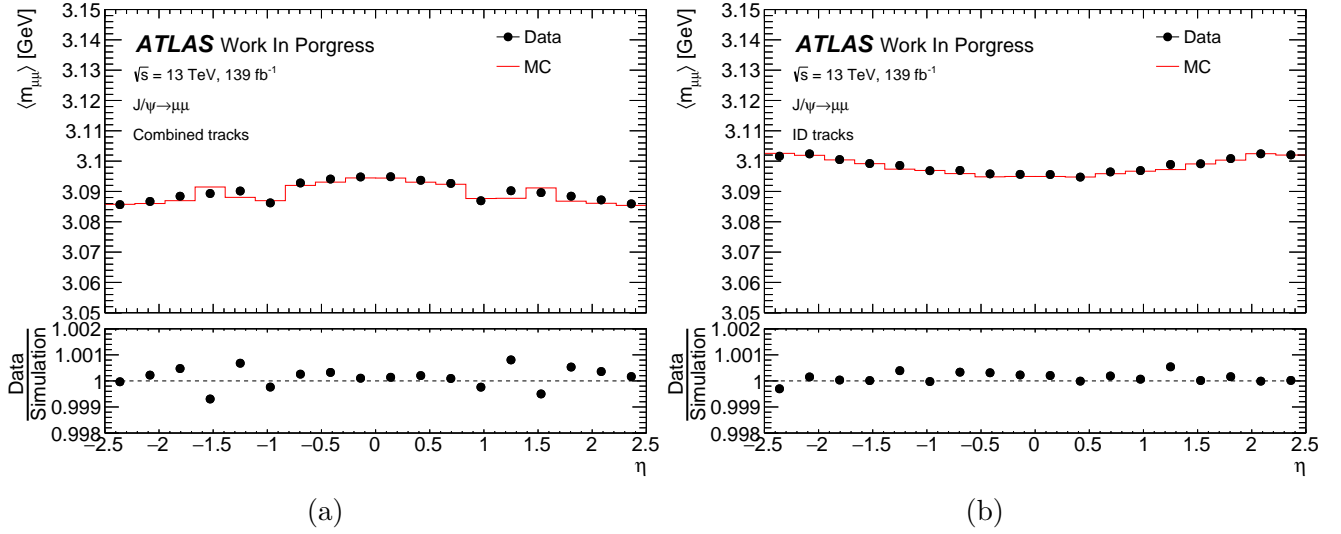
Figure 5.16: Mean mass of the dimuon system for $J/\psi \to \mu\mu$ in (a) CB and (b) ID tracks with sagitta and ID geometrical distortion corrections applied in data.
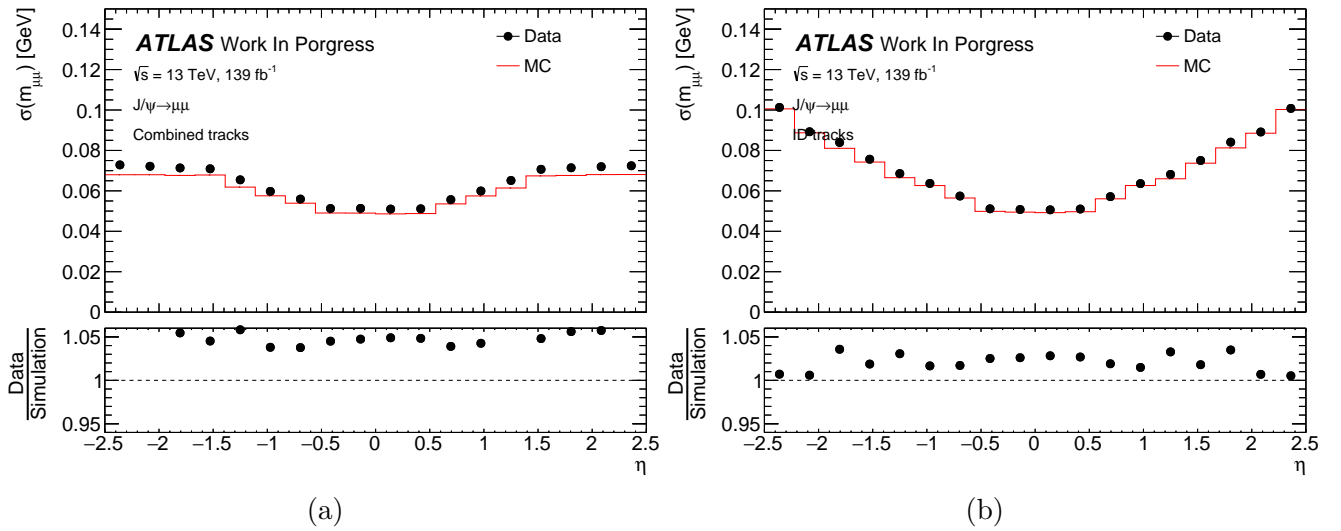
Figure 5.17: Dimuon invariant mass resolution for $J/\psi \to \mu\mu$ in (a) CB and (b) ID tracks with sagitta and ID geometrical distortion corrections applied in data.

alignment that potentially improves the track reconstruction in combined (CB) muons.

The MS alignment is mainly based on an array of optical sensors that are constantly monitoring the positions and deformations of the precision chambers. This is in charge of the internal MS alignment but it does not see a global displacement between the muon spectrometer and the inner detector. Even though the system is sophisticated it has deficiencies such as the knowledge of the sensor calibrations, lack of external optical links, etc. By consequence, extra information has to be provided in the alignment procedure. After studying the ID distortions, the next step is to examine any potential residuals between the MS and ID that persist after the calibration procedure, i.e. MS/ID residuals.

5.5.1 Residual misalignment parameters

To study the alignment distortions between the MS and the ID two quantities are considered: $(z_{MS} - z_{ID}) \sin \theta = \Delta z_0 \sin \theta$ and $\Delta \theta = \theta_{MS} - \theta_{ID}$. The first one corresponds to the distance between the MS and ID track in the precision plane of the MS where θ is the combined (MS and ID) angle between the momentum and the beam axis. The second one corresponds the polar angle difference measured in both tracks MS and ID. Previous studies in Ref. [165] showed that the MS/ID residuals for $\Delta z_0 \sin \theta$ have a value of about ± 1.5 mm with systematic shape in all the sectors and a different behavior from the end-cap to the barrel. In the same way, for the $\Delta \theta$ a residual of few mrad was found. One of the first steps is to reproduce these results and to understand their origin. On what follows, the sector and pseudo-rapidity region definitions described in subsections 2.2.5 and 2.2.6 are implemented. The muons selection is performed as described in 3.2.1.1.

5.5.1.1 Fit of the residual misalignment parameters

The first MS/ID residual studies are carried out purely with muon extrapolated (ME) tracks, i.e. MS tracks constrained to the beam spot. The inclusive distributions of the MS/ID residuals for $\Delta \theta$ and $\Delta z_0 \sin \theta$ in $Z \to \mu\mu$ and $J/\psi \to \mu\mu$ are shown in Fig. 5.18 where the distributions are fitted using two models, Gaussian fit with polynomial background (Blue line) and Cauchy fit (red line).

In the case of the Z resonance, $\Delta \theta$ is distributed around zero but when $\Delta \theta \sim 0$ the values tend
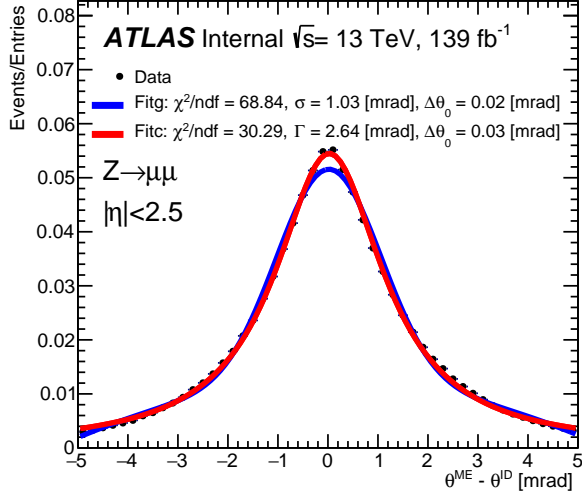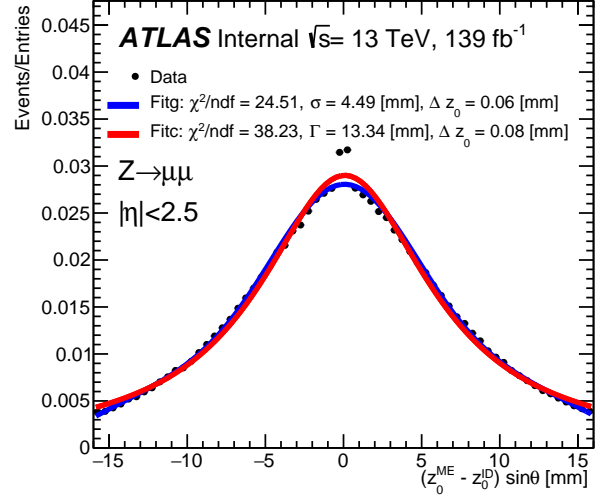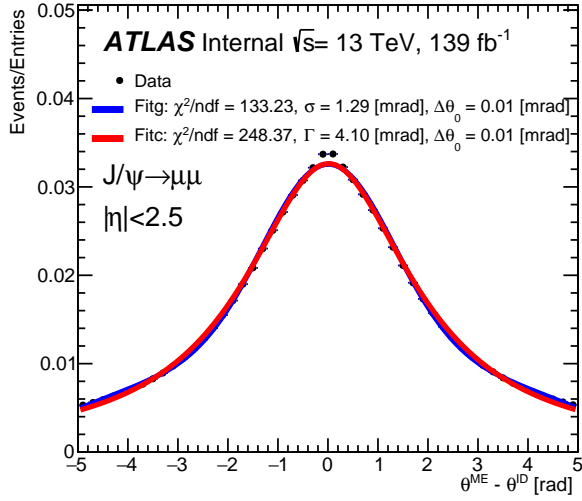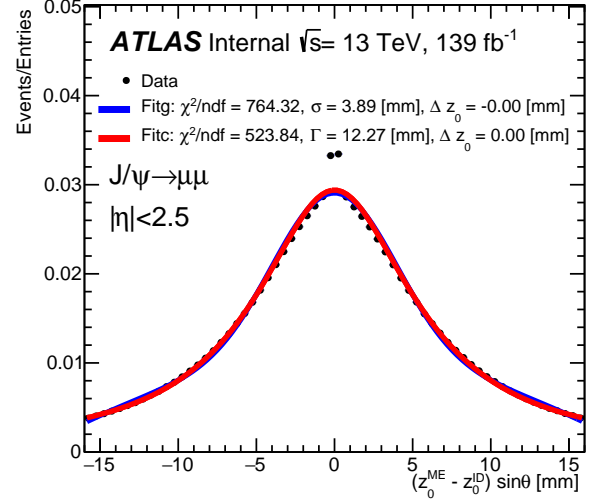
Figure 5.18: MS/ID residual distributions for (left) $\Delta\theta$ and (right) $\Delta z_0 \sin\theta$ in $Z \to \mu\mu$ (top) and $J/\psi \to \mu\mu$ (bottom). Two type of fits are implemented: Gaussian fit (blue) and Cauchy fit (red).

to deviate significantly from the rest of the data, resulting in a bad goodness of fit. However, the fit information can be extracted showing a mean value of order $\sim 10^{-2}$ mrad with standard deviation $\sim$ mrad. For $\Delta z_0 \sin \theta$ distribution, a similar result is obtained when $\Delta z_0 \sin \theta \sim 0$ that results in a large χ^2. However, the central value and the standard deviation are obtained to be of order $\sim 10^{-2}$mm and $\sim$mm, respectively.

For the J/ψ resonance, results for both $\Delta \theta$ and $\Delta z_0 \sin \theta$ are similar to the ones obtained for the Z resonance, this is, central value of 10^{-2} mrad and standard deviation few mrad for $\Delta \theta$ and 10^{-2} mm and few mm for $\Delta z_0 \sin \theta$.

Distributions in Fig. 5.18 show a discontinuity around zero that has to be solved in to improve the fits. A probable explanation of this behavior arises from the fact that ME tracks are reconstructed taking into account the beam spot as a constraint. However, if the beam spot is removed and the track reconstruction is performed only in the muon spectrometer (Muon Spectrometer Only Extrapolated (MSOE) track) the discontinuity disappears.

Fig. 5.19 shows that once the MSOE track is implemented the discontinuity at zero disappears, nevertheless, the distribution tends to decrease in amplitude and spread over the tails. Results for $J/\psi \to \mu\mu$ with MSOE track reconstruction show that the MSOE tracks solve the discontinuity but the amplitude is highly reduced compared to the previous distributions and the spreading over the tails is highlighted for low momentum. This effect could be related to the fact that the track reconstruction is performed only in the muon spectrometer, resulting in reduced resolution in both the angles and p_T. This has a greater impact for low momentum muons like in the J/ψ case. Once the distributions do not present the discontinuity at zero, the fits are performed again as shown in Fig. 5.20.

5.5.1.2 Detector mapping of $\Delta \theta$ and $\Delta z_0 \sin \theta$

To study the misalignment parameters for every sector in the detector, a binning in $\eta - \phi$ space is performed using MOSE tracks[1] taking into account the sixteen sectors of the detector. For each bin, the distributions, $\Delta \theta$ and $\Delta z_0 \sin \theta$, are computed and the misalignment central values are retrieved

---

[1]On what follows MSOE tracks are simply noted as MS tracks.
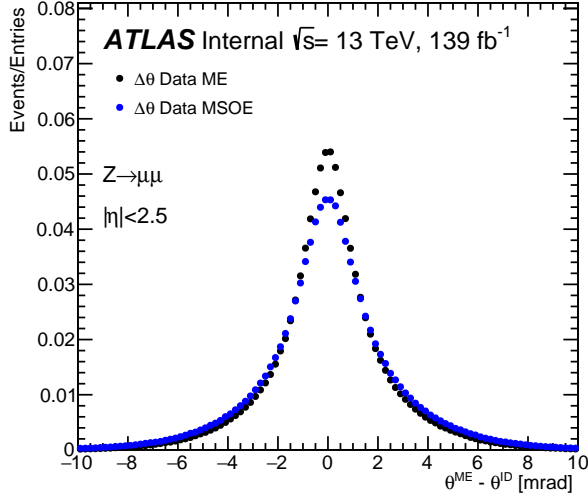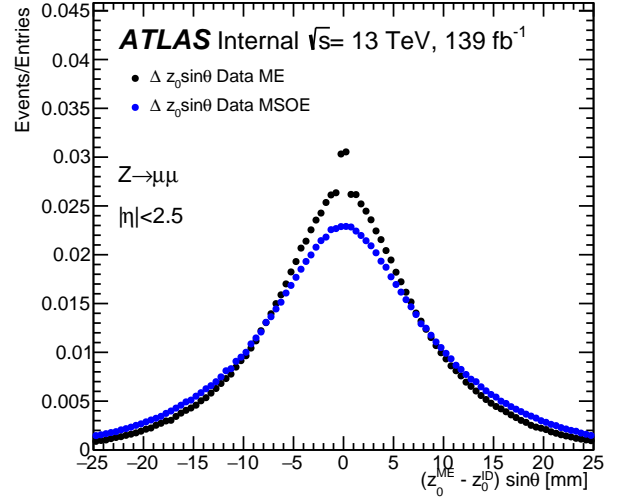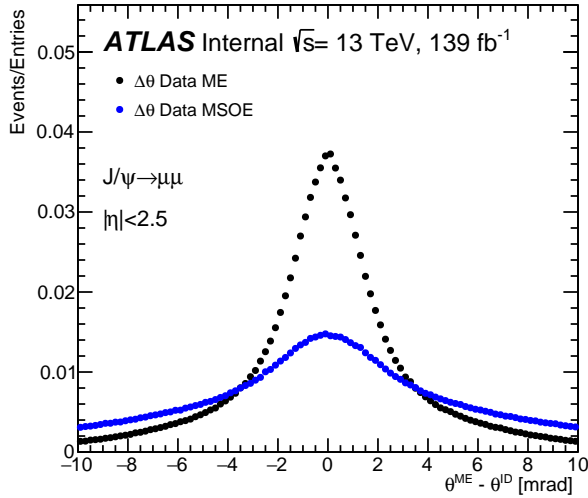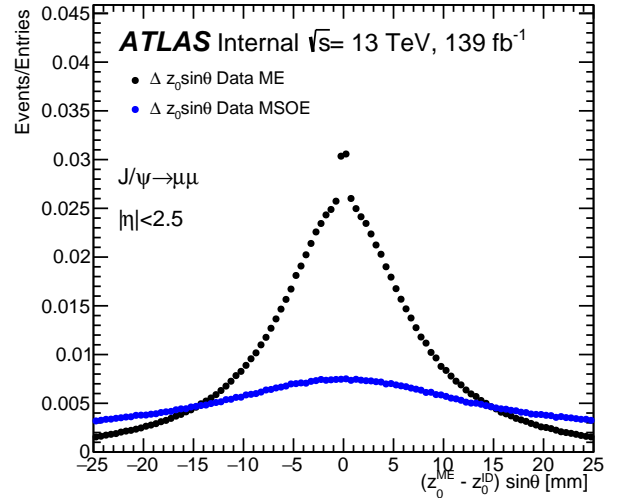
Figure 5.19: MS/ID residual distributions for (left) $\Delta\theta$ and (right) $\Delta z_0 \sin\theta$ in $Z \to \mu\mu$ (top) and $J/\psi \to \mu\mu$ (bottom) using different track reconstruction ME (black) and MSOE (blue).
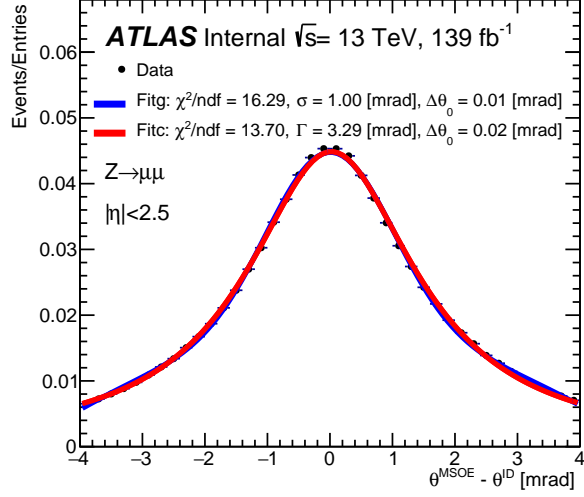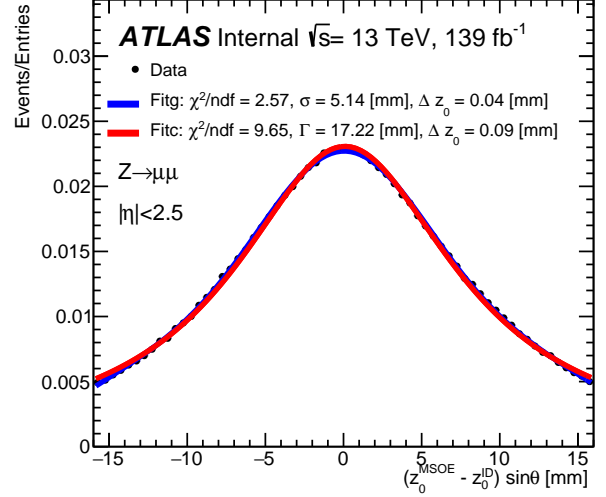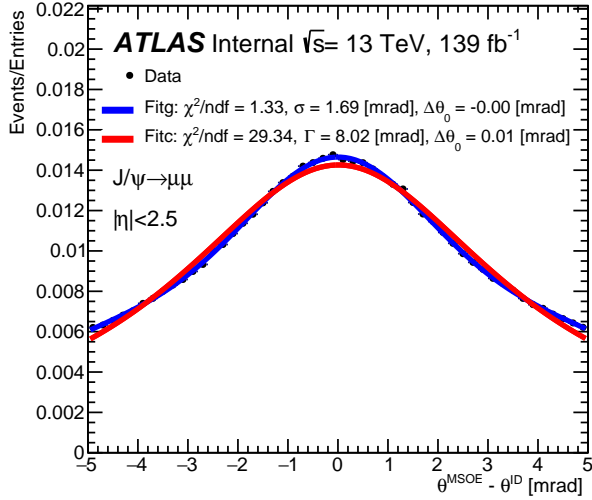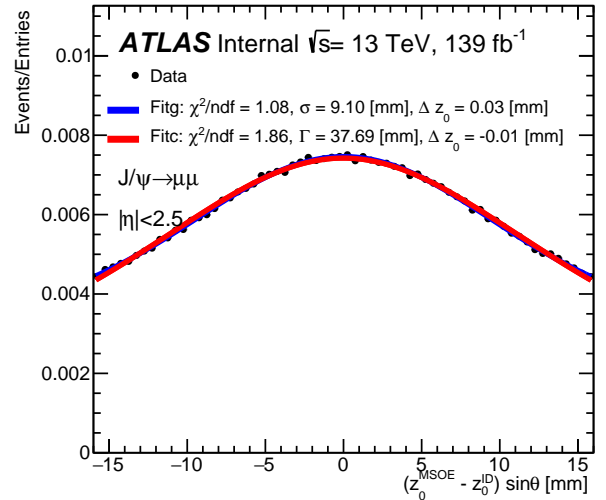
Figure 5.20: Fits using MSOE track reconstruction in MS/ID residual distributions for (left) $\Delta\theta$ and (right) $\Delta z_0 \sin\theta$ in $Z \to \mu\mu$ (top) and $J/\psi \to \mu\mu$ (bottom). Two type of fits are implemented: Gaussian fit (blue) and Cauchy fit (red)

from the fits. The 1D profiles for the residuals are shown in Fig. 5.21 that are in agreement with results from Ref. [165].

For $\Delta\theta$, the residuals are in a range of $\sim \pm 0.3$ mrad and the larger deviations are located mainly in the barrel region. Nevertheless, some deviations in the ECT region are observed. The results obtained with the simulation show that these effects are not considered on it.

For $\Delta z_0 \sin\theta$, a residual of few millimeters $\sim \pm 1.5$ mm is found. One of the relevant effects in this misalignment parameter is the systematic shape, negative slope (decreasing) in the ECT region as well as the positive slope (increasing) in the barrel. For $\eta < -1$ the residual starts around ~ 1 mm and it decreases up to ~ -1 mm once the barrel region is reached. At this point, the slope changes and the residual increases up to ~ 1 mm for $-1 \leq \eta \leq 1$. Once the barrel region is over, the slope changes and the residual decreases in the ECT forward. A *possible* origin of this effect is explained in Section 5.7.

The same study is carried out using the J/ψ resonance but the results are not comparable to the ones in Ref. [165] since they are obtained for high p_T. From Fig. 5.22 the misalignment values in $\Delta\theta$ are larger compared to the Z boson reaching values up to $\sim \pm 1.5$ mrad with the larger deviations located in the barrel region. For the longitudinal impact parameter the values go up to $\sim \pm 3$ mm. In the low p_T case, the slopes are present and the transition ECT backward to barrel and barrel to ECT forward remains with mean values that changes considerably among the η bins. In this case, the simulation is matching for $\Delta\theta$ and $\Delta z_0 \sin\theta$ with the obtained results since results are obtained at low momentum.

5.5.2   Charge dependency of the residual parameters

MS/ID residuals are present for both parameters $\Delta\theta = \theta_{MSOE} - \theta_{ID}$ and $(z_{MSOE} - z_{ID})\sin\theta$. To look for possible charge dependent dependencies, the same study is performed in η and ϕ taking into account positive (Pos) and negative (Neg) muons.
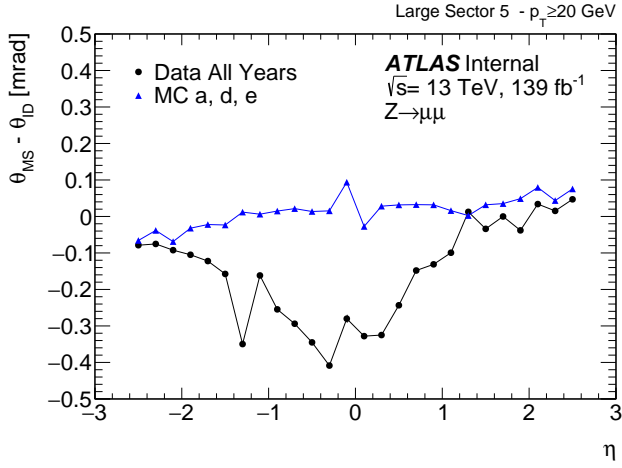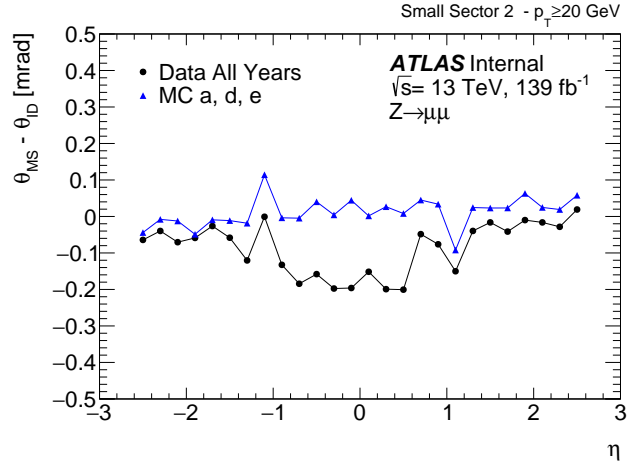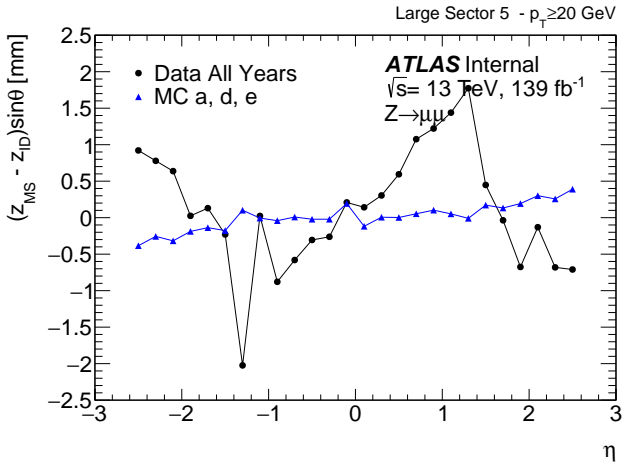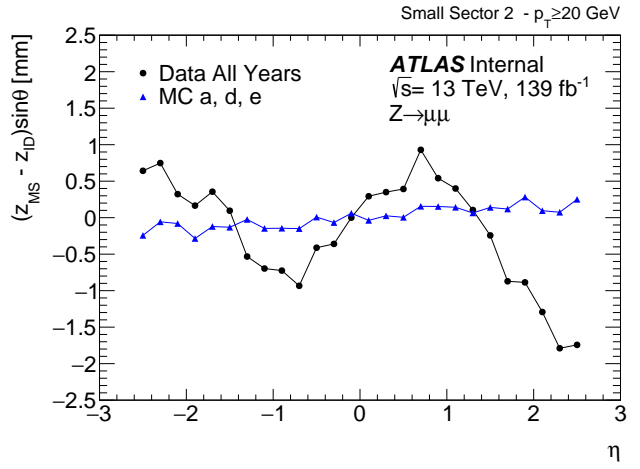
Figure 5.21: MS/ID residual Profiles for (top) $\Delta\theta$ and (bottom) $\Delta z_0 \sin\theta$ vs η for (left) large and (right) small sectors in $Z \to \mu\mu$.
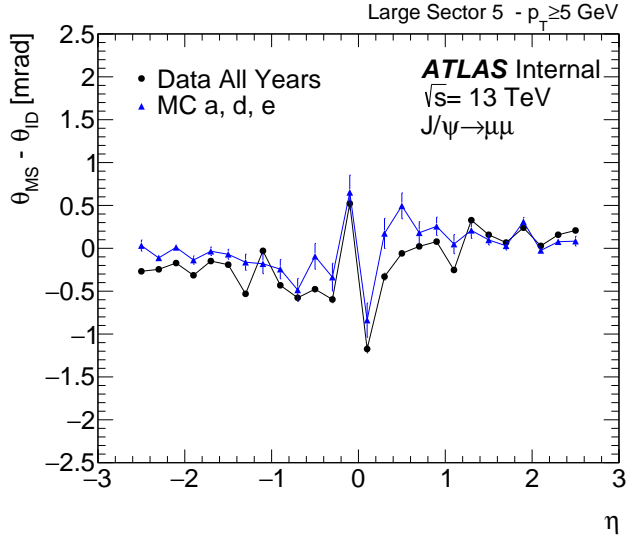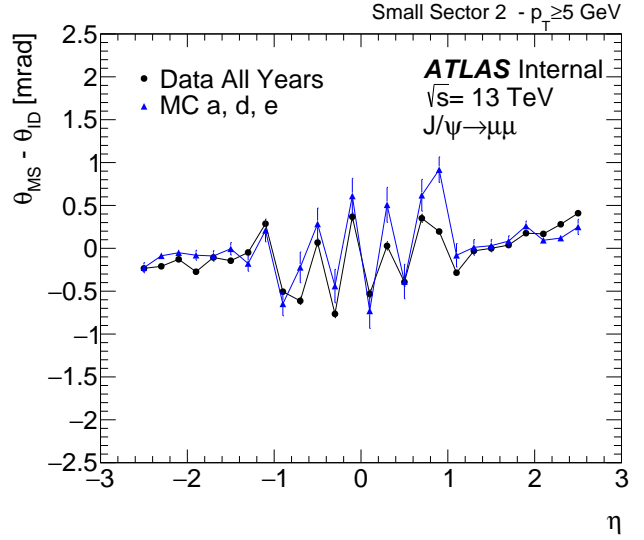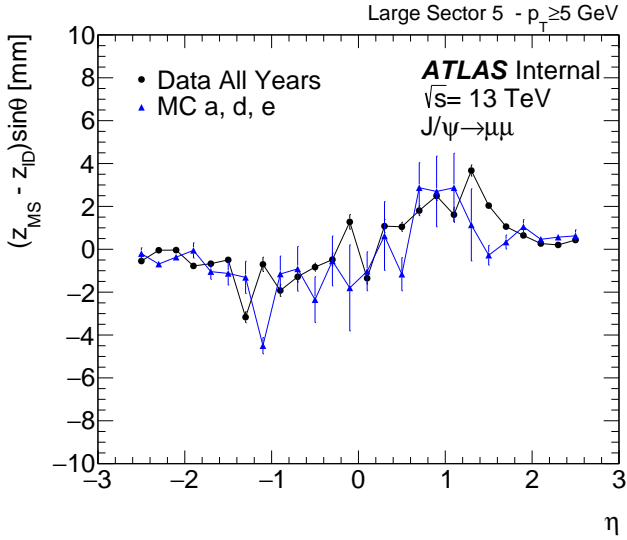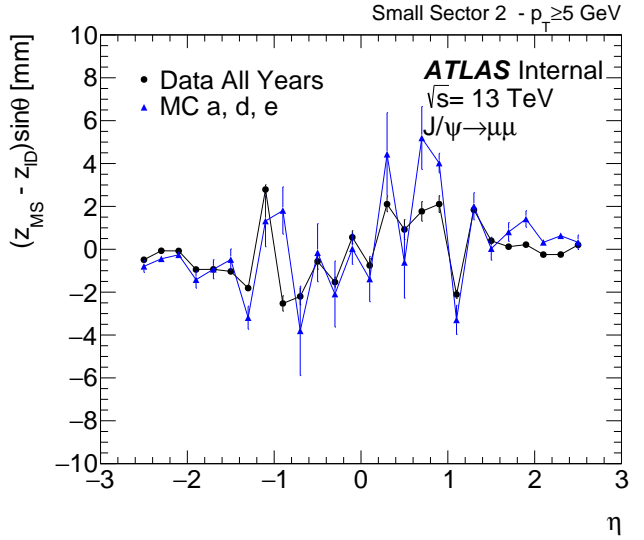
Figure 5.22: MS/ID residual Profiles for (top) $\Delta\theta$ and (bottom) $\Delta z_0 \sin\theta$ vs η for (left) large and (right) small sectors in $J/\psi \to \mu\mu$.

5.5.2.1 $Z \to \mu\mu$ analysis

To reproduce the same results in different momentum ranges and to ensure a good number of Z candidates, two regimes are defined, the p_T larger and lower than $p_{T,0} = 40$ GeV.

Impact on $\Delta\theta$

Results for $p_T > 40$ GeV and $p_T < 40$ GeV are shown in Fig. 5.23, where a charge asymmetry between μ^+ and μ^- is present. For the high p_T, the same behavior observed in section 5.5.1 remains but with larger values compared to the few mrad previously described. To this, the charge dependency is also considered in which the smallest asymmetry is located in the ECT region for $|\eta| > 1.7$, the largest asymmetry is located in the intermediate region, $1 < |\eta| < 1.7$, with characteristic "peaks" at $|\eta| \sim 1$. The barrel region for $|\eta| < 1$ presents deviations of about the same order. In general, these asymmetry values correspond to ~ 0.2 mrad. A transition effect is also observed from large to small sectors where the negative mean values are always larger than the positive mean values in the large sectors, while for small sectors is the opposite. This behavior is observed in general for all the sectors 1 to 16.

For $p_T < 40$ GeV, the misalignment values tend to increase when the momentum decreases, this implies that the charge asymmetry is also momentum dependent. Notice that the two effects, the charge asymmetry and the large to small sector transition are not present in the simulation.

Impact on $\Delta z_0 \sin\theta$

The same analysis is performed for the longitudinal impact parameter with $p_T > 40$ GeV and $p_T < 40$ GeV and results are shown in Fig. 5.24. These show that the slope from ECT to Barrel and barrel to ECT remains when positive or negative muons are considered. To this, new effects are observed such as the increase in the misalignment scale from few mm up to ~ 2.5 mm. The lowest values are located in the ECT for $|\eta| > 1.7$, while the largest values of around ~ 1 mm are located at the intermediate region $1 < |\eta| < 1.7$ and characterized by "peaks" around $|\eta| \sim 1$. The barrel region for $|\eta| < 1$ has a value of ~ 0.5 mm.

For $\Delta\theta$ the transition effect from large sectors to small sectors is also observed. This is, the
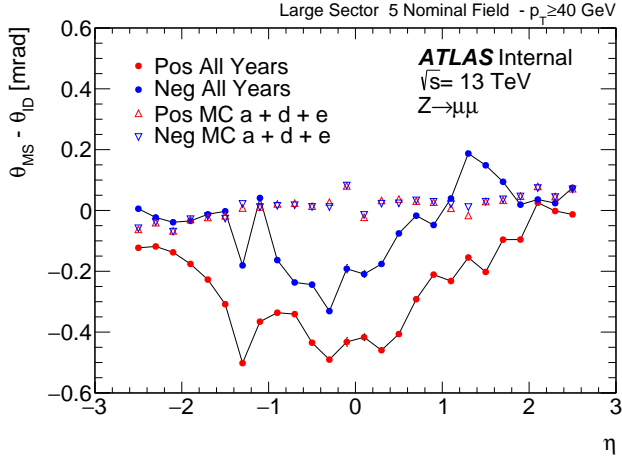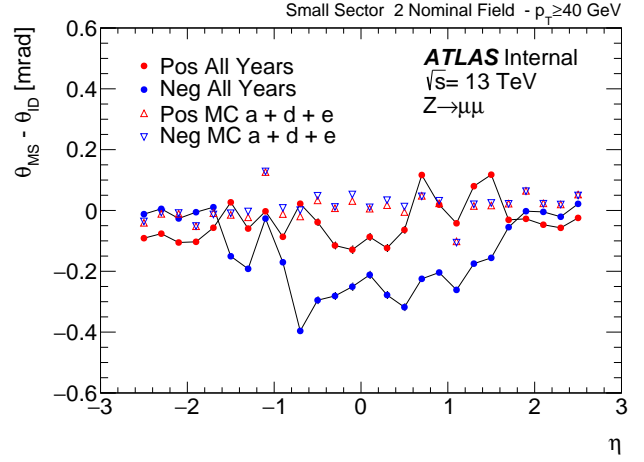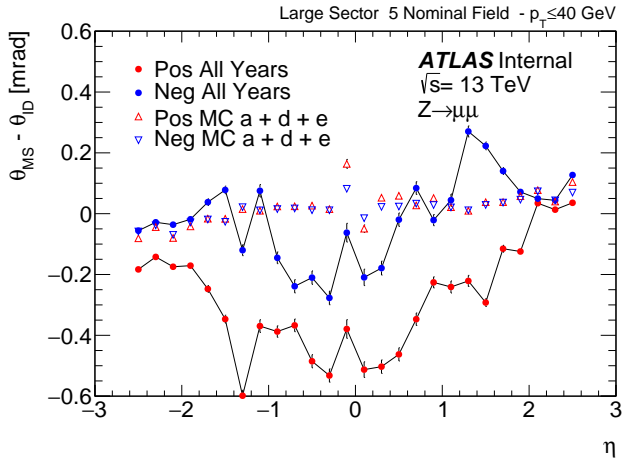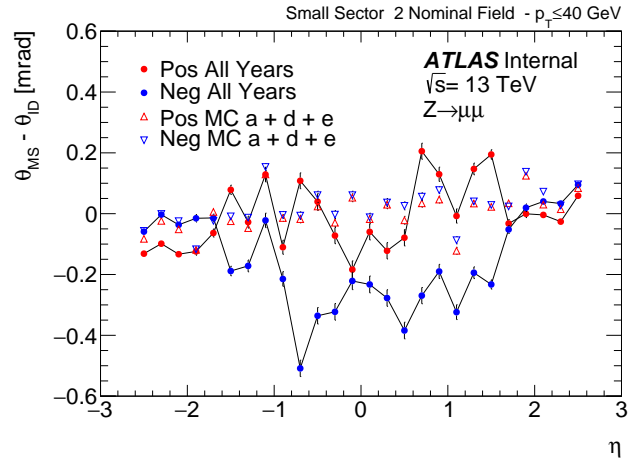
Figure 5.23: MS/ID residual profile for $\Delta\theta$ for positive and negative muons in (left) large and (right) small sectors with (top) $p_T > 40$ GeV and (bottom) $p_T < 40$ GeV.

negative mean values for a given η are larger than the positive mean values in the large sectors while this is inverted for small sectors where the mean values of positive muons are larger than the mean values of negative muons. Therefore, results obtained in Fig. 5.24 show a charge dependency in which the asymmetry tends to increase when the momentum decreases.
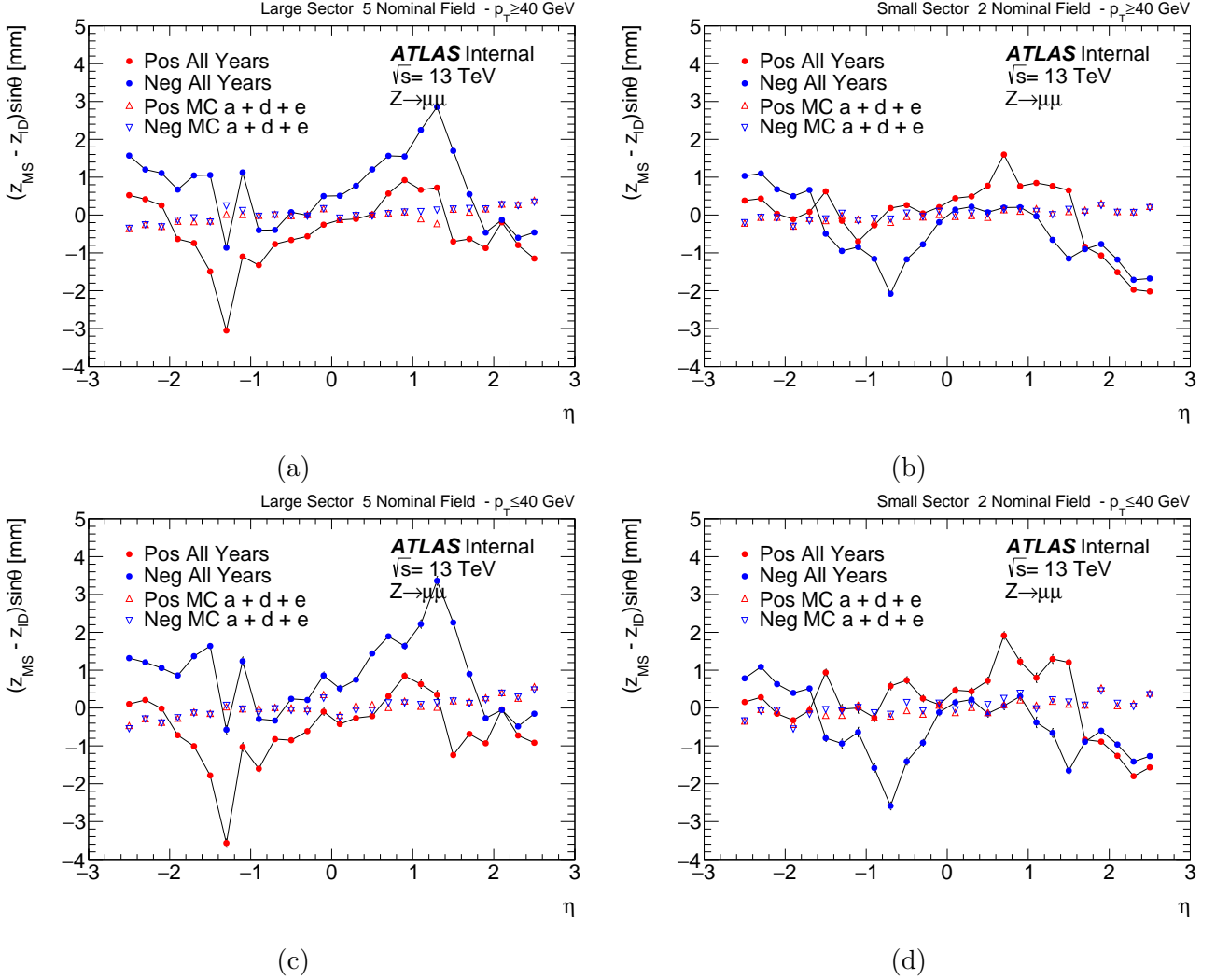
Figure 5.24: MS/ID residual profile for $(z_{MS} - z_{ID})\sin\theta$ for positive and negative muons in (left) large and (right) small sectors with (top) $p_T > 40$ GeV and (bottom) $p_T < 40$ GeV.

After the charge dependency studies in $Z \to \mu\mu$ resonance, the MS/ID residuals are directly related to different effects:

- Slope effect from ECT to Barrel present in $\Delta z_0 \sin\theta$ only.

- Fluctuations for $\Delta\theta$ and $\Delta z_0 \sin\theta$ in the barrel region.

124

- Large sector to small sector transition for positive and negative muons.

- Charge dependency asymmetry related to muon momentum.

5.5.2.2 $J/\psi \to \mu\mu$ analysis

The studies are performed for using the J/ψ at low p_T to ensure a good number of candidates.

Impact on $\Delta\theta$

Results are shown in Fig. 5.25 where the effects described in Section 5.5.1 remains for positive and negative muons. A charge asymmetry is observed as for the Z resonance but in this case with larger values compared to the high momentum up to $\sim \pm 3$ mrad. The transition from large sectors to small sectors is also present.
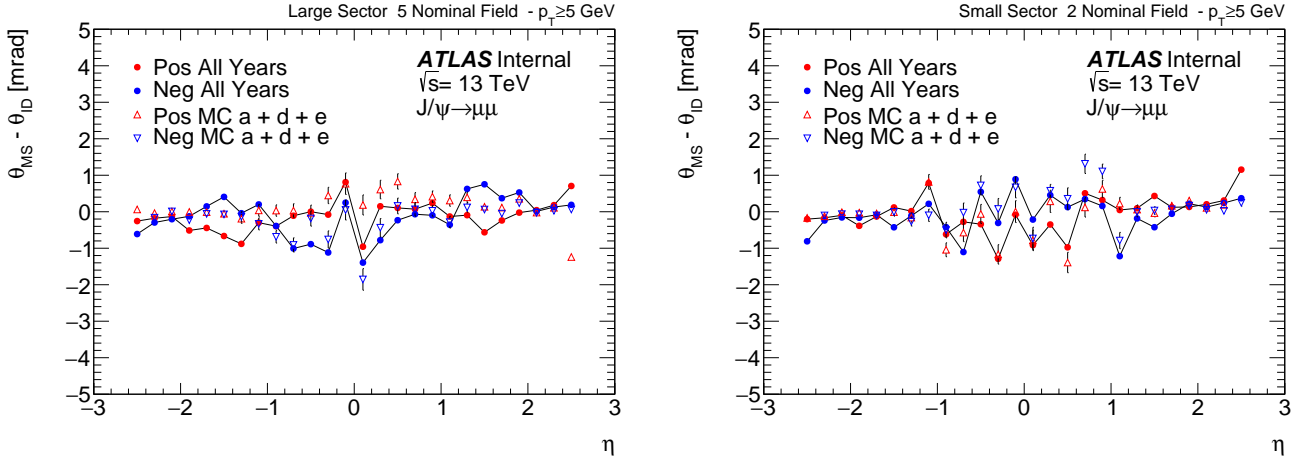
Figure 5.25: MS/ID residual profile $\Delta\theta$ for positive and negative muons in (left) large and (right) small sectors with low p_T.

Impact on $\Delta z_0 \sin\theta$

For the longitudinal impact parameters results are shown in Fig. 5.26 where the charge asymmetry is observed with misalignment residual of about ± 5 mm that changes considerably among the η bins and the slope is still present.
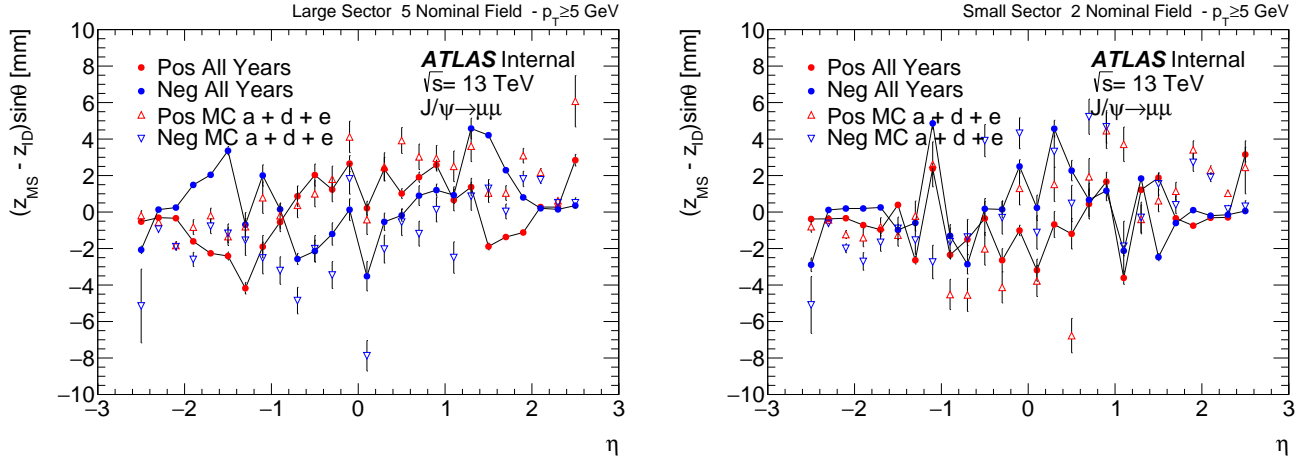
Figure 5.26: MS/ID residual profile $\Delta z_0 \sin\theta$ for positive and negative muons in (left) large and (right) small sectors with low p_T.

5.5.2.3 Large and Small Sectors inclusive study

The large and small sectors play an important role in the charge dependency since there is a transition from one to another. To increase the statistics and to obtain a global sector behavior, the information per sector is combined in one (folded). This gives place to only one large sector and one small sector encoding all the information.

The results for Z resonance with $p_T > 40$ GeV and $p_T < 40$ GeV are shown in Fig. 5.27 and Fig. 5.28, respectively. For $\Delta\theta$ the main effect is an asymmetry in the barrel region $|\eta| < 1$ with prominent peaks located in the intermediate region $1 < |\eta| < 1.7$ and small asymmetry in the ECT region $|\eta| > 1.7$. There is a transition from large to small sector, this is, the mean values in the large sectors for negative muons are larger than the mean values for positive muons and vice-versa for small sectors.

In a similar way, the inclusive behavior for $\Delta z_0 \sin\theta$ in the large and small sectors are studied. The highlighted effects are the slopes where a decreasing behavior for $|\eta| > 1$ and increasing in the barrel $|\eta| < 1$ are found. The asymmetry in the barrel region is around ~ 0.5 mm while two prominent "peaks" in the intermediate region, $1 < |\eta| < 1.7$, are observed with the larger asymmetry about 1.5 mm. The small asymmetry is located at the ECT region with a value of about 0.15 mm. The transition, large to small sector is still present.

Moreover, from Fig. 5.28, it follows that a momentum dependency is present. This is, the

asymmetry increases when the momentum decreases. These effects remain at low momentum.
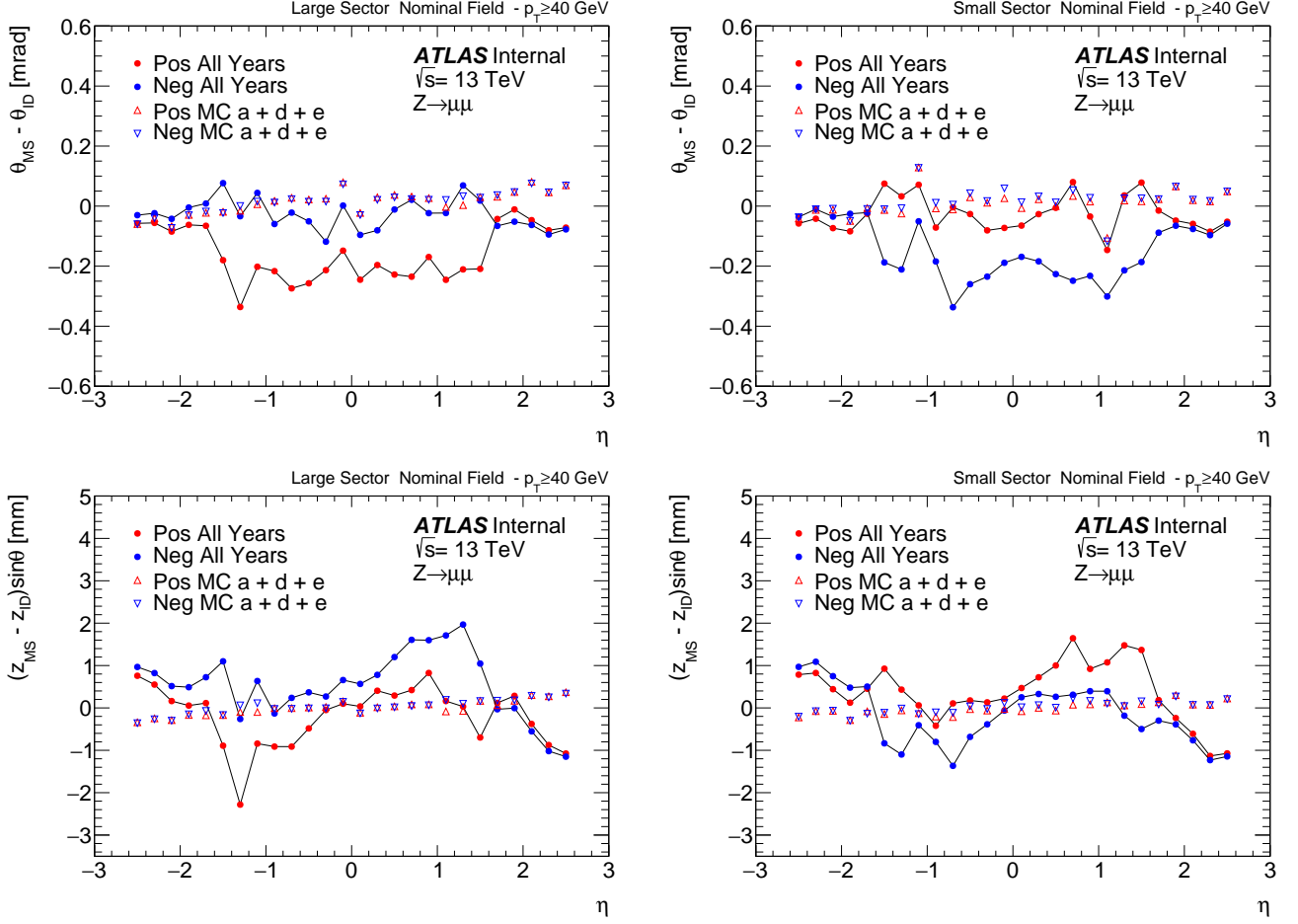
Figure 5.27: MS/ID residual profiles for (top) $\Delta\theta$ and (bottom) $\Delta z_0 \sin\theta$ in $Z \to \mu\mu$ for (left) large and (right) small sectors at $p_T > 40$ GeV.

The same analysis was carried out for the J/ψ as shown in Fig. 5.29. In this case, due to the low momentum a charge asymmetry in all the parameters is observed. For $\Delta\theta$, values around $\sim \pm 1.5$ mrad are found for large and small sectors with prominent peaks and fluctuations over all the η values. For $\Delta z_0 \sin\theta$ the asymmetry is higher than for the Z resonance with values of about ± 6 mm. The slope is observed in the barrel region with peaks in the intermediate region. As mentioned, J/ψ results with MSOE tracks are not good in resolution and for low momentum the magnetic field and multiple scattering effects in the material play an important role that until now have not been considered. Further investigation and extension of work at low p_T are necessary. However, the analysis of MS/ID residuals using $J/\psi \to \mu\mu$ concludes at this point, with subsequent results focusing exclusively on $Z \to \mu\mu$.
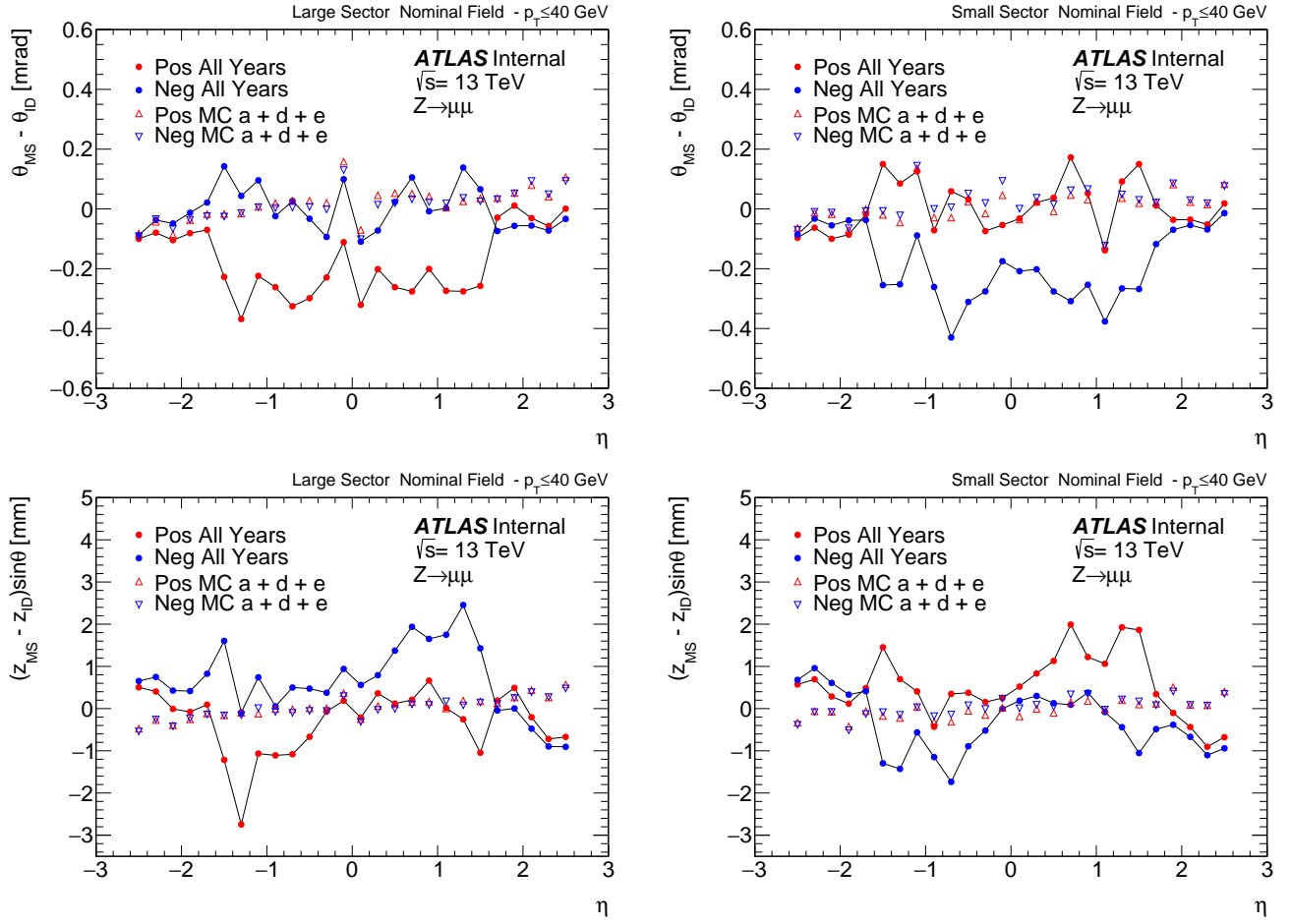
Figure 5.28: MS/ID residual profiles for (top) $\Delta\theta$ and (bottom) $\Delta z_0 \sin\theta$ in $Z \to \mu\mu$ for (left) large and (right) small sectors at $p_T < 40$ GeV.
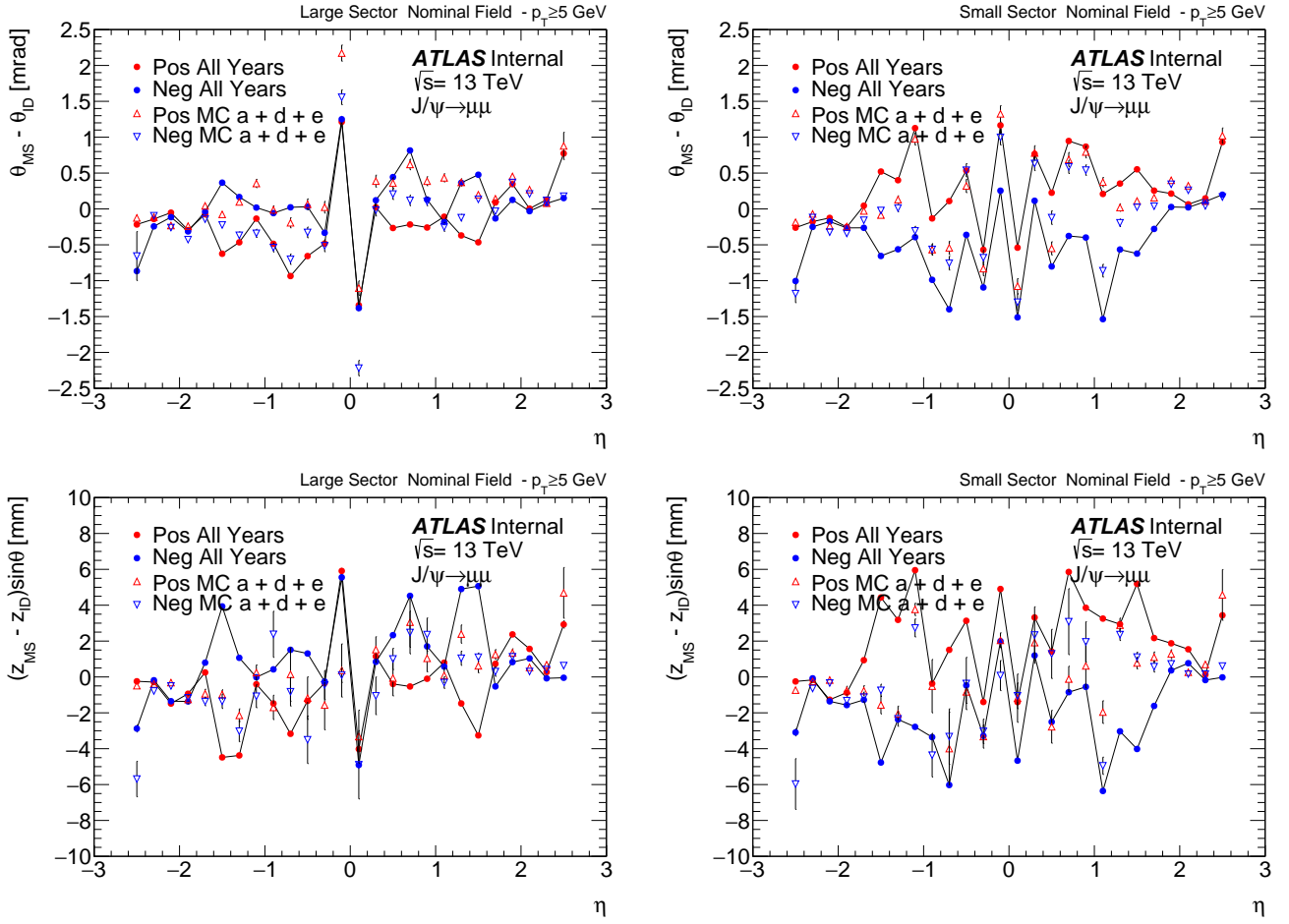
Figure 5.29: MS/ID residual profiles profiles for (top) $\Delta\theta$ and (bottom) $\Delta z_0 \sin\theta$ in $J/\psi \to \mu\mu$ for (left) large and (right) small sectors at $p_T > 5$ GeV.

5.6 Magnetic field residuals

The magnetic field in the ATLAS detector presents significant challenges for modelling and track reconstruction. The solenoid map is well-understood and characterized by relatively small uncertainties in contrast to the magnetic field in the toroid region that has larger uncertainties. However, the magnetic field in the tile calorimeter (TileCal) requires careful study due to potential mismodelling related to the material in this region. One initial indication of this issue is the need to compute the magnetic field in the tile calorimeter region using the Biot-Savart law, specifically accounting for an iron contribution within the girder of approximately 0.1 meters in width. An overestimation of the magnetic field in this region could be contributing to the observed charge asymmetry.

To determine if the MS/ID residuals could be linked to magnetic field mismodelling, it is necessary to study the charge-dependent effects to map regions where the magnetic field effects might be overestimated. This section focuses on the connection between the MS/ID residuals, charge-dependent effects, and their relation to the magnetic field, as well as their origin. Previous studies [166] of the magnetic field modelling have provided insights into significant uncertainties and potential overestimations of field strength in specific regions, possibly related to material issues. To study the impact of the magnetic field strength in the track reconstruction a study with modified magnetic fields is carried out. For this, a track extrapolation of the muons is performed and an adjustment of the $B_\phi-$strength in the girder region is obtained to remove the charge asymmetry.

5.6.1 Large and small sectors transition

Results showed that the mean values of the bias for positive and negative muons are inverted when these are obtained in the large and small sectors, indicating that a possible inversion in the large to small sectors is happening. To further investigate this, Fig. 5.30 shows the B_ϕ component of the magnetic field covering large and small sectors a how the field lines flow in this region near the tile calorimeter. The direction of the $B_\phi-$field map changes from the large sector to the small sector and the toroidal part near to the tile calorimeter shows a different direction. Zooming in the girder region around $R \simeq 4.2$ m (Fig. 5.30b), the B_ϕ magnitude is not constant but the field strength

could be taken as $B \sim 0.7$ T over ~ 10 cm.
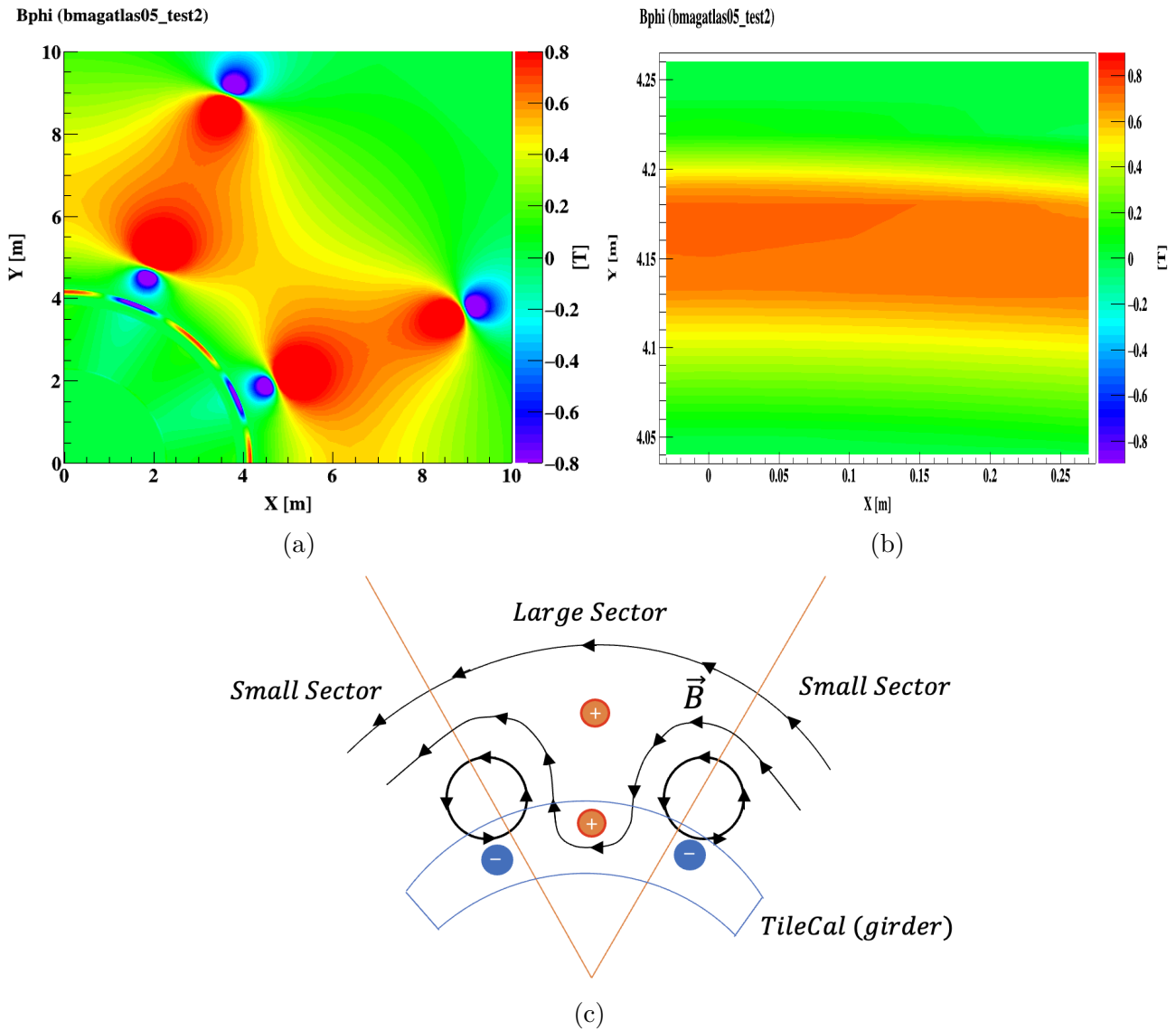
Figure 5.30: (a) B_ϕ component of the magnetic field in ATLAS detector. (b) Zoom of the B_ϕ component of the magnetic field around the girder region. (c) Sketch of the magnetic field flux through large and small sectors.

Taking this into account and using a simplified scheme of a charged particle in the muon spectrometer (Fig. 5.31) is possible to obtain the variation in the angle and the distance as a function of the magnetic field,
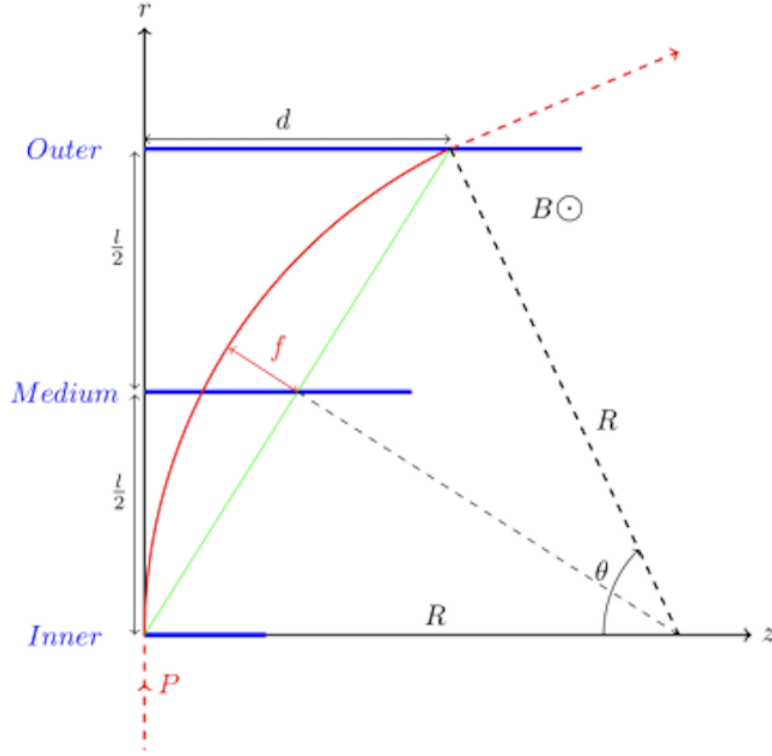
Figure 5.31: Simplified scheme of a charge particle crossing the muon spectrometer.

$$\delta\theta = \frac{0.3 \cdot q \cdot B(x) \cdot \delta x}{p},$$

$$d^B = 0.3 \frac{q}{p} \int_{in}^{out} (L - x) \cdot B(x) \cdot dx,$$

(5.18)

where $\delta\theta$ corresponds to the misalignment in θ, d^B is the total deflection due to the magnetic field, $B(x)$ is the magnitude of the field, L is the size of the muon spectrometer, q is the electric charge, p is the magnitude of the momentum and 0.3 is a constant with units GeV/Tm.

Using Eq. (5.18) and taking into account an average $\langle p_T \rangle = 20.46$ GeV, the obtained order of magnitude is $\delta\theta \sim$ mrad and $d^B \sim \pm 6$ mm. Previous results in the residuals showed deviations of about ± 1.5 mm, which implies a rough correction of the magnetic field of 25% in the girder region, i.e. 0.1 meters where the magnetic field is around 0.7 T. This gives one of the first clues about the relation between the magnetic field and the MS/ID residuals and where to focus for correcting the charge asymmetry. At the same time, Eq. (5.18) shows that the misalignment parameters are in an

inverse proportion with the momentum, such that for low momentum $\delta\theta$ and d^B increase, as shown in subsection 5.5.2.

This *toy model* allows to provide a simplified explanation to the charge asymmetry and the momentum dependency. Moreover, the sector transition form large sectors to small sectors is observed in Fig. 5.30a and the scheme in Fig. 5.30c, where the magnetic field lines flow in one direction and when it crosses from one sector to another (small to large for example), these are inverted around the toroid coil in the girder region. In this way, the muons with a given electric charge would experiment an inversion of the B_ϕ−field direction, switching from one sector to the other giving the profiles in Fig. 5.27.

5.6.2 Correction of the charge asymmetry

Results show that a modification of the magnetic field around the girder region is required. This implies to quantify the correction to modify the magnitude of the field only int the B_ϕ component (either increasing or decreasing) when the muon goes into the tile calorimeter girder.

The strategy is the following: Once the muons are produced, the tracks are propagated to the muon spectrometer using the nominal magnetic field. Once the muon reaches the MS, the backward track is performed from the entrance of the muon spectrometer back to the interaction point, following a modified magnetic field. Then, the magnetic field strength is adjusted to remove the charge dependency and finally the track parameters are recomputed as shown in Fig. 5.32a. The work scheme is shown in Fig. 5.32b.

Here, the track reconstruction is performed only using the equations of motion inside the magnetic field, such that material of any kind was not considered. Stochastic processes and multiple scattering in the calorimeter were not taken into account. Only the magnetic field effects in the MSOE tracks are studied.

5.6.3 Modification of the magnetic field in the girder region

A simplified evaluation of Eq. (5.18) showed that to reduce the bias in the residual misalignement parameters, a modification of the magnetic field in the girder region is needed. Here, the girder
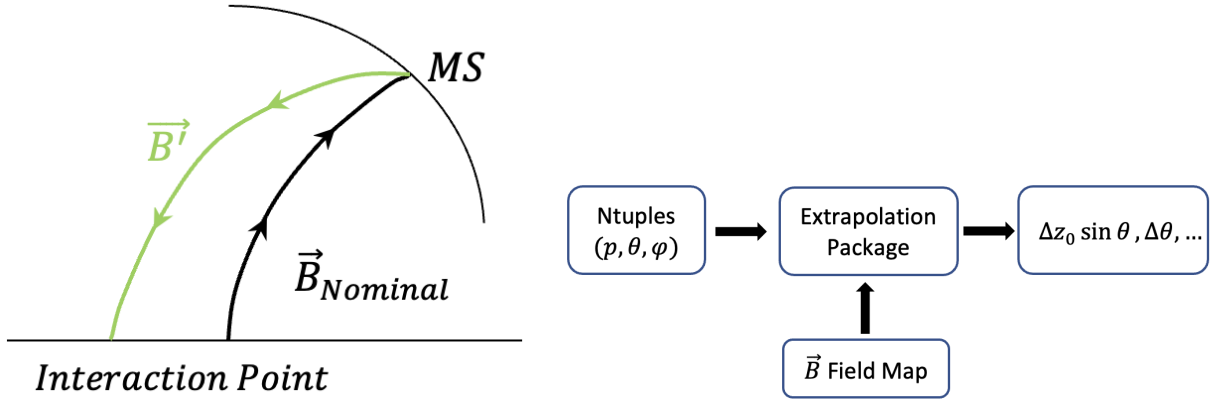
(a) Forward and backward extrapolation scheme.

(b) Work scheme for the track extrapolation and magnetic field modification.

Figure 5.32: Work strategy for the implementation of the magnetic field and track extrapolation.

is defined in the volume covered by $R(m) \in [4, 4.23]$ and $|z| < 6.92\,m$, i.e. $|\eta| < 1.3$. Within this volume, the nominal magnetic field is modified in the $B_\phi-$component and the backward track extrapolation is performed using the modified field.

The magnetic field models implemented in the present work are shown in Fig. 5.33, where the nominal field corresponds to the no modified magnetic field, $1.25 \times B_\phi$ is the nominal magnetic field increased by 25% while $0.75 \times B_\phi$ is the nominal magnetic field decreased by 25%. The magnetic field "bmagatlas05" has not been modified but it contains a different iron contribution for the Biot-Savart calculation in the girder region. For bmagatlas05 the lamination calculations for different layer permeability is chosen while for the nominal field the homogenization permeability with a non diagonal matrices is used (μ_r, μ_z, μ_ϕ).

5.6.4 Misalignment residuals for modified magnetic fields

After the implementation of the magnetic field maps, the following results for the Z resonance are obtained. For $\Delta\theta = \theta_{MS} - \theta_{ID}$ the results for $p_T > 40$ GeV and $p_T < 40$ GeV are shown in Fig. 5.34 and 5.35, respectively. At high p_T, the increasing effect of the magnetic field in the girder region leads to a reduction of the asymmetry in the barrel region while for lower magnetic field $(0.75 \times B_\phi)$ the effects are increased. The correction shows a good result in the large sectors where the asymmetry is higher while for the small sectors, a 25% correction enhances the bias. This allows to conclude that
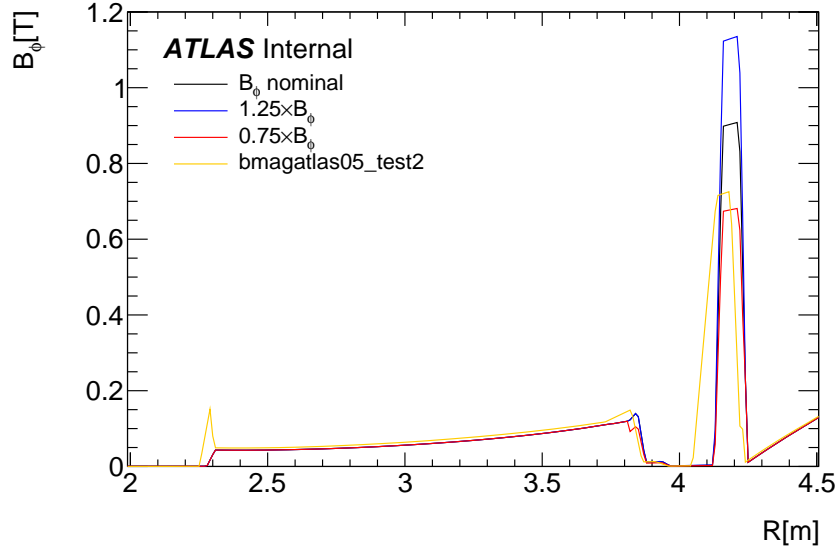
Figure 5.33: Modifications of $\pm 25\%$ in the nominal $B_\phi-$component of the magnetic field and bmagatlas05.

both large and small sectors require a different treatment in the correction magnitude of B_ϕ. These results point out that to correct the charge asymmetry an increment of the magnetic field strength is needed. On the other hand, bmagatlas05 provides a better treatment of the charge asymmetry compared to the nominal field. However, in the intermediate region $1 < |\eta| < 1.7$ the magnetic field shows a higher asymmetry that produces two prominent peaks, effect that is small with the other maps.

At low p_T, all the effects are highlighted producing larger asymmetries and peaks as shown in Fig. 5.35. Nevertheless, $1.25 \times B_\phi$ modification works for large sectors in the barrel region as well as bmagatlas. This needs a better treatment for small sectors since the results are not well corrected in the expected region.

For the longitudinal impact parameter $(z_{MS} - z_{ID})\sin\theta$ the results for $p_T > 40$ GeV and $p_T < 40$ GeV are shown in Figures 5.36 and 5.37, respectively. These show that increasing the magnetic field in the girder region leads to a reduction of the asymmetry in the barrel with better results in the large sectors than the small sectors where the magnetic field strength needs to be reduced below 25%. The opposite behavior is obtained when the magnetic field is decreased in the girder region giving as result an increment in the asymmetry effect. Both analysis indicates that increasing the
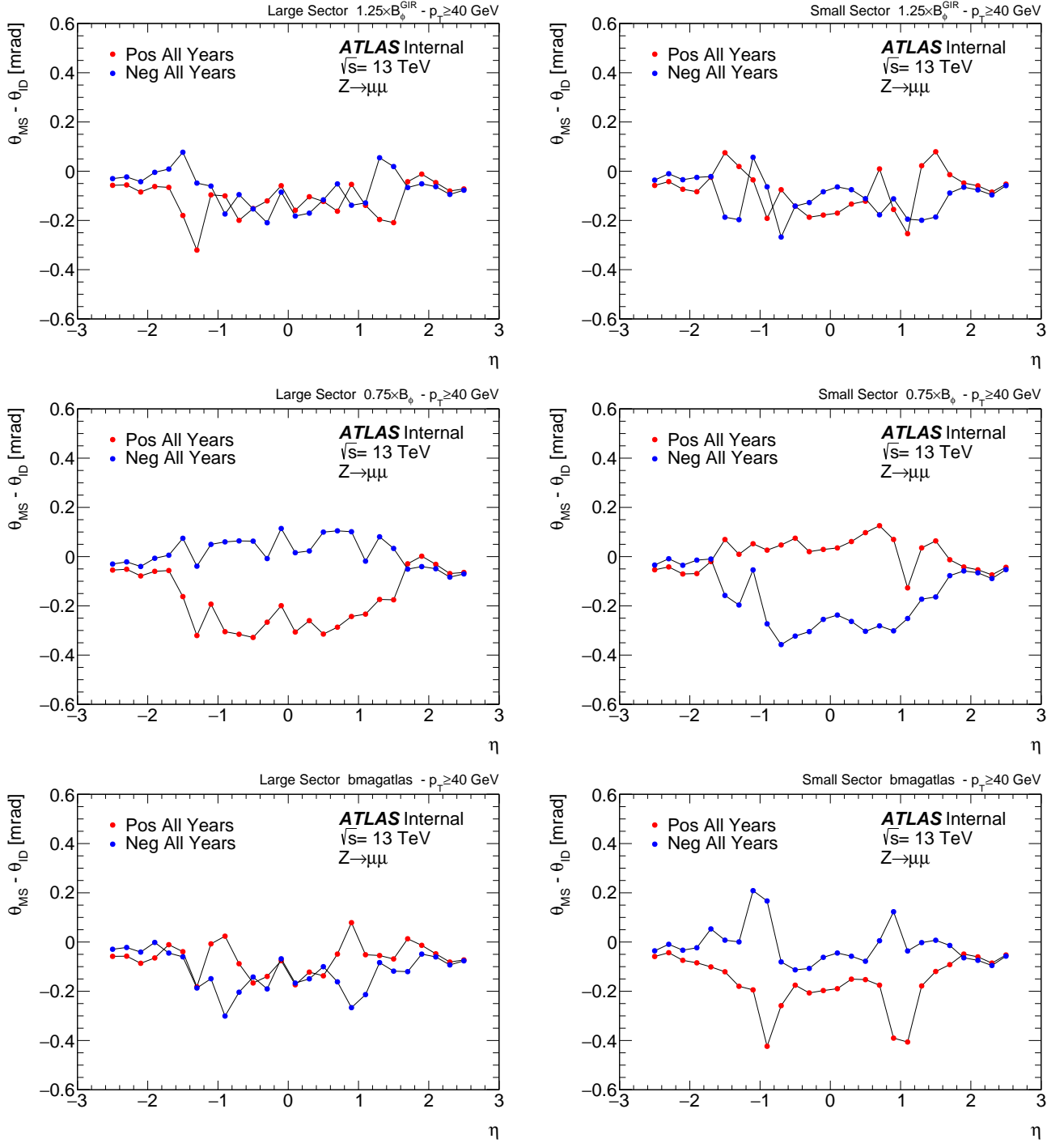
Figure 5.34: MS/ID residual $\Delta\theta$ profiles for (top) $1.25 \times B_\phi$, (middle) $0.75 \times B_\phi$ and (bottom) bmagatlas magnetic field maps in $Z \to \mu\mu$ for (left) large and (right) small sectors at $p_T > 40$ GeV.
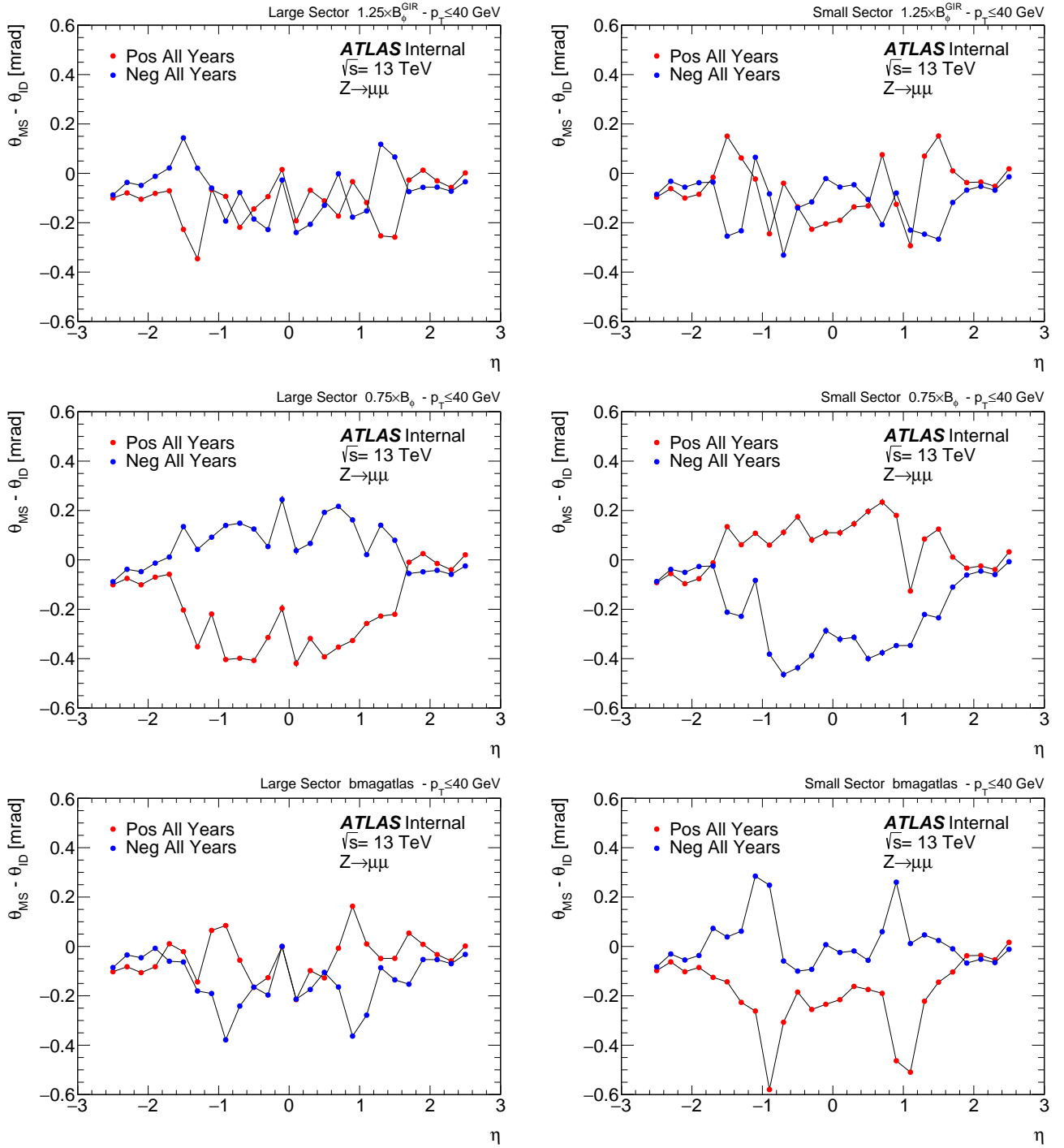
Figure 5.35: MS/ID residual $\Delta\theta$ profiles for (top) $1.25 \times B_\phi$, (middle) $0.75 \times B_\phi$ and (bottom) bmagatlas magnetic field maps in $Z \to \mu\mu$ for (left) large and (right) small sectors at $p_T < 40$ GeV.

magnetic field strength, B_ϕ, is the correct approach.

On the other hand, the bmagatlas results are promising with a good correction for the asymmetry effect in the barrel region. However, the same effect appearing in $\Delta\theta$ is observed for $1 < |\eta| < 1.7$ where the asymmetry is highlighted and two prominent peaks appear. Although this effect is greater in the small sector it is also present in the large sector but in a lower amount, as well as the nominal field.

The obtained results showed that by increasing the magnetic field in the girder region both $\Delta\theta$ and $\Delta z_0 \sin\theta$ charge dependent effects are partially solved. This indicates that the magnetic field in the tile calorimeter needs to be re-evaluated with a correction factor between 1 and 1.25, while for $|\eta| > 1$ a different approach is needed. This correction does not allow to solve the slope effect observed in $\Delta z_0 \sin\theta$.

5.6.5   Sector dependency and correction maps

The correction described shows that the observed effects are sector dependent, this means the correction for large and small sectors is not the same. While for Large sectors 25% shows an improvement, for small sectors the factor needs to be smaller, around $10\% - 15\%$. These results show an impact in the barrel region and the $\Delta z_0 \sin\theta$ asymmetry could be studied sector by sector for $|\eta| < 0.9$. It is convenient to define $\langle \Delta z_0 \sin\theta \rangle^\pm$ as the average of the difference of the mean values between μ^+ and μ^- that quantifies the asymmetry level for every sector. If there is not asymmetry, $\langle \Delta z_0 \sin\theta \rangle^\pm$ should be zero for every sector. Results for the nominal magnetic field and the 25% modification for $p_T > 40$ GeV and $p_T < 40$ GeV are shown in Fig. 5.38

For $p_T > 40$ GeV, the average $\langle \Delta z_0 \sin\theta \rangle^\pm$ changes from large to small sectors but the values are similar sector by sector in the large and small sectors as shown in Fig. 5.38. The average asymmetry for large sectors corresponds to 0.74 mm while for small sectors a value of 0.67 mm is found, indicating that the larger deviations are produced in the large sectors than the small ones. Once the 25% correction is applied, $\langle \Delta z_0 \sin\theta \rangle^\pm$ gets close to zero and the same fluctuations sector by sector are present. In general, the average value for large sectors after correction is 0.06 mm and for small sectors is -0.08 mm. Such that the correction for small sectors is pulling considerably low
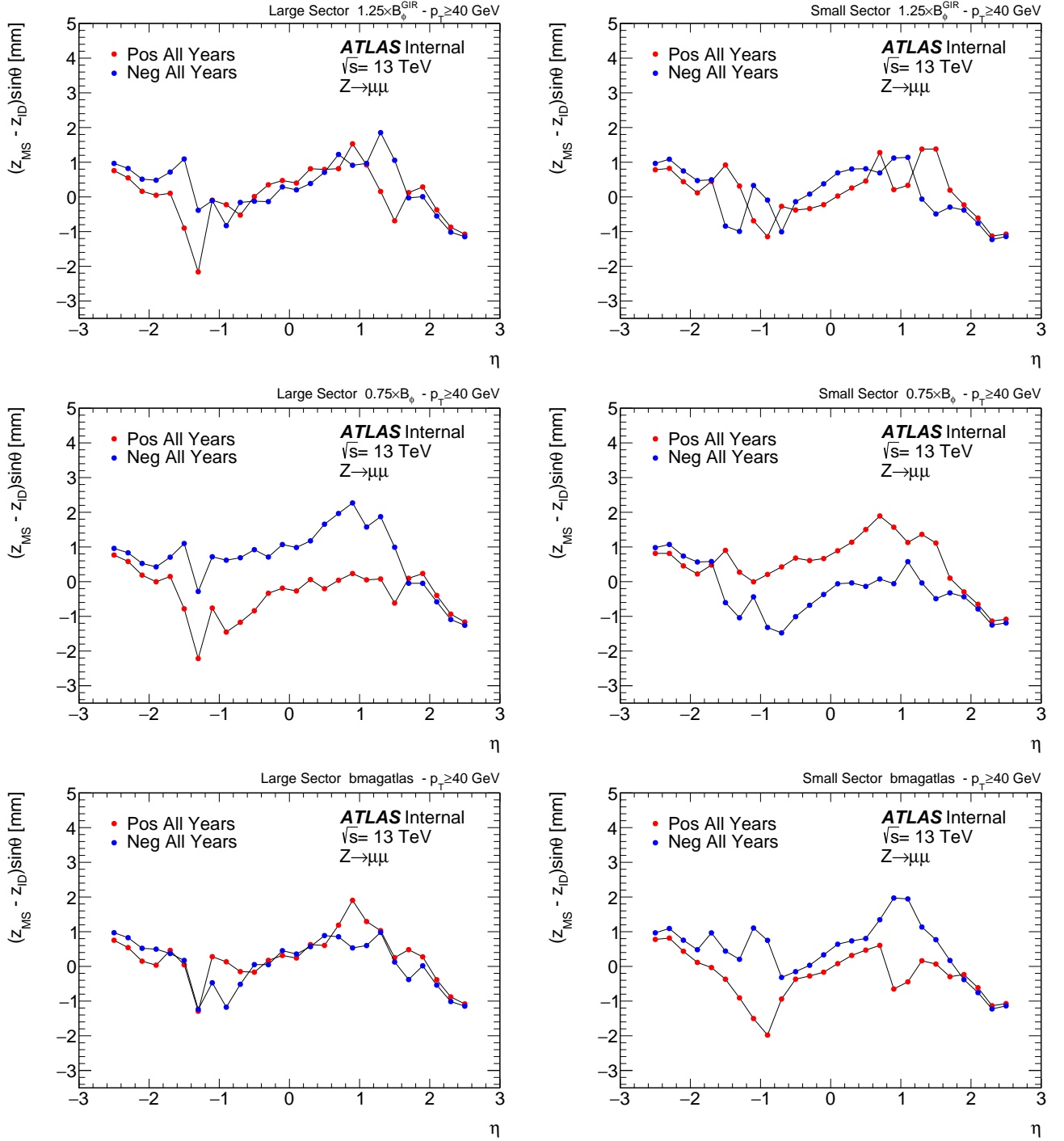
Figure 5.36: MS/ID residual $\Delta z_0 \sin\theta$ profiles for (top) $1.25 \times B_\phi$, (middle) $0.75 \times B_\phi$ and (bottom) bmagatlas magnetic field maps in $Z \to \mu\mu$ for (left) large and (right) small sectors at $p_T > 40$ GeV.
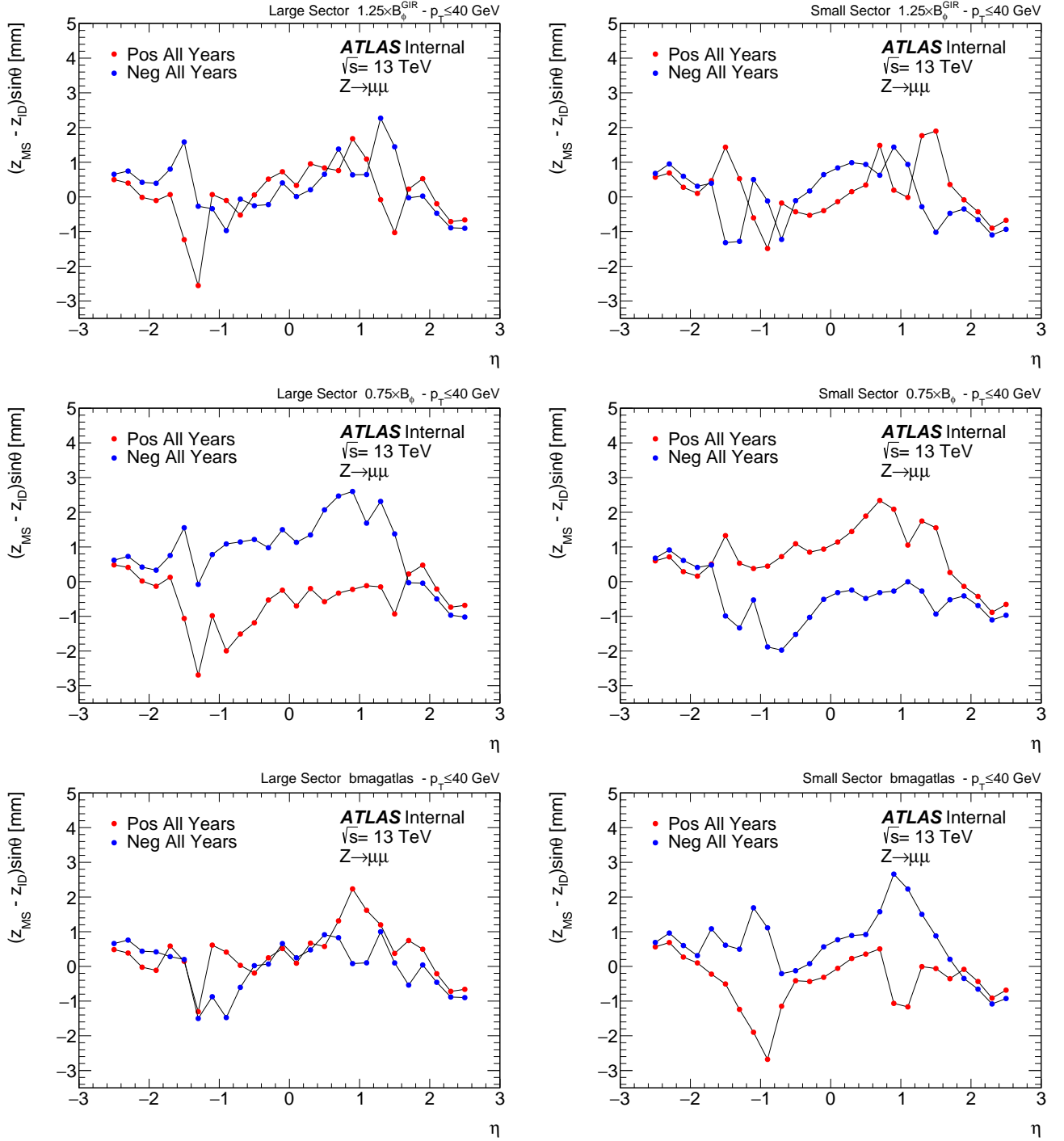
Figure 5.37: MS/ID residual $\Delta z_0 \sin\theta$ profiles for (top) $1.25 \times B_\phi$, (middle) $0.75 \times B_\phi$ and (bottom) bmagatlas magnetic field maps in $Z \to \mu\mu$ for (left) large and (right) small sectors at $p_T < 40$ GeV.

and it needs to be less than 25%.
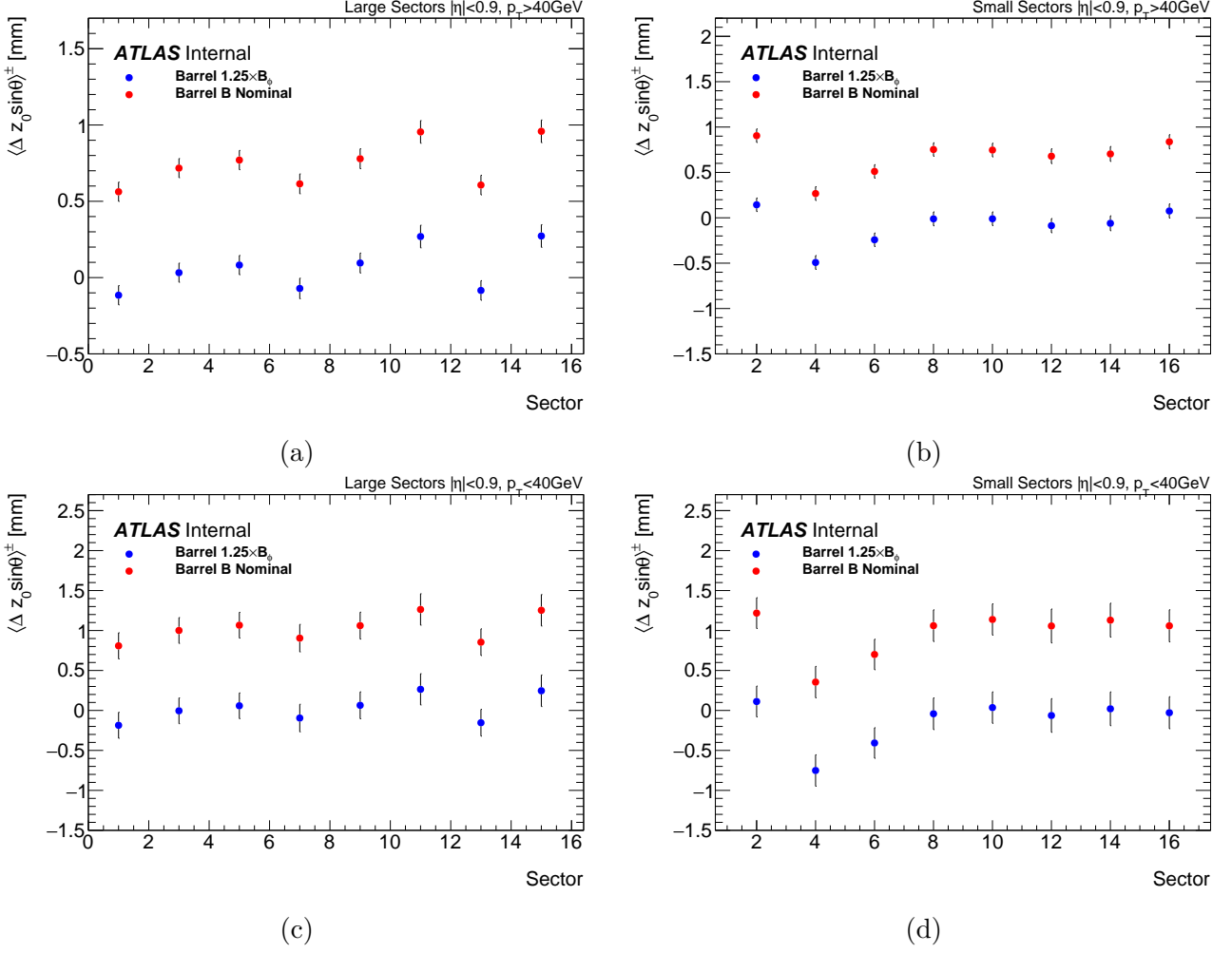
Figure 5.38: $\langle \Delta z_0 \sin \theta \rangle^{\pm}$ vs. Sector number for (left) large and (right) small sectors with (top) $p_T > 40$ GeV and (bottom) $p_T < 40$ GeV.

In the low momentum case, $p_T < 40$ GeV, the asymmetry increases such that $\langle \Delta z_0 \sin \theta \rangle^{\pm}$ is expected to be greater than for high p_T. Fig. 5.38 shows that the values for large and small sectors are different but almost similar in all the large sectors and all the small sectors, respectively. The average $\langle \Delta z_0 \sin \theta \rangle^{\pm}$ value found for large sectors corresponds to 1.02 mm and 0.96 mm for small sectors. Once the correction in the magnetic field is applied the asymmetry is reduced to an average of 0.02 mm in the large sectors and -0.14 mm for small sectors. This is in agreement with Figures 5.36 and 5.37, where the $1.25 \times B_\phi$ modification works better for large sectors than for small sectors and an adjustment of correction the factor has to considered.

Fig. 5.38 show that in average the misalignment residual behave similar for all large sectors

and all small sectors. Therefore, to study the behavior is enough to take a portion of the detector covering both one large sector and one small sector. This allows to compute the parameters by portions of the detector and then these portions can be folded to increase the statistics, then a final correction could be derived. In this way, a map that contains all the information for $(\phi, \eta, \Delta z_0 \sin\theta)$ can be obtained.

In principle the two variables $\Delta\theta$ and $\Delta z_0 \sin\theta$ are variables of interest but the effects in both cases are similar. However, $\Delta z_0 \sin\theta$ contains the systematic shape (slope effect) that provides extra information and for that reason is better to map it in η and ϕ space. For this, the η space is binned using 50 bins with 0.1 resolution between $\eta \in [-2.5, 2.5]$ while for ϕ, 45 bins with 1 degree resolution in $\phi \in [0, 45°]$ is used. This region for ϕ is considered since it contains 1 large sector and 1 small sector. To increase the statistics, the p_T cut is lowered to $p_T >20$ GeV and two regions of the detector are considered, top region and bottom region. This is done to distinguish the region containing the feet that hold the detector[2].

By this procedure, a 2D map for positive and negative muons in the top region and bottom region of the detector are obtained as shown in Fig. 5.39 with a detailed description of its content in Fig. 5.40. The Y axis (ϕ rad) describes the transition effect from large to small sectors for every value of η. The X axis (η axis) describes all the information contained in the 1D profiles until now. The slopes appearing from ECT to Barrel transition and the peaks in the intermediate region $1 < |\eta| < 1.7$. The Z axis corresponds to the misalignment parameter $\Delta z_0 \sin\theta$ and it shows the MS/ID residual mean value for every (ϕ_i, η_j).

In principle, results from top and bottom regions should be similar due to the symmetry of the detector. Nevertheless, this is not the case since larger deviations in the bottom region are observed (white region for values larger than 3.5 mm) located at $1 < |\eta| < 1.7$. For this reason, the results are focused on the top region since it does not contain extra material. Fig. 5.39 shows those residuals that after correction should be set to zero.

---

[2]The bottom region contains the feet that hold the detector and other kind of material that were not considered in the analysis.

(a) Top region μ^+

(b) Top region μ^-

(c) Bottom region μ^+
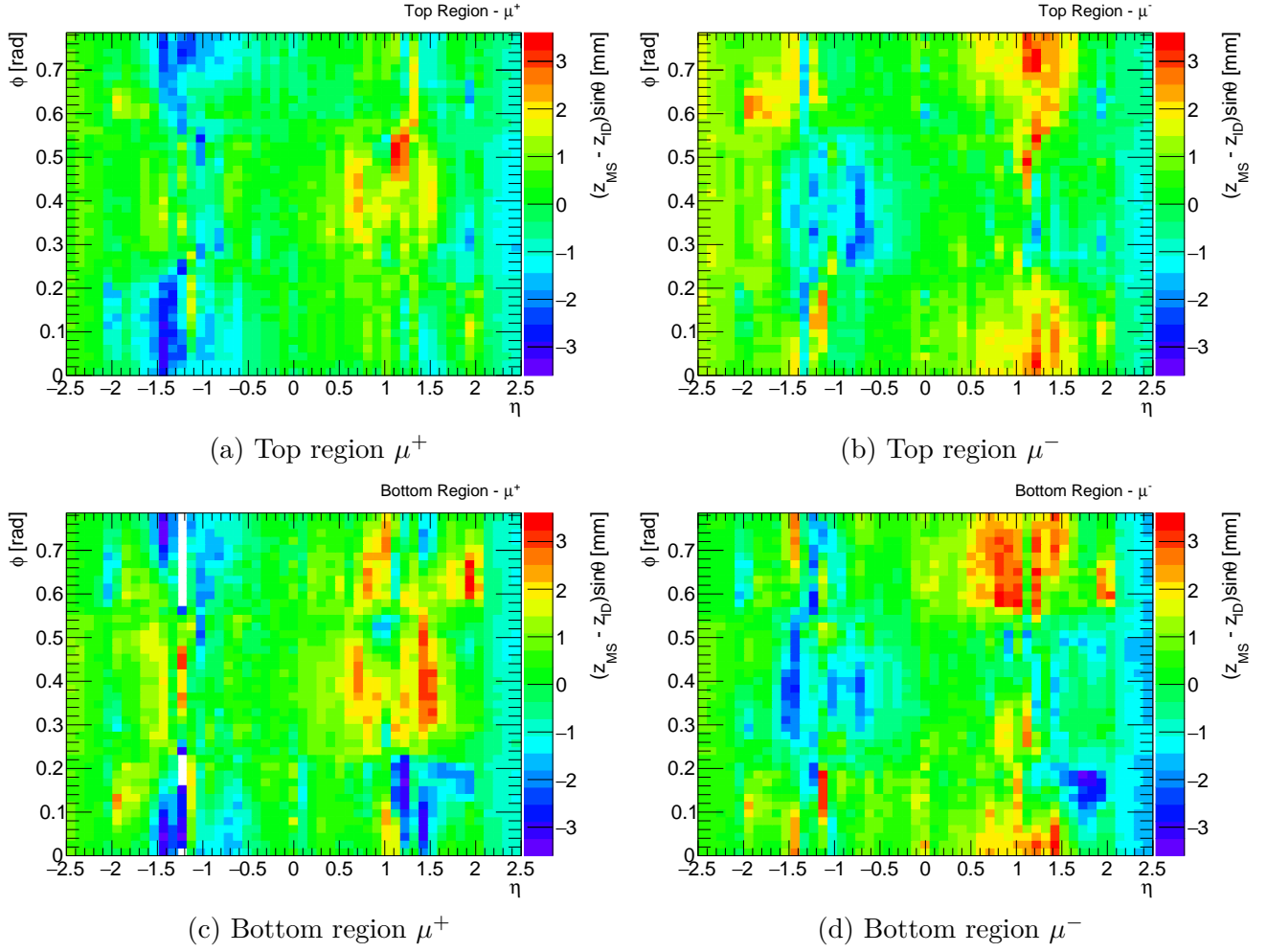
(d) Bottom region μ^-

Figure 5.39: MS/ID ϕ, η map for the misalignment parameters in the top and bottom regions for $p_T > 20$ GeV.
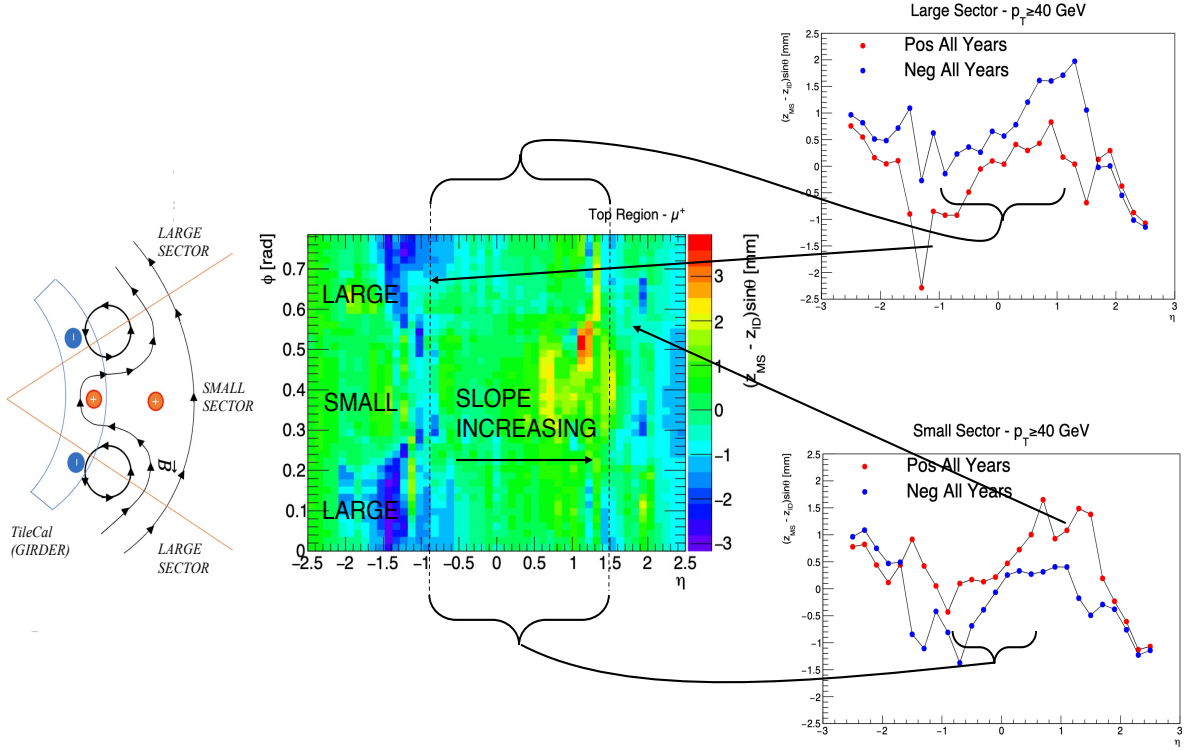
Figure 5.40: Analysis of the misalignment 1D profiles and 2D maps for the top region for positive muon.

5.6.6 Magnetic field correction map

The misalignment parameters were shown to be ϕ, η, B_ϕ and p_T dependent and the $\Delta z_0 \sin\theta$ parameter has been mapped as shown in Fig. 5.39. To determine a relation between the previous map and the magnetic field in the girder region, a magnetic field mapping in (ϕ, η)−space is obtained as shown Fig. 5.41. These results could be linked through a relation as shown in Eq. (5.18) where B is considered as the field strength in the girder region.

To quantify the asymmetry level between the two muons, an asymmetry map can be obtained by subtracting the maps for negative and positive muons in Fig. 5.39. This quantity is defined as,

$$\delta z s_\theta^\pm = (z_{MS} - z_{ID}) \sin\theta|_{\mu^-} - (z_{MS} - z_{ID}) \sin\theta|_{\mu^+}.$$

Which indicates those η values where the larger deviations take place. Similarly for θ it follows,

$$\delta\theta^\pm = (\theta_{MS} - \theta_{ID})|_{\mu^-} - (\theta_{MS} - \theta_{ID})|_{\mu^+}.$$

144
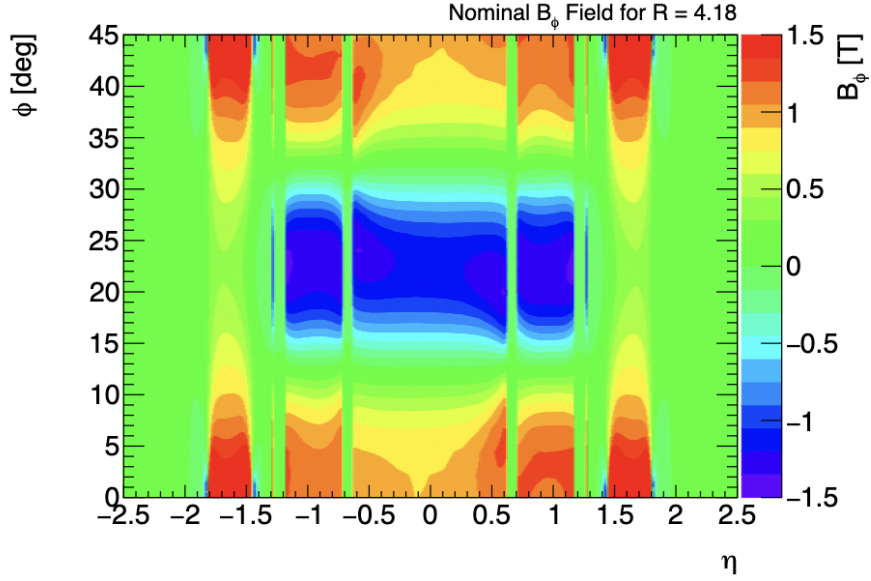
Figure 5.41: B_ϕ component of the magnetic field in the girder region at $R = 4.18$ m for nominal field.

Resulting 1D profiles and 2D maps are shown in Fig. 5.42. For the ECT region (forward and backward) the asymmetry is small such that a large correction is not needed. For $1 < \eta < 1.7$ values up to $\sim \pm 2$ mm are present and they decrease in the barrel region to values around $\sim \pm 0.5$ mm. In ϕ, η space, results show a similar structure as the magnetic field map in Fig. 5.41 with the greater asymmetries located in the intermediate and barrel regions. In a similar way, there is a discrepancy between the top and bottom asymmetries where the larger values are found in the bottom part of the detector for the reasons already explained.

Using the asymmetry maps a correction can be derived that once applied in Fig. 5.42 is capable to set the misalignment values to zero for every (ϕ, η) pair. A first trial is by implementing the $1.25 \times B_\phi$ modified field where the asymmetry parameters are re-computed with results in Fig. 5.43. This correction works in the barrel region with a better yield in the large sectors ($\phi[\text{rad}] \in [0, 0.2] \cup [0.6, 0.78]$) while for the small sectors ($\phi[\text{rad}] \in [0.2, 0.6]$) the correction factor needs to be reduced. Something to take into account is that the larger deviations are in the intermediate regions where the correction does not have a great effect. The ECT does not require a strong correction since the asymmetry is small as shown in the 1D profiles of Fig. 5.43.

The same study was carried out using bmagatlas with results in Fig. 5.44. In this case, the
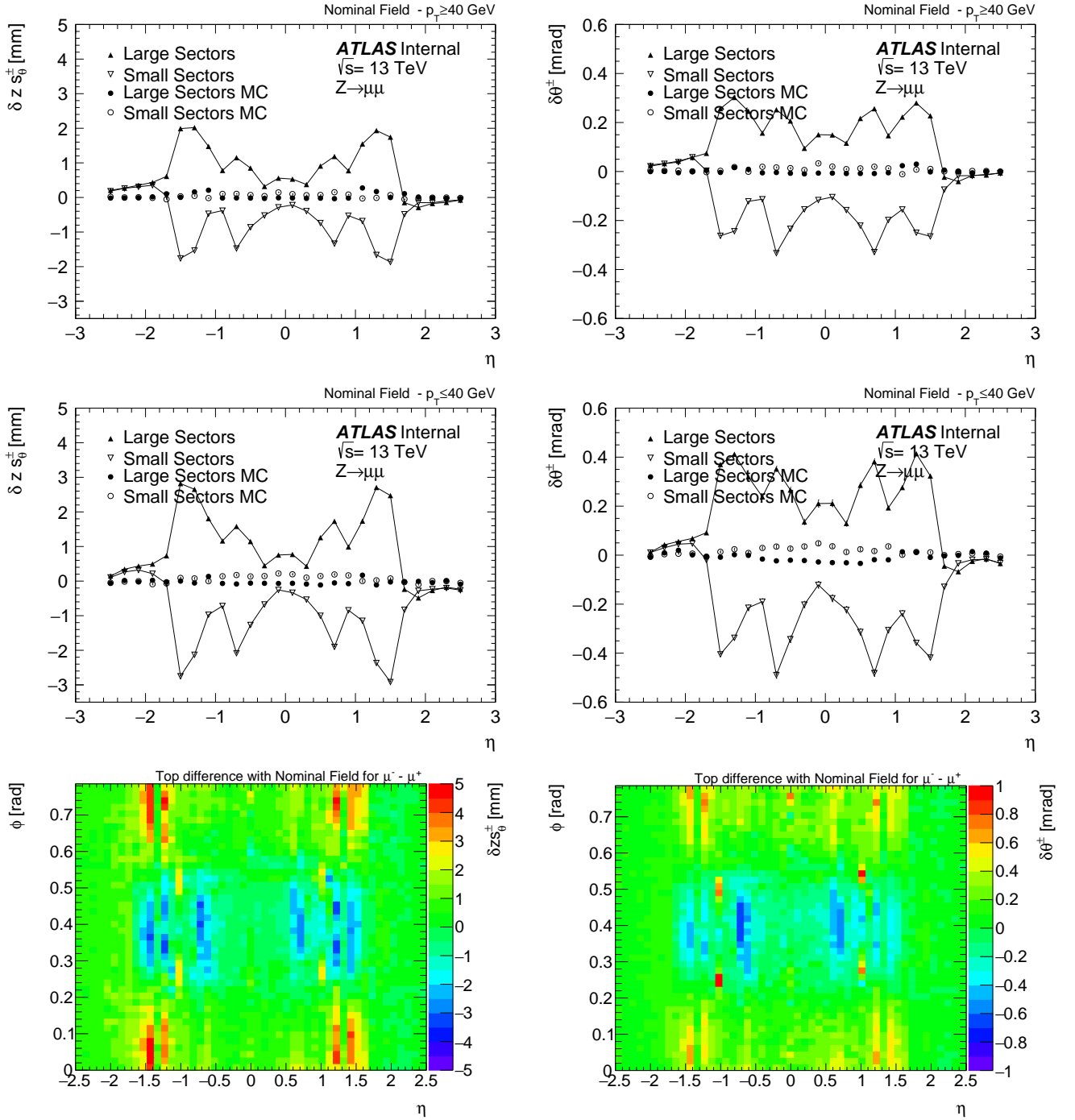
Figure 5.42: Asymmetry 1D profiles and 2D top region maps for $\delta z s_\theta^\pm$ and $\delta \theta^\pm$ for $\mu^- - \mu^+$ using nominal magnetic field with (top) $p_T > 40$ GeV, (middle) $p_T < 40$ GeV and (bottom) $p_T > 20$ GeV. 2D bottom region maps are shown in appendix Fig. A.1.
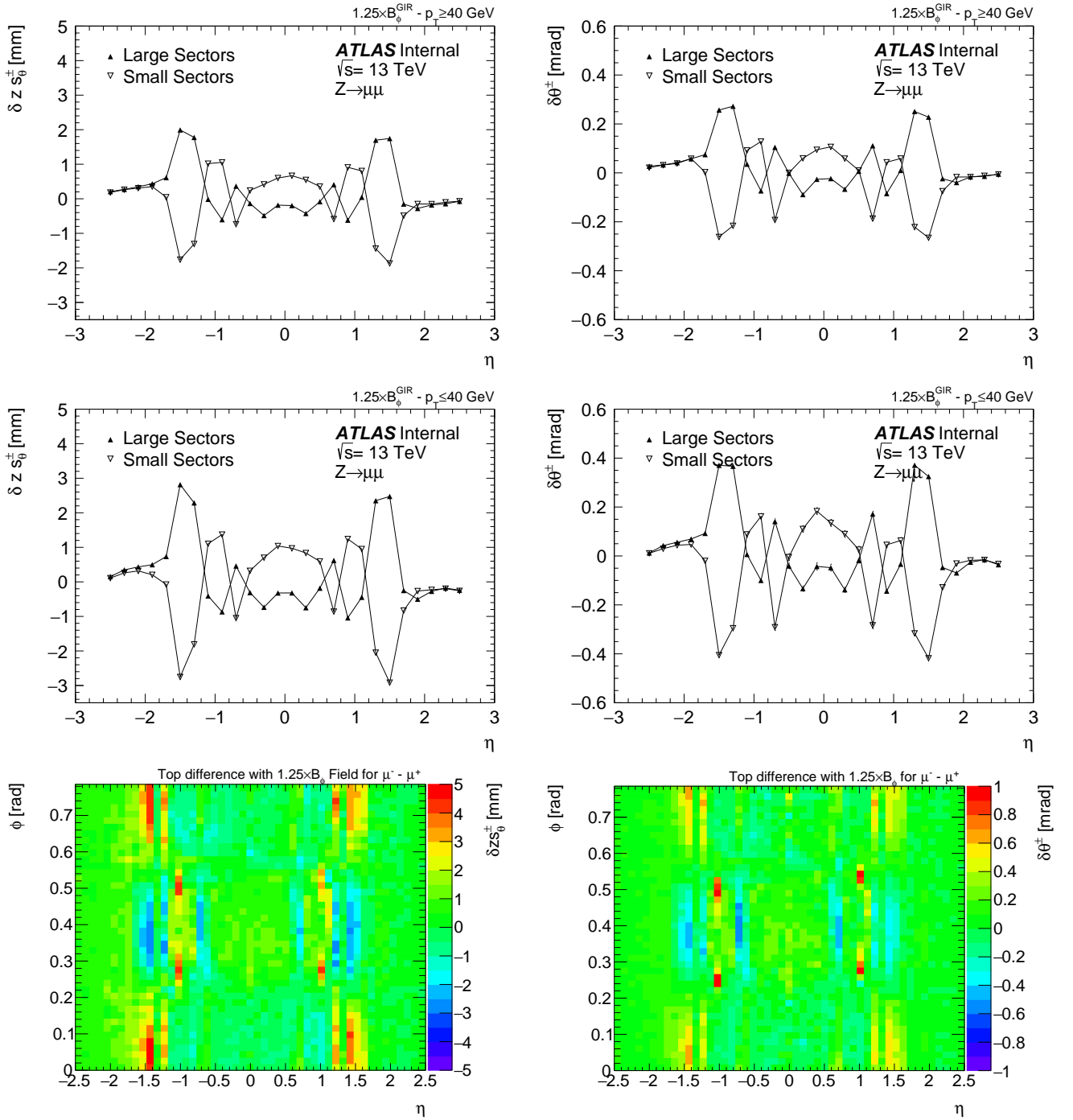
Figure 5.43: Asymmetry 1D profiles and 2D top region maps $\delta z s_{\theta}^{\pm}$ and $\delta\theta^{\pm}$ for $\mu^{-} - \mu^{+}$ using $1.25 \times B_{\phi}$ modified magnetic field with (top) $p_T > 40$ GeV, (middle) $p_T < 40$ GeV and (bottom) $p_T > 20$ GeV. 2D bottom region maps are shown in appendix Fig. A.2

asymmetry is corrected more effectively in the barrel region for large sectors but for the small sectors the correction is as good as for the $1.25 \times B_\phi$ correction. However, bmagatlas gives place to two prominent peaks in the intermediate regions producing larger deviations.

5.6.7 Residual magnetic field correction map

The implemented toy model for the magnetic field in the backward extrapolation shows that is possible to improve the track reconstruction using an effective model. Nevertheless, this correction is considered in a specific region of the Tile Calorimeter, this is, the girder of approximately 10 cm. To correct properly the charge asymmetries a dedicated mapping of the magnetic field residuals, $\delta B(x)$, is needed. To estimate it, the first equation in (5.18) for the deflection in θ is used. This equation allows to determine the deflection $\delta\theta$ of the muon track due to the magnetic field $B(x)$. Using the data, the "residual magnetic field $\delta B(x)$" that gives place to the observed misalignment can be derived as,

$$\delta B(x) = \frac{\delta\theta}{0.3 \cdot \delta x} \cdot \frac{p}{q}. \tag{5.19}$$

This expression is only for one muon with charge q. To express $\delta B(x)$ as a function of the asymmetry quantities is convenient to compute the "residual $\int B_\phi dl \equiv \delta B(x) \cdot \delta x$" taking into account both muons, Eq. (5.19) can be expressed as,

$$\delta B(x) \cdot \delta x = \frac{\delta\theta^\pm}{0.3} \cdot \frac{\langle p^+ \rangle \cdot \langle p^- \rangle}{\langle p^+ \rangle + \langle p^- \rangle}, \tag{5.20}$$

where $\langle p^\pm \rangle$ is the average momentum of $\mu^\pm$ and $\delta\theta^\pm = (\theta_{MS} - \theta_{ID})|_{\mu^-} - (\theta_{MS} - \theta_{ID})|_{\mu^+}$. Using Eq. (5.20) the magnetic field can be corrected over a full track length of a muon to the MS. Since the "theoretical magnetic field map" is available from simulation, the theoretical $\int B_\phi dl$ can be determined and using this, it is possible to map those regions where the asymmetries are taking place. Therefore, the following dimensionless correction map in $(\eta, \phi)-$space can be computed,

$$\alpha_{\eta\phi} = \left(\frac{\delta B(x) \cdot \delta x}{\int B_\phi dl} \right)_{\eta\phi}, \tag{5.21}$$
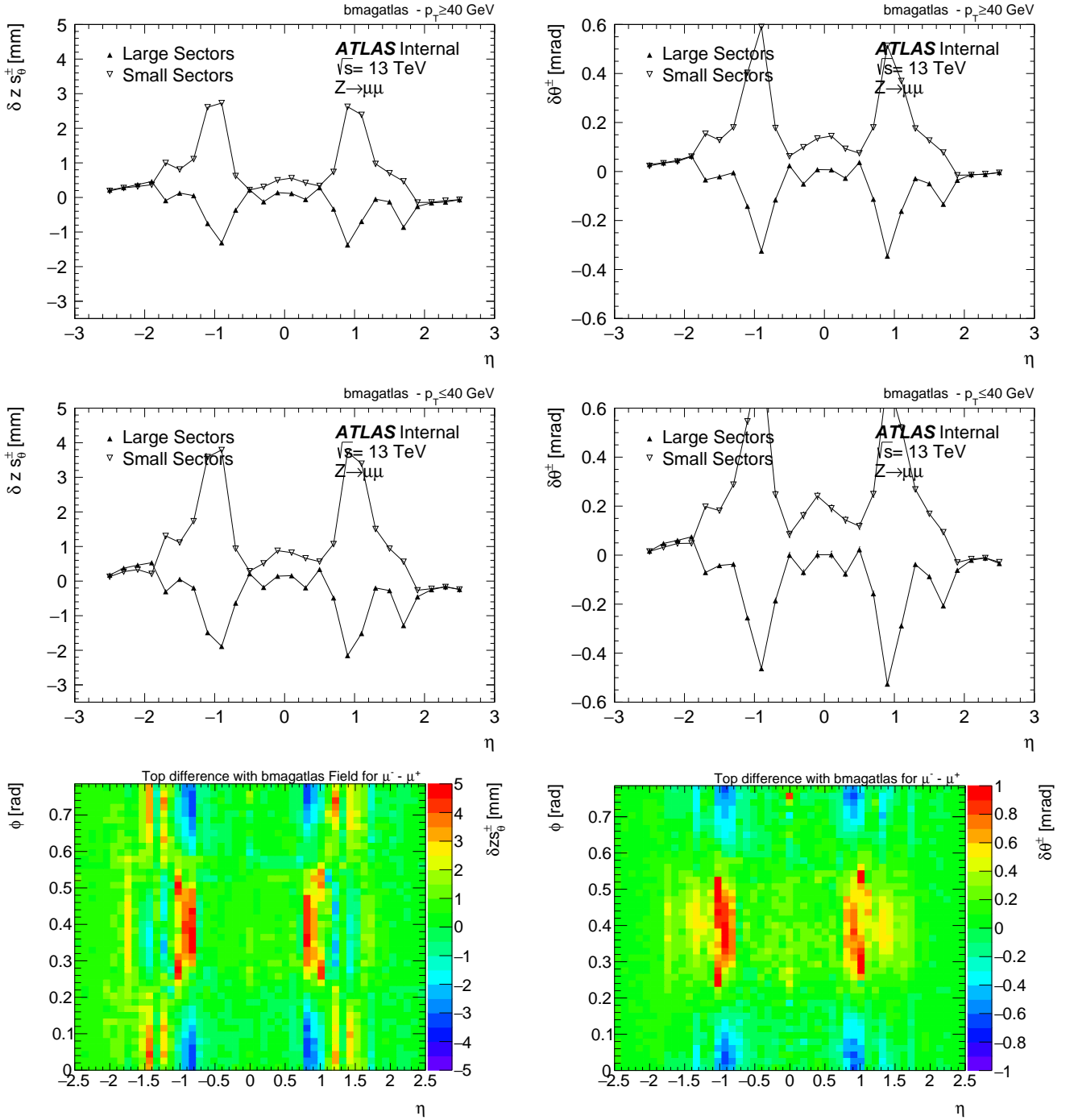
Figure 5.44: Asymmetry 1D profile and 2D top region maps $\delta z s_\theta^\pm$ and $\delta\theta^\pm$ for $\mu^- - \mu^+$ using bmagatlas field with (top) $p_T >$40 GeV, (middle) $p_T <$40 GeV and (bottom) $p_T >$20 GeV. 2D bottom region maps are shown in appendix Fig. A.3.

that is zero for those regions where no correction is needed $\delta B = 0 \Rightarrow \alpha_{\eta\phi} = 0$. The correction map is shown in Fig. 5.45 where a $\sim 20\%$ factor is applied in the barrel region, $|\eta| < 1$, as described in the toy model. Moreover, the $\alpha_{\eta\phi}-$map provides a new set of values that would be able to correct the intermediate region where the larger values take place and they are difficult to reduce. Notice that these result is valid over a full track in the tile calorimeter volume.
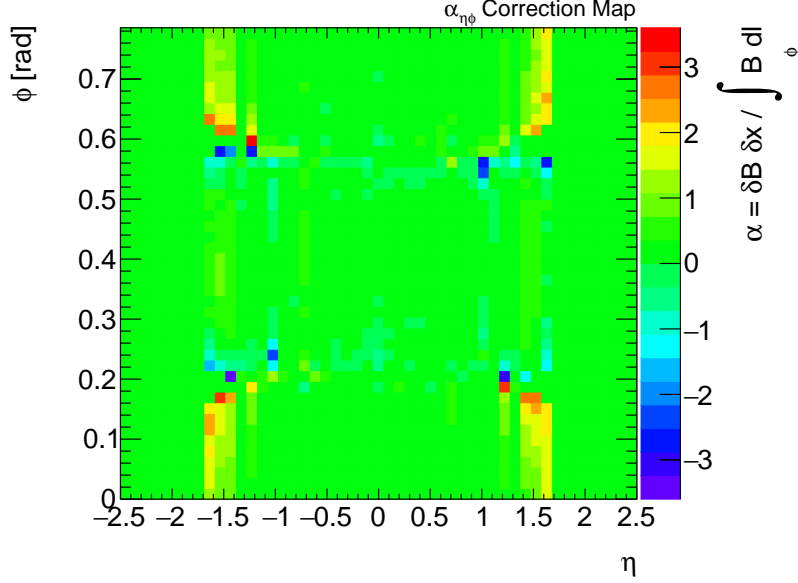
Figure 5.45: $\alpha_{\eta\phi}$ correction map for a given muon track valid in the Tile Calorimeter $R(m) \in [0, 4.36]$ and $z(m) \in [-6.92, 6.92]$.

To correct the magnetic field, a linear model is considered, as follows,

$$B'_\phi = (1 + \alpha_{\eta\phi}) \cdot B_\phi(x). \tag{5.22}$$

After correction, the new magnetic fields as a function of the radius are shown in Fig. 5.46.

After correction, the 1D profiles of the misalignment parameters in Fig. 5.27 are re-computed for $p_T > 40$ GeV as shown in Fig. 5.47 where an improvement compared to the previous results is obtained. In this case, the correction is working for both large and small sectors in the barrel region. Moreover, this correction is also taking into account those values for which $|\eta| > 1$. The peaks appearing in the intermediate region are highly reduced in both misalignment parameters.

Once the charge dependency in the misalignment profiles has been studied and corrected, the next quantity to look at is the asymmetry $\delta z s_\theta^\pm$, $\delta\theta^\pm$ in the large and small sectors (averaged in
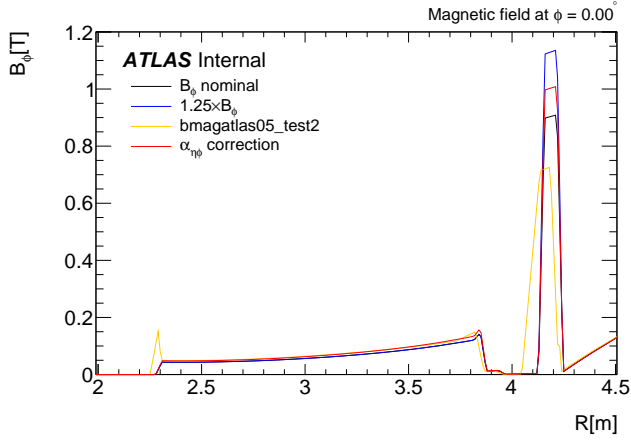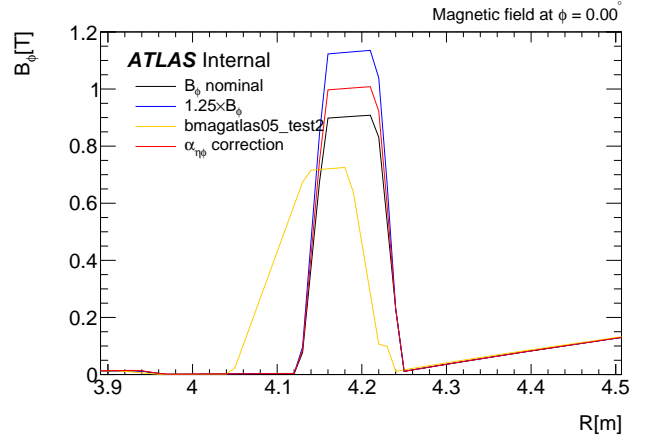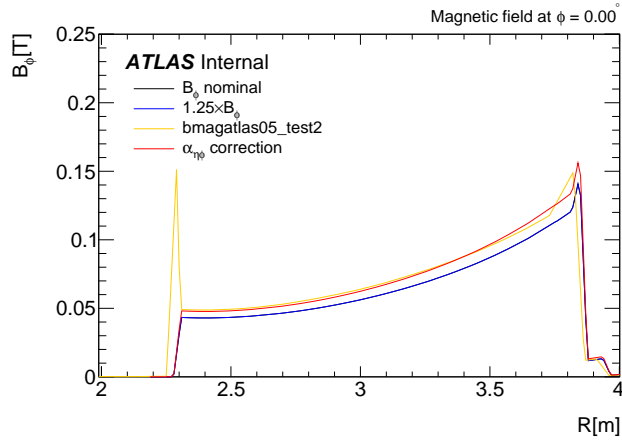
Figure 5.46: B_ϕ component of the magnetic field in the tile calorimeter for different implemented models in (a) $R(m) \in [2, 4.5]$, (b) $R(m) \in [3.9, 4.5]$ and (c) $R(m) \in [2, 4]$.
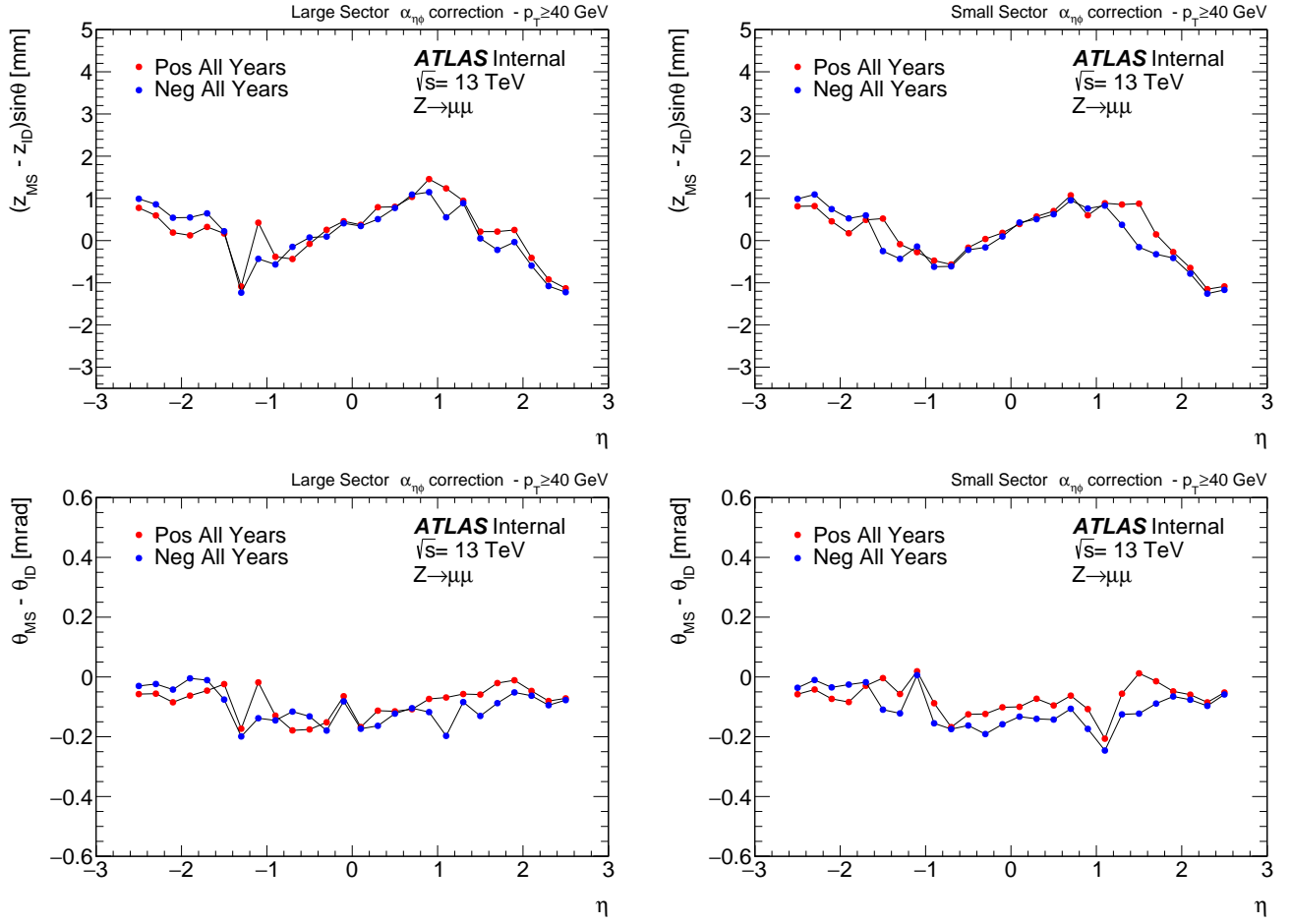
Figure 5.47: MS/ID residual profiles for (top) $\Delta z_0 \sin \theta$ and (bottom) $\Delta \theta$ vs η after correction in $Z \to \mu\mu$ for (left) large and (right) small sectors with $p_T > 40$ GeV.

ϕ) and 2D maps in (η, ϕ)−space, these are shown in Fig. 5.48. After correction, results show a considerably improvement compared to the initial results in Fig. 5.42. The new correction is capable to manage both large and small sectors in such a way that the asymmetry is set to almost zero in the barrel as well as in the intermediate region.

5.7   Bias in d_0, ϕ and relation to z_0

In the residual misalignment parameters, the charge dependent effects were covered by a magnetic field mismodelling and an effective correction allowed to solve the charge asymmetry in the barrel region. However, an explanation for the origin and behavior of the systematic shape (slope) and bias observed in the 1D profiles of $\Delta z_0 \sin \theta$ and $\Delta \theta$ (Fig. 5.21) and 2D maps (Fig. 5.39) has not been provided. In the following section a possible explanation that could originate the slope is proposed. The following consider that a RPC strips displacement in the Muon Spectrometer could induce a bias in the second coordinates d_0 and ϕ measured by the RPC that later on produces a second order bias effect in z_0 and θ that are translated into the systematic shapes and biases observed.

5.7.1   RPC strips displacement

A simplified Muon Spectrometer (MS) scheme with the $R − z$ plane (left) and the transverse $x − y$ plane (right) is shown in Fig. 5.49. On what follows, two tracks are taken into account, the Unbiased Track with an Unbiased point of closest approach (p.o.c.a) (blue) and the Biased Track with a biased p.o.c.a (red) produced by a Muon in the detector. For simplicity only one Resistive Plate Chamber (RPC) located at the Barrel Outer (BO) is considered. The RPC (Yellow) represents the RPC displaced in the second coordinate[3], this means, in "the local $x − y$ plane" that gives the biased track. The RPC (Green) corresponds to the RPC without displacement that should measure the unbiased track.

Using this setup two points of view take place when the tracks are reconstructed. In the $R − z$ plane (left panel of Fig. 5.49) both tracks Unbiased Track and Biased Track are overlap since both

---

[3]The second coordinate is a local frame in the RPC but for simplicity the second coordinates are considered to be in the $x − y$ plane.
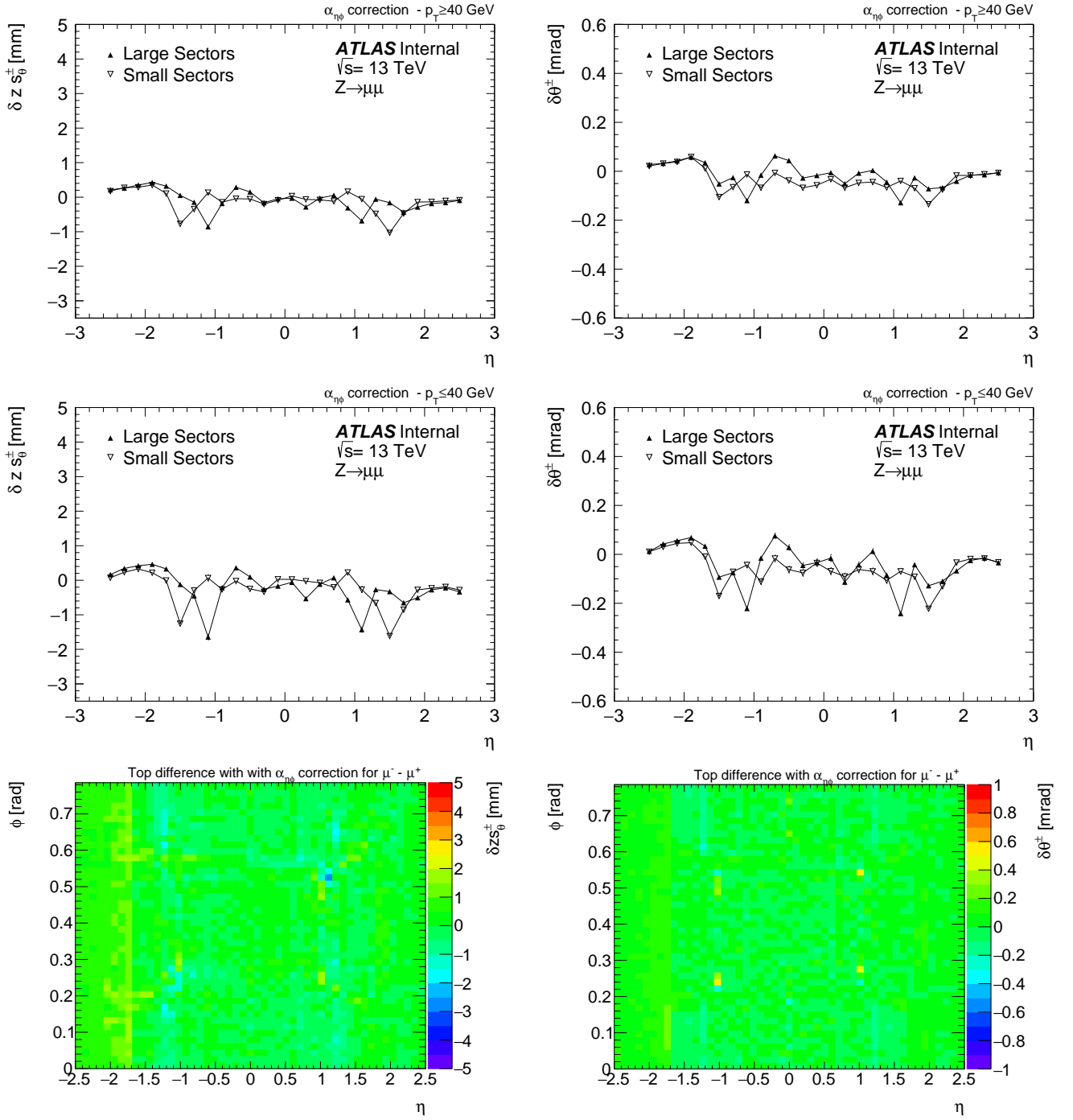
Figure 5.48: Asymmetry maps $\delta z s_\theta^\pm$ and $\delta\theta^\pm$ for $\mu^- - \mu^+$ after correction with (top) p_T >40 GeV, (middle) p_T <40 GeV and (bottom) p_T >20 GeV. 2D bottom region maps are shown in appendix Fig. A.4.
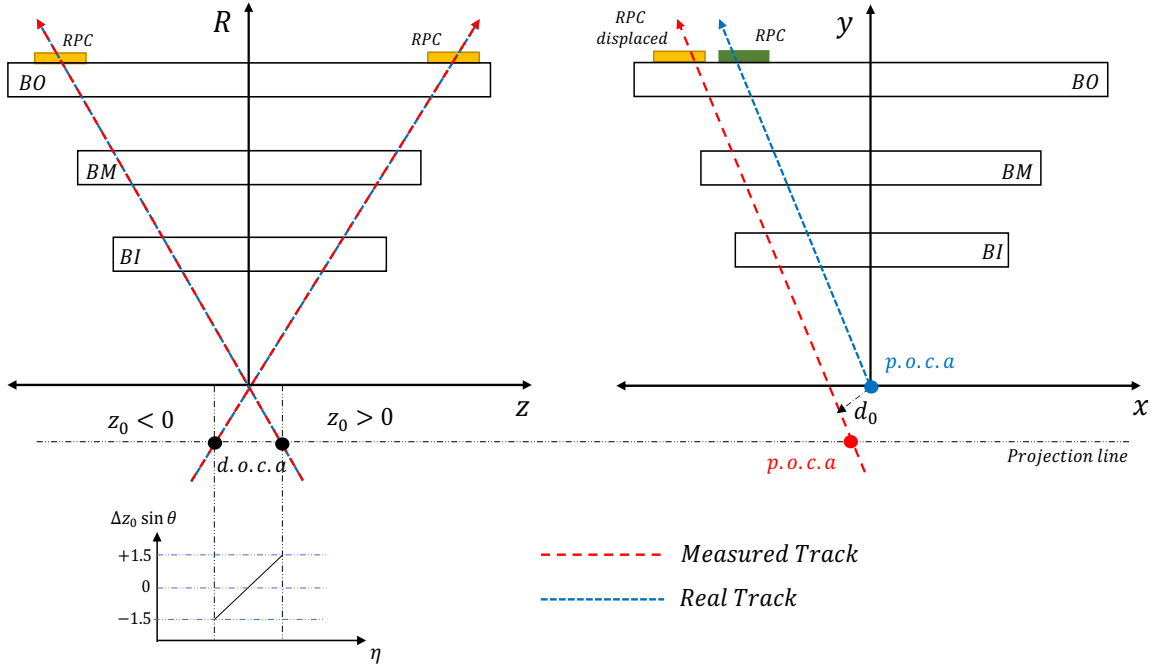
Figure 5.49: Sketch for the bias in the second coordinate d_0 that could originate the bias in the z_0 for (left) longitudinal $R - z$ plane and (right) transverse $x - y$ plane.

RPC displaced and RPC corrected are located in the same position[4]. Therefore, the reconstruction is performed without any bias. On the other hand, if the RPC is displaced in the second local coordinate of the $x - y$ plane (right panel of Fig. 5.49) the tracks are reconstructed in a different way. Since the Biased Track is reconstructed using the displaced RPC the point of closest approach (p.o.c.a) will also carry a bias. To avoid this, the Unbiased Track should be reconstructed by the no displaced RPC that ensures a non-biased p.o.c.a .

Finally, considering a projection of this bias into the $R - z$ plane (dotted bottom line), it shows that when the z_0 coordinate is measured by the distance of closest approach (d.o.c.a) in the $z-$axis, the bias in the $x - y$ plane induces a displacement from the correct position in z_0, and a bias in the θ angle is also induced. Therefore, when the track reconstruction is performed the values of z_0 are positive and negative and symmetric around zero. Once the z_0 distributions are retrieved and represented as a function of η, the profiles in Fig. 5.21 are obtained. This simplified scheme of a translation displacement in the RPC is capable to reproduce the systematic shape.

However, this is not the most general case, since if a translation plus rotation in ϕ for the

---

[4]The displacement is only in the local $x - y$ plane such that the $R - z$ plane is unbiased.

RPCs is introduced (Fig. 5.50) a more complex scenario takes place producing the systematic shape (slope) effect. Notice that to reproduce the bias in z_0 is enough to have only one bias in the second coordinate either d_0 or ϕ, or both (d_0, ϕ). These effects plus the magnetic field effects previously described should be able to reproduce the results in Fig. 5.24 as well as the maps in Fig. 5.39.
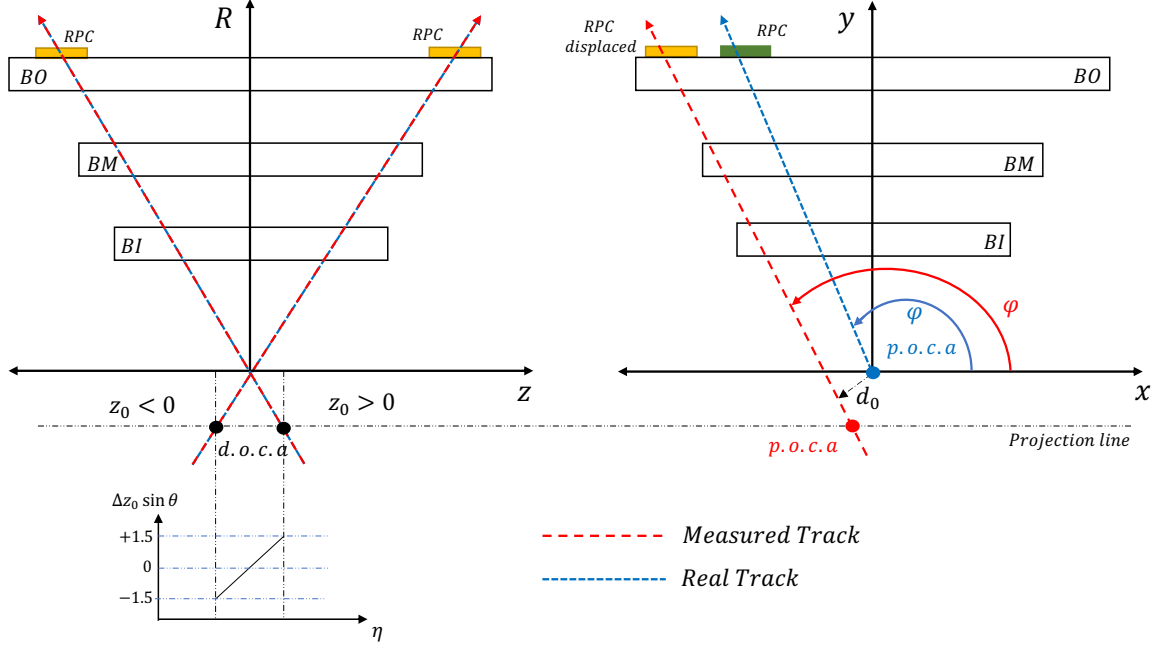
Figure 5.50: Sketch for the bias in the second coordinate d_0 and ϕ that could originate the bias in the z_0 for (left) longitudinal $R - z$ plane and (right) transverse $x - y$ plane.

This analysis shows that under the assumption of a displaced RPC, the slope and moreover, the bias in both z_0 and θ can be explained. The bias should be a **second order** effect, this means, the values in d_0 should be few cm to induce a few mm bias in z_0. Similarly for ϕ where the bias should be in the mrad scale but around two or three times greater than the bias in θ.

The idea of a "displaced RPC" does not imply necessarily a physical displacement of the RPC, this could go from a problem in the reconstruction software that is providing a bad reconstruction up to a physical displacement of few cm in the detector, this should be revisited. Moreover, the real scenario is more complicated since in reality there are several RPCs in the MS and not only one, such that the real effect is more complex than this simple scheme. This explanation is purely qualitative and to understand if there is a real bias in the second coordinates d_0, ϕ or both (d_0, ϕ)

156

a further analysis of this quantities is needed. For this, three regions are considered:

$$
\begin{cases}
\text{Barrel} & |\eta| < 1 \\
\text{Intermediate} & 1 < |\eta| < 1.7 \\
\text{ECT} & |\eta| > 1.7
\end{cases}
$$

such that the regions with greater deviations can be localized. Moreover, a sector by sector analysis is needed to understand the effect in each sector. Similarly to z_0 and θ, the residuals $d_0^{MSOE} - d_0^{ID}$ and $\phi^{MSOE} - \phi^{ID}$ in bins of ϕ_{ID} (in every sector) and for different η bins are computed.

5.7.2 Bias in d_0

Results for the barrel, intermediate and ECT are shown in Fig. 5.51. For the barrel a bias of about ± 1 cm for is observed with a systematic shape (positive slope) and a discontinuity around $\phi_{ID} = 0$. The origin of this discontinuity is not well understood in the scope of this work. For the intermediate region a bias is found with values up to ± 0.5 cm with a positive slope as for the barrel. In the ECT region, similar values for the bias are found to be around ± 0.5 cm and a negative slope with a discontinuity in the middle ($\phi_{ID} = 0$) of the sectors is also present. From the three regions the larger deviations are located in the barrel and they are reduced in the intermediate and ECT regions.

Similarly as for z_0 and θ a charge asymmetry is observed in the $d_0^{MSOE} - d_0^{ID}$ profiles with larger values in the middle of every sector and for the three regions, barrel, intermediate and ECT. However, the magnetic field effects and the bias in d_0 are independent effects that need different approaches. These results show that at least a d_0 bias is present and it can induce a second order effect of few mm in z_0.

5.7.3 Bias in ϕ

Results for the barrel, intermediate and ECT regions are shown in Fig. 5.52. The barrel region shows a bias in ϕ for values up to ~ -2 mrad with no systematic shape (slope) but with discontinuity in
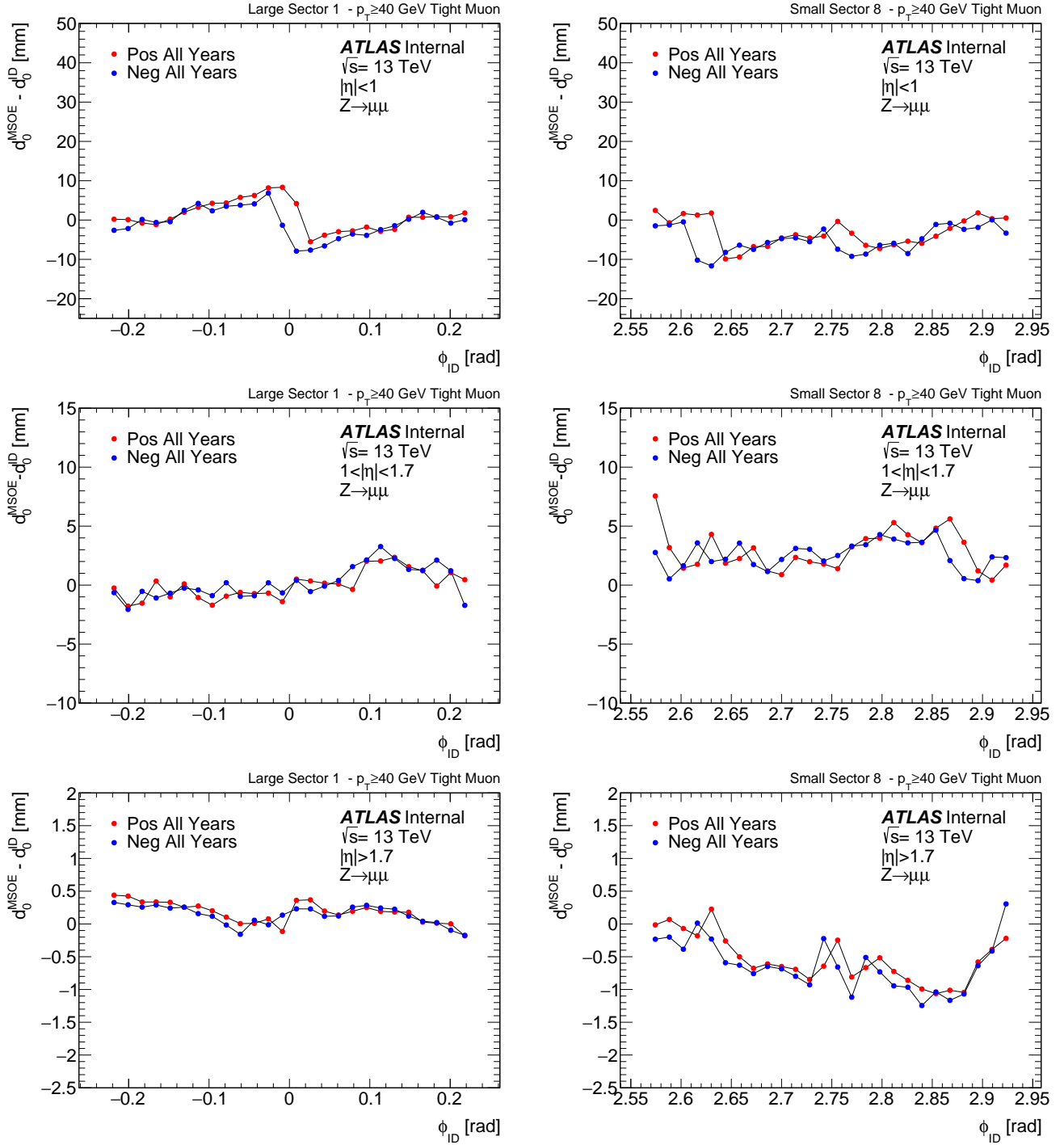
Figure 5.51: $d_0^{MSOE} - d_0^{ID}$ profiles for (top) barrel, (middle) intermediate and (bottom) ECT regions in $Z \to \mu\mu$ for (left) large and (right) small sectors at $p_T > 40$ GeV.

the middle of the sector, $\phi_{ID} = 0$. In the intermediate region, the bias takes values between $[-2, -1]$ mrad with signficant systematic shape and small discontinuity compared to the barrel region. In the ECT region several effects are present, the bias takes different values up to -2.5 mrad with a discontinuity located at the middle of the sector, $\phi_{ID} = 0$. The slope is present for both cases positive (increasing) and negative (decreasing). Similarly to $d_0^{MSOE} - d_0^{ID}$, the charge asymmetry is also present in the azimuthal residual. Notice that azimuthal angle residual have larger values compared to those related to the polar angle, $\theta^{MSOE} - \theta^{ID}$ and by consequence this can induced a second order effect.

Residuals obtained for the second coordinates showed that both d_0 and ϕ have a global bias, systematic shape and charge dependent asymmetry. These results could be explained by the model in Fig. 5.50. However, this results can not conclude if really the displacement of the RPCs is the origin of the systematic shape observed in z_0, such that a more exhaustive study is required.

5.8 Second coordinates correction maps

The present studies showed that effective corrections can be proposed to manage the misalignment parameters. For the charge dependent effects, z_0 and θ, a function parameterizing the effect of the magnetic field correction in the MS is proposed. For the neutral effects d_0 and ϕ (including z_0 and θ without charge effect), a correction based on the residuals charge-independent biases of the MS with respect to the ID can be proposed.

5.8.1 Correction maps for $d_0^{MSOE} - d_0^{ID}$ and $\phi^{MSOE} - \phi^{ID}$

To correct the bias in the second coordinates, d_0 and ϕ, the residual charge-independent biases, $d_0^{MSOE} - d_0^{ID}$ and $\phi^{MSOE} - \phi^{ID}$, are mapped with respect to the ID in (η, ϕ)−space. The purpose of this is to apply the magnetic field corrections to the MSOE tracks and then correcting for the final bias using the neutral maps. Notice that the magnetic field map correction modifies the B_ϕ component affecting only the first coordinates, z_0 and θ, such that for d_0 and ϕ, the correction should be propagated as a second order effect.
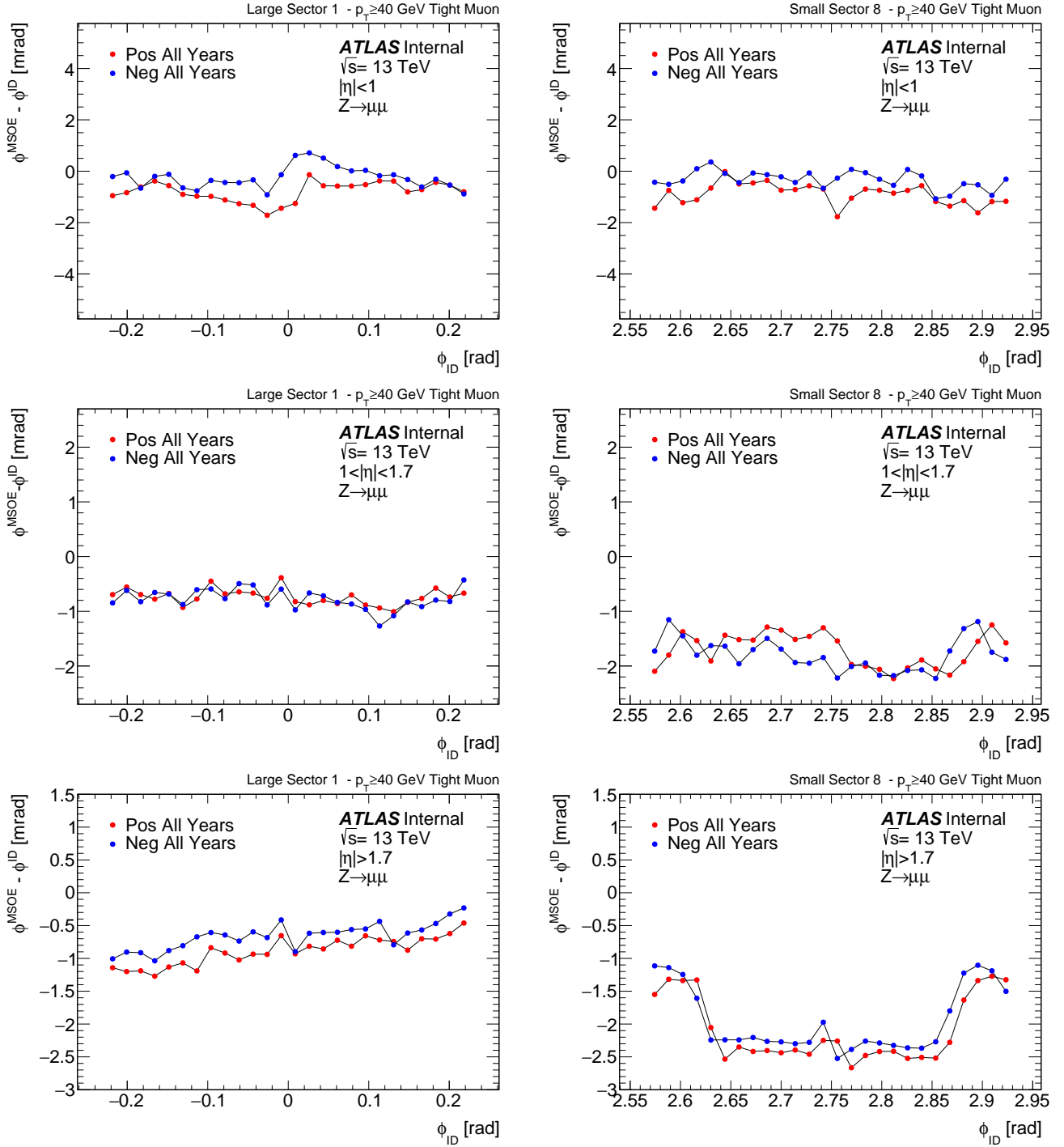
Figure 5.52: $\phi^{MSOE} - \phi^{ID}$ profiles for (top) barrel, (middle) intermediate and (bottom) ECT regions in $Z \to \mu\mu$ for (left) large and (right) small sectors at $p_T > 40$ GeV.

The maps for $d_0^{MSOE} - d_0^{ID}$, $\phi^{MSOE} - \phi^{ID}$, $(z_{MSOE} - z_{ID})\sin\theta$ and $\theta_{MSOE} - \theta_{ID}$ are shown in Fig. 5.53, respectively. In principle, these effects are charge independent, such that they are removed in the same amount for μ^+ and μ^- once the magnetic field is corrected.
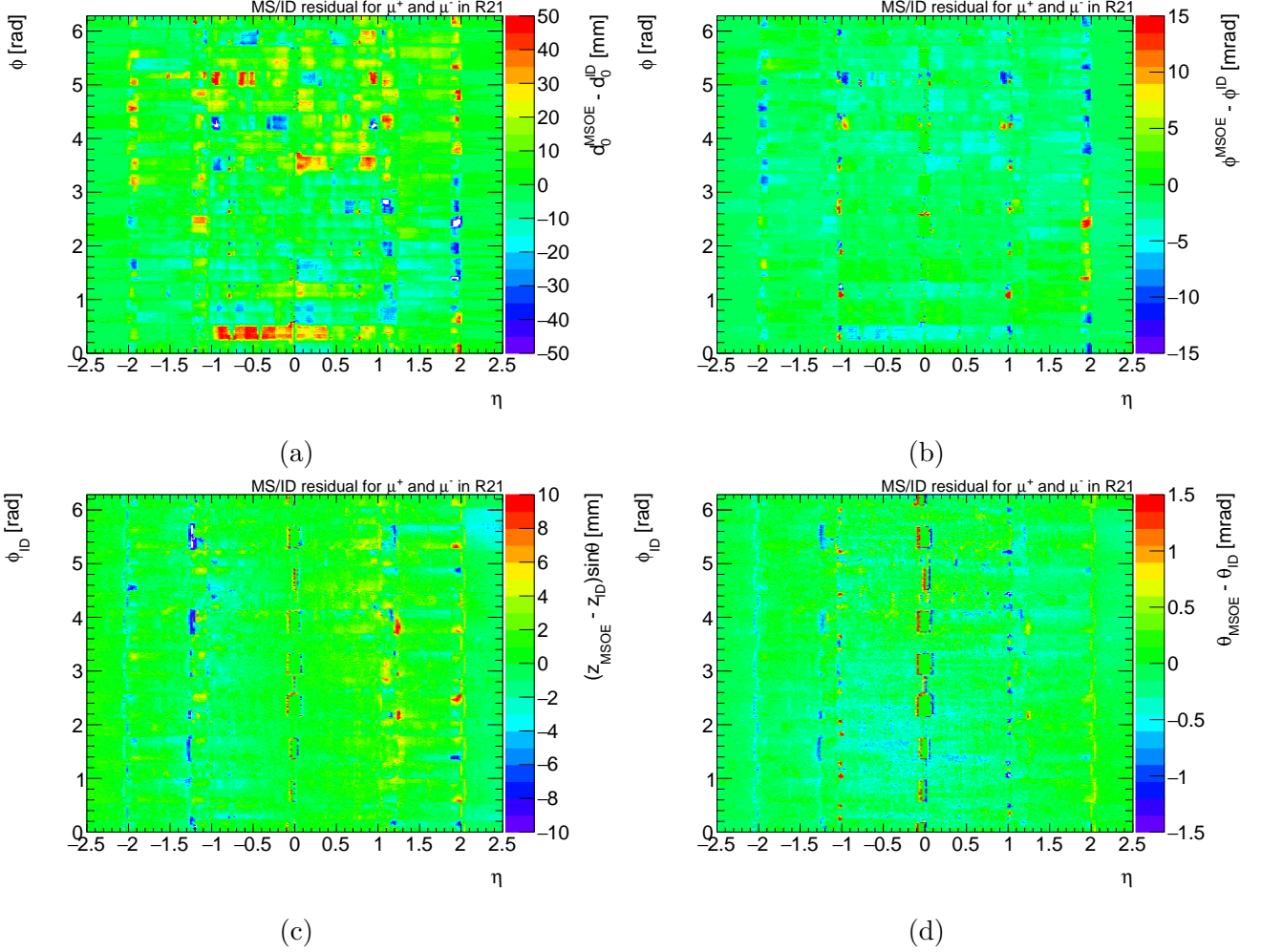
Figure 5.53: 2D maps for misalignment residuals in (a) $d_0^{MSOE} - d_0^{ID}$, (b) $\phi^{MSOE} - \phi^{ID}$, (c) $\Delta z_0 \sin\theta$ and (d) $\Delta\theta$ with MSOE - ID tracks.

5.8.2 Magnetic field and bias correction

Once the neutral corrections maps are computed these can be applied after the magnetic field correction ($\alpha_{\eta\phi} - $ map). The correction chain can be summarized as follows, a muon is forward extrapolated with the nominal field to the MS and then at the entrance of the MS, the muon is backward extrapolated with a modified the magnetic field. In this process, the charge-independent bias for both μ^+ and μ^- is removed.

Results for $(z_{MS} - z_{ID})\sin\theta$ and $\theta_{MS} - \theta_{ID}$ at $p_T > 40$ GeV are shown in Fig. 5.54. After correction, the charge effects have been removed and the systematic shape (slope) in $(z_{MS} - z_{ID})\sin\theta$ has been corrected reducing the bias to less than 1 mm for the ECT and below 0.2 mm in the barrel. On the other hand, for $\theta_{MS} - \theta_{ID}$ the charge effect is reduced and the bias has been corrected from 0.2-0.4 mrad to less than 0.1 mrad in the ECT and below 0.05 mrad in the barrel. After corrections, there is still a small charge asymmetry residual, this is due to the fact that using a charge-independent map the same value is removed for both muons, giving a second order effect.
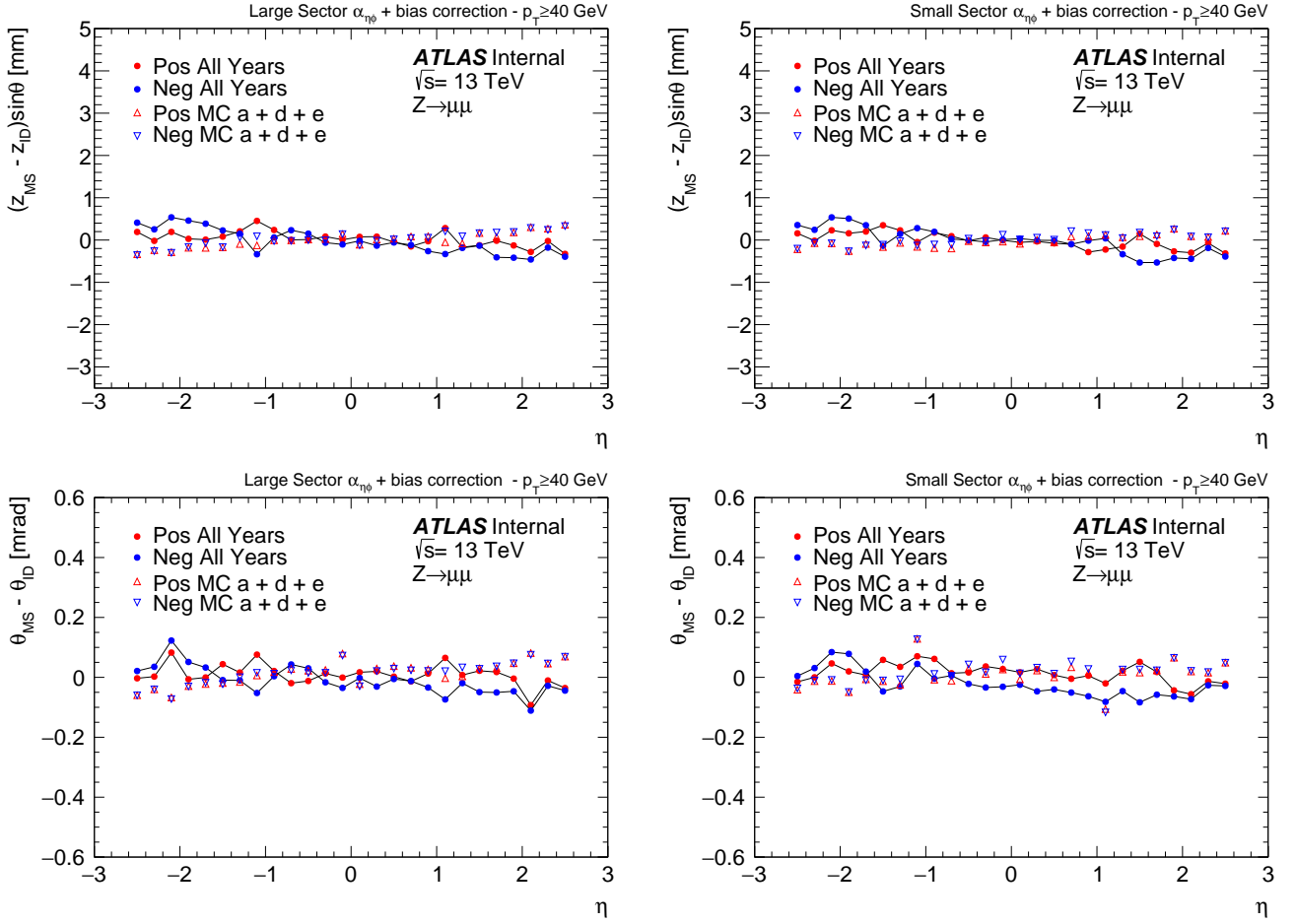
Figure 5.54: MS/ID residual profiles for (top) $\Delta z_0 \sin\theta$ and (bottom) $\Delta\theta$ vs η after corrections in $Z \to \mu\mu$ for (left) large and (right) small sectors at $p_T > 40$ GeV.

The same study is performed taking into account the low momentum regime in Fig. 5.55, i.e. $20 < p_T(\text{GeV}) < 40$. The results indicate that the bias has been successfully eliminated in both the large and small sectors. Additionally, applying the magnetic field corrections addresses the charge asymmetry, though a residual effect remains. Importantly, these maps were constructed for

high momentum scenarios, but they remain valid even at low momentum. This demonstrates the effectiveness of the correction in both regimes.
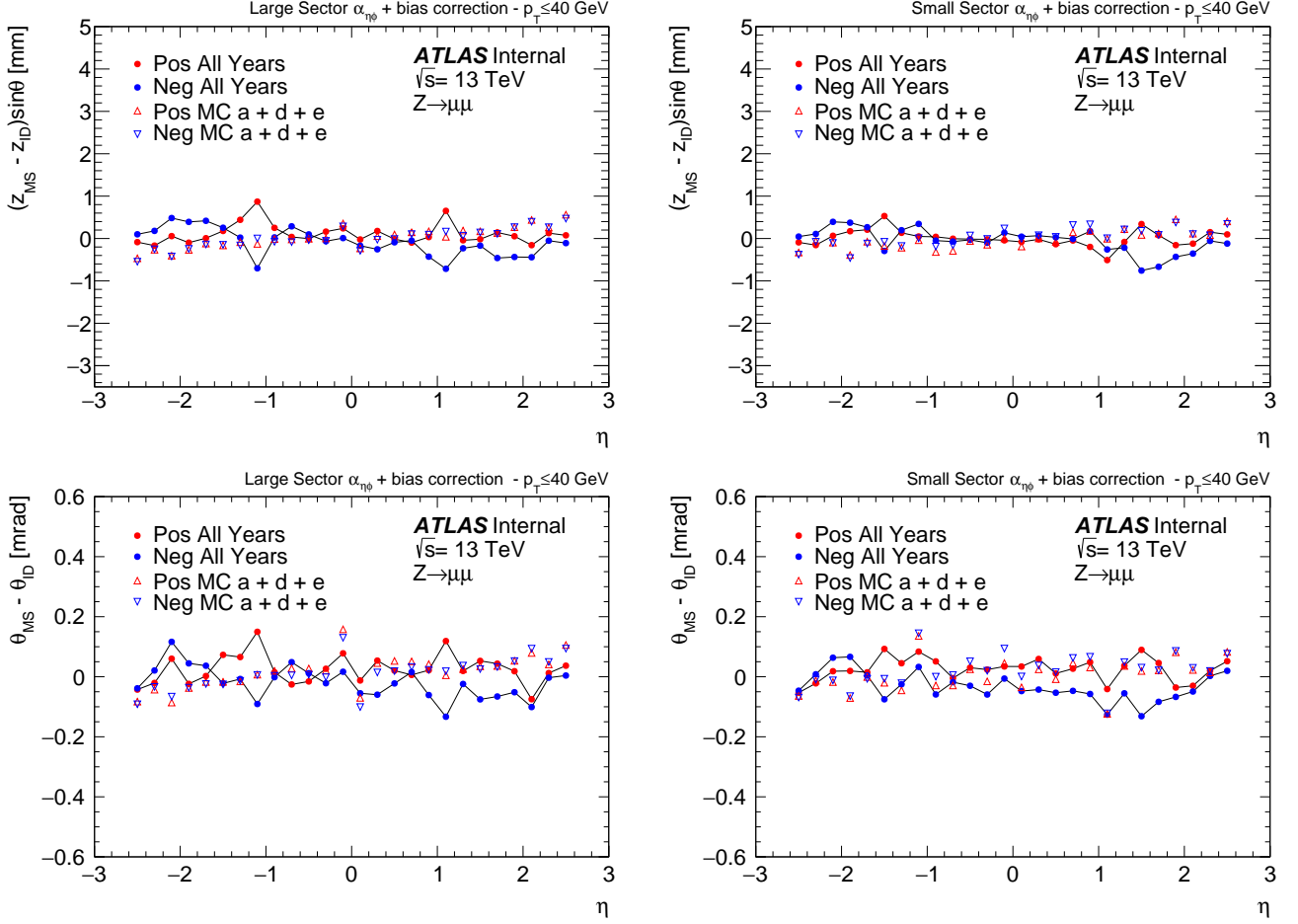
Figure 5.55: MS/ID residual profiles (top) $\Delta z_0 \sin \theta$ and (bottom) $\Delta \theta$ vs η after corrections in $Z \to \mu\mu$ for (left) large and (right) small sectors at $p_T < 40$ GeV.

Second coordinates correction

The same corrections are applied to the second coordinates, d_0 and ϕ, and the MS/ID residuals are re-evaluated in the barrel, intermediate and ECT regions as shown in Fig. 5.56 and Fig. 5.57 for $d_0^{MSOE} - d_0^{ID}$ and $\phi^{MSOE} - \phi^{ID}$, respectively.

These results show that the magnetic field correction is almost negligible in the second coordinates but the bias effect is playing an important role setting the values around zero. Larger biases are found in the barrel while for the intermediate and ECT regions it decreases fast compared to the barrel. Moreover, since the magnetic field correction is not having a considerably impact, those

163

sectors where the charge asymmetry is large, the residual effect is still present. This is mainly observed in the center of each sector, where a discontinuity was previously observed. In d_0 the effect is small compared to ϕ where the charge asymmetry reaches few $\sim$mm and $\sim$mrad, respectively.

5.9 Momentum scale and resolution calibration

Corrections obtained in Section 5.4.2 aim to address potential charge-dependent effects and ID geometrical distortions in the data. The first one accounts for charge dependent effects that improve the resolution in the invariant mass while the second one allows for a reduction in the scale in data with respect to the simulation, as well as a slight improvement in the resolution. These corrections are directly impacting the momentum performance of the muon and by consequence the invariant mass. On the other hand, Section 5.5.1 describes the approach in data to potentially improve the track reconstruction accounting for possible biases in the perigee parameters and charge dependent effects in the tile calorimeter region. Notice that sagitta and ID distortions aim to correct the momentum of the muons while the MS/ID residual corrections aim to improve the track reconstruction.

However, after these corrections are applied residuals between data and simulation are still present. For reaching a good agreement, the muon momentum still needs a calibration procedure that aims to correct the simulation. In general, this calibration can take into account several effects but the present work considered two, scale and resolution. The scale correction accounts the inaccuracy in the description of the magnetic field integral and the dimension of the detector in the direction perpendicular to the magnetic field. On the other hand, the resolution accounts for multiple scattering, uncertainties related to, and inhomogeneities in, the modelling of the local magnetic field, and length-scale radial expansions of the detector layers.

5.9.1 Calibration parameters

To account the scale and resolution effects, the momentum needs to be expressed as function of $\eta-$ and $\phi-$dependent parameters that can be measured in data with respect to the simulation ensuring
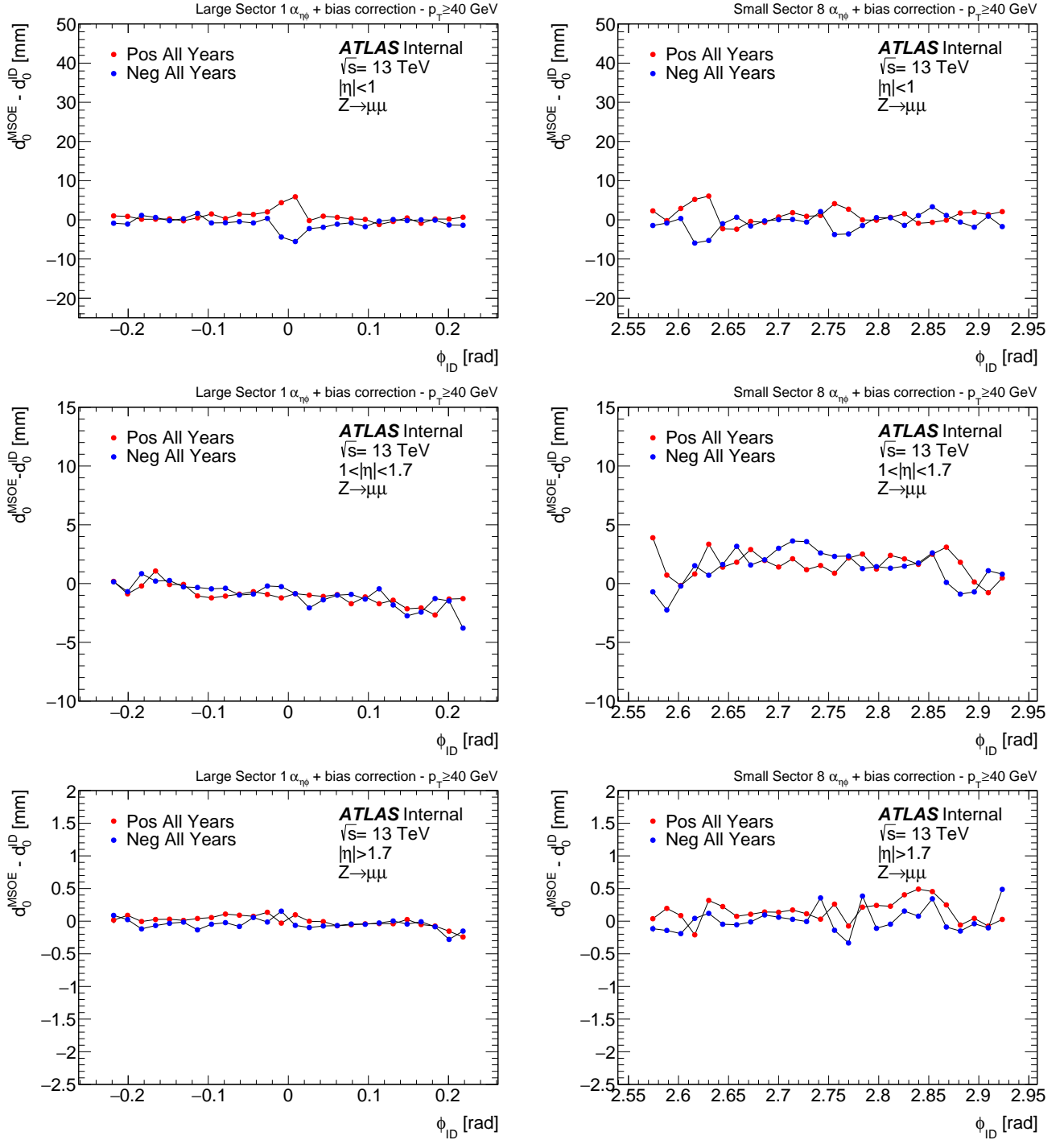
Figure 5.56: $d_0^{MSOE} - d_0^{ID}$ profiles with magnetic field and bias correction for (top) barrel, (middle) intermediate and (bottom) ECT regions in $Z \to \mu\mu$ for (left) large and (right) small sectors at $p_T > 40$ GeV.
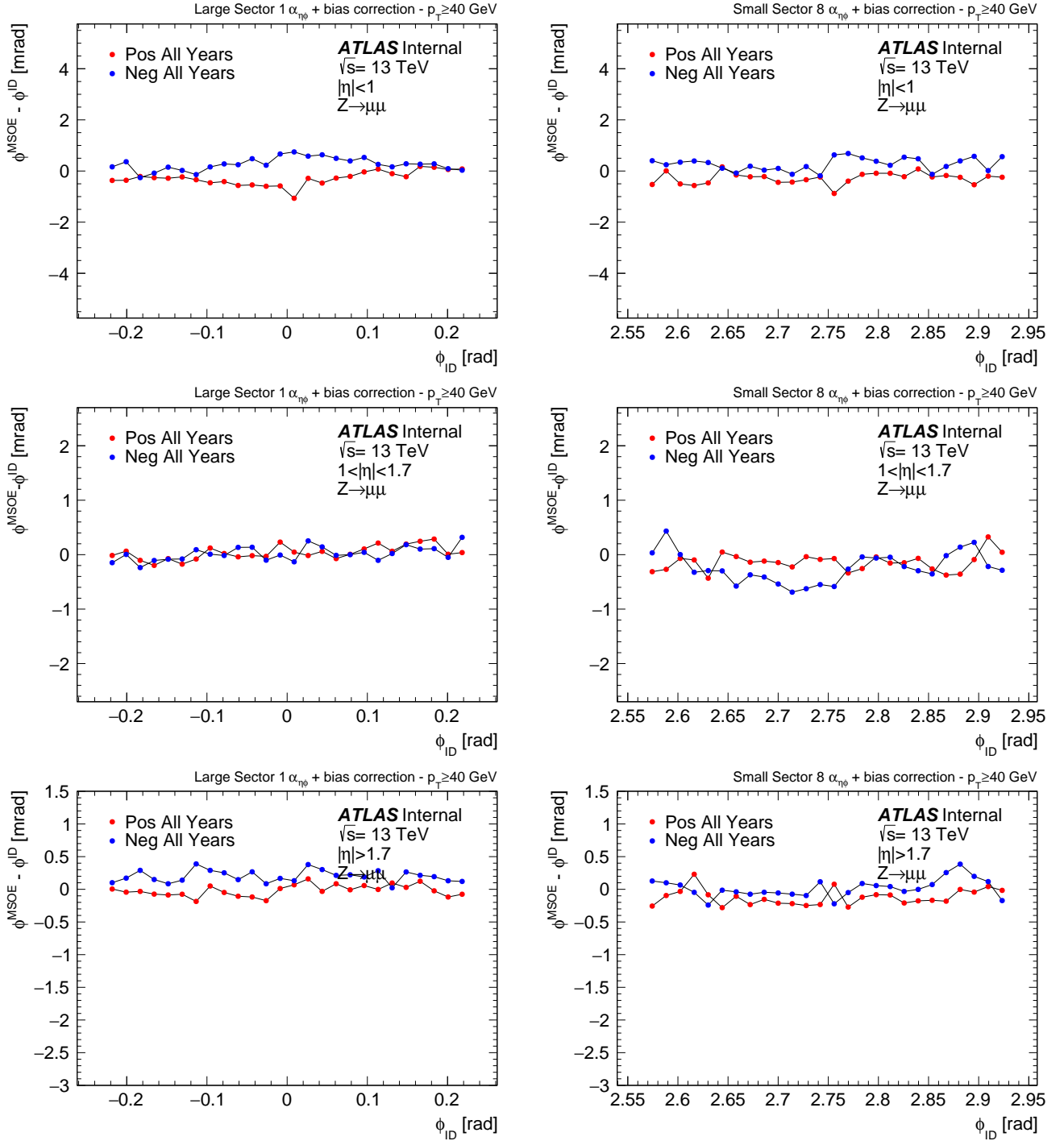
Figure 5.57: $\phi^{MSOE} - \phi^{ID}$ profiles with magnetic field and bias correction for (top) barrel, (middle) intermediate and (bottom) ECT regions in $Z \to \mu\mu$ for (left) large and (right) small sectors at $p_T > 40$ GeV.

a high precision on them to avoid the propagation of uncertainties. Commonly, iterative procedures are used as described in [117]. In this approach, the momentum scale and resolution parameters are computed in a first iteration to correct the simulation and to determine the agreement within a certain threshold. If the residual between data and simulation is below this threshold, the parameters are taken, if not, the procedure is repeated until the tolerance in the calibration is reached. This approach in some cases can lead to instabilities or a large number of iterations to reach a good precision. The present work has for objective to perform a calibration procedure using an analytical approach that ensures high precision while being fast and non-iterative.

The scale effect can be introduced as a shift of the momentum of the particles. To parameterize it, bins in $\eta-$space are considered such that the momentum in each $i-$bin is shifted by a given scale parameter α_i that is a function of η in that bin. This means,

$$p_i \rightarrow (1 + \alpha_i(\eta)) \cdot p_i, \tag{5.23}$$

such that the di-Muon mass m_{ij} can be reconstructed as,

$$m_{ij} \rightarrow m_{ij} \left(1 + \frac{\gamma_{ij}^{\alpha}}{2}\right), \tag{5.24}$$

where γ_{ij}^{α} is a 2D map in $\eta-$space of the two muons obtained from the invariant mass in a category (i, j) given by,

$$\gamma_{ij}^{\alpha} = \alpha_i + \alpha_j. \tag{5.25}$$

On the other hand, the resolution describes the momentum smearing that broadens the relative p_T resolution in simulation, $\sigma(p_T)/p_T$, to properly describe the data. This can be directly related to the relative mass resolution, $\sigma(m_{\mu\mu})/m_{\mu\mu}$, by the following equation,

$$\frac{\sigma(m_{\mu\mu})}{m_{\mu\mu}} = \frac{1}{2}\left[\frac{\sigma(p_T^+)}{p_T^+} \oplus \frac{\sigma(p_T^-)}{p_T^-}\right], \tag{5.26}$$

where $a \oplus b = \sqrt{a^2 + b^2}$ and the $\pm$ is the muon charge. The resolution in the invariant mass and

momentum between data and monte carlo simulation (MC) are related as,

$$\sigma^{\text{data}}(m_{\mu\mu}) = r_m \cdot \sigma(m_{\mu\mu})^{\text{MC}},$$

$$\sigma^{\text{data}}(p_T^{\pm}) = r_p^{\pm} \cdot \sigma(p_T^{\pm})^{\text{MC}}, \tag{5.27}$$

where r_m and $r_p^{\pm}$ represent scaling factors that are used to adjust the simulation to better match the distribution in real data. To correct for the resolution effects, the goal is to perform a data-to-simulation fit to obtain $r_p^{\pm}$ based on r_m input data. Injecting Eq. (5.27) into Eq. (5.26), an expression that relates the resolution in momentum with respect to the resolution in data can be obtained,

$$f_m \cdot r_m^2 = g^+ \cdot (r_p^+)^2 + g^- \cdot (r_p^-)^2. \tag{5.28}$$

where f_m is a 2D map in $\eta-$space of the two muons and $g^{\pm}$ are 1D maps in $\eta-$space of a single muon (positive or negative) given by,

$$f_m = \left[\frac{\sigma(m_{\mu\mu})}{m_{\mu\mu}}\right]_{\text{MC}}^2, \quad g_p^{\pm} = \frac{1}{4}\left[\frac{\sigma(p_T^{\pm})}{p_T^{\pm}}\right]_{\text{MC}}^2, \tag{5.29}$$

Since, r_m and $r_p^{\pm}$, are expected to be close to one an approximation at first order is used. This is, for the mass resolution $r_m = 1 + \gamma^m$ and in momentum $r_p^{\pm} = 1 + \beta_p^{\pm}$ where $|\gamma^m| \ll 1$ and $|\beta| \ll 1$. This allows to expand Eq. (5.28) around γ^m, β_p and neglecting higher order contributions. Then, it follows,

$$f_m \cdot \gamma^m = g^+ \cdot \beta_p^+ + g^- \cdot \beta_p^-. \tag{5.30}$$

Notice that both Eq. (5.25) and Eq. (5.30) are similar in the parameter determination. For example, Eq. (5.25) describes the momentum scale, α, as a function of previous knowledge of γ_{ij}^{α} (measured in data). Meanwhile, the resolution in momentum, $\beta_p^{\pm}$, is obtained from γ^m, f_m 2D maps and $g_p^{\pm}$ 1D maps. In the limit where $f_m = 1$ and $f_p^{\pm} = 1$, both Equations (5.25) and (5.30) are the same.

5.9.2 Analytical fit of calibration parameters

The Gaussian limit described in section 4.3 is implemented to determine the scale and resolution parameters with no systematics sources. A likelihood function to find α and β is given as,

$$-2\ln\mathcal{L} \equiv \chi^2 = \sum_{ij}\left(\frac{f^{ij}\gamma_{ij} - g^i \cdot \theta_i - g^j \cdot \theta_j}{\sigma_{ij}}\right)^2, \qquad (5.31)$$

where i, j run over the categories, σ_{ij} is the uncertainty in $f^{ij}\gamma_{ij}$, f_{ij} and g^i are the 2D and 1D weight matrices obtained from simulation, respectively. These matrices are equal to 1 in the scale determination and given by Eq. (5.29) in the resolution case. γ_{ij} are the 2D maps obtained from the invariant dimuon mass fit, $\vec{\theta}$ is the POI either scale ($\vec{\alpha}$) or resolution ($\vec{\beta}$). The Eq. (5.31) admits an analytical solution given by,

$$\theta_i = \sum_{\ell} U_{i\ell}^{-1} B_\ell, \qquad (5.32)$$

where

$$B_\ell = \sum_k \frac{g^\ell}{\sigma_{k\ell}^2}(f^{k\ell} \cdot \gamma_{k\ell}), \qquad (5.33)$$

and,

$$U_{i\ell} = \frac{g^i g^\ell}{\sigma_{i\ell}^2} + \delta_{i\ell}\sum_k\left(\frac{g^i}{\sigma_{ik}}\right)^2, \qquad (5.34)$$

with $\delta_{i\ell}$ the Kronecker delta function and $\text{cov}(\theta_p, \theta_q) = U_{pq}^{-1}$. For the analytical solution to be valid a symmetry in electric charge is required such that resolution parameter for the negative and positive particles are the same, this is, $\beta_p^+ = \beta_p^-$ as well as the 1D maps $g^+ = g^-$. However, as shown in section 5.3 a charge asymmetry is present in data and this should be treated to obtained accurate results.

In the case of resolution, the weights matrices f, g (relative reslolutions) are obtained as the RMS of the distribution from the difference of the reconstructed (reco) quantity and the true quantity

169

divided by its true value of the simulation,

$$\frac{\sigma(m_{\mu\mu})}{m_{\mu\mu}} = \left(\frac{m_{\mu\mu}^{\mathrm{reco}} - m_{\mu\mu}^{\mathrm{true}}}{m_{\mu\mu}^{\mathrm{true}}}\right)_{\mathrm{RMS}},$$
$$\frac{\sigma(p_T^{\pm})}{p_T^{\pm}} = \left(\frac{p_T^{\mathrm{reco}} - p_T^{\mathrm{true}}}{p_T^{\mathrm{true}}}\right)_{\mathrm{RMS}}^{\pm}. \tag{5.35}$$

These quantities are computed in different $(i, j)-$categories and in a perfect scenario, they should be symmetric in the simulation and the relative momentum resolution should also be symmetric in electric charge, i.e. $\sigma(p_T^+)/p_T^+ = \sigma(p_T^-)/p_T^-$. However, this is not the case, since the simulation present small variations between the categories $(i, j) \simeq (j, i)$. To correct this, the 2D maps γ_{ij} (relative mass resolution) are symmetrized as follows,

$$\gamma_{ij}^{\mathrm{sym}} = \omega_{ij}\gamma_{ij} + \omega_{ji}\gamma_{ji}, \tag{5.36}$$

where,

$$\omega_{ij} = \left(\frac{1}{\sigma_{ij}}\right)^2 \Big/ \sum_{k\ell} \left(\frac{1}{\sigma_{k\ell}}\right)^2, \tag{5.37}$$

and the uncertainty is given as,

$$\sigma_{ij}^{\mathrm{sym}} = \sqrt{(\omega_{ij} \cdot \sigma_{ij})^2 + (\omega_{ji} \cdot \sigma_{ji})^2}. \tag{5.38}$$

with σ_{ij} the error associated to γ_{ij}. Final 2D maps before and after symmetrization are shown in Fig. 5.58.

In the case of the 1D maps $g_p^{\pm}$ (relative momentum resolution), both muons show an asymmetry with respect to η but also a charge asymmetry. To obtain one single symmetric map, first, each muon is symmetrized with respect to η, as follows,

$$\tilde{g}_k^{\pm} = \tilde{g}_{N-k}^{\pm} = \tilde{w}_k^{\pm} g_k^{\pm} + \tilde{w}_{N-k}^{\pm} g_{N-k}^{\pm} \tag{5.39}$$
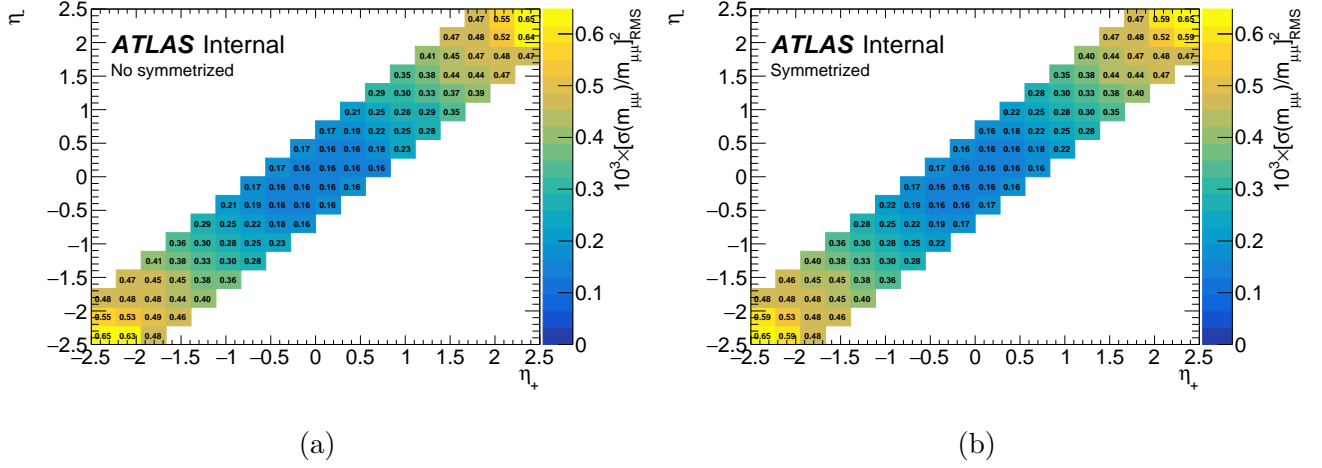
Figure 5.58: f^{ij} relative invariant mass resolution maps for (a) no symmetrized and (b) symmetrized.

where,

$$\tilde{w}_k^\pm = \left(\frac{1}{\sigma_k^\pm}\right)^2 \bigg/ \left[\left(\frac{1}{\sigma_k^\pm}\right)^2 + \left(\frac{1}{\sigma_{N-k}^\pm}\right)^2\right], \qquad (5.40)$$

and the uncertainty

$$\tilde{\sigma}_k^\pm = \tilde{\sigma}_{N-k}^\pm = \sqrt{(w_k^\pm \cdot \sigma_k^\pm)^2 + (w_{N-k}^\pm \cdot \sigma_{N-k}^\pm)^2}. \qquad (5.41)$$

where $k = 1, 2, .., N/2$ with N the number of η bins and $\sigma_k^\pm$ is the uncertainty in $g_k^\pm$. Once the maps are symmetrized with respect to η, the final map is obtained as a weighted average of both electric charges symmetric maps $\tilde{g}^\pm$ as follows,

$$g_i^{\mathrm{cmb}} = w_i^+ \tilde{g}_i^+ + w_i^- \tilde{g}_i^-, \qquad (5.42)$$

where,

$$w_i^\pm = \left(\frac{1}{\tilde{\sigma}_i^\pm}\right)^2 \bigg/ \left[\left(\frac{1}{\tilde{\sigma}_i^+}\right)^2 + \left(\frac{1}{\tilde{\sigma}_i^-}\right)^2\right], \qquad (5.43)$$

and the uncertainty

$$\sigma_i^{\mathrm{cmb}} = \sqrt{(w_i^+ \cdot \tilde{\sigma}_i^+)^2 + (w_i^- \cdot \tilde{\sigma}_i^-)^2}. \qquad (5.44)$$

where $i = 1, ..., N$. The relative momentum resolution maps before and after symmetrization are shown in Fig. 5.59.
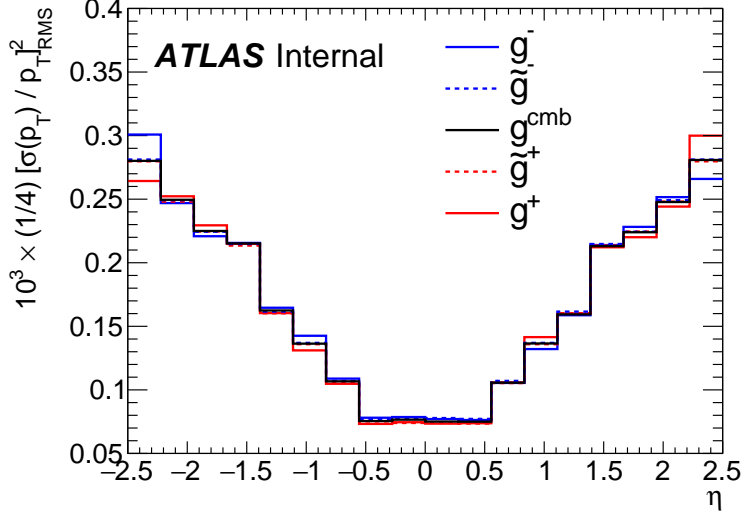
Figure 5.59: Relative momentum resolution maps for positive (red) and negative (blue) muons, statistical combination and symmetrization. $\tilde{g}^{\pm}$ represents the map after symmetrization of $g^{\pm}$ in η and g^{cmb} is the statistical combination of both $\tilde{g}^{+}$ and $\tilde{g}^{-}$.

5.9.3 Invariant mass fit

To perform the momentum calibration, the scale and resolution need to be obtained using the γ_{ij} matrices coming from the invariant mass fits. There are several approaches to determine them such as parametric fits. For example, the mass distribution can be modelled by analytical functions like Gaussian functions, Crystal-Ball functions, Polynomials of different orders, combinations of different models, etc. And then reading the invariant mass from the fit. These kind of fits commonly involve several degrees of freedom related to the parameters to be fitted. For example, a usual approach considers two crystal ball plus a Gaussian and a polynominal of order n. This means, $14 + n$, parameters to be fitted in order to model the data, which in some cases are not capable to fully reproduce the physics effects. On what follows, the invariant mass fit is carried out by a numerical template fit with a quadratic morphing between the templates.

A data-to-simulation fit of the di-muon mass distribution is performed to extract from it the 2D data maps γ^{α} and γ^{m} for the scale and resolution, respectively. Once the 2D maps are obtained an analytical fit is carried out by minimizing the Eq. (5.31). The fit is performed using $J/\psi \rightarrow \mu\mu$ resonance in η−categories of the two muons. This means, for each muon the η−space is binned in

18×18 categories (bins) from $\eta \in [-2.5, 2.5]$. Then, a fit is carried out in each $(i, j)-$category, i.e. $18 \times 18 = 324$ fits.

5.9.3.1 Templates for scale and resolution

Theoretical models or "templates" are constructed for both the signal process (the phenomenon of interest) and the background processes (other known or expected phenomena). These templates describe the expected distributions of certain observables such as scale or resolution and then they are fitted to the experimental data by adjusting their parameters to minimize the difference between the observed data and the predicted distributions.

Since the study is performed with muons in $\eta-$space, the templates are prepared in each category to mimic the effects of the scale and the resolution in that given category. For the scale, the momentum of the muons is decalibrated using Eq. (5.23) by a constant factor in all the categories. These factors are chosen to be,

$$\alpha = \pm(5, 4, 3, 2, 1, 0.9, 0.8, 0.7, 0.6, 0.5, 0.4, 0.3, 0.2, 0.1, 0.0) \times 10^{-3}, \tag{5.45}$$

resulting in 29 templates for which $\alpha = 0.0$ means no scale applied (nominal simulation). Some scale templates are shown in Fig. 5.60a.

In the case of the resolution sample, a common methodology is to smear the momentum using random numbers as,

$$p^{\text{smear}} = p^{\text{MC}} \cdot (1 + \beta \cdot G(0, 1)), \tag{5.46}$$

where $G(0, 1)$ is a univariate Gaussian random number centered at 0 and with standard deviation equal to one. This method only allows for the generation of broader smeared samples that are stochastic. Consequently, the fit may encounter limitations if the data being fitted is narrower than the template itself. For that reason, the resolution templates are constructed directly at the mass level by smearing the reconstructed mass,

$$m_{\mu\mu}^{\text{smear}} = m_{\mu\mu}^{\text{true}} + (1 + \beta) \cdot (m_{\mu\mu}^{\text{reco}} - m_{\mu\mu}^{\text{true}}), \tag{5.47}$$

173

where the distribution is wider for $\beta > 0$, narrower for $\beta < 0$ and $\beta = 0$ means no smearing. For the template production the following values are used,

$$\beta = \pm(0, 1, 2, 3, 4, 5, 6, 7, 8, 9, 10)\% \tag{5.48}$$

resulting in 21 templates with $\beta = 0.0$ the nominal distribution matching with $\alpha = 0.0$ template. Some smeared distributions using Eq. (5.47) are shown in Fig. 5.60b.

The generated templates are capable to mimic independently the effects in scale and resolution and they are suitable to perform combined fits. However, Equations (5.23) and (5.47) can be applied simultaneously to generate templates that simulate the effect of scale and resolution together. For example, once the momentum is scaled, the scaled mass (m^{scale}) is reconstructed and then smeared using the true mass, as follows,

$$p \rightarrow (1 + \alpha_i) \cdot p \implies m_{\mu\mu}^{\text{smear + scale}} = m_{\mu\mu}^{\text{true}} + (1 + \beta) \cdot (m_{\mu\mu}^{\text{scale}} - m_{\mu\mu}^{\text{true}}). \tag{5.49}$$

Some templates generated by this approach are shown in Fig. 5.60c.

Templates in Fig. 5.60 model properly the signal region of the fit. However, when using data, the background events play an important role and they need to be introduced also in the modelling as systematic sources. For this, they can also be treated by the template fit method. Often parametric fits use Cristal Ball + Gaussian functions to model the signal region while for the background a polynomial or exponential (or combinations) are used. In this work, to model the background, analytical functions are implemented. The background in the data is fitted using an exponential function $f_{\text{bkg}}(x) = A \exp(-ax)$, where the parameters are retrieved in each category to construct a background distribution. Once this is done, the nominal background is obtained and the templates are computed by varying the nominal within its uncertainty $\pm\sigma$. This allows to have a suitable description of the background that can be applied in the model. To provide more flexibility to the fit, templates with $\pm 2\sigma$ variations were prepared to be used as control regions for the background such that a better convergence in the fit is ensured. Background templates are shown in Fig. 5.61. Having under control the templates the numerical fit can be performed.
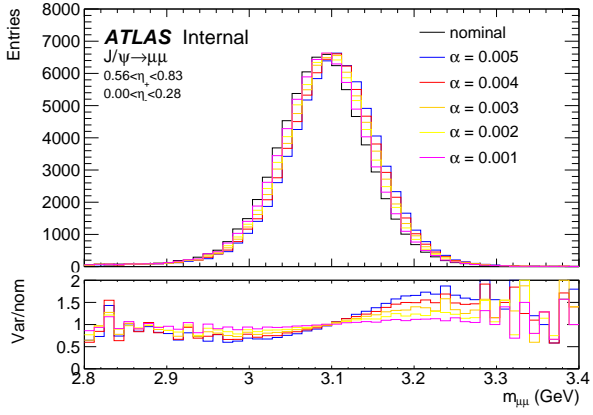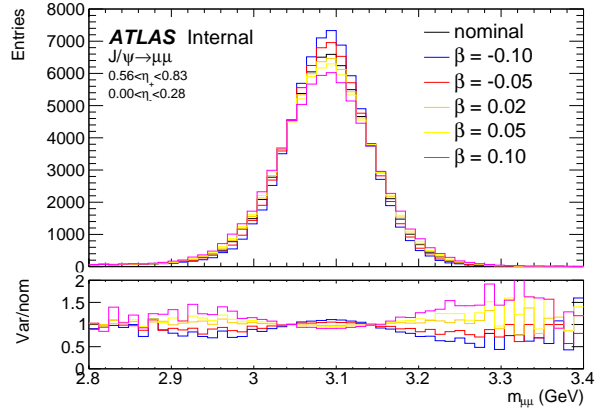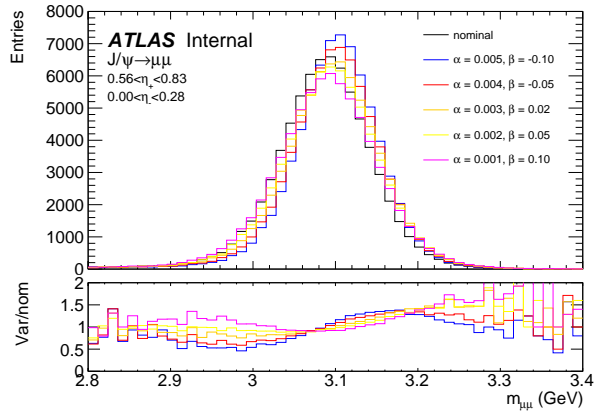
Figure 5.60: Templates for (a) Scale, (b) resolution and (c) scale + resolution. Upper panel: generated templates using mc20 mote carlo samples for different injected values. Bottom panel: Ratio of variations (Var) with respect to the nominal monte carlo simulation (nom).
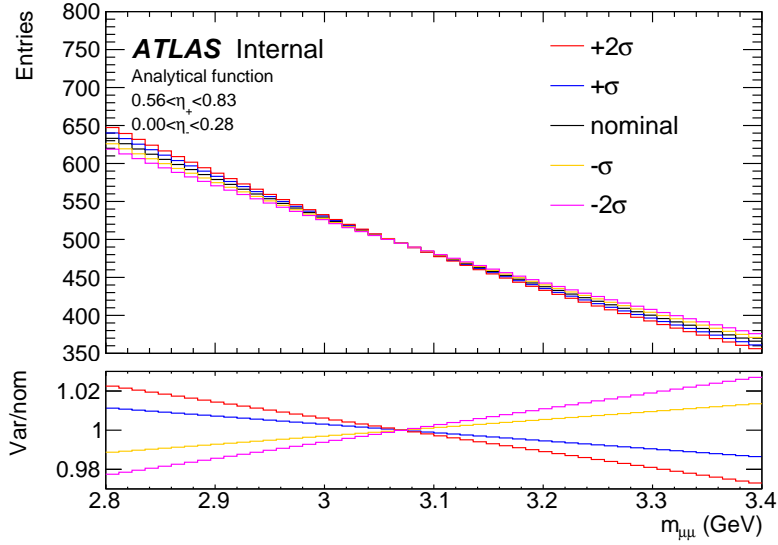
Figure 5.61: Exponential background templates. Upper panel: $\pm\sigma, \pm2\sigma$ variations generated using analytical functions of fits with respect to the data. Bottom panel: Ratio of variations (Var) with respect to the nominal background function (nom).

5.9.3.2 Template morphing

When performing a binned template fit is crucial to study the dependence of the templates with respect to the parameter of interest to determine the sensitivy of the POI with respect to the probability model as shown in Eq. (4.17). To choose the template interpolation (template morphing), the template yield behavior with respect to the template variation in each bin needs to be studied. If the templates behave linearly a straight line model should be accurate, otherwise a more sophisticated function is required (Piecewise, Polynominal of higher orders, etc). In the case of the linear morphing an analytical solution of the POIs can be found. If the morphing is quadratic, the POI can be found only in a perturbation approach for $|\theta| \ll 1$. To decide the morphing type, Fig. 5.62 shows the resolution template yields in three bins, tails (bins 10 and 45) and peak of the resonance (bin 25). Around the peak of the resonance, the templates behave linearly since the distribution tends to be narrower or wider without changing the mean value. However, in the tails, the yields are not fully linear and a quadratic model is more accurate.

In the case of the scales, the template yields for the same bins (tails and resonance peak) are shown in Fig. 5.63. Where a non-linear behaviour is observed and the quadratic model leads to
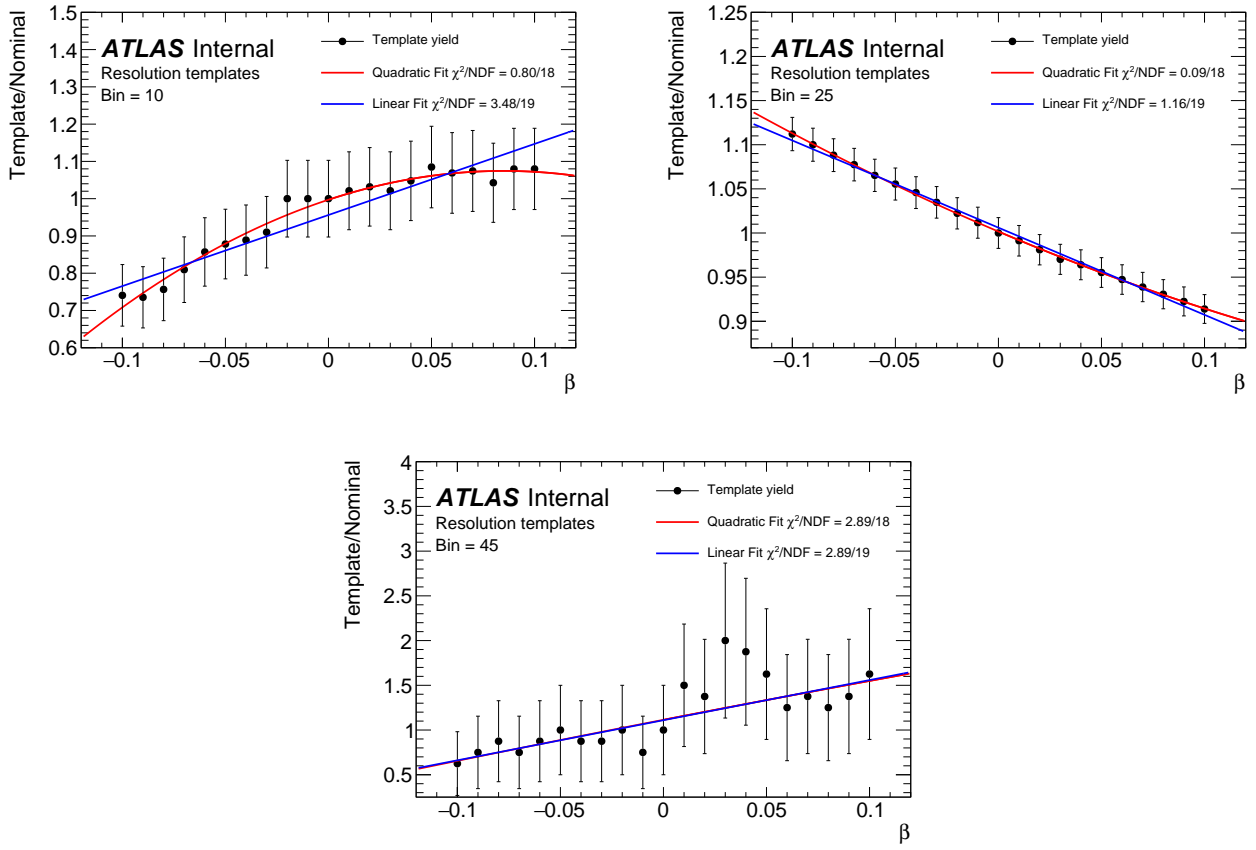
Figure 5.62: Resolution (smearing) template yields versus template variation. Two fits are showed, linear (blue line) and quadratic (red line).

a better fitting strategy. Finally, if a simultaneous fit of scale and resolution is performed, both templates should be fitted in a 2D space as shown in Fig. 5.64. Since the scale behaves linearly when the resolution behaves quadratically and vice-versa, it is convenient to use a quadratic morphing as follows,

$$\text{morphing} = \sum_{k=0}^{2} \sum_{\ell=0}^{2} c_k d_\ell \alpha^k \beta^\ell, \tag{5.50}$$

where c_k, d_ℓ are fitted parameters. For the systematics, since they correspond to $\pm\sigma$ variations, they are perfectly described by a linear morphing.

Since a quadratic morphing is required at this stage, the di-muon invariant mass fit is carried out numerically to obtain the 2D maps γ_{ij}. Finally, the calibration parameters α, β are obtained by an analytical minimization as described in subsection 5.9.2.
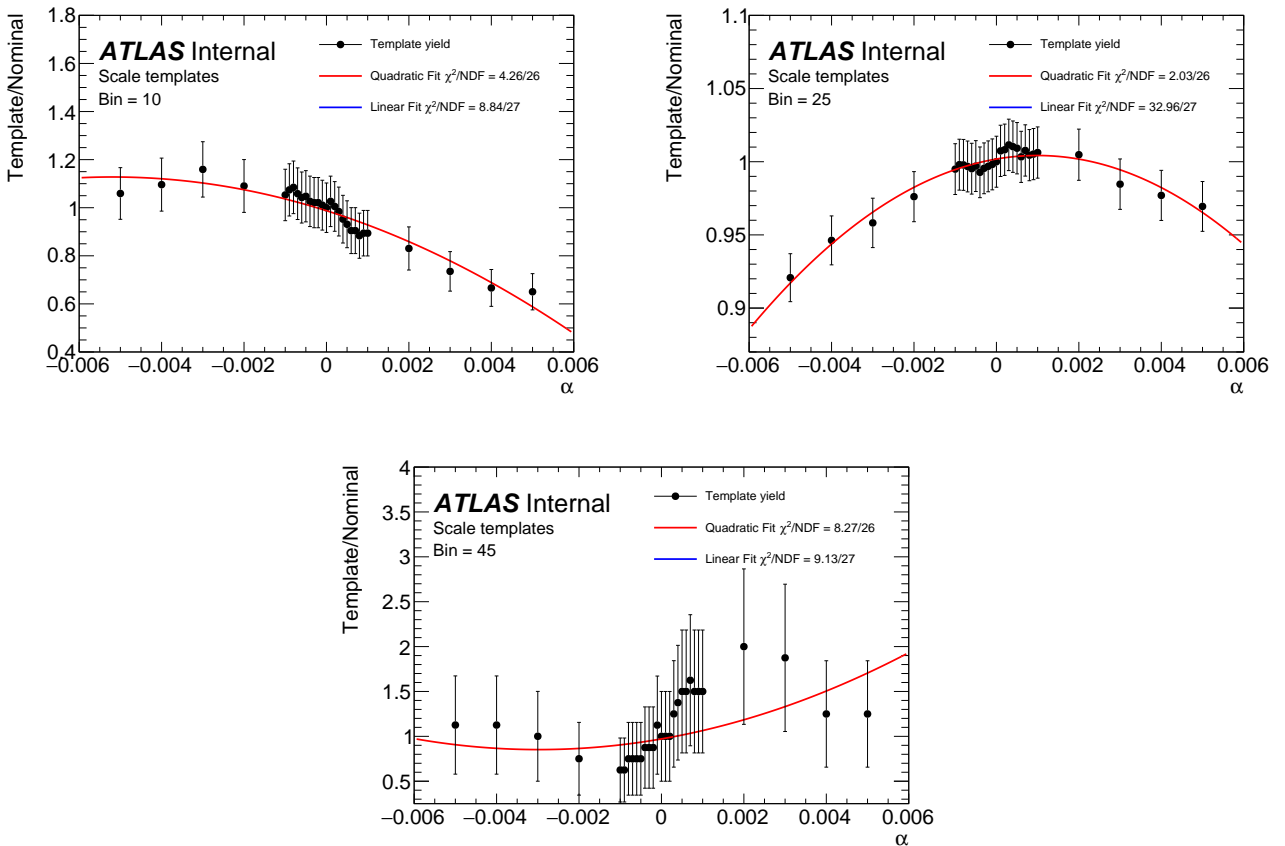
Figure 5.63: Scale template yields versus template variation. Two fits are showed, linear (blue line) and quadratic (red line).
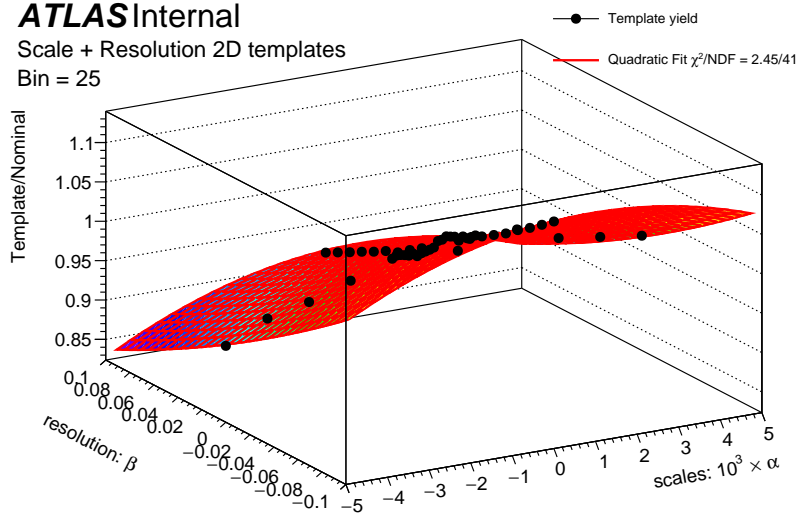
Figure 5.64: Scale + resolution 2D template yields versus template variation with quadratic morphing (red plane).

5.9.3.3 Closure test and fit validation

To verify that the fit strategy is working properly a closure test was carried out. In this a pseudo-data is prepared by decalibrating the simulation. In the sample, the momentum of the muons is scaled by $\alpha_{\mathrm{inj}} = 5 \times 10^{-4}$ factor in all the $\eta-$categories of the muons and smeared by $r_{p,\mathrm{inj}} = 92.75\% \rightarrow \beta_{\mathrm{inj}} = -7.25\%$. This generates a shift and a narrower peak than the original sample. Finally a pseudo-data background is prepared as $+0.5\sigma$ variation and added to the signal. Once this is done, the pseudo-data is fitted using a quadratic morphing with the templates already described, pre-fit and post-fit plots of the dimuon invariant mass are shown in Fig. 5.65. These fits are repeated in each $(i,j)-$category from which the γ_{ij} maps for scale and resolution are obtained as shown in Fig. 5.66. Finally, they are introduced into the χ^2 of Eq. (5.31) with the relative resolution maps in Figures 5.58 and 5.59 returning the calibration parameters. Since the injected value is known, is convenient to compute the residual with respect to the fitted values as shown in Fig. 5.67. Results for scale and resolution parameters are retrieved with an average residual $\langle \alpha_{\mathrm{fit}} - \alpha_{\mathrm{inj}} \rangle = 7 \times 10^{-6}$ and $\langle \beta_{\mathrm{fit}} - \beta_{\mathrm{inj}} \rangle = -2 \times 10^{-6}$, respectively or roughly $\sim 10^{-5}$. This validates the fitting strategy and it is ready to be implemented in data.
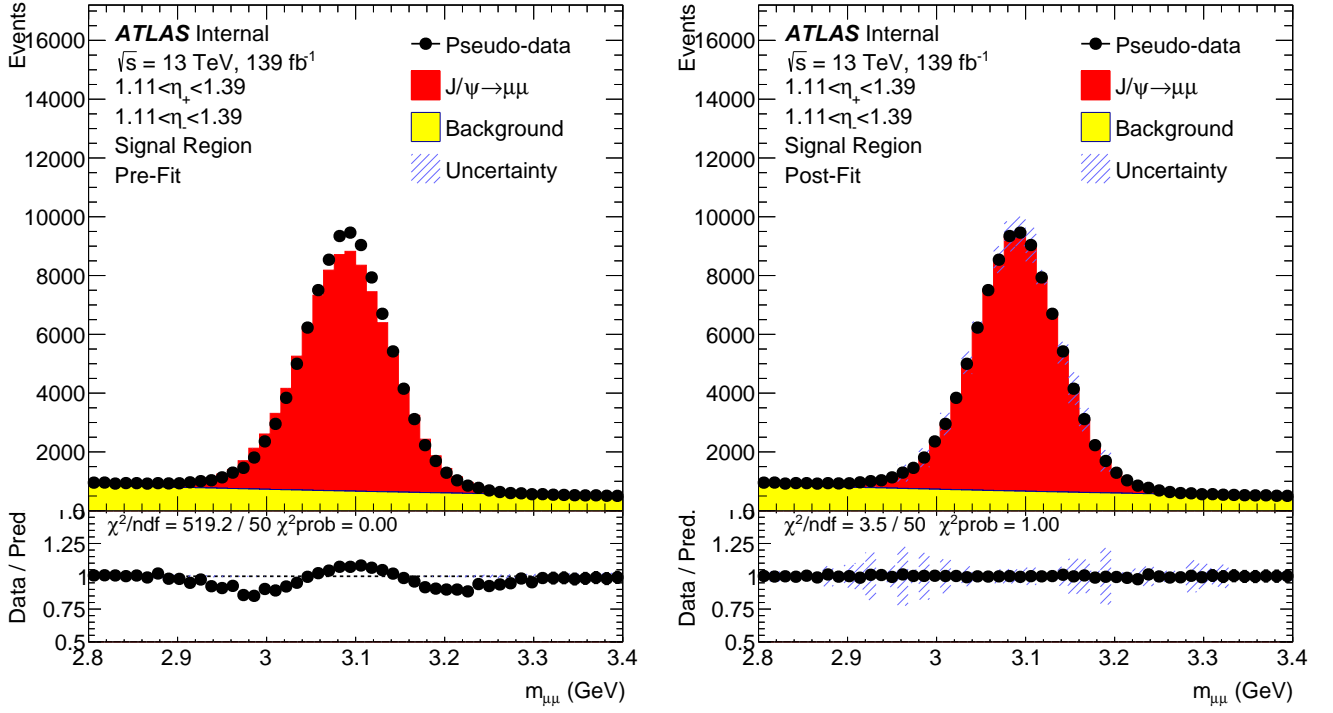
Figure 5.65: Numerical fit using the di-muon invariant mass for scale and resolution (2POI) + background (1 NPs).
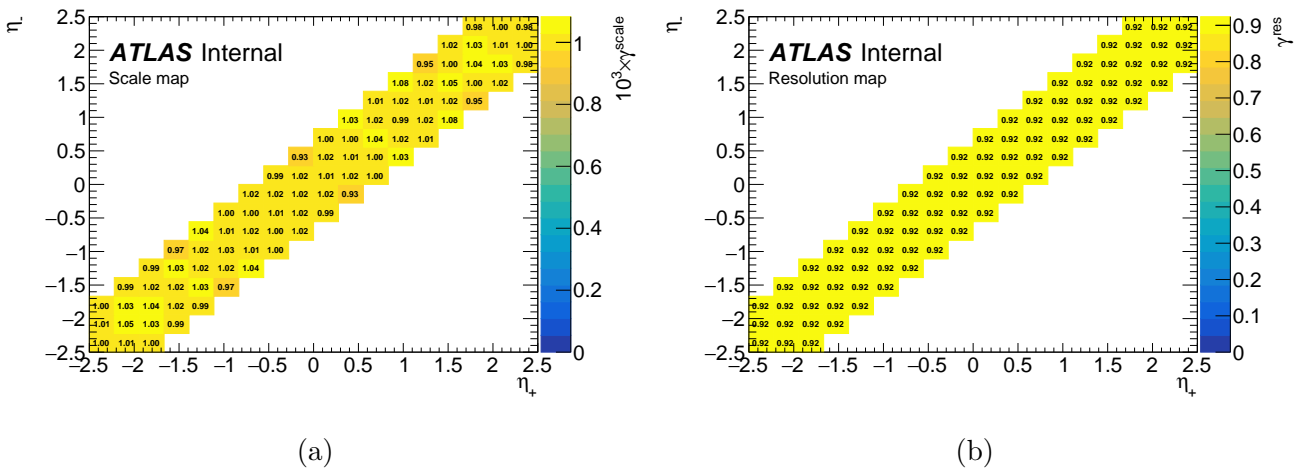
Figure 5.66: Invariant mass γ^{ij} maps for (a) scale and (b) resolution for the simulation closure test.

(a) scale
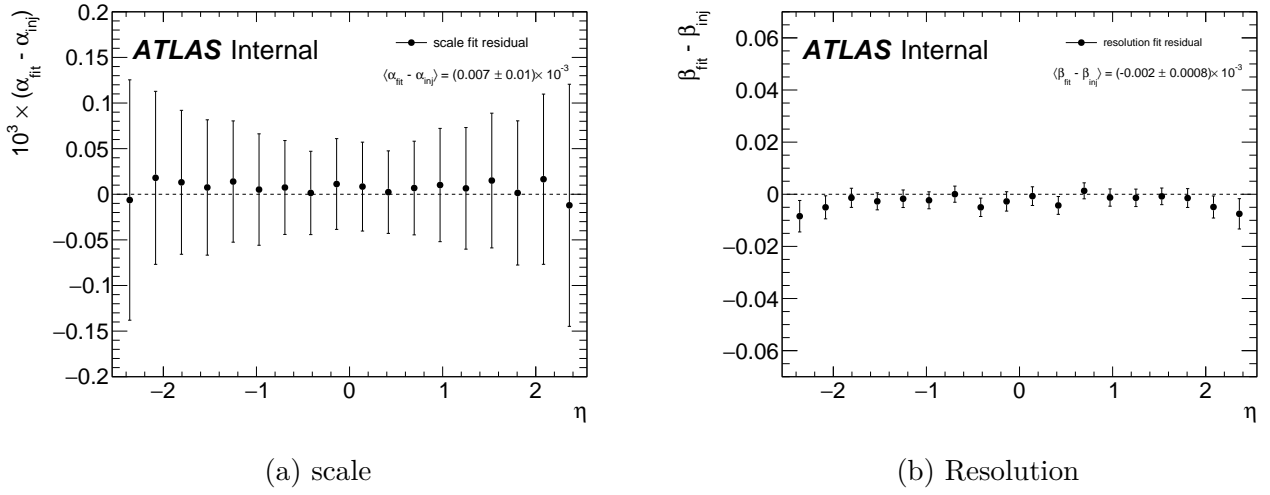
(b) Resolution

Figure 5.67: Residuals for scale and resolution using analytical fit method.

5.9.4 Scale and resolution maps

The fit is performed with the data-sets pre-corrected for charge dependent effects (sagitta) and ID geometrical distortions as described in Section 5.4.2 for data-taking years (2015, 2016, 2017 and 2018) and different track types, CB and ID. The final calibration parameters are obtained by the template fit and they are shown in Fig. 5.68, 5.69, 5.70 and 5.71. The large values of the ID track for the ECT regions are related to the fact that the quality of this track and the invariant mass reconstruction is degraded at high η values and by consequence the parameter estimation is not as good as for the CB.

In the case of the scale parameters, both tracks CB and ID show similar values in the barrel region $|\eta| < 1$ since this region is mainly dominated by the Inner tracker. However, in the case of the case of the ECT $|\eta| > 1$, the ID and CB tracks are not longer around the same values. This is due to the fact that the Muon Spectrometer dominates this region and the CB track allows a better performance for these values.

In the case of the resolution, for the barrel region the ID tracks show values around 5% smearing while the CB tracks around 10% for 2018 and 2017 while for 2015 and 2016 the ID tracks show almost a good compatibility with 0% smearing and the CB track decreases to 5%.
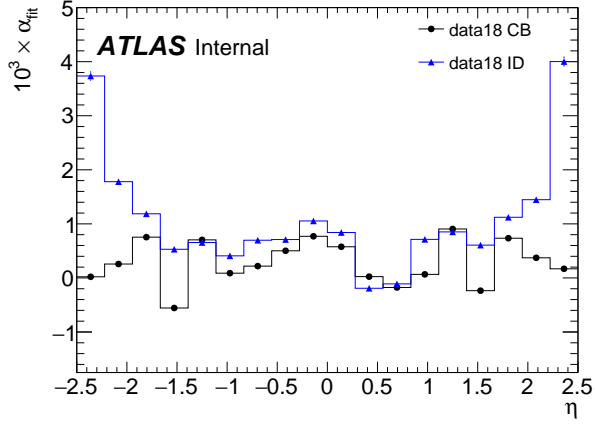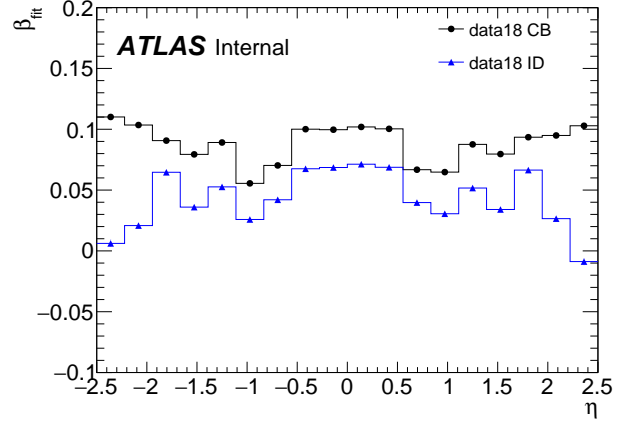
Figure 5.68: Calibration parameters for (a) scale and (b) resolution for muon momentum calibration in year 2018.
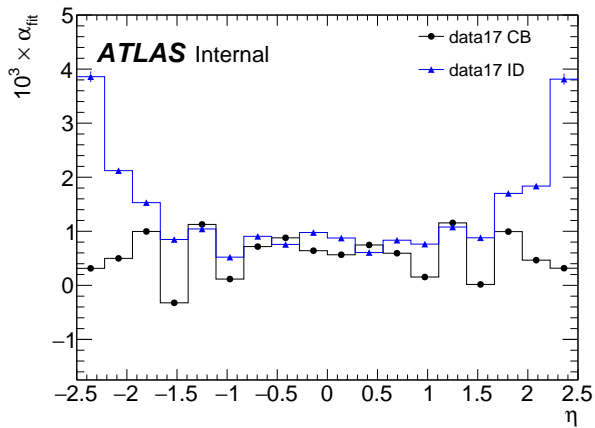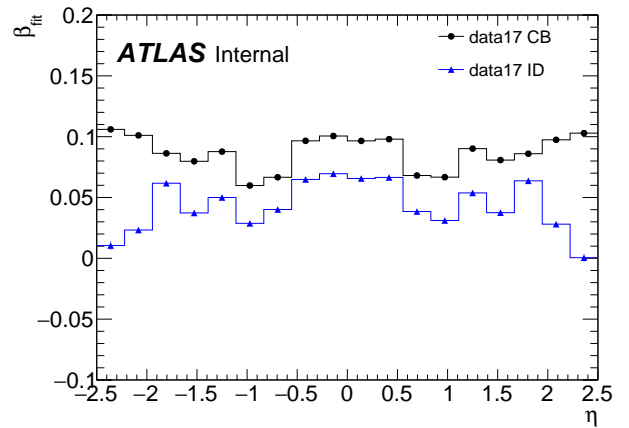
Figure 5.69: Calibration parameters for (a) scale and (b) resolution for muon momentum calibration in year 2017.
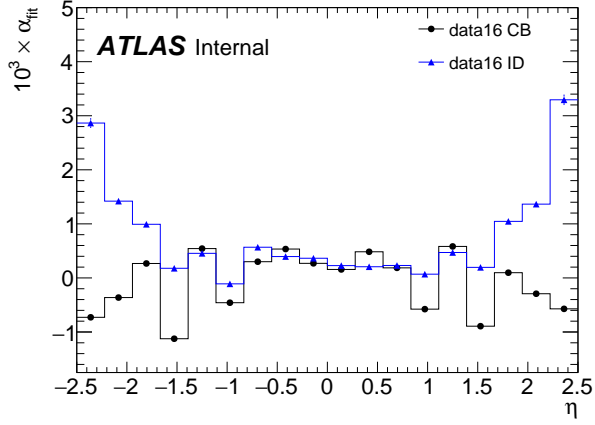
(a)
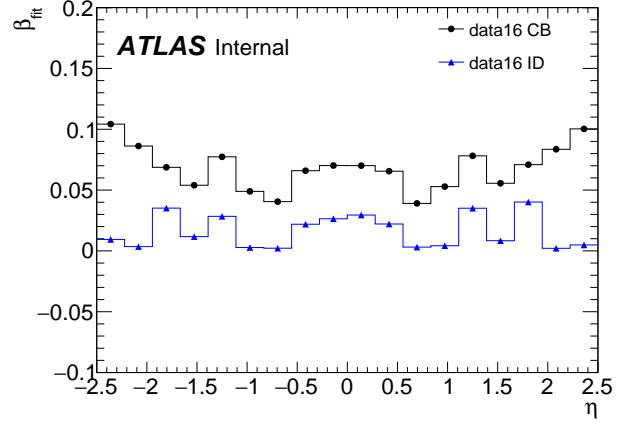
(b)

Figure 5.70: Calibration parameters for (a) scale and (b) resolution for muon momentum calibration in year 2016.
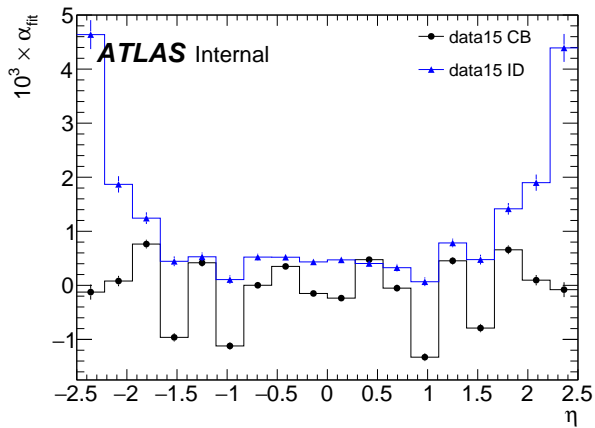
(a)
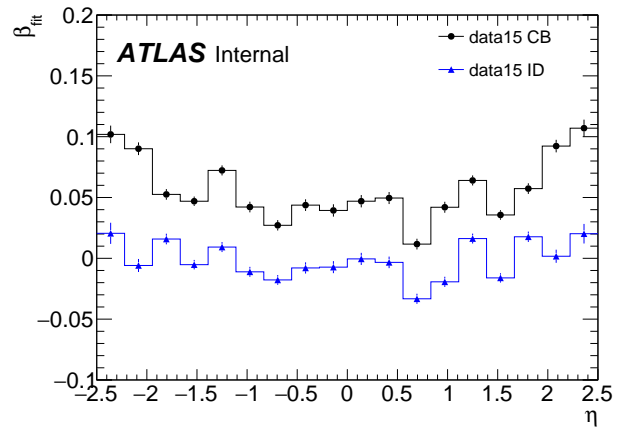
(b)

Figure 5.71: Calibration parameters for (a) scale and (b) resolution for muon momentum calibration in year 2015.

5.9.4.1 Final Muon Momentum Calibration (MMC)

Once the scale and resolution parameters are determined, the simulation is corrected to match the data. The muons in simulation are corrected as,

$$p_T^{\text{corr}} = (1 + \alpha) \cdot \left[p_T^{\text{true}} + (1 + \beta) \cdot \left(p_T^{\text{UnCorr}} - p_T^{\text{true}} \right) \right], \tag{5.51}$$

where p_T^{UnCorr} is the uncorrected momentum of the muons. After correction, the data-to-simulation residual is evaluated for both, scale and resolution. These residuals are considered as a systematic source that are introduced into the correction function to propagate them and to generate up and down variations that represent the systematic error. This leads to the final muon momentum calibration results shown in Fig. 5.72 for CB tracks and Fig. 5.73 for the ID track. The gray error band accounts for systematic uncertainties arising from the final scale and resolution and the green error band accounts only for the systematic uncertainty arising due to the scale correction. After correction, a data-to-simulation agreement at the per mille level within the uncertainties is obtained.

5.10 Summary

The charge dependent effects related to the muon sagitta have been evaluated by minimising the variance of the invariant mass distributions. This correction was applied in data for both CB and ID tracks reducing the bias from an average value of 0.05 TeV^{-1} to 2×10^{-4} TeV^{-1}. Showing a good performance at high and low transverse momentum, p_T.

The Inner Detector geometrical deformations have been studied by different models involving radial and longitudinal distortions as well as magnetic field mismodelling. These models were implemented by an analytical template fit showing that more than one parameter model is required in order to correct the global scale and modulations observed in the invariant mean mass values in the Collins-Soper frame. A radial-magnetic field distortion model was chosen with relative bias in the barrel region of $\langle \varepsilon_B \rangle = -1.5 \times 10^{-3}$ and $\langle \varepsilon_R \rangle = 1.0 \times 10^{-3}$ for the magnetic field and radial
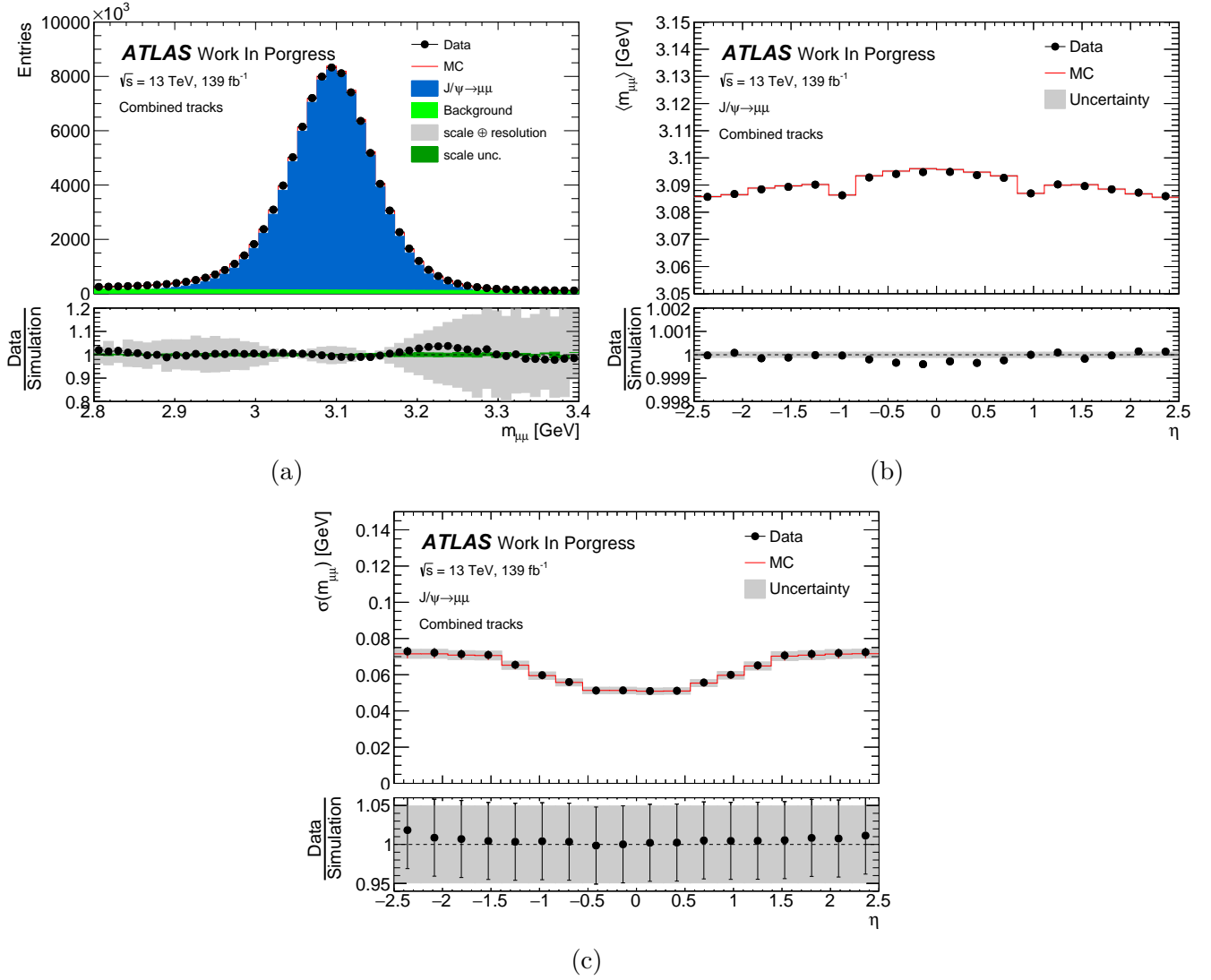
Figure 5.72: Muon momentum calibration in CB tracks for (a) inclusive invariant mass (b) mean invariant mass and (c) invariant mass resolution versus rapidity of both muons in the same category $(\eta_{\mu^+} = \eta_{\mu^-})$.
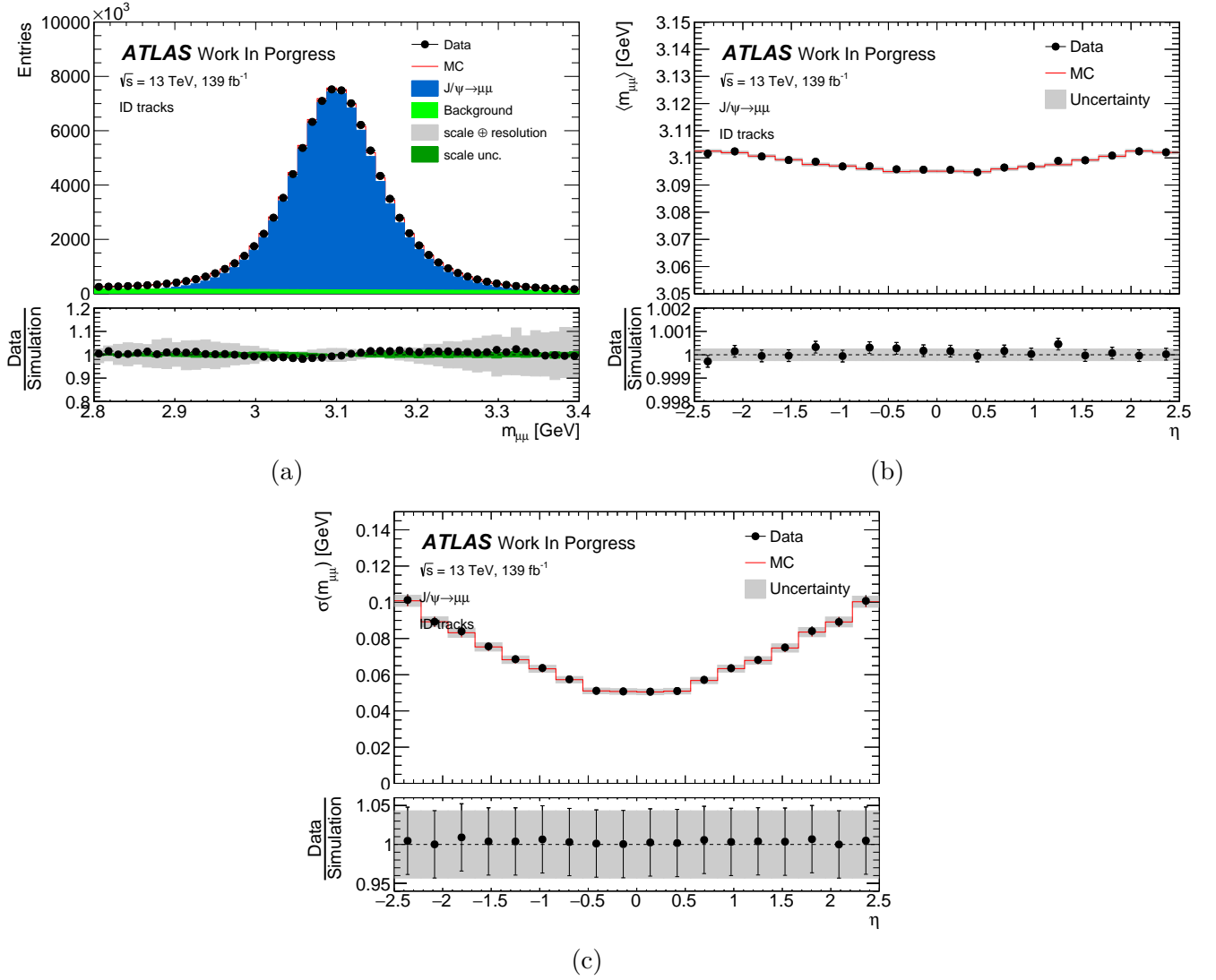
Figure 5.73: Muon momentum calibration in ID tracks for (a) inclusive invariant mass (b) mean invariant mass and (c) invariant mass resolution versus rapidity of both muons in the same category $(\eta_{\mu^+} = \eta_{\mu^-})$.

distortions, respectively. After correction, a good performance over all η values was found, reducing the bias and improving the data-to-simulation agreement at the per mille level in the scales with a small improvement in the resolution. These corrections together were applied to the data affecting directly the transverse and longitudinal components of the momentum of the muons.

On the other hand, the MS/ID misalignment residuals were studied in order to improve the track reconstruction by correcting the perigee parameters $(d_0, z_0, \theta, \phi, q/p)$ in the ID and MS. These studies initially showed a charge dependent effects and a global bias of few mrad in θ and a bias of about 1.5 mm in z_0 with a slope effect, with positive slope for $|\eta| < 1$ and negative slope for $1 < |\eta| < 2.5$. The charge asymmetry effects were corrected by re-evaluating the magnetic field in the tile calorimeter by proposing an initial correction of about 25% of the $\phi-$component (B_ϕ) of the magnetic field in this region. This initial model was extended by mapping the magnetic field integral over the $(\eta, \phi)-$space allowing to get a correction map that once implemented it successfully solved the charge asymmetry in the tracks. On the other hand, to solve the bias associated to the slope and the overall bias observed in z_0 and θ, the second coordinates d_0 and ϕ were also studied in both tracks CB and ID. The second coordinate results showed a bias that could directly be related to the first coordinates (z_0, θ) as a second order effect. These biases were mapped in $(\eta, \phi)-$space and then applied in the tracks in order to correct both, the first and second coordinates. Mixing these corrections next to the magnetic field corrections a good agreement with the simulation was obtained.

Finally, once the pre-corrections were applied to the data the final muon momentum calibration was performed taking into account the scale and resolution parameters. The invariant mass distribution was fitted by a numerical template fit with a quadratic morphing. Different scale templates were prepared by decalibrating the momentum of the muons while the resolution templates were prepared with a deterministic approach at the mass level, allowing to generate narrower and wider samples to better emulate the data. The background was modelled by analytical functions (exponential function) which were varied within their uncertainties to be introduced as systematic sources. The invariant mass fit results were retrieved to perform 2D maps for scale and resolution that later on were introduced into an analytical χ^2 that allowed to obtain the final calibration pa-

rameters with a precision of about 10^{-5}. This correction was applied in the simulation by affecting the transverse component of the momentum of the muons allowing a data-to-simulation agreement at the per mille level. The systematic sources were evaluated by computing the residual between data and simulation after correction, then they were propagated in the simulation. Final results were found to be within the uncertainties.

Chapter 6

W-boson mass

In the Standard Model, the W boson mass at the lowest order can be expressed as a function of the Z boson mass (m_Z), the Fermi constant (G_F) and the fine structure constant (α). When considering higher-orders, the radiative corrections (Δr) introduce additional dependencies of the W boson mass with the gauge couplings and heavy particles. In the SM, these contributions come mainly from the top quark and the Higgs boson. The electroweak theory also predicts the decay width of the W boson (Γ_W) to be equal to the sum of the partial widths over three generations of lepton doublets and two generations of quark doublets. In the presence of new particles that couple to the W boson, the value of Γ_W could be altered. For BSM scenarios, new exotic particles such as SUSY particles or Dark Matter particles (among others) can potentially generate a shift in m_W and Γ_W through loop corrections. These new scenarios could be probed through precise measurements of these parameters and then to be compared with the SM prediction [83],

$$m_W^{\text{SM}} = 80355 \pm 6 \text{ MeV},$$
$$\Gamma_W^{\text{SM}} = 2088 \pm 1 \text{ MeV}.$$

(6.1)

The current average of m_W using LEP [80], D0 [167], ATLAS [76] and LHCb [77] leads to $m_W = 80369.2 \pm 13.3$ MeV [82] that is in tension with the recent CDF collaboration result $m_W = 80433.5 \pm 9.4$ MeV [168]. While for Γ_W the world average leads to $\Gamma_W = 2085 \pm 42$ MeV [16].

The following chapter is focused on the study of the current status of m_W and Γ_W using the 7 TeV

dataset recorded by the ATLAS detector in 2011. As well as the preliminary results and prospects in the precise measurement of m_W using the low pile-up dataset at 5.02 TeV and 13 TeV. The present analysis implements the profile likelihood fit to perform simultaneous determination of m_W and Γ_W as well as the treatment of the systematic sources and a proper uncertainty components by analytical fits as described in Chapter 4. This chapter is organized as follows, Section 6.1 describes the production, physics correction and decay model of the EW vector bosons through the resonance parametrization, electroweak and QCD corrections and angular coefficients. Section 6.2 describes the signal region and background determination used for the present studies and how the different type of background contributions are obtained by simulation and data driven approach. Section 6.3 describes the data samples and the event simulation for the W boson studies. Section 6.4 describes the propagation of calibration uncertainties in m_W. Section 6.5 describes the probability model implemented for the W boson mass and width determination. Section 6.6 shows the study and results for the m_W and Γ_W measurement at $\sqrt{s} = 7$ TeV applying the PLH fit with analytical studies. Section 6.7 study the preliminary results and prospects in m_W uncertainty using PLH fits at low pile-up. Section 6.8 provides the expected precision in m_W measurement exploiting the $\sqrt{s} = 5.02, 7$ and 13 TeV centre-of-mass energy dataset in ATLAS. Section 6.9 studies the compatibility of the new world W-boson mass measurements considering the new ATLAS result discussed in this work, LHCb, CDF, D0 and LEP with different PDF sets.

6.1 Production, physics correction and decay model

The inclusive cross section of the of the $W \rightarrow \ell\nu$ and $Z \rightarrow \ell\ell$ bosons into two leptons final state is a six-dimensional equation. It has been shown that this equation can be factorized into four components in the di-lepton (or boson) system as shown in [76, 146]. It is given by,

$$\frac{d\sigma}{dp_1 dp_2} = \left[\frac{d\sigma(m)}{dm}\right]\left[\frac{d\sigma(y)}{dy}\right]\left[\frac{d\sigma(p_T)}{dp_T}\bigg|_y \frac{d\sigma(y)}{dy}\right]^{-1}\left[(1 + \cos^2\theta) + \sum_{i=0}^{7} A_i(p_T, y, m)P_i(\cos\theta, \phi)\right],$$

(6.2)

where p_1 and p_2 are the lepton and anti-lepton four-momenta, m, p_T, and y, are the invariant mass, transverse momentum, and rapidity of the di-lepton system, respectively. θ and ϕ are the polar and azimuthal angles of the lepton in the di-lepton system rest frame, P_i are the spherical harmonics functions and A_i are the angular coefficients. The angular coefficients are functions of p_T, y and m, and they represent the ratios of the helicity cross sections with respect to the unpolarized cross section of the boson production. The $A_5 - A_7$ coefficients are non-zero only at order $\mathcal{O}(\alpha_s^2)$ and above.

Eq. (6.2) provides a simplified modelling of the mass-distribution $d\sigma(m)/dm$ (boson resonance) with respect to the pole-mass of the W boson using Breit-Wigner distribution and including electroweak corrections. The differential cross section, $d\sigma(y)/dy$, and the angular coefficients, A_i, are modelled with fixed-order perturbative QCD predictions, at $\mathcal{O}(\alpha_s^2)$ in the perturbative expansion of the strong coupling constant. The transverse momentum spectrum at given rapidity, $(d\sigma(p_T)/dp_T)(d\sigma(y)/dy)$ is given by analytic resummation or tuned parton shower.

6.1.1 Resonance Parameterization

The boson resonance, $d\sigma(m)/dm$, is parameterized by a Breit-Wigner distribution based on the gauge interactions and couplings for the Neutral Currents (NC) and Charged Currents (CC). This is giving by the following lagrangians,

$$
\begin{aligned}
\mathcal{L}_{NC} &= \sum_{i=\gamma,Z} \alpha_i f \bar{f} \gamma^\mu (v_{fi} - a_{fi}\gamma^5) f V_{i\mu} \\
\mathcal{L}_{CC} &= \alpha_W V_{ff'} \bar{f} \gamma^\mu (1 - \gamma^5) f W_\mu
\end{aligned}
\tag{6.3}
$$

where α_i, $V_{f\bar{f}}$, v_{fi} and a_{fi} are the coupling constants, CKM matrix mixing elements and the vector and axial couplings for the incoming and outgoing fermions. These are summarized in the Table 6.1.

At leading order, the parton-level cross sections for $q\bar{q} \to \ell\ell$ and $q\bar{q}' \to \ell\nu$ can be generically

Table 6.1: Vertex factors for different interactions in the Standard Model. α corresponds to the Gauge couplings, v_i and a_i are the vector and axial couplings and V_i the CKM matrix elements.

Vertex	γff	Zff	Wff'
α_i	α_{em}	$\frac{G_\mu m_Z^2}{2\sqrt{2}\pi}$	$\frac{G_\mu m_W^2}{\sqrt{2}\pi}$
v_i	Q_f	$I_{3f} - 2Q_f \sin^2\theta_W$	$\frac{I_{3f}}{I_{3f}}$
a_i	0	I_{3f}	$\frac{I_{3f}}{I_{3f}}$
V_i	1	1	$V_{ff'}$

written as,

$$\hat{\sigma}(\hat{s}) \quad \propto \quad \sum_{i,j} \alpha_i \alpha_j V_i V_j B_{ij} P_{ij}(\hat{s}), \tag{6.4}$$

$$B_{ij} \quad = \quad (v_i v_j + a_i a_j)_{\text{in}}(v_i v_j + a_i a_j)_{\text{out}}, \tag{6.5}$$

$$P_{ij}(\hat{s}) \quad = \quad \hat{s}\frac{(\hat{s} - m_i^2)(\hat{s} - m_j^2) + m_i m_j \Gamma_i \Gamma_j}{[(\hat{s} - m_i^2)^2 + (m_i \Gamma_i)^2][(\hat{s} - m_j^2)^2 + (m_j \Gamma_j)^2]}, \tag{6.6}$$

where the summation runs over the exchanged gauge bosons in the $s-$channel. In the case of NC interactions, the indices i, j can run over the γ and Z boson. For the CC interactions, they run only over the W boson. This allows to interpret the equal terms $i = j$ as the squared amplitude corresponding to the exchange of a given boson while for $i \neq j$ corresponds to the $\gamma - Z$ interference. The mass and width of gauge boson i are denoted as m_i and Γ_i, and $\hat{s}$ is the available energy for the parton-level process.

Eq. (6.6) corresponds to a fixed-width Breit-Wigner parametrization that is suitable for generators. However, for other analyzes such as the one for m_Z at LEP [169] and m_W [76] a running-width parametrization is used. In this, the terms $m\Gamma$ are replaced by $\frac{\hat{s}}{m}\Gamma$ as follows,

$$P'_{ij}(\hat{s}) = \hat{s}\frac{(\hat{s} - m_i'^2)(\hat{s} - m_j'^2) + \frac{\hat{s}^2}{m_i' m_j'}\Gamma_i' \Gamma_j'}{\left[(\hat{s} - m_i'^2)^2 + \left(\frac{\hat{s}}{m_i'}\Gamma_i'\right)^2\right]\left[(\hat{s} - m_j'^2)^2 + \left(\frac{\hat{s}}{m_j'}\Gamma_j'\right)^2\right]} \tag{6.7}$$

where the primed quantities refers to the running variables and they should not be confused with their fixed-width quantities. However, both Eq. (6.6) and (6.7) are equivalent through the

parametrization,

$$m_i = m'_i \sqrt{1 + \left(\frac{\Gamma'_i}{m'_i}\right)^2}$$
$$\Gamma_i = \Gamma'_i \sqrt{1 + \left(\frac{\Gamma'_i}{m'_i}\right)^2}$$

(6.8)

If Eq. (6.7) is used, the physical masses and widths of the gauge bosons should be taken from the PDG values [170] for the nominal simulation.

6.1.2 Electroweak corrections

The formalism described above is only valid when no real photons are emitted, since this is not the case, it needs to be corrected. In ATLAS, the simulations are corrected using PHOTOS [156] that are in charge of generating photon emissions and modifying the final state lepton kinematics starting from the Born-level.

PHOTOS is a Monte Carlo algorithm used to apply QED radiative corrections in the decay processes of particles. It operates as an "after-burner", adding bremsstrahlung photons to decay events generated by other programs. This allows for the simulation of radiative corrections without needing the host generator to consider these effects. The algorithm can add multiple photons to an event, ensuring coverage of the phase space and treating collinear regions by considering the masses of the charged particles. Photons are calculated using an iterative procedure where each photon's four-momentum is adjusted to respect energy-momentum conservation, while also considering the photon's probability distribution according to QED matrix element. The algorithm takes into account various factors, such as interference effects, to ensure that the radiation pattern matches the precise predictions of QED. The algorithm can be applied to any decay process and is designed to work seamlessly with other Monte Carlo generators, improving the accuracy of simulations involving radiative decays. The iteration ends when the photon energy is smaller than 10^{-7} times the energy of the parent in the decay rest frame. The iterative FSR approach is shown in Fig. 6.1. The present study is performed by generating events using POWHEG+PYTHIA 8 and PHOTOS as done for the

main analysis samples, only changing the settings in PHOTOS.
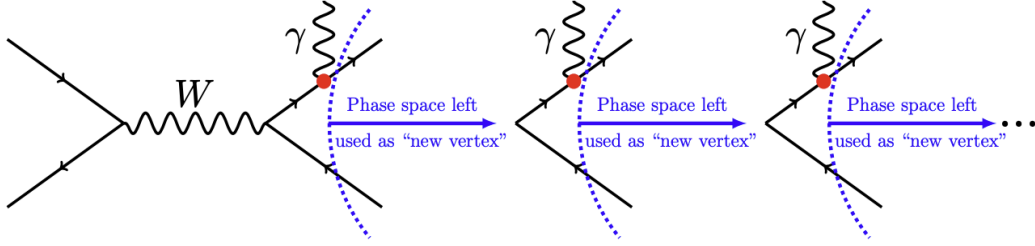
Figure 6.1: Iterative FSR treatment using PHOTOS. The dot represents the matrix element for a single photon emission. After each photon emission, the outgoing lepton lines (right of the dashed line) are considered by Photos again for further photon emissions, in an interactive way [171].

6.1.3 Boson rapidity and transverse momentum

In the m_W measurement analysis, the differential cross section as a function of boson rapidity, $d\sigma(y)/dy$, is modelled with fixed order perturbative QCD predictions at $\mathcal{O}(\alpha_S^2)$ in the perturbative expansion of the strong-coupling constant. However, the majority of the W bosons used in the present analysis are at low value of boson transverse momentum ($p_T^W < 30$ GeV) where the resummation of large logarithms $\log(m_V/p_T)$ is needed and non-perturbative effects should be accounted. For this, the parton showers are introduced to predict the transverse momentum spectrum of vector boson at a given boson rapidity $d\sigma(p_T)/dp_T|_y$. In the present analysis, the parton shower AZNLO tune of Powheg+PYTHIA8 is used. This employs leading order matrix elements for the $q\bar{q}' \to W, Z/\gamma^*$ processes, complemented by a reweighting of the first parton shower emission to the leading order $V +$ jet cross section, with $V = W, Z/\gamma^*$. Current study in Ref. [75] performed a precision measurement of the W and Z boson transverse momentum at 5.02 and 13 TeV with low pile-up data. In this study, a direct measurement of p_T^W is performed instead of modelling it based on the measured p_T^Z. This approach avoids the uncertainty due to the extrapolation.

6.1.4 Angular coefficients

At leading order without Initial State Radiation (ISR) QCD, the bosons are only transvely polarized and the angular distribution of the decay leptons depends only depends in the polar angle θ.

When going to higher order amplitudes, the colliding partons ISR QCD interactions provide transverse momentum to the W or Z bosons. This affects the polarization state resulting in azimuthal asymmetries that are encoded into eight the angular coefficients A_i. Eq. (6.2) can be expressed as follows,

$$
\begin{aligned}
\frac{d\sigma}{dp_T^2 dy dm d\cos\theta d\phi} = \frac{3}{16\pi} \frac{d\sigma}{dp_T^2 dy dm} \times &\left[(1 + \cos^2\theta) + A_0 \frac{1}{2}(1 - 3\cos^2\theta) \right. \\
&+ A_1 \sin 2\theta \cos\phi + A_2 \frac{1}{2}\sin^2\theta \cos 2\phi \\
&+ A_3 \sin\theta \cos\phi + A_4 \cos\theta \\
&\left. + A_5 \sin^2\theta \sin 2\phi + A_6 \sin 2\theta \sin\phi + A_7 \sin\theta \sin\phi \right]
\end{aligned}
\tag{6.9}
$$

that using the completeness of the spherical harmonics,

$$
\langle P_i(\theta, \phi) \rangle = \frac{\int_{-1}^{1} d\cos\theta \int_0^{2\pi} d\phi d\sigma(\theta, \phi) P_i(\theta, \phi)}{\int_{-1}^{1} d\cos\theta \int_0^{2\pi} d\phi d\sigma(\theta, \phi)},
\tag{6.10}
$$

the angular coefficients A_i can be obtained as a function of the polar and azimuthal angles,

$$
\begin{aligned}
A_0 &= 4 - 10\langle \cos^2\theta \rangle, \\
A_1 &= 5\langle \sin(2\theta)\cos\phi \rangle, \\
A_2 &= 10\langle \sin^2\theta \cos(2\phi) \rangle, \\
A_3 &= 4\langle \sin\theta \cos\phi \rangle, \\
A_4 &= 4\langle \cos\theta \rangle, \\
A_5 &= 5\langle \sin^2\theta \sin(2\phi) \rangle, \\
A_6 &= 5\langle \sin(2\theta)\sin\phi \rangle, \\
A_7 &= 4\langle \sin\theta \sin\phi \rangle,
\end{aligned}
\tag{6.11}
$$

where θ and ϕ are obtained defined in the Collins-Soper frame. In general, the A_i coefficients are functions of the transverse momentum, rapidity and boson mass but the dependence on the boson mass is negligible such that, the predictions can be performed with a fixed boson mass. The correlations between the two decay leptons due to the polarization of the vector boson are not well

modelled in the baseline simulation since only NLO QCD accuracy can be reached. To improve this, the coefficients are reweighted to NNLO predictions following the same strategy as described in Ref. [76]. The reweighting is carried out using DYTURBO at $\mathcal{O}(\alpha_s^2)$ and POWHEG+PYTHIA 8 as follows,

$$w = \frac{1 + \cos^2\theta + \sum_{i=0}^{7} A_i'(p_T, y)P_i(\cos\theta, \phi)}{1 + \cos^2\theta + \sum_{i=0}^{7} A_i(p_T, y)P_i(\cos\theta, \phi)}. \tag{6.12}$$

where A_i is the initial prediction of an angular coefficient and A_i' is an alternative prediction.

6.2 Signal region and Background determination

The signal region encompasses the muon channel and electron channel in different η regions for the 7 TeV while for 5.02 TeV and 13 TeV categories in u_T and η regions are considered. The background encodes the contributions from the electroweak and top processes modelled by MC simulation while the multijet (MJ) estimation is obtained from data-driven method.

6.2.1 Signal region

Electrons: are reconstructed from clusters of energy deposited in the EM calorimeter and associated with at least one ID track. They are required to pass the tight identification criterion of a cut-based discriminating variables, to have a transverse momentum of $p_T^e > 15$ GeV and an absolute pseudorapidity of $|\eta| < 2.47$ excluding the calorimeter crack region (transition barrel to end-cap) $1.2 < |\eta| < 1.82$. Background from jets misidentified as electrons is reduced using additional isolation requirements. For this, the activity in the ID and calorimeter nearby the electron candidates passing the kinematic and identification selections is used as measured by tracks in a cone of size $\Delta R < 0.2$ around the candidate.

Muons: the reconstruction of the muons is performed independently in the ID and the MS and a combined muon candidate (CB) is formed from the statistical combination of the two tracks information. To ensure that the reconstructed muons are originated from the primary vertex (PV) the track-to-vertex association requirement is imposed, i.e. $|z_0 \sin\theta| < 0.5$mm and $|d_0|/\sigma(d_0) < 3$. Candidates are selected by single-muon trigger with kinematic properties that considers transverse

momentum of $p_T^\mu > 20$ GeV and absolute pseudorapidity of $|\eta| < 2.4$ with Medium identification criteria ensuring a good distribution of the channel $W \to \mu\nu$ from the background. The multijet background is reduced by applying an isolation requirement as in the electrons selection.

W **boson selection:** *W* boson candidates are chosen to contain exactly one identified and isolated lepton candidate satisfying the criteria described above. If an event has more than one lepton associated, this is rejected to reduce the *Z* background. The transverse momentum of the decay neutrino is inferred from the missing transverse momentum ($\vec{p}_T^{\mathrm{miss}}$) and its magnitude ($E_T^{\mathrm{miss}}$) that are defined from $\vec{p}_T^\ell$ and $\vec{u}_T$, as $\vec{p}_T^{\mathrm{miss}} = -(\vec{p}_T^\ell + \vec{u}_T)$. The transverse mass is reconstructed as $m_T = \sqrt{2p_T^\ell p_T^{\mathrm{miss}}(1 - \cos\Delta\phi)}$, with $\Delta\phi$ the azimuthal opening angle between the charged lepton and the missing transverse momentum. The recoil, $\vec{u}_T$ is reconstructed from the vector sum of the transverse energy of all clusters measured in the calorimeters, excluding clusters located at a distance $\Delta R < 0.2$ from electron or muon candidates.

To minimize the background contribution (mainly multijet) and the model uncertainties, the following cuts in the *W* kinematics are used at 7 TeV,

- Lepton transverse momentum $p_T^\ell > 30$ GeV.

- Hadronic recoil as a measure of p_T^W: $u_T < 30$ GeV.

- Neutrino transverse momentum: $E_T^{\mathrm{miss}} > 30$ GeV.

- W boson transverse mass: $m_T^W > 60$ GeV.

leading to 5.9×10^6 candidate events in the $W \to e\nu$ channel and 7.8×10^6 candidate events in the $W \to \mu\nu$ channel after cuts. Final studies considered the 28 categories for electrons and muons as shown in Table 6.2.

Table 6.2: Summary of the 28 categories and kinematic distributions used in the m_W measurement for the electron and muon decay channels at $\sqrt{s} = 7$ TeV.

Decay channel	$W \to e\nu$	$W \to \mu\nu$
Kinematic distributions	p_T^ℓ, m_T	p_T^ℓ, m_T
Charge categories	W^+, W^-	W^+, W^-
$|\eta_\ell|$ categories	[0, 0.6], [0.6, 1.2], [1.8, 2.4]	[0, 0.8], [0.8, 1.4], [1.4, 2.0], [2.0, 2.4]

For the low pile-up at 5.02 TeV and 13 TeV, the cuts are,

- Lepton transverse momentum $p_T^\ell > 25$ GeV.

- Hadronic recoil as a measure of p_T^W: $u_T < 25$ GeV.

- Neutrino transverse momentum: $E_T^{\mathrm{miss}} > 25$ GeV.

- W boson transverse mass: $m_T^W > 50$ GeV.

leading to a total number of 7.1×10^5 (2.2×10^6) W-boson candidate events in the $W \to e\nu$ channel and 7.5×10^5 (2.2×10^6) in the $W \to \mu\nu$ channel for the 5.02 TeV (13 TeV) data after cuts. Samples are categorized in u_T and η with 20 bins as shown in Table 6.3. This results in a total 20 categories per channel and energy.

Table 6.3: Summary of the 20 categories per channel and centre-of-mass energy and kinematic distributions used in the m_W measurement at $\sqrt{s} = 5.02$ and 13 TeV for the electron and muon decay channels.

Decay channel	$W \to e\nu$	$W \to \mu\nu$
Kinematic distributions	p_T^ℓ, m_T	p_T^ℓ, m_T
Charge categories	W^+, W^-	W^+, W^-
$|\eta_\ell|$ categories	[0, 0.6], [0.6, 1.2], [1.2, 1.8], [1.8, 2.47]	[0, 0.8], [0.8, 1.4], [1.4, 2.0], [2.0, 2.4]
u_T categorites	[0, 5], [5, 10], [10, 15], [15, 20], [20, 25]	[0, 5], [5, 10], [10, 15], [15, 20], [20, 25]

6.2.2 Electroweak and top quark background

In the $W \to \ell\nu$ channels for $\ell = e, \mu$, the background receives contributions from $W \to \tau\nu$, $Z \to \ell\ell, \tau\tau$, Gauge-boson pair production (diboson: WW, ZZ, WZ), top processes ($t\bar{t}$ and single top t) and multijet (MJ) events. Apart from the MJ, the EW and top can be modelled with high accuracy with respect to the theoretical predictions directly from the MC simulation. Top processes are generated with POWHEG+PYTHIA 8 and TOP++ prediction reported by CMS [172]. For the di-boson background, SHERPA [173] is implemented in all the decay channels for at least one real lepton in the final state. The impact of the uncertainty is considered by assigning a 10% relative uncertainty to the top-quark and diboson background cross sections except for the $t\bar{t}$ cross-section where a 7% is assigned.

From the mentioned backgrounds, the larger contribution is coming from $Z \to \ell\ell$ events in both channels when one of the leptons escapes detection and mimics missing transverse momentum. The

second largest background is coming from leptonic decays such as τ decaying into electrons or muon. However, the Z boson events as well as the τ at the LHC are very well understood as well as its background such that the contribution can be well estimated from MC simulations.

6.2.3 Multijet (MJ) estimation

The W candidates are accompanied by multijet background that originates from semi-leptonic decays of heavy quarks ($b-$ and $c-$quarks) and in-flight pion decays. These have an important contribution due to its large cross-section. In the muon channel, long-lived hadrons passing through the calorimeter represent an additional source of background since they can mimic a muon signal. In the electron channel the processes already mentioned are included but also the pion faking an electron or photon conversion are sources of background. In contrast to the EW and top processes, the MJ background cannot be well simulated using MC predictions and by consequence, the data-driven approach is implemented [174, 175]. In this method, the MJ background estimate in the signal region is constructed from a jet-enriched control region in data by reversing or relaxing some of the isolation requirements. From this control region is posible to obtain the shape of the background.

The W-boson phase-space in the signal region (SR) used for the main measurement is defined by the following selections:

- $p_T^\ell > 25$ GeV and $|\eta^\ell| < 2.4$.

- $E_T^{\mathrm{miss}} > 25$ GeV.

- $m_T > 50$ GeV.

- Lepton isolation as $p_T^{\mathrm{cone20}}/\min(p_T, 50 \text{ GeV}) < 0.1$.

Four regions are defined by relaxing the kinematic cuts and inverting the lepton isolation selection as shown in Table 6.4. The four signal regions are given by,

- Signal region (SR): Isolated leptons and signal phase-space for p_T^ℓ, E_T^{miss} and m_T.

- Fit region (FR): Isolated leptons, but without E_T^{miss} or m_T cut.

- Control region 1 (CR1): Anti-isolated leptons ($p_T^{\text{cone20}}/\min(p_T, 50 \text{ GeV}) > 0.1$) and relaxed kinematic cuts like FR.

- Control region 2 (CR2): Anti-isolated leptons with full kinematic cuts like SR.

Table 6.4: Selection criteria for the four different regions in the data driven method for MJ estimation.

Fit Region (FR)	Signal Region (SR)
$p_T^\ell > 25$ GeV	$p_T^\ell > 25$ GeV
$m_T > 0$ GeV	$m_T > 50$ GeV
$E_T^{\text{miss}} > 0$ GeV	$E_T^{\text{miss}} > 25$ GeV
Lepton isolation < 0.1	Lepton isolation < 0.1
Control Region 1 (CR1)	Control Region 2 (CR2)
$p_T^\ell > 25$ GeV	$p_T^\ell > 25$ GeV
$m_T > 0$ GeV	$m_T > 50$ GeV
$E_T^{\text{miss}} > 0$ GeV	$E_T^{\text{miss}} > 25$ GeV
Lepton isolation > 0.1	Lepton isolation > 0.1

To extract the fraction and shape of the MJ in the SR, the two CR are used, CR1 and CR2 through the fraction fit method. This is based on a binned maximum likelihood fit of the combination of all samples modelling in Monte Carlo (signal, multijet, top, electroweak) to the observed candidate events from data. In this fit, the relative normalisation of all modelled in Monte Carlo samples (signal $W \to \ell\nu$ and backgrounds $W \to \tau\nu_\tau, Z \to \ell\ell$, di-bosons, Top processes), is fixed according to proton-proton cross-section. While the normalizations of the multijet background and total MC-based contributions are allowed to float. Once the fit has been performed and the multijet samples has been normalized, the MJ background is calculated in the SR by the ratio of the MJ events to the number of all selected events in data.

Since the MJ is mainly produced for lower values of p_T^ℓ, E_T^{miss} and m_T, it is convenient to determine the MJ fraction in the FR, that is the region where the E_T^{miss} and m_T cuts are relaxed. Then, the total number of data events in the FR, $N_{\text{data}}^{\text{FR}}$, is given by,

$$N_{\text{data}}^{\text{FR}} = \alpha \cdot N_{\text{EW+Top}}^{\text{FR}} + T \cdot N_{\text{MJ}}^{\text{CR1}}, \tag{6.13}$$

where $N_{\text{EW+Top}}^{\text{FR}}$ is the expected contribution from electroweak and top-quark process in the FR and $N_{\text{MJ}}^{\text{CR1}}$ is the number of MJ events in CR1 given by, $N_{\text{MJ}}^{\text{CR1}} = N_{\text{data}}^{\text{CR1}} - N_{\text{EW + Top}}^{\text{CR1}}$. T is the scale of the MJ template in FR to be determined by the fit and α is the overall normalization of contribution from electroweak and top process approximately equal to one, within the uncertainties in luminosity and production cross-sections. This, allows to approximate the MJ yield as,

$$N_{\text{MJ}}^{\text{FR}} \approx T \cdot N_{\text{MJ}}^{\text{CR1}}. \tag{6.14}$$

Notice that FR and CR1 share the same kinematic cuts similarly to SR and CR2 (with difference in E_T^{miss} and m_T). Therefore, the FR yield can be extrapolated to the obtain the SR yield by introducing a transfer factor $\varepsilon = N_{\text{MJ}}^{\text{CR2}}/N_{\text{MJ}}^{\text{CR1}}$ derived from the two control regions, such that,

$$N_{\text{MJ}}^{\text{SR}} = \varepsilon \cdot N_{\text{MJ}}^{\text{FR}} = \frac{N_{\text{data}}^{\text{CR2}} - N_{\text{EW+top}}^{\text{CR2}}}{N_{\text{data}}^{\text{CR1}} - N_{\text{EW+top}}^{\text{CR1}}} \times N_{\text{MJ}}^{\text{FR}}. \tag{6.15}$$

In this way, the CR1 and CR2 are used to derived the shape of the MJ template used in the fraction fit in the FR and the MJ shape in the SR region, respectively.

6.3 Data samples and event simulation

Two datasets are implemented corresponding to different data-taking periods, Run1 and Run2 at different centre-of-mass energy and luminosities.

6.3.1 Dataset at 7 TeV

The data sample considers $W \to e\nu$ and $W \to \mu\nu$ candidate events, collected in 2011 in proton$-$proton collisions at a centre-of-mass energy of $\sqrt{s} = 7$ TeV. The data collected with all relevant detector systems operational correspond to integrated luminosity of 4.6 fb^{-1} and 4.1 fb^{-1} in the electron and muon channels, respectively.

For the simulation, the W and Z boson production and decay in the electron, muon and tau channels have been produced using POWHEG+PYTHIA 8 MC generator and parton shower. The

effect of virtual photons are included in the Z simulation and the QED final state radiation (FSR) is simulated using PHOTOS. Several PDF sets are implemented, in particular, CT10 is used for hard processes while CTEQ6L1 is used for the parton shower. Kinematically, the W and Z bosons rapidity and p_T^ℓ are reweighted to optimized the data. The $\tau-$lepton decays are handled by PYTHIA8 taking into accoun the polarisation effects. The W and Z boson event yields are normalised according to their measured cross sections with a 1.8% and 2.3% uncertainties assigned to the W^+/Z and W^-/Z production cross-section ratios, respectively. The W production samples assume $m_W = 80399$ MeV and $\Gamma_W = 2085$ MeV. Background processes such as top-quark pair and single-top-quark production are modelled using the MC@NLO MC generator interfaced to HERWIG and JIMMY for the parton shower. Gauge-boson pair production (WW, WZ, ZZ) is simulated with HERWIG v6.520. The CT10 PDF set is used in all these samples. The detector response is simulated using a software suite based on GEANT4. The hard-scattering process is overlaid with additional proton–proton interactions, simulated with PYTHIA8 (v8.165) using the A2 tune. The distribution of the average number of interactions per bunch crossing $\langle \mu \rangle$ spans the range 2.5–16.0, with a mean value of approximately 9.0. The present analysis is performed using different PDF sets such as ATLASpdf21, CT18, CT18A, MSHT20, NNPDF3.1 and NNPDF4.0 to study the PDF dependence.

The m_W is extracted using the template fit approach in which W-boson width, Γ_W, is treated as a source of systematic uncertainty, considering the SM value and uncertainty of $\Gamma_W^{\mathrm{SM}} = 2088 \pm 1$ MeV. In the $\sqrt{s} = 7$ TeV case, the Γ_W has been also obtained using a similar approach in which m_W is treated as a systematic uncertainty assuming the SM prediction and uncertainty of the $m_W^{\mathrm{SM}} = 80355 \pm 6$ MeV. Templates for p_T^ℓ and m_T with different values of m_W or Γ_W are shown in Fig. 6.2.

6.3.2 Low pile-up dataset at 5.02 TeV and 13 TeV

Similarly to the 7 TeV dataset, the low pile-up dataset consists of $W \to e\nu$ and $W \to \mu\nu$ candidate events. During 2017 and 2018, the LHC carried out a low pile-up run with an average number of proton$-$proton interactions, $\langle \mu \rangle$, of about two, as compared to $\langle \mu \rangle \sim 34$ for the nominal LHC Run 2. The low pile-up datasets correspond to an integrated luminosities of 254.9 pb^{-1} at $\sqrt{s} = 5.02$ TeV
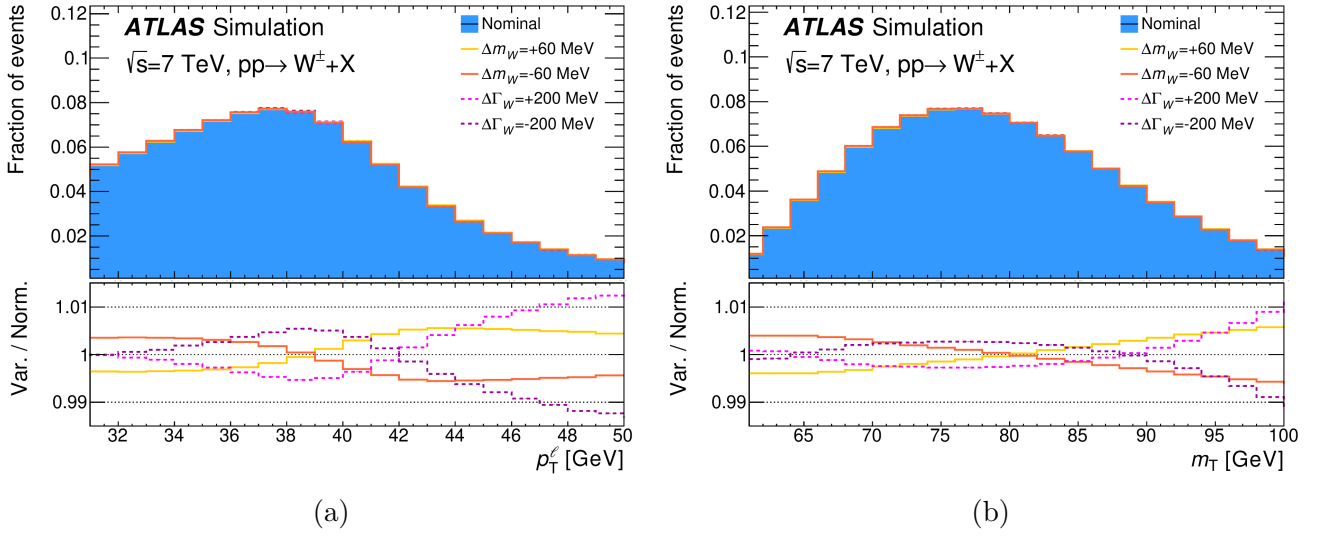
Figure 6.2: Simulated kinematic distributions of (a) p_T^ℓ and (b) m_T, for W-boson mass and width values of $m_W = 80399$ MeV and $\Gamma_W = 2085$ MeV. The ratio panels represent the relative effect (sensitivity) of varying these parameters by ± 60 MeV and ± 200 MeV, respectively.

and 338.1 pb^{-1} at $\sqrt{s} = 13$ TeV and only data collected with all relevant detector systems operational are considered [108]. The low pile-up dataset is of particular interest since it can provide a good hadronic recoil resolution for which the thresholds applied to suppress noise in the reconstruction of clusters of energy in the calorimeters were lowered. The data was collected with triggers that require at least one electron or muon with transverse momentum thresholds of $p_T^e > 15$ GeV and $p_T^\mu > 14$ GeV, respectively [108–110]. Loose identification criteria are applied at the trigger level for electron or muon candidates.

For the simulation, a dedicated MC campaign at low pile-up has been performed. In which no further pile-up reweighting needs to be applied to the MC samples since the low pile-up distributions are already considered. The signal process takes into account the W-boson decay into the leptonic channels.

The W and Z signal processes are generated using POWHEG with CT10 PDF set interfaced with PYTHIA8 for the parton shower using the AZNLO tune. To keep the PDF baseline matching the variations at 7 TeV, a reconstructed level PDF reweighting is applied to the unrolled distributions, p_T^ℓ and m_T, to replace the baseline PDF by CT18A PDF set. The QED final state radiation (FSR) is simulated using PHOTOS++ and the W and Z cross sections are normalized to the

NNLO calculation performed using DYTurbo with the MMHT2014nnlo PDF set. Similarly to the $\sqrt{s} = 7$ TeV analysis, the signal region is considered to be the electron ($W \to e\nu$) and muon ($W \to \mu\nu$) channels while the $\tau-$lepton decay ($W \to \tau\nu$) is taken as one of the electroweak background as well as the top-quark related process.

Given the uncertainties in the choice of the PDF set, including its internal uncertainties (approximately 3-4%), the dependence on factorization and renormalization scales (less than 1%), and the uncertainty of the strong coupling constant α_s (about 1-2%), a conservative total uncertainty of 5% is assigned to the event count predictions normalized using these cross-sections.

The top-quark pair production $t\bar{t}$ and the single top-quark production corresponding to Wt, $t-$channel and $s-$channel are generated with Powheg+Pythia 8. The $t\bar{t}$ the crosssection at $\sqrt{s} = 5.02$ TeV is taken from the Top++ prediction reported by CMS [172]. The Gauge boson pair-production (di-boson background: WW, WZ, ZZ) are produced with Sherpa [173] in all the decay channels for at least one real lepton in the final state. Uncertainties of 10% are assigned to the top-quark related background and the di-boson background cross-sections, except for $t\bar{t}$ process, for which a cross-section uncertainty of 7% is assigned.

To model the multiple interactions per bunch crossing (pile-up) effect, simulation of minimum bias events were generated using Pythia8 with NNPDF2.3LO global PDF set and the A3 tune to be superimposed over the hard-scattering events. The soft QCD background (multijet) were obtained by data-driven approach.

Similarly to the 7 TeV, the m_W is extracted using the template fit approach for the W boson for two observables, p_T^ℓ and m_T, corresponding to projection of the same data in the case of 5.02 TeV and 13 TeV. For each observable, channel and centre-of-mass energy, five categories in u_T are implemented in which four categories in η_ℓ are considered with 20 bins (20 distributions with 400 bins in total). Templates for m_W in $W \to e\nu$ and $W \to \mu\nu$ are shown in Fig. 6.3 and 6.4.
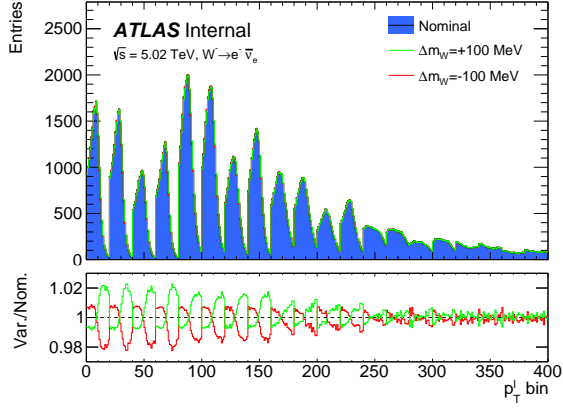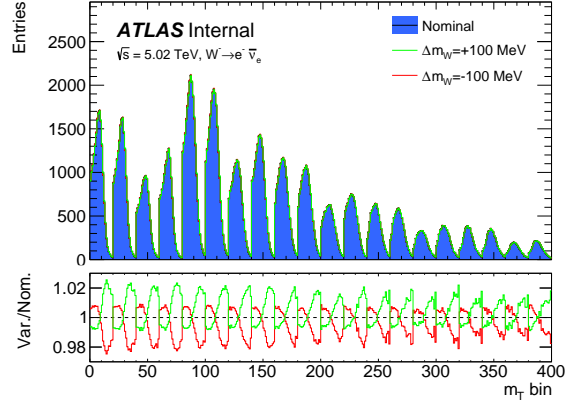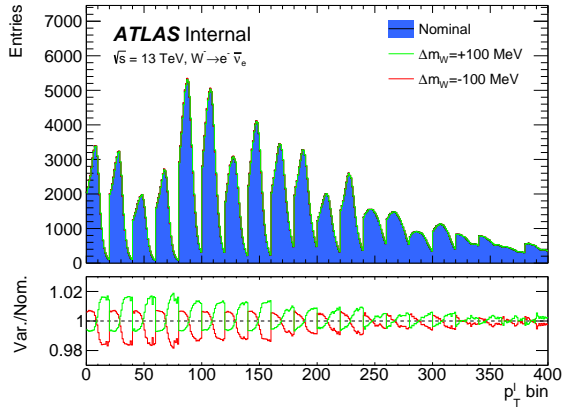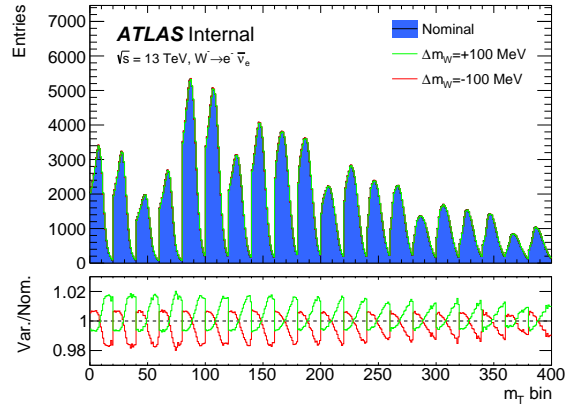
Figure 6.3: Simulated $W \rightarrow e\nu$ kinematic distributions at $\sqrt{s} = 5.02$ TeV for (a) p_T^ℓ and (b) m_T and $\sqrt{s} = 13$ TeV for (c) p_T^ℓ and (d) m_T for W-boson mass of $m_W = 80399$ MeV. The ratio panels represent the relative effect of varying the m_W parameter by ± 100 MeV in all the categories.
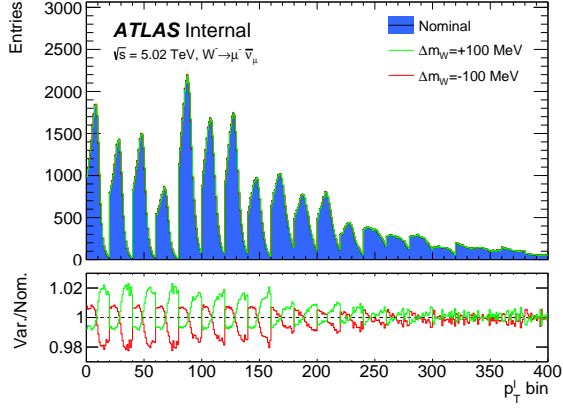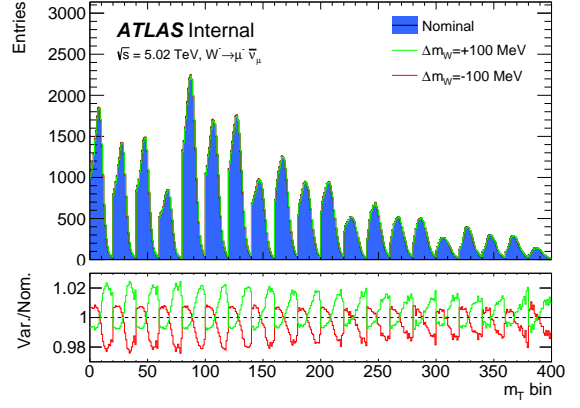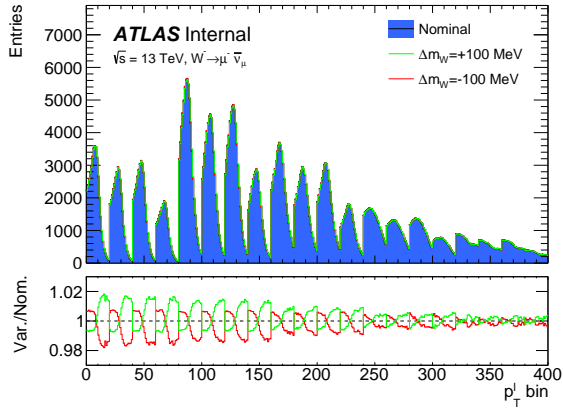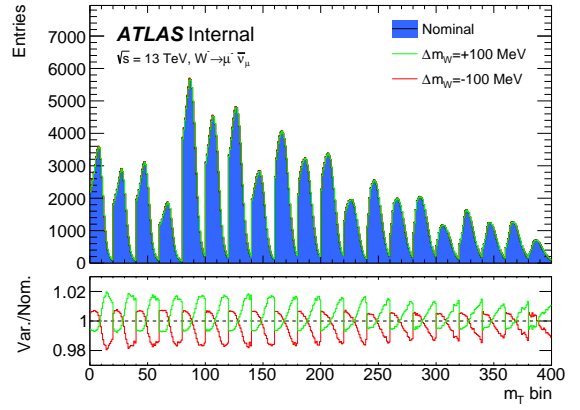
Figure 6.4: Simulated $W \to \mu\nu$ kinematic distributions at $\sqrt{s} = 5.02$ TeV for (a) p_T^ℓ and (b) m_T and $\sqrt{s} = 13$ TeV for (c) p_T^ℓ and (d) m_T for W-boson mass of $m_W = 80399$ MeV. The ratio panels represent the relative effect of varying the m_W parameter by ±100 MeV in all the categories.

6.4 Propagation of uncertainties in m_W

The main sources of uncertainties affecting the p_T^ℓ and m_T distributions are the lepton energy calibration and the recoil calibration. The lepton momentum corrections are obtained using $Z \rightarrow \ell\ell$ resonance and measuring its mass, m_Z. The recoil response is calibrated using the expected momentum balance between u_T and $p_T^{\ell\ell}$. The tag-and-probe method is implemented for the lepton identification and reconstruction efficiency corrections. After the corrections, a precision of $\mathcal{O}(10^{-4})$ in the energy and momentum scale for electrons and muons is obtained while the response and resolution of the hadronic recoil, u_T, is determined with a few percent precision.

6.4.1 Uncertainty propagation

The methodology for evaluating and managing the systematic uncertainties in the W-boson mass, m_W, and width measurement, Γ_W, involves varying the calibration model parameters within their known uncertainties and generating templates for these variations. Principal Component Analysis (PCA) is employed to transform these variations into a set of uncorrelated, two-sided uncertainties, allowing for a streamlined and efficient representation of uncertainties. This approach aids in a more precise and accurate determination of the W-boson's properties by effectively handling and minimizing the impact of systematic uncertainties on the analysis.

Due to the finite size of the MC samples, a smoothing process is applied to the systematic variations to remove statistical fluctuations. This step is important for ensuring that the uncertainty estimates accurately reflect true systematic effects rather than random noise or sample size limitations. The smoothing process helps in maintaining the integrity of the measurement by focusing on genuine systematic trends and minimizing the impact of statistical anomalies on the final results.

6.4.2 Sources of uncertainties at 7 TeV

The sources of uncertainties comes from electrons, muons and hadronic recoil mainly. For electrons, the sources considered are the electron calibration and selection efficiencies including the energy scale and resolution as well as the electron identification, isolation, and trigger efficiencies that

correspond to 75 sources on p_T^ℓ and 58 in m_T. From which 23 are originated from the energy calibration while 52 in p_T^ℓ and 35 in m_T comes from the trigger, reconstruction, identification and isolation efficiencies. In the case of the muons, the muon response and efficiencies contribute to 83 sources in p_T^ℓ and 76 sources in m_T. The calibration of the hadronic recoils leads to 36 sources of systematic uncertainties for the m_T distributions, but only 7 sources for the p_T^ℓ distributions since the impact on the p_T^ℓ are only due to the hadronic recoil requirement in the signal selection.

6.4.3   Sources of uncertainties at low pile-up

Several sources of experimental, background, and luminosity uncertainties are considered. For electron reconstruction and calibration, scale factors (SFs) are measured from high pile-up and extrapolated to low pile-up regimes and applied to datasets at 5.02 and 13 TeV. Identification SFs are measured in-situ using Z boson samples. Isolation and trigger efficiency SFs are measured in-situ using combined low pile-up datasets. Uncertainties in electron SFs include statistical uncertainties from limited tag-and-probe pairs and systematic uncertainties dominated by photon and background control performance. Electron energy scale and resolution corrections are derived from Z events using standard ATLAS procedures. For muon reconstruction and calibration, reconstruction SFs are extrapolated from high pile-up measurements, and trigger, isolation, and track-to-vertex association SFs are measured in-situ using low pile-up data. Muon SF uncertainties consist of statistical uncertainties from the tag-and-probe method and systematic uncertainties mainly from background subtraction and selection criteria variations. The momentum scale and resolution are derived from high pile-up data and sagitta bias corrections from 2017 low pile-up datasets.

The hadronic recoil calibration addresses mis-modelling of underlying events, recoil direction, and recoil response and resolution. The uncertainties arise from the non-closure in the extrapolation of the calibration from Z events to W events, and from statistical uncertainties in the response and resolution corrections. Background cross-section uncertainties for simulated top-quark-related and di-boson backgrounds are generally set at 10%, with 7% for the $t\bar{t}$ process, and Z-boson, charge flip, and W-boson to tau-neutrino decay backgrounds have a conservative 5% cross-section uncertainty. Luminosity uncertainties are 1.0% for 5 TeV and 0.92% for 13 TeV, determined from LUCID-2

detector measurements and complementary measurements from the ID and calorimeters. Finally, the multijet background is estimated using the data-driven method.

6.4.4 Physics corrections and uncertainties

Two physics corrections are considered, electroweak (EW) and QCD uncertainties. The dominant uncertainty in the EW is the QED Final State Radiation (FSR) that is modelled with PHOTOS. The Initial State Radiation (ISR) is included in the parton shower modelled with PYTHIA8. The remaining non-modelled EW effects are introduced as systematic uncertainties evaluated at detector level whose variations are obtained by applying detector response and efficiency migration matrices derived from samples of simulated signal events.

To improve the data-to-simulation agreement, the higher-order QCD corrections are accounted by reweighting the rapidity, transverse momentum and decay distributions of the simulated $W-$ and $Z-$boson samples. The differential cross section as a function of the boson rapidity, $d\sigma(y)/dy$, and the angular coefficients, A_i, are calculated at $\mathcal{O}(\alpha_s^2)$ in fixed-order QCD. The transverse-momentum spectrum at a given rapidity, $d\sigma(p_T,y)/(dp_T\,dy) \cdot (d\sigma(y)/dy)^{-1}$, is modelled using the PYTHIA8 MC generator, with parameters adjusted to reproduce the measured $Z-$boson p_T distribution at $\sqrt{s} = 7$ TeV. The resulting tune, called AZ in the following, predicts W-boson p_T distributions that agree with measurements at $\sqrt{s} = 5$ and 13 TeV.

For the PDFs, the uncertainties are calculated for CT10, CT14, CT18, CT18A, MMHT2014, MSHT20, NNPDF3.1, NNPDF4.0 and ATLASpdf21 sets using the Hessian method. In which each eigenvector of the PDF fit covariance matrix defines a pair of PDF uncertainty variations and a corresponding nuisance parameter in the PLH fit.

The initial-state charm and bottom quark masses affect the p_T spectrum, and the corresponding uncertainties have been estimated by varying their respective masses by ± 0.5 GeV and ± 0.8 GeV, respectively. Uncertainties in the shower evolution are parameterised through variations of the factorisation scale, μ_F, by factors of 0.5 and 2.0 with respect to the central choice $\mu_F^2 = p_{T,0}^2 + p_T^2$, where $p_{T,0}$ is an infrared cut-off, and p_T is the evolution variable of the parton shower. The variations are applied independently to the light-quark, charm-quark and bottom-quark-induced processes, and

are propagated considering only the relative impact on the p_T^W and p_T^Z distributions.

The angular coefficients A_0–A_7 NNLO predictions are validated by comparing to the corresponding measured values in Z-boson production. The Z-boson data uncertainties are propagated to the W-boson predictions, which assumes that NNLO predictions have similar accuracy for the W and Z boson processes, and are validated within the experimental precision of the Z-boson data. The observed disagreement between data and prediction for the A_2 coefficient is taken as additional uncertainty. Similarly to some experimental uncertainties, random angular coefficient variations are treated with a PCA to produce uncorrelated two-sided uncertainties.

6.5   Fitting strategy for the W boson mass and width

A global profile likelihood fit in all event categories described in Tables 6.2 and 6.3 is considered. The implemented likelihood function is given by Eq. (4.15) with probability model,

$$
\begin{aligned}
\nu_{ji}\left(\vec{\theta}, \vec{\alpha}\right) = \Phi \times & \left[S_{ji}^{\mathrm{nom}} + \sum_p \theta_p \times \left(S_{ji}^{\theta_p} - S_{ji}^{\mathrm{nom}} \right) \right] \\
& + \sum_s \alpha_s \times \left(S_{ji}^s - S_{ji}^{\mathrm{nom}} \right) \\
& + B_{ji}^{\mathrm{nom}} + \sum_b \alpha_b \times \left(B_{ji}^b - B_{ji}^{\mathrm{nom}} \right),
\end{aligned}
\tag{6.16}
$$

where Φ is an overall, unconstrained normalisation factor ensuring that the total $W^\pm$ signal rate always adjusts to the number of events in data, S_{ji}^{nom} and B_{ji}^{nom} are the nominal distributions of signal and background, respectively, while s and b represent nuisance parameters acting on signal and background contributions. The multijet is considered as a background sample next to the electroweak, top, etc.

The fit ranges for m_W and Γ_W are $30 < p_T^\ell < 50$ GeV and $60 < m_T < 100$ GeV and the baseline results at 7 TeV rely on a numerical minimization of the likelihood (4.15). While studies as the decomposition of uncertainties, fit range variations, and to estimate the correlation between the m_T and p_T^ℓ fits, the following assumptions are made: In the limit where all uncertainties are Gaussian and the dependence of $\nu_{ji}(\vec{\theta}, \vec{\alpha})$ on $\vec{\theta}$ and $\vec{\alpha}$ is linear, the likelihood can be written as shown in Eq. (4.19)

Table 6.5: Best-fit value of m_W, total and PDF uncertainties, in MeV, and goodness-of-fit for the p_T^ℓ and m_T distributions For different PDF sets. Each fit uses 14 event categories with 40 bins, for 558 degrees of freedom.

	p_T^ℓ fit				m_T fit			
PDF set	m_W	σ_{tot}	σ_{PDF}	χ^2/n.d.f.	m_W	σ_{tot}	σ_{PDF}	χ^2/n.d.f.
CT14	80358.3	$^{+16.1}_{-16.2}$	4.6	543.3/558	80401.3	$^{+24.3}_{-24.5}$	11.6	557.4/558
CT18	80362.0	$^{+16.2}_{-16.2}$	4.9	529.7/558	80394.9	$^{+24.3}_{-24.5}$	11.7	549.2/558
CT18A	80353.2	$^{+15.9}_{-15.8}$	4.7	525.3/558	80384.8	$^{+23.5}_{-23.8}$	10.9	548.4/558
MMHT2014	80361.6	$^{+16.0}_{-16.0}$	4.5	539.8/558	80399.1	$^{+23.2}_{-23.5}$	10.0	561.5/558
MSHT20	80359.0	$^{+13.8}_{-15.4}$	4.3	550.2/558	80391.4	$^{+23.6}_{-24.1}$	10.0	557.3/558
ATLASpdf21	80362.1	$^{+16.9}_{-16.9}$	4.2	526.9/558	80405.5	$^{+28.2}_{-27.7}$	13.2	544.9/558
NNPDF31	80347.5	$^{+15.2}_{-15.7}$	4.8	523.1/558	80368.9	$^{+22.7}_{-22.9}$	9.7	556.6/558
NNPDF40	80343.7	$^{+15.0}_{-15.0}$	4.2	539.2/558	80363.1	$^{+21.4}_{-22.1}$	7.7	558.8/558

and the minimization and uncertainty estimation can be performed analytically as described in section 4.3 and in [128]. For the low pile-up the baseline results rely in the full analytical solution as well as the uncertainty decomposition where an extensive numerical validation was carried out using `HistFactory` [176]. Similarly, for the combination between the 7 TeV and low pile-up, the results are considered in the Gaussian limit.

6.6 m_W measurement at $\sqrt{s} = 7$ TeV

6.6.1 Fit results for m_W

Fits are performed in the two observables, p_T^ℓ and m_T, independently since they are projection of the same data and due to the PCA treatment over some systematic uncertainties, different sets of nuisance parameters for the two distributions arise and a dedicated study on their correlations is needed. Fit results for different PDF sets are shown in Table 6.5 with a good fit quality and CT18 result being the baseline. The best-fit values of m_W for different PDF sets span a range of about 18 MeV for the p_T^ℓ fits, and about 42 MeV for the m_T fits. Where the lowest fit values are obtained from NNPDF3.1 and NNPDF4.0. Without those PDFs, the spanned values are aound 9 MeV for p_T^ℓ and about 21 MeV for the m_T. The influence of the size of the initial PDF uncertainties on the best-fit values is studied in Fig. 6.5, where the fits are repeated with pre-fit PDF uncertainties

scaled by factors 1–3. Enlarged uncertainties allow the models to better adapt to the data, resulting in a reduced PDF model dependence. This shows that for factors of 2 and above, the residual of the model dependence is below 5 MeV and 25 MeV for p_T^ℓ and m_T, respectively. This results in an increased uncertainty by less than 1.5 MeV.
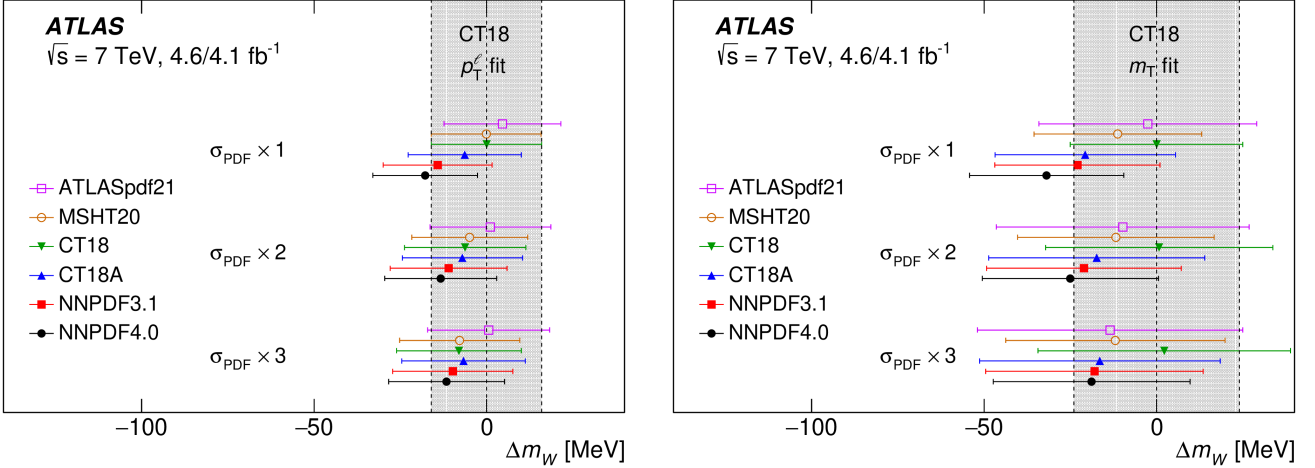
Figure 6.5: Variation of the fitted value of m_W with the PDF set used in the fit, for different scalings of the pre-fit PDF uncertainties. The reference value is defined by the CT18 PDF set.

The compatibility of the results for m_W in the different measurement categories has been verified by repeating the fit assuming independent parameters of interest in each category with independent systematic sources as shown in Fig. 6.6. The case with shared systematic sources among the categories is shown in Fig. 6.7 where small differences with respect to the baseline fit are found.

The dependence of the fit result on the p_T^ℓ and m_T ranges used for the fit is shown in Fig. 6.8, with good stability. The post-fit, $|\eta|$-inclusive p_T^ℓ distributions obtained with CT18 are shown in Fig. 6.9, and agree with the data within the uncertainties.

The ten nuisance parameters that induce the largest shift of m_W in fits to the p_T^ℓ and m_T distributions are shown in Fig. 6.10 as well as their pulls. The main sources that generates a shift in m_W are those related to electron and muon calibration, to the charm-induced production for the p_T^W description, to the specific eigenvectors (EV) of the CT18 PDF set, and to missing higher-order electroweak corrections.
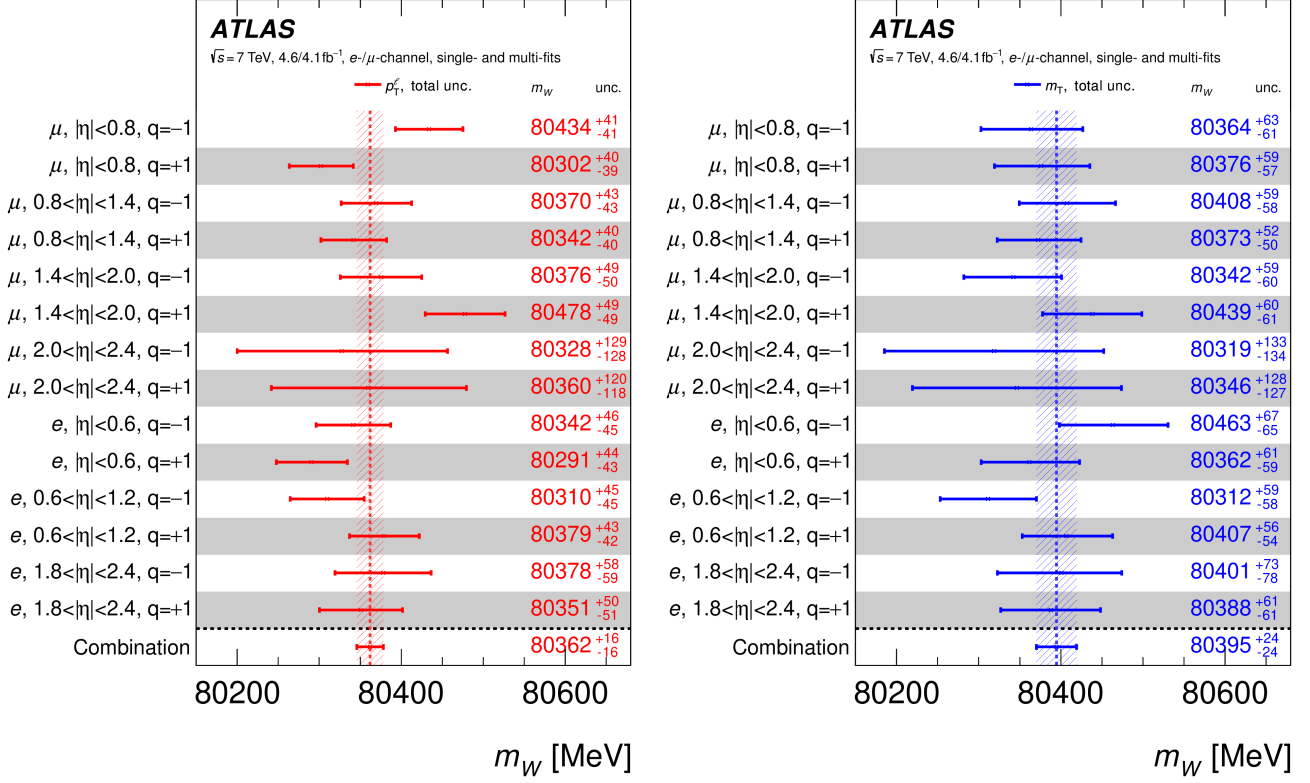
Figure 6.6: Overview of the m_W PLH fit results in all categories for the (a) p_T^ℓ and the (b) m_T distributions, with the CT18 PDF set. The points labelled as "Combination" correspond to the result of a joint PLH fit to all categories.

Figure 6.7: Overview of the m_W PLH fit results in all categories for the (a) p_T^ℓ and the (b) m_T distributions, with the CT18 PDF set. Each category takes into account an independent POI for m_W with shared systematics between the fits, this means 14 m_W fitted. The points labelled as Joint fit is the Joint PLH fit of all categories with one single m_W.

213

Figure 6.8: Dependence of the variation Δm_W of the fitted W-boson mass on the range of the (a) p_T^ℓ and (b) m_T distributions. The nominal ranges are $30 < p_T^\ell < 50$ GeV and $60 < m_T < 100$ GeV, respectively. The outer dashed lines indicate the total measurement uncertainty for the nominal range. Results are shown for the combined fit over all categories, and for the CT18 PDF set.

Combination

The two observable distributions, p_T^ℓ and m_T, are projection of the same data and by consequence to perform a single measurement of m_W a detailed correlation study should be carried out. The correlation between the final $p_T^\ell-$ and m_T-based results for m_W is computed from an ensemble of fit results obtained by fluctuating the data and the most probable values of the nuisance parameters within their respective uncertainties. Once the correlation is obtained, the final combination is performed using the BLUE approach as described in [177]. The result for all PDF sets are shown in Table 6.6 where p_T^ℓ has the larger weight and by consequence dominates the final result. The CT18 combined m_W result is given by,

$$m_W = 80366.5 \pm 9.8 \text{ (stat.)} \pm 12.5 \text{ (syst.) MeV} = 80366.5 \pm 15.9 \text{ MeV},$$

where the first uncertainty component is statistical and the second corresponds to the total systematic uncertainties and the post-fit uncertainty decomposition is performed according to Ref. [128] and shown in Table 6.7. From here, the statistical component corresponds to about 10 MeV that is larger than the 6 MeV result obtained from statistical only fits in which all the nuisance parameters
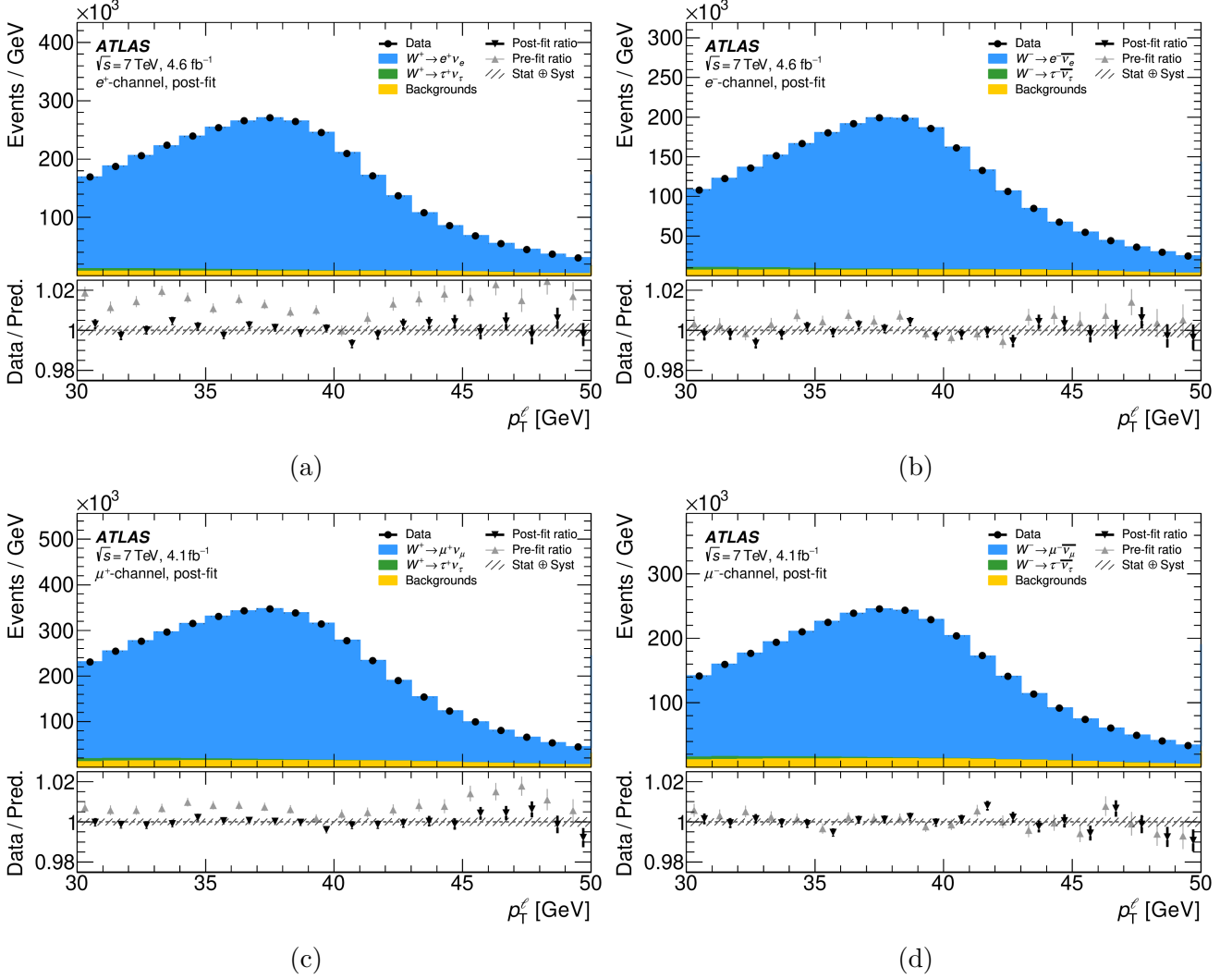
Figure 6.9: Post-fit distributions of p_T^ℓ with data and MC for (a) $W^+ \to e^+ \nu_e$, (b) $W^- \to e^- \overline{\nu}_e$, (c) $W^+ \to \mu^+ \nu_\mu$ and (d) $W^- \to \mu^- \overline{\nu}_\mu$, inclusive over all η regions, and using the CT18 PDF set. In the bottom panels, the black points represent the post-fit ratio of data-to-simulation, while the gray color points indicate the ratio before the fit. The hatched band represents the total uncertainty of the data.
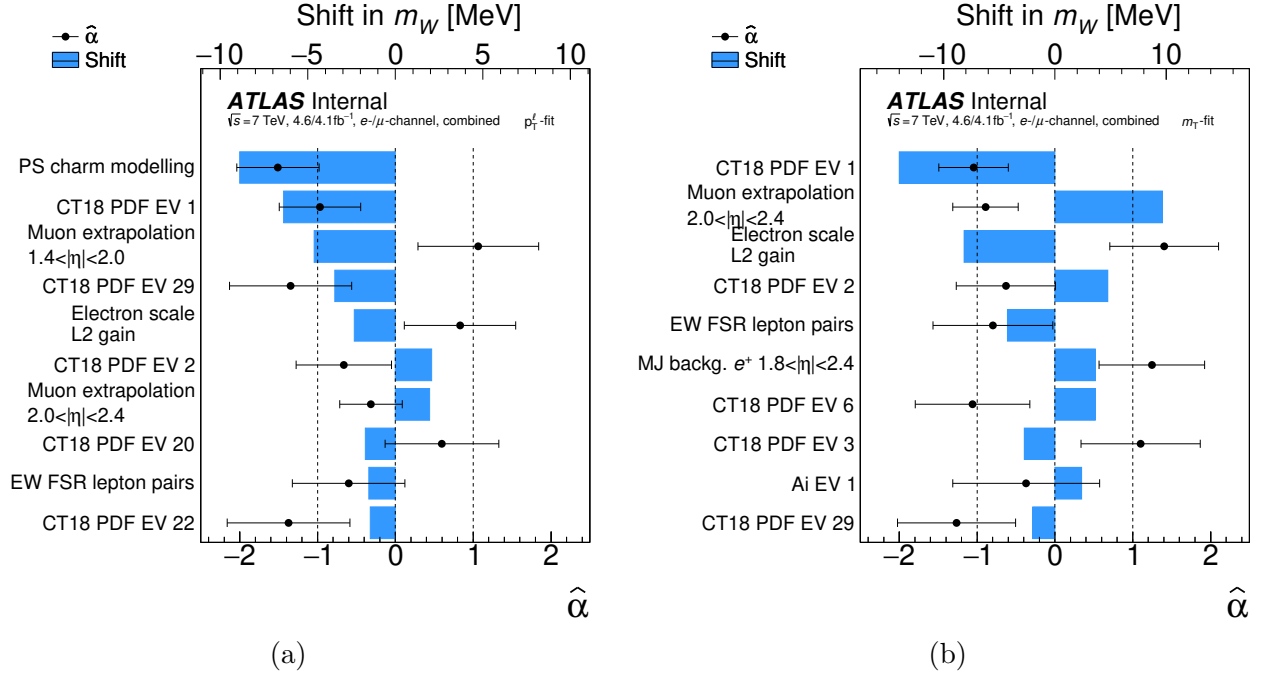
Figure 6.10: The ten nuisance parameters inducing the largest shifts on the fitted value of m_W in the combined PLH fits, using the (a) p_T^ℓ and the (b) m_T distributions and the CT18 PDF set. For a given NP α, the shift is defined as the product of its post-fit value $\hat{\alpha}$ and its pre-fit impact on m_W.

are fixed to their best-fit values. This difference reflects the larger number of parameters determined from the same data. The total systematic uncertainty contributes about 13 MeV and is dominated by PDF uncertainties, missing higher-order electroweak corrections, and electron and muon calibration uncertainties. The systematic uncertainty components show smaller values compared to the systematic impacts conventionally reported from the PLH fits[1].

Table 6.6: Uncertainty correlation between the p_T^ℓ and m_T fits, combination weights and combination results for m_W and the indicated PDF sets.

PDF set	Correlation	weight (p_T^ℓ)	weight (m_T)	Combined m_W [MeV]
CT14	52.2%	88%	12%	80363.6 ± 15.9
CT18	50.4%	86%	14%	80366.5 ± 15.9
CT18A	53.4%	88%	12%	80357.2 ± 15.6
MMHT2014	56.0%	88%	12%	80366.2 ± 15.8
MSHT20	57.6%	97%	3%	80359.3 ± 14.6
ATLASpdf21	42.8%	87%	13%	80367.6 ± 16.6
NNPDF3.1	56.8%	89%	11%	80349.6 ± 15.3
NNPDF4.0	59.5%	90%	10%	80345.6 ± 14.9

---

[1]Impacts are obtained from the quadratic subtraction between the total fit uncertainty and the uncertainty of a fit with selected nuisance parameters removed and overestimate the genuine systematic uncertainty.

Table 6.7: Uncertainty components for the p_T^ℓ, m_T and combined m_W measurements using the CT18 PDF set. The first columns give the total, statistical and overall systematic uncertainty in the measurements. The following columns show the contributions of modelling and experimental systematic uncertainties, grouped into categories.

Unc. [MeV]	Total	Stat.	Syst.	PDF	A_i	Backg.	EW	e	μ	u_T	Lumi	Γ_W	p_T^W
p_T^ℓ	16.2	11.1	11.8	4.9	3.5	1.7	5.6	5.9	5.4	0.9	1.1	0.1	1.5
m_T	24.4	11.4	21.6	11.7	4.7	4.1	4.9	6.7	6.0	11.4	2.5	0.2	7.0
Combined	15.9	9.8	12.5	5.7	3.7	2.0	5.4	6.0	5.4	2.3	1.3	0.1	2.3

Fig. 6.11a illustrates the compatibility of the W-boson mass using CT18 PDF set with respect to the Standard Model expectation and previous measurements. Fig. 6.11b show the two-dimensional 68% and 95% confidence limits for the m_W and m_t predictions obtained from the Standard Model electroweak fit and the comparison to the present measurement of m_W and to the combined value of the LHC top-quark mass determinations at 7 and 8 TeV [178].

(a)   (b)

Figure 6.11: (a) Present measured value of m_W, compared to SM prediction from the global electroweak fit [83], and to the measurements of LEP [80], Tevatron [179, 180] and the LHC [76, 77]. (b) The 68% and 95% confidence level contours of the m_W and m_t indirect determinations from the global electroweak fit [31], compared to the 68% and 95% confidence-level contours of the present ATLAS measurement of m_W, the ATLAS measurement of m_H [181] and the LHC measurement of m_t [178].

6.6.2 Fit results for Γ_W

Similarly to the m_W fits, the Γ_W result is obtained by fitting the two observables p_T^ℓ and m_T independently with m_W treated as a nuisance parameter and CT18 being the baseline PDF set. Results

for all PDF sets are shown in Table 6.8 where a good fit quality is obtained. The PDF dependence of the fit result is weaker than for m_W, and all central values are well within the uncertainties obtained with CT18. The compatibility of Γ_W for each category including all systematic uncertainties for the CT18 PDF set are shown in Fig. 6.12 yielding to the total values of $\Gamma_W = 2221^{+68}_{-76}$ MeV and $\Gamma_W = 2200^{+47}_{-48}$ MeV for p_T^ℓ and m_T distributions, respectively. Good agreement between the categories can be observed. Similarly to m_W, the dependence of the fit result on the p_T^ℓ and m_T ranges is studied as shown in Fig. 6.13 where stable results are found.

Table 6.8: Best-fit value of Γ_W, total and PDF uncertainties, in MeV, and goodness-of-fit for the p_T^ℓ and m_T distributions and the PDF sets. Each fit uses 14 event categories with 40 bins, for 558 degrees of freedom.

PDF set	p_T^ℓ fit				m_T fit			
	Γ_W	σ_{tot}	σ_{PDF}	χ^2/n.d.f.	Γ_W	σ_{tot}	σ_{PDF}	χ^2/n.d.f.
CT14	2228	$^{+67}_{-83}$	24	550.0/558	2202	$^{+48}_{-48}$	5	556.8/558
CT18	2221	$^{+68}_{-76}$	21	534.5/558	2200	$^{+47}_{-48}$	5	548.8/558
CT18A	2207	$^{+68}_{-75}$	18	533.0/558	2181	$^{+47}_{-48}$	5	550.6/558
MMHT2014	2155	$^{+71}_{-78}$	19	546.0/558	2186	$^{+48}_{-48}$	5	562.2/558
MSHT20	2206	$^{+66}_{-79}$	15	556.5/558	2179	$^{+47}_{-48}$	4	559.4/558
ATLASpdf21	2213	$^{+67}_{-73}$	18	531.3/558	2190	$^{+47}_{-48}$	6	545.6/558
NNPDF31	2203	$^{+65}_{-78}$	20	531.7/558	2180	$^{+47}_{-47}$	6	560.4/558
NNPDF40	2182	$^{+69}_{-68}$	12	550.5/558	2184	$^{+47}_{-47}$	4	564.0/558

For the uncertainty decomposition study, the same approach as for m_W was implemented with results shown in Table 6.9 where the largest contributions are coming from systematics sources mainly for p_T^ℓ while for m_T both statistical and systematic components are almost of the same magnitude. The uncertainties components show a dominant effect of the parton shower modelling for p_T^ℓ while for m_T, the lepton and recoil performance have the largest impact.

Table 6.9: Uncertainty components for the p_T^ℓ, m_T and combined Γ_W measurements using the CT18 PDF set. The first columns give the total, statistical and overall systematic uncertainty in the measurements. The following columns show the contributions of modelling and experimental systematic uncertainties, grouped into categories.

| Unc. [MeV]	Total	Stat.	Syst.	PDF	A_i	Backg.	EW	e	μ	u_T	Lumi	m_W	p_T^W
p_T^ℓ	72	27	66	21	14	10	5	13	12	12	10	6	55
m_T	48	36	32	5	7	10	3	13	9	18	9	6	12
Combined	47	32	34	7	8	9	3	13	9	17	9	6	18
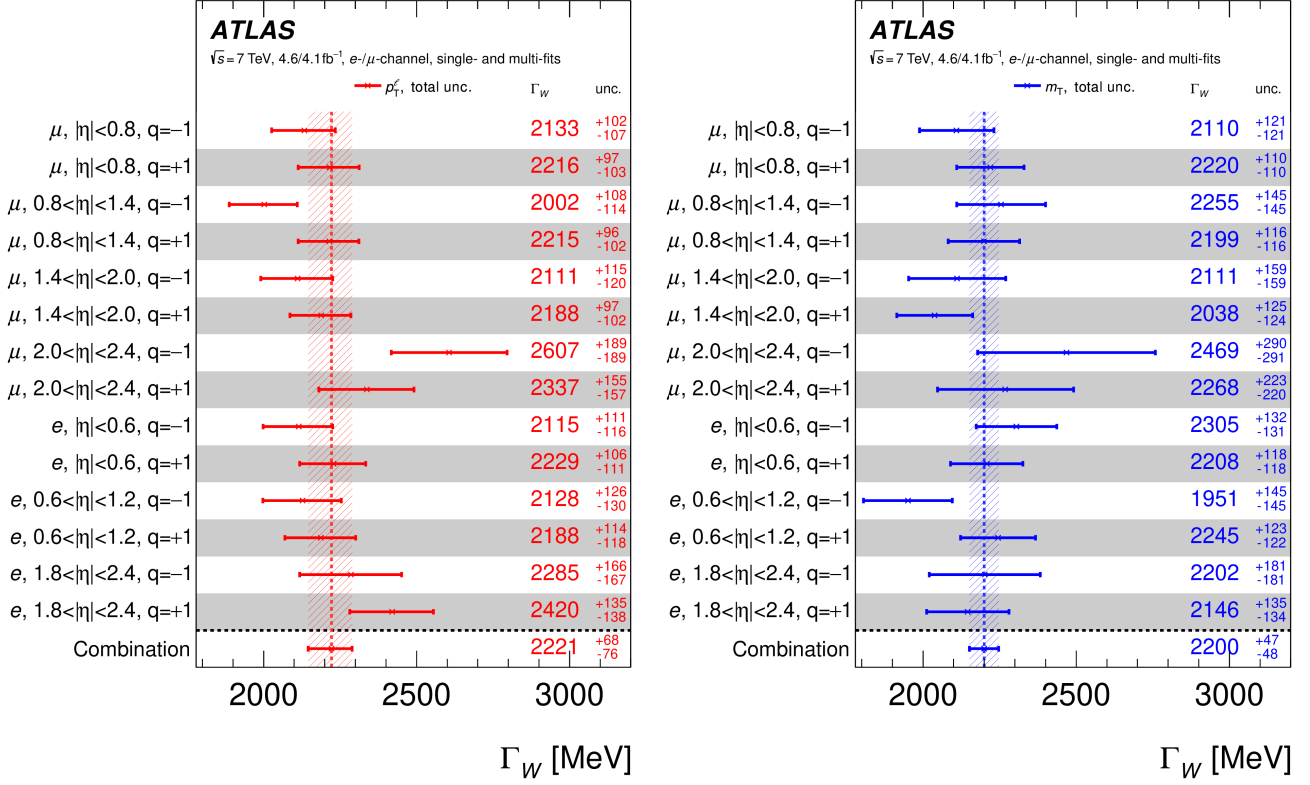
Figure 6.12: Overview of the Γ_W PLH fit results in all categories for the (a) p_T^ℓ and (b) m_T distributions, with the CT18 PDF set. The points labelled as 'Combination' correspond to the result of a joint PLH fit to all categories.
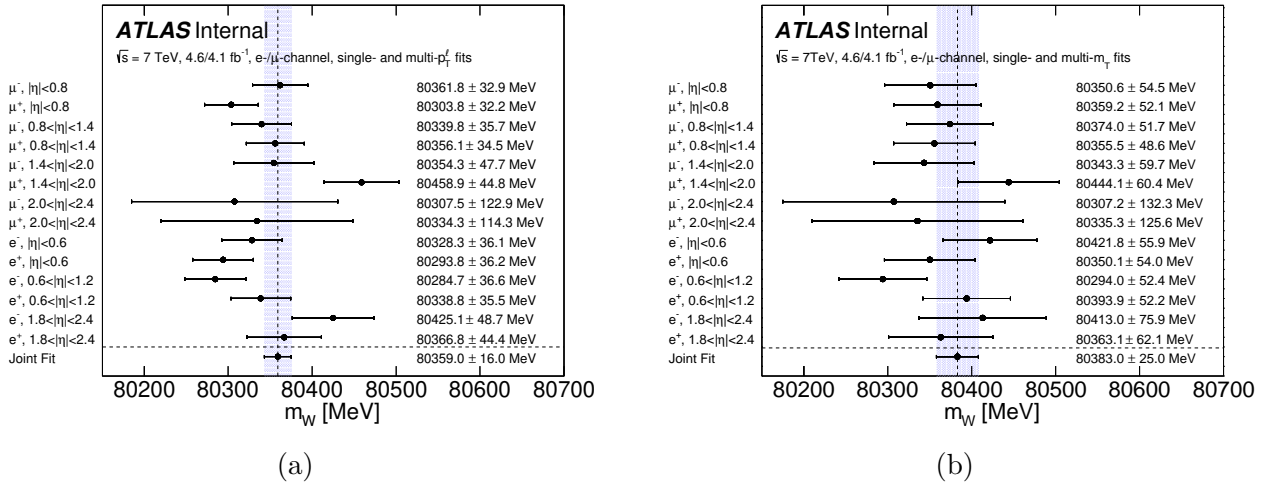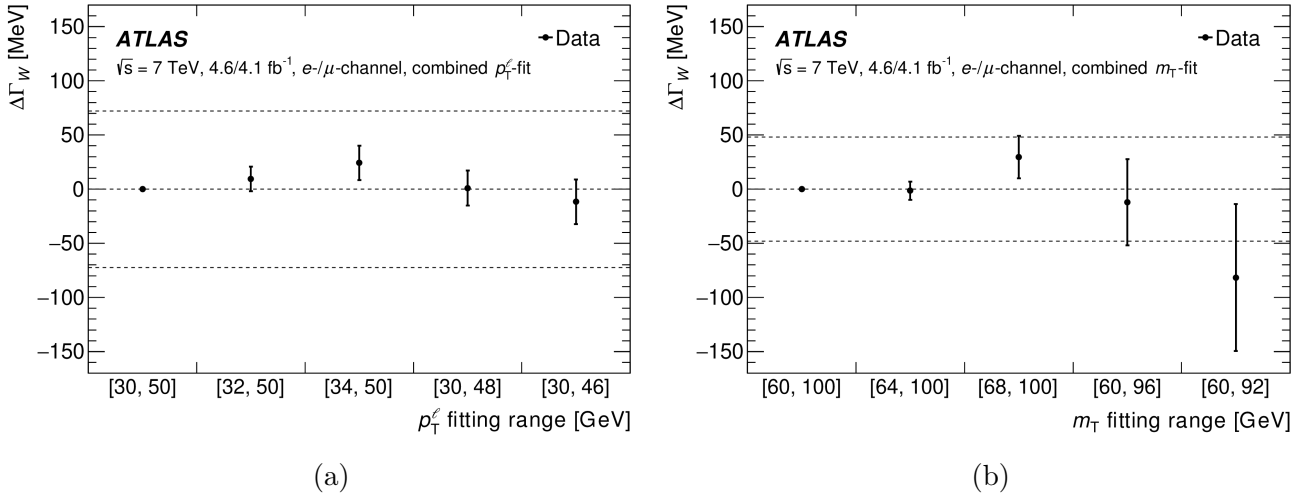

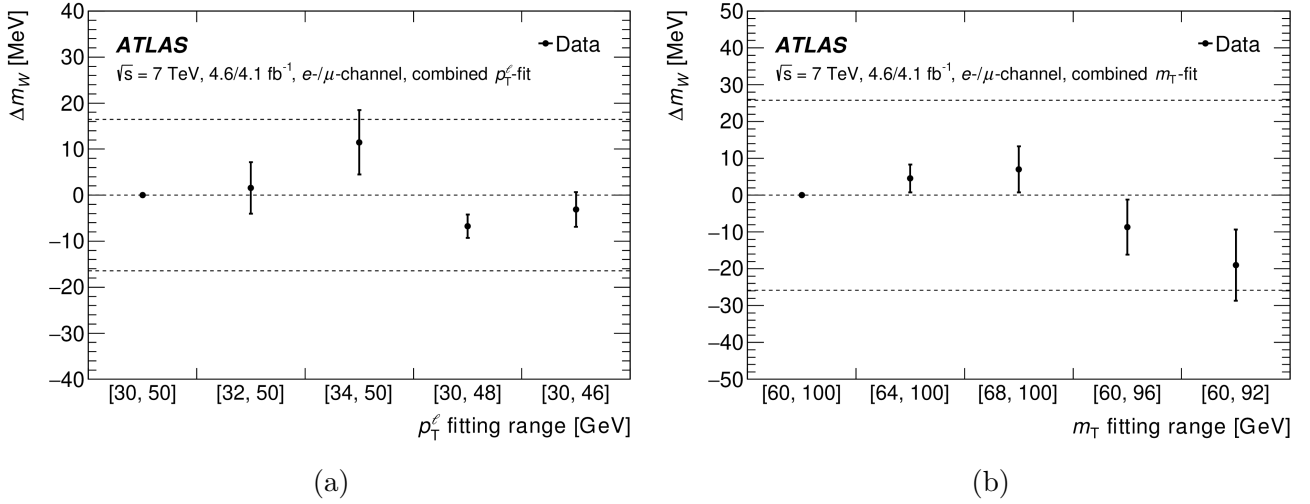Figure 6.13: Dependence of the variation $\Delta\Gamma_W$ of the fitted W-boson width on the of the (a) p_T^ℓ and (b) m_T distributions. The nominal ranges are $30 < p_T^\ell < 50$ GeV and $60 < m_T < 100$ GeV, respectively. The outer dashed lines indicate the total measurement uncertainty for the nominal range. Results are shown for the combined fit over all categories, and for the CT18 PDF set.

219

An overview of selected pre- and post-fit distributions of m_T is shown in Fig. 6.14, where a general better agreement can be observed for the post-fit case. The post-fit distributions use the final measured value of Γ_W.
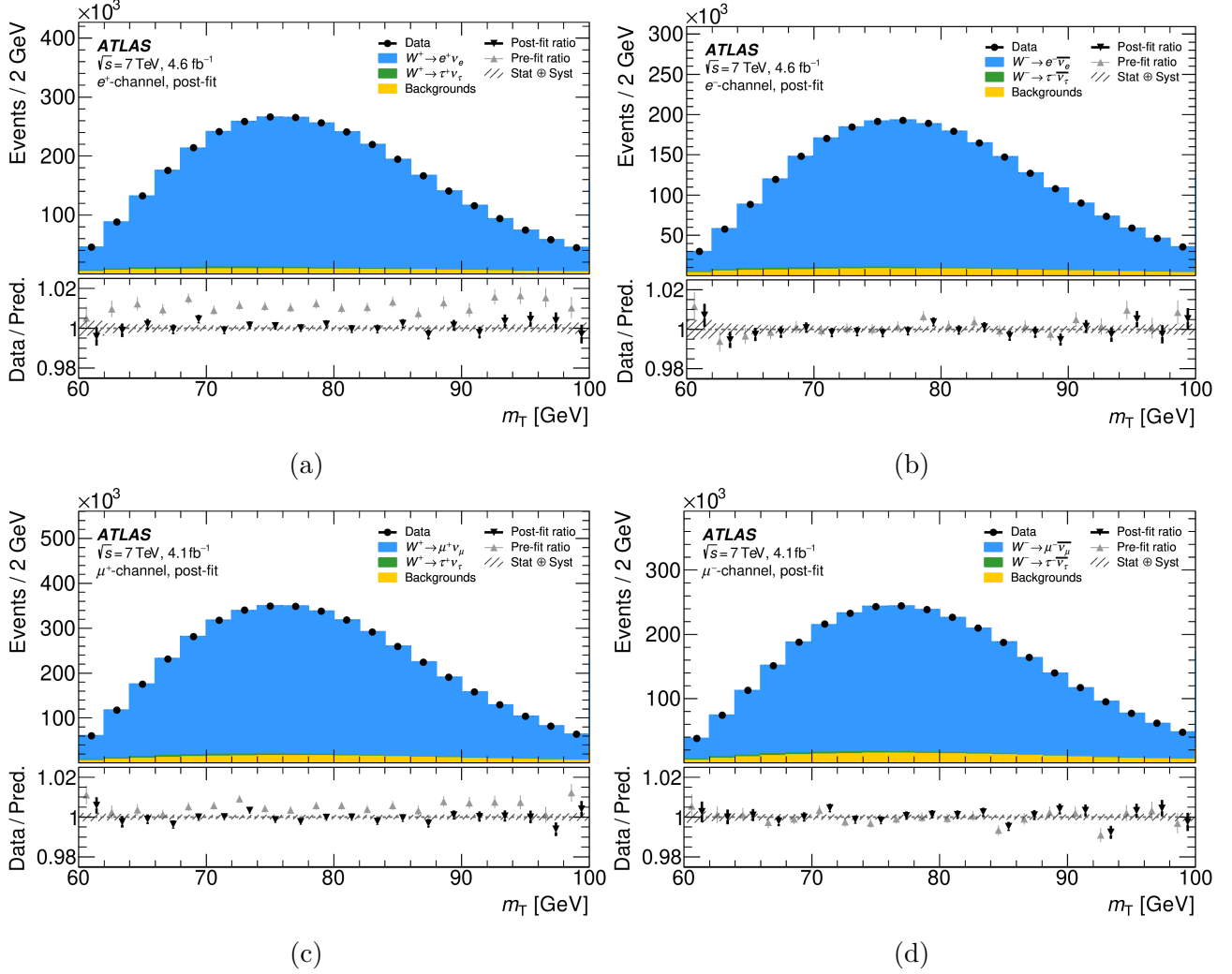
Figure 6.14: Post-fit distributions of m_T with data and MC for (a) $W^+ \to e^+\nu_e$, (b) $W^- \to e^-\overline{\nu}_e$, (c) $W^+ \to \mu^+\nu_\mu$ and (d) $W^- \to \mu^-\overline{\nu}_\mu$, inclusive over all η regions, and using the CT18 PDF set. In the bottom panels, the black points represent the post-fit ratio of data-to-simulation, while the gray color points indicate the ratio before the fit. The hatched band represents the total uncertainty of the data.

The ten nuisance parameters that induce the largest shift in Γ_W for p_T^ℓ and m_T are shown in Fig. 6.15. These are related to the multijet (MJ) background, to the lepton calibration, to specific eigenvectors of the CT18 PDF set, to the luminosity, and to the uncertainty in charm-induced production for the p_T^W description.
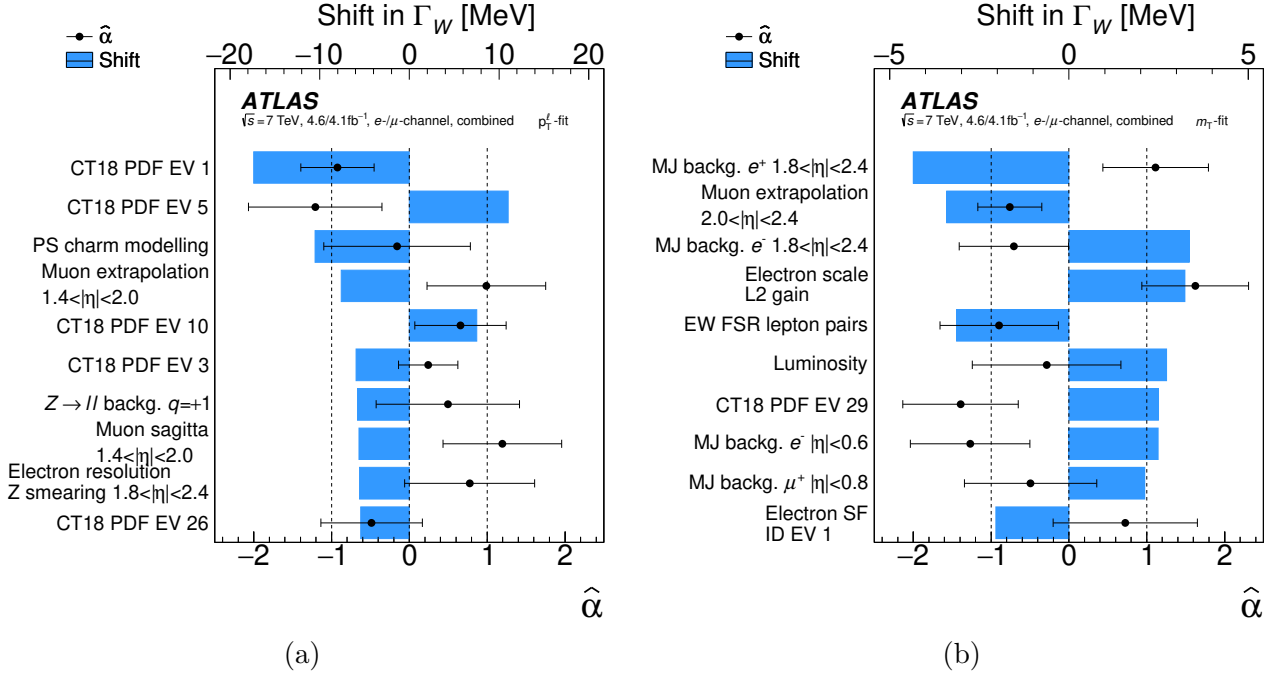
Figure 6.15: The ten nuisance parameters inducing the largest shifts on the fitted value of Γ_W in the combined PLH fits, using the (a) p_T^ℓ and (b) m_T distributions and the CT18 PDF set. For a given NP α, the shift is defined as the product of its post-fit value $\hat{\alpha}$ and its pre-fit impact on Γ_W.

Combination

As for m_W, the final Γ_W result is obtained by the BLUE combination [177] of p_T^ℓ and m_T distributions as shown in Table 6.10 for all PDF sets that in this case, m_T has the larger weight dominating the final result. For CT18, the final Γ_W is given by,

$$\Gamma_W = 2202 \pm 32 \text{ (stat.)} \pm 34 \text{ (syst.) MeV} = 2202 \pm 47 \text{ MeV},$$

where the first uncertainty component is statistical and the second corresponds to the total systematic uncertainties. Fig. 6.16a shows the compatibility of the measured Γ_W value with the SM expectation and selected previous measurements.

6.6.3 Simultaneous fit of m_W and Γ_W

The previous results were obtained by considering one floating parameter of interest (m_W or Γ_W) while the other is treated as a nuisance parameter with its SM value. To study the interplay of

Table 6.10: Uncertainty correlation between the p_T^ℓ and m_T fits, combination weights and combination results for Γ_W and the indicated PDF sets.

PDF set	Correlation	weight (m_T)	weight (p_T^ℓ)	Combined Γ_W [MeV]
CT14	50.3%	88%	12%	2204 ± 47
CT18	51.5%	87%	13%	2202 ± 47
CT18A	50.0%	86%	14%	2184 ± 47
MMHT2014	50.8%	88%	13%	2182 ± 47
MSHT20	53.6%	89%	11%	2181 ± 47
ATLASpdf21	49.5%	84%	16%	2193 ± 46
NNPDF31	49.9%	86%	14%	2182 ± 46
NNPDF40	51.4%	85%	15%	2184 ± 46

the PLH fit between the two parameters, a 2 POI simultaneous fit is performed. The fit yields values of $m_W = 80351.8 \pm 16.7$ MeV and $\Gamma_W = 2216 \pm 73$ MeV for the p_T^l distributions and $m_W = 80369.4 \pm 26.8$ MeV and $\Gamma_W = 2186 \pm 53$ MeV for the m_T distributions using the CT18 PDF set.

The final combination is performed using the total post-fit covariance matrices of the independent fits and the post-fit covariance matrices between the fits as described on Ref. [128]. For the CT18 PDF set, the combination yields values of

$$m_W = 80354.8 \pm 16.1 \text{ MeV}$$

$$\Gamma_W = 2198 \pm 49 \text{ MeV}$$

with a correlation of -30%. Fig. 6.16b shows the 68% and 95% CL uncertainty contours.
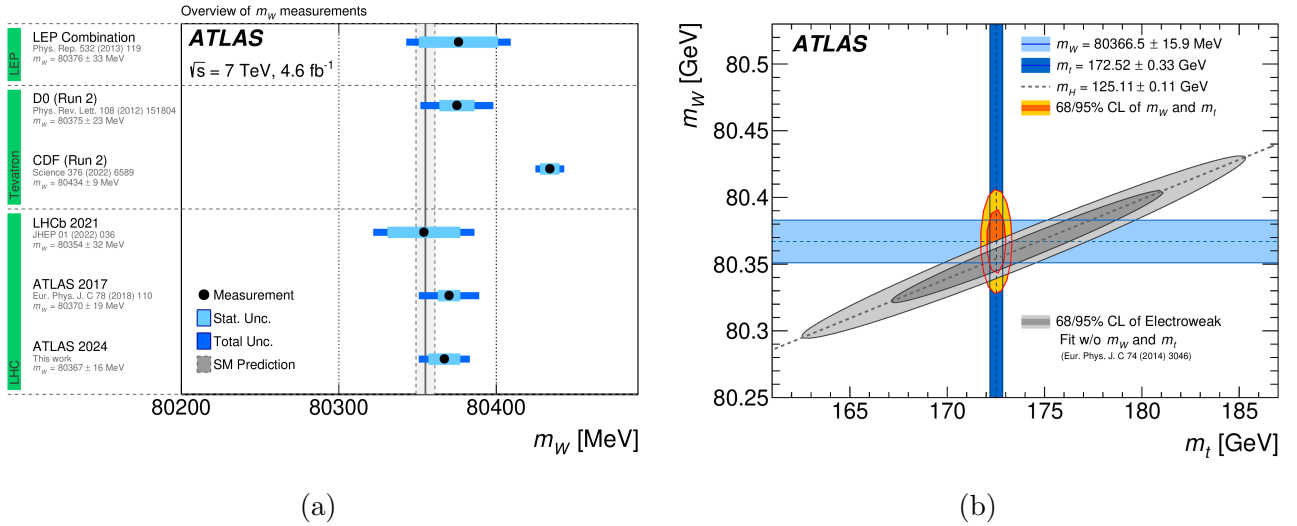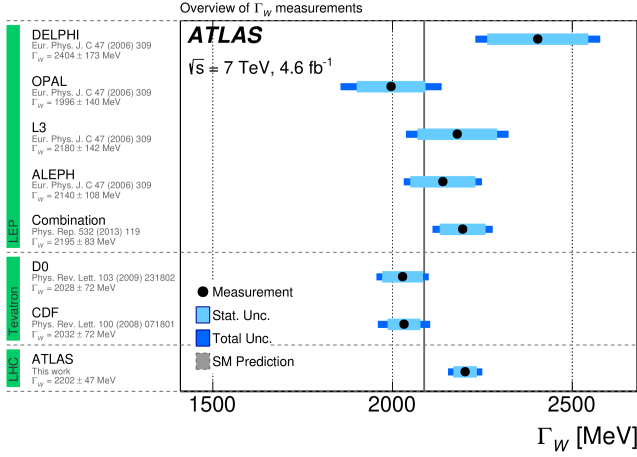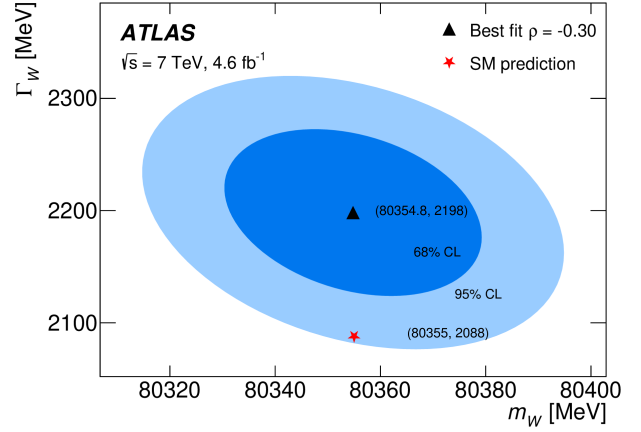
Figure 6.16: (a) Present measurement of Γ_W, compared to the SM prediction from the global electroweak fit [83], and to the measurements of LEP [80] and Tevatron [182]. (b) 68% and 95% CL uncertainty contours for the simultaneous determination of m_W and Γ_W using the CT18 PDF set and combining results from the p_T^ℓ and m_T distributions. The triangular marker represents the best fit, while the star corresponds to the SM prediction of Ref. [83].

6.7 Prospects of the low pile-up fit at $\sqrt{s} = 5$ and 13 TeV

The following section is focused on the W-boson mass measurement using the low pile-up dataset at the centre-of-mass energy of 5.02 TeV and 13 TeV. Contrary to the 7 TeV analysis, the transverse momentum of the W boson (p_T^W) has not been determined by extrapolating the Z boson transverse momentum. In this case, this distribution was measured directly from the low pile-up dataset allowing a granularity of about 7 GeV in p_T^W and a final precision at the level of $1-2\%$ [75]. Ref. [75] shows that the p_T^W distribution model derived using 7 TeV data fails at $\sqrt{s} = 5$ and 13 TeV. Therefore using the measured p_T^W distribution at these energies has the double advantage of predicting a spectrum that is unbiased by construction, and of potentially reducing the corresponding uncertainties. These results have been implemented in the following studies. Given its importance for the measurement of m_W, a detailed bibliographical description is given subsection 6.7.1 and Ref. [183].

At the time of writing this work, electron calibration uncertainties are finalized. Muon calibration uncertainties are about to be implemented based on the studies of chapter 5. Electroweak corrections and QCD predictions (PDFs and spin correlations) are the major subject of study.

6.7.1 Modelling of the W-boson's transverse momentum

In the m_W determination, one of the implemented observables is the lepton transverse momentum spectrum, p_T^ℓ, that is strongly dependent in the W boson transverse momentum (p_T^W) modelling. For that reason, a precise knowledge in p_T^W is required for a controlled uncertainty in this systematic source that requires a good precision of around 1% for low values of $p_T^W < 20 - 30$ GeV.

In section 6.6, the p_T^W distribution is modelled by extrapolating the experimentally measured transverse momentum spectrum of the Z-boson. This spectrum is used to tune the PYTHIA parton shower, and the tuning parameters carry an experimental uncertainty that propagates to the p_T^W modelling, together with PDF uncertainties, the mass of the charm and bottom quarks and high-order QCD correction. The modelling of this distribution is one of the largest sources of uncertainty in the analysis.

From these sources, the variations of the masses of the charm and bottom quarks show a small impact in the determination of m_W while the high-order QCD needs to be treated carefully. In particular, the missing higher-order QCD corrections to the parton shower are estimated by the variations of the factorization scale (μ_F) for QCD ISR. However, the QCD scales variations only provide an approximate size of the missing higher-order effect without an insured coverage and moreover, the variations do not offer an indication of the uncertainties correlation among the distributions.

For these reasons, it is worth to perform a direct measurement of the p_T^W spectrum directly from the data instead of extrapolating the p_T^Z. This will avoid uncertainties due to the QCD scale variations.

6.7.1.1 Methodology

Due to the neutrino involved in the decay, the p_T^W cannot be inferred directly in the transverse plane. To determine it, the hadronic recoil, u_T, needs to be used, which originates with a non-zero component due to the QCD ISR. The p_T^W measurement corresponds to a direct measurement of the differential Drell-Yan cross-section in $W \to \ell\nu$ decays. However, the detector effects introduce bias and smearing into the measurement of p_T^W through the hadronic recoil. To achieve a precise

measurement, it is essential to correct for detector effects such as detector response, limited detector acceptance, object reconstruction efficiency, and finite detector resolution. The true p_T^W spectrum can be obtained from the response of the detector by an unfolding procedure.

Results are reported in a fiducial region close to the event selection criteria outlined in subsection 6.2.1, minimizing the need for extrapolation. This is done for electrons, muons and their combination with the selection criteria:

$$W \to \ell\nu : p_T^\ell > 25 \text{ GeV}, \ |\eta_\ell| < 2.5, \ p_T^\nu > 25 \text{ GeV}, \ m_T > 50 \text{ GeV}.$$

with binning in u_T and p_T,

- u_T is chosen in three intervals, $u_T \in [1, 100]$ GeV, $[100, 200]$ GeV and $[200, 600]$ GeV with 1, 5 and 10 GeV bin size, respectively.

- p_T at 5.02 TeV is divided in the following categories $[0, 7, 14, 21, 28, 35, 42, 49, 56, 63, 77, 92, 115, 145, 175, 220]$ GeV.

- p_T at 13 TeV is divided in the following categories $[0, 7, 14, 21, 28, 35, 42, 49, 56, 63, 77, 92, 115, 145, 175, 220, 310, 600]$ GeV.

To determine the p_T^W spectrum at the truth-level with u_T at the reco-level the following is considered: an observed distribution, D_i, can be seen as the product of a true distribution, T_j, with a detector response matrix, R_{ik} (including efficiency and resolution effects), such that,

$$D_i = \sum_j R_{ij} T_j. \tag{6.17}$$

Were i runs over u_T and j over p_T. The unfolding implies that Eq. (6.17) can be inverted to get an estimate of the true distribution T. This is done using the observed distribution from data, and the response matrix from simulation plus corrections. Then,

$$T_j = \sum_i R_{ji}^{-1} D_i. \tag{6.18}$$

The response matrix R_{ij} can be derived from the conditional probability of observing a reconstructed value of u_T in bin i and a given truth value of p_T^W in bin j as,

$$R_{ij} = M_{ij}\epsilon_j, \tag{6.19}$$

where M_{ij} is the migration matrix and ϵ_j is the efficiency. M_{ij} represents the migration from p_T^W at the truth-level to u_T at the reco-level and is given by,

$$M_{ij} = \frac{N_{ij}}{\sum_k N_{kj}}, \tag{6.20}$$

where N_{ij} is the number of events in u_T bin i and p_T^W bin j and is normalized to unity in each truth bin j. The efficiency, ϵ_j, of reconstructing a truth level signal, in bin j is computed as,

$$\epsilon_j = \frac{N_j^{\text{reco\&gen}}}{N_j^{\text{gen}}} = \frac{\sum_i N_{ij}}{N_j^{\text{gen}}}, \tag{6.21}$$

where $N_j^{\text{reco\&gen}}$ refers to the events in the $j-$bin of p_T^W passing the fiducial and reconstructed-level selection and N_j^{gen} is the number of events passing the fiducial selection. To account for the presence of background, B_j, after the reconstructed level cuts. Eq. (6.17) can be extended as,

$$D_i = \sum_j R_{ij}T_j + B_i, \tag{6.22}$$

and the unfolded is given by,

$$T_j = \sum_i R_{ji}^{-1}(D_i - B_i). \tag{6.23}$$

In general, the inversion of R is not well defined. If R is strongly non-diagonal (large resolution effects), instabilities could appear in this process and a regularization procedure needs to be applied to tame the fluctuations in T. In this work, p_T^W is the same as in Ref. [75] and R is determined by the iterative Bayesian regularized unfolding approach with the implementation of the D'Agostini iterative scheme [184, 185]. Since events beyond the fiducial selection can be reconstructed, an additional correction of purity has to be applied to the reconstructed level distribution in the

unfolding. Then Eq. (6.23) is given by,

$$T_j = \sum_i R_{ji}^{-1}(D_i - B_i)p_i. \tag{6.24}$$

where p_i is the purity correction given by,

$$p_i = \frac{N_i^{\text{reco\&gen}}}{N_i^{\text{reco}}} = \frac{\sum_k N_{ik}}{N_i^{\text{reco}}}. \tag{6.25}$$

From Eq. (6.24) the following sources of uncertainties can be identified, data statistics coming from D matrix at the reco level. In this, the data is fluctuated using bootstrap such that the spread of the distributions are associated to the data statistics. The MC statistics coming from the unfolding, R^{-1}, is originated from the fluctuation of the migration matrix, purity and efficiency via bootstrap, such that the spread of the distribution is considered to be the MC uncertainty. For the experimental systematic, the systematic variation is applied to the unfolding transformation U_{ij}, including migration matrix, efficiency correction and purity correction. After that, the change in the unfolded spectrum is taken to be the experimental systematic of the given source. Finally, the background uncertainty is estimated from B at the reconstructed level by varying according to the relevant systematics. The change in the unfolded spectrum is then the background systematic of source under study.

6.7.1.2 p_T^W reweighting and bias uncertainties

In general, if the p_T^W modelling in the simulation is inaccurate, it can cause significant discrepancies between the data and the simulation. This, can lead to a percent-level bias in the unfolding strategy, introducing a source of uncertainty at the unfolded level. To avoid this and to ensure a better data-to-simulation agreement on the reconstructed u_T distribution, a reweighting of the simulation is carried out. This reweighting is performed using a p_T^W function whose form can be obtained by

minimizing the following χ^2,

$$\chi^2 = \sum_{ij} \Delta_i C_{ij}^{-1} \Delta_j,$$

$$\Delta_i = (D_i - B_i) + \sum_j R_{ij} \times \left(w_T \left(p_T^W \right) \right)_j, \quad (6.26)$$

where C_{ij} is the total covariance matrix at the reconstructed level. A satisfactory data-to-simulation agreement is achieved using the following form for $w_T \left(p_T^W \right)$,

$$w_T \left(p_T^W \right) = N \times \left[1 + a \cdot p_T^W + b \cdot \left(p_T^W \right)^2 \right] \cdot \left[1 - c + c \cdot r_{\text{NNPDF/CT10}} \left(p_T^W \right) \right], \quad (6.27)$$

where a, b, c, N are parameters to be fitted and $r_{\text{NNPDF/CT10}}(p_T^W)$ represents the correction in the full phase space, from the default PDF set (CT10) used in the POWHEG samples to a different PDF set (NNPDF3.0). This quantity is estimated using DYTURBO in the range $p_T^W \in [0, 100]$ GeV and for $p_T^W > 100$ GeV the correction value is frozen at the 100 GeV value. To determine the parametrization uncertainty of Eq. (6.27), the reweighting procedure is repeated using different functions for $w_T \left(p_T^W \right)$. Only those functions that provide a good data-to-simulation agreement (good χ^2) of u_T at the reconstructed level are kept as a variation of the parametrization.

The uncertainty in the (p_T^W, y) distribution in simulation is obtained from a reweighting of p_T. The nominal MC is reweighted in 2D to the possible alternative prediction of (p_T^W, y) varying between different functions to asses the best data-to-simulation agreement in u_T at the reconstructed level. At the end, the best data-to-simulation agreement is obtained by choosing DYTURBOCT10 as proxy of initial (p_T^W, y) uncertainty variation at 13 TeV and DYTURBONNPDF3.0 for all 5.02 TeV channels. These variations are injected into the probability model for template morphing, and nine nuisance parameters (NPs) are assigned to the p_T^W systematics per boson charge and centre-of-mass energy. Despite this detailed method, the approach has limitations, such as ignoring correlations between boson p_T and rapidity and not fully accounting for recoil calibration uncertainties.

A dedicated study of the p_T^W and p_T^Z precise measurement at $\sqrt{s} = 5$ and 13 TeV is presented in Reference [183] in which the optimization of the iterative Bayesian unfolding is largely discussed.

An alternative method to derive a model for the p_T^W distribution would be to include the recoil distributions, u_T, in the W mass fitting procedure. This would yield a simultaneous determination of m_W and p_T^W.

After reweighting, the detector-level distributions for m_T and p_T^ℓ at 5.02 TeV (13 TeV) are shown in Fig. 6.17 and Fig. 6.18 (Fig. 6.19 and Fig. 6.20), respectively. Where the MC predictions are normalised to the integral of the data distribution. The grey band in ratio panels represents total systematic uncertainty, while the brown band includes small statistical uncertainties from the MC simulation. The systematic uncertainty is normalized to the data integral and excludes luminosity and alternative simulation uncertainties from SHERPA. The χ^2 per degree of freedom (χ^2/dof) calculation includes all uncertainties and accounts for bin-to-bin correlations in the covariance matrix. Overall, a good data-to-simulation agreement across all kinematic distributions is found. However, minor mismodellings are observed indicating the need for further work in areas such as muon calibration, electroweak and QCD corrections. These results show that low pile-up scenarios yield higher quality signals with better-defined m_T distributions, while high pile-up conditions result in broader distributions with larger uncertainties as in the case of $\sqrt{s} = 7$ TeV.

6.7.2   Correlation studies for joint $p_T^\ell - m_T$ fits

The low pile-up datasets share the same systematic sources, such that, it is possible to perform a joint fit in the Gaussian limit by accounting for the statistical correlations in the statistical covariance matrix and the systematic correlations in the systematic covariance matrix. To evaluate the correlation between the two observables, p_T^ℓ and m_T, the 2D distribution in the same category is required. This means that only those distributions within the same u_T and η_ℓ categories are correlated while for the others, the statistical correlation is zero.

To compute the covariance of the 2D distributions with non-trivial correlations, a set of pseudo-experiments (toys) are performed by fluctuating the bin contents within the uncertainties for a given number of toys (N_{toy}). For each pseudo-experiment, the 2D distribution is projected in the p_T^ℓ and
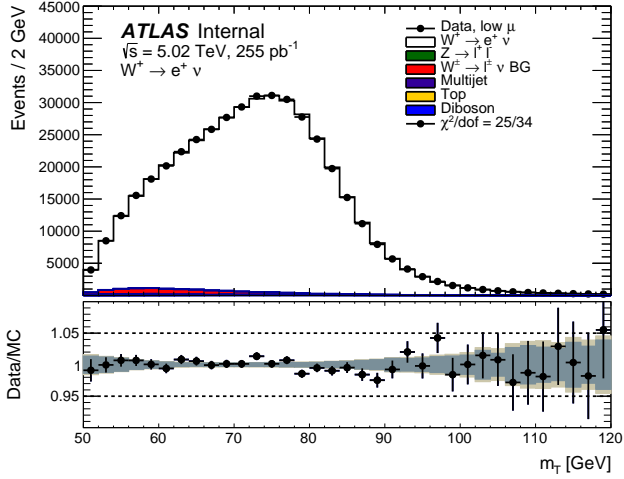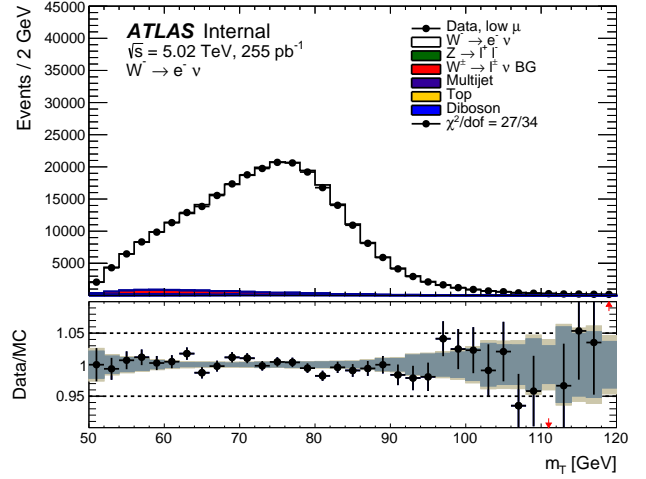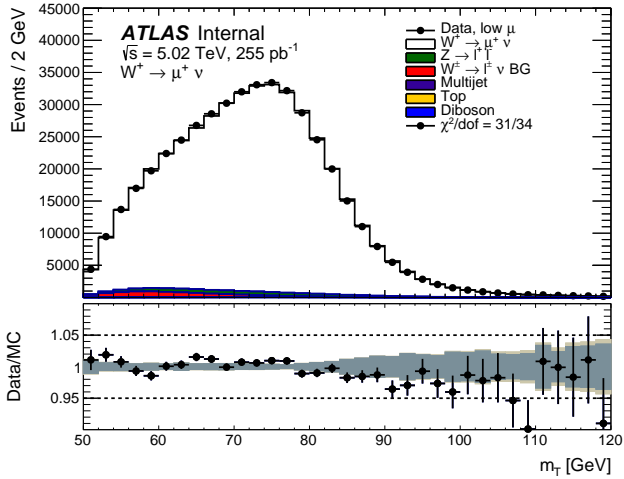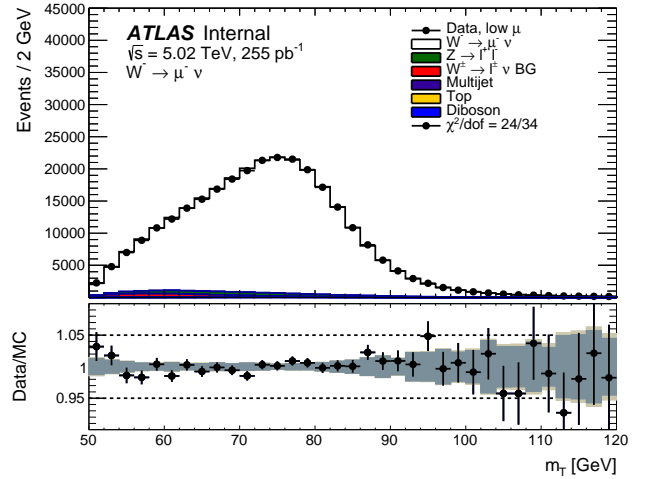
Figure 6.17: Transverse mass m_T distribution of the W boson in the (a) $W^+ \rightarrow e^+\nu_e$, (b) $W^- \rightarrow e^-\bar{\nu}_e$, (c) $W^+ \rightarrow \mu^+\nu_\mu$ and (d) $W^- \rightarrow \mu^-\bar{\nu}_\mu$ channels for the $\sqrt{s} = 5.02$ TeV dataset. The lower panel displays the ratio of the data to the full prediction (black points), along with the prediction uncertainties around 1. These uncertainties are shown as a dark band when excluding the MC simulation statistical component and as a light band when including it. The prediction uncertainties presented exclude those from the luminosity measurement and the alternative signal modeling.
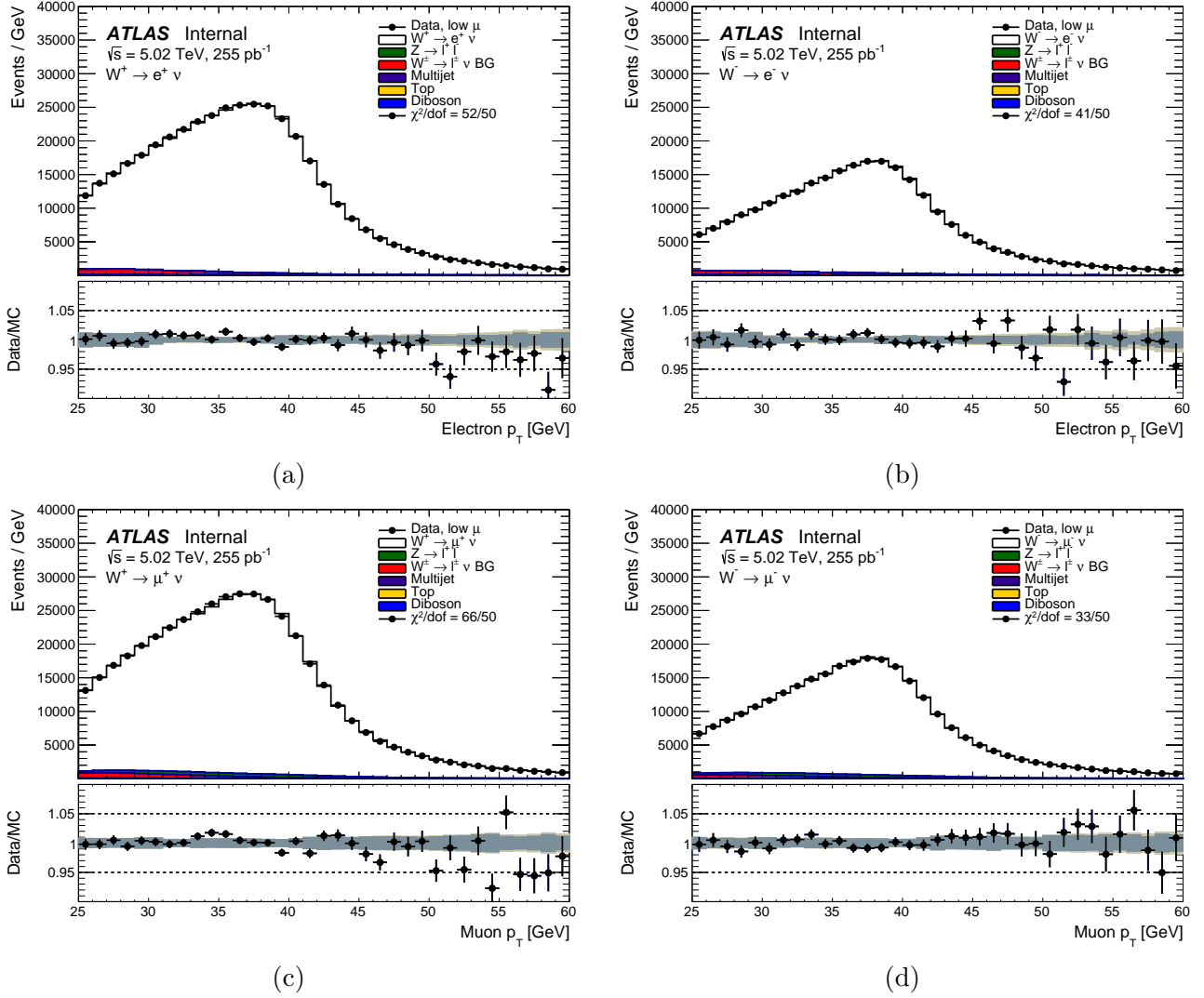
Figure 6.18: Lepton transverse momentum p_T distribution of the W boson in the (a) $W^+ \to e^+\nu_e$, (b) $W^- \to e^-\bar{\nu}_e$, (c) $W^+ \to \mu^+\nu_\mu$ and (d) $W^- \to \mu^-\bar{\nu}_\mu$ channels for the $\sqrt{s} = 5.02$ TeV dataset. The lower panel displays the ratio of the data to the full prediction (black points), along with the prediction uncertainties around 1. These uncertainties are shown as a dark band when excluding the MC simulation statistical component and as a light band when including it. The prediction uncertainties presented exclude those from the luminosity measurement and the alternative signal modeling.
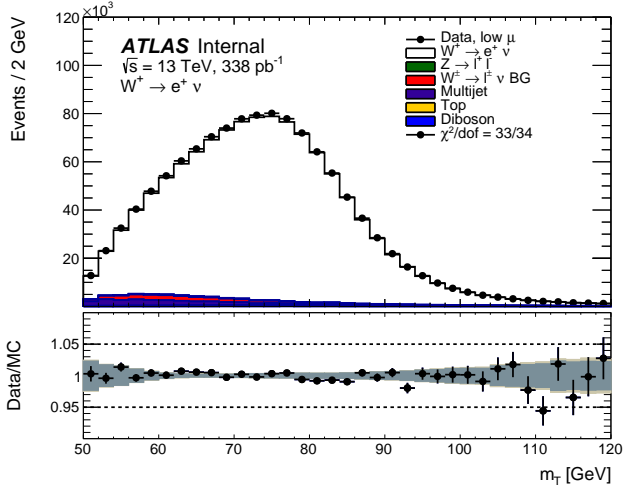
Figure 6.19: Transverse mass m_T distribution of the W boson in the (a) $W^+ \to e^+\nu_e$, (b) $W^- \to e^-\bar{\nu}_e$, (c) $W^+ \to \mu^+\nu_\mu$ and (d) $W^- \to \mu^-\bar{\nu}_\mu$ channels for the $\sqrt{s} = 13$ TeV dataset. The lower panel displays the ratio of the data to the full prediction (black points), along with the prediction uncertainties around 1. These uncertainties are shown as a dark band when excluding the MC simulation statistical component and as a light band when including it. The prediction uncertainties presented exclude those from the luminosity measurement and the alternative signal modeling.
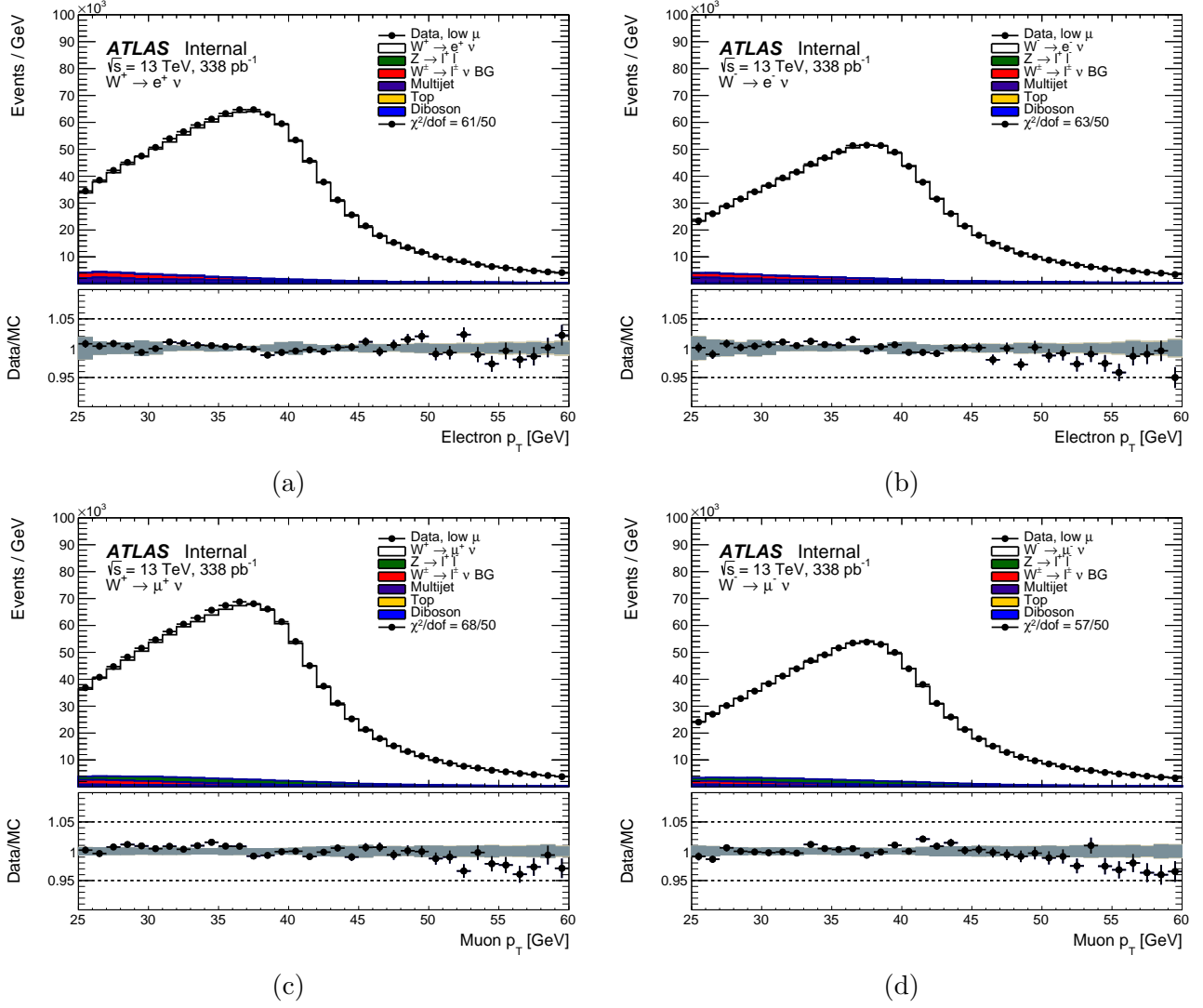
Figure 6.20: Lepton transverse momentum p_T distribution of the W boson in the (a) $W^+ \rightarrow e^+ \nu_e$, (b) $W^- \rightarrow e^- \bar{\nu}_e$, (c) $W^+ \rightarrow \mu^+ \nu_\mu$ and (d) $W^- \rightarrow \mu^- \bar{\nu}_\mu$ channels for the $\sqrt{s} = 13$ TeV dataset. The lower panel displays the ratio of the data to the full prediction (black points), along with the prediction uncertainties around 1. These uncertainties are shown as a dark band when excluding the MC simulation statistical component and as a light band when including it. The prediction uncertainties presented exclude those from the luminosity measurement and the alternative signal modeling.
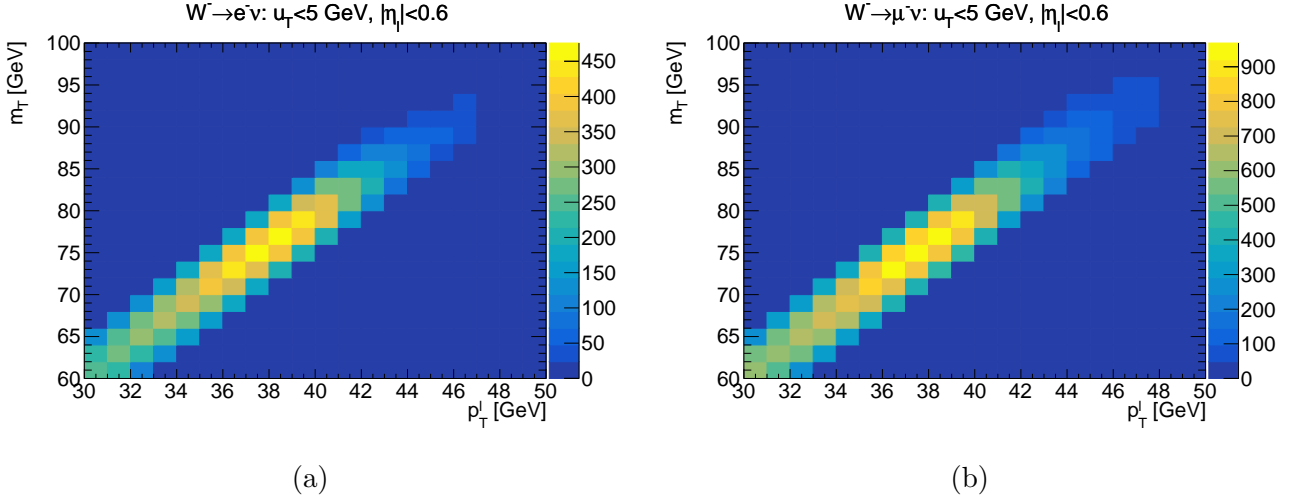
Figure 6.21: 2D distributions for (a) $W \to e\nu$ at 5.02 TeV and (b) $W \to \mu\nu$ at 13 TeV in the same category.

m_T axes and then, the covariance matrix element C_{ij} can be obtained as,

$$C_{ij}^{p_T^\ell - m_T} = \frac{1}{N_{\text{toy}}} \sum_{k=1}^{N_{\text{toy}}} \left(p_T^{\ell,(i,k)} - \overline{p}_T^{\ell,i} \right) \left(m_T^{(j,k)} - \overline{m}_T^j \right), \quad (6.28)$$

where $p_T^{\ell,(i,k)}$ and $m_T^{(j,k)}$ are the content in the $(i,j)-$bin of the p_T^ℓ distribution in the $k^{\text{th}}-$toy and $\overline{p}_T^{\ell,i}$ and $\overline{m}_T^j$ are the values of the original p_T^ℓ and m_T distributions in the bin (i,j). Once this is done, the correlation matrix is obtained from the covariance matrix. The 2D distributions in the electron and muon channels at 5.02 TeV and 13 TeV are shown in Fig. 6.21. By bootstrapping the corresponding distributions the correlation matrices can be constructed for the four channels at different centre-of-mass energy (eight channels in total) as shown in Fig. 6.22. Each matrix is obtained by generating 5×10^4 pseudo-experiments to ensure the symmetry and positive semi-definiteness. Notice that those matrices represent simplified versions and the total low pile-up correlation matrix that involves all the channels and categories has dimension 6400×6400, i.e. 3200 bins coming from p_T^ℓ and 3200 bins from m_T.

6.7.3 Fit results for m_W

The fitting strategy in this case considers two overall normalization factors Φ, one to normalize the signal at 5.02 TeV and one for the signal at 13 TeV. The fits are performed as an unrolled
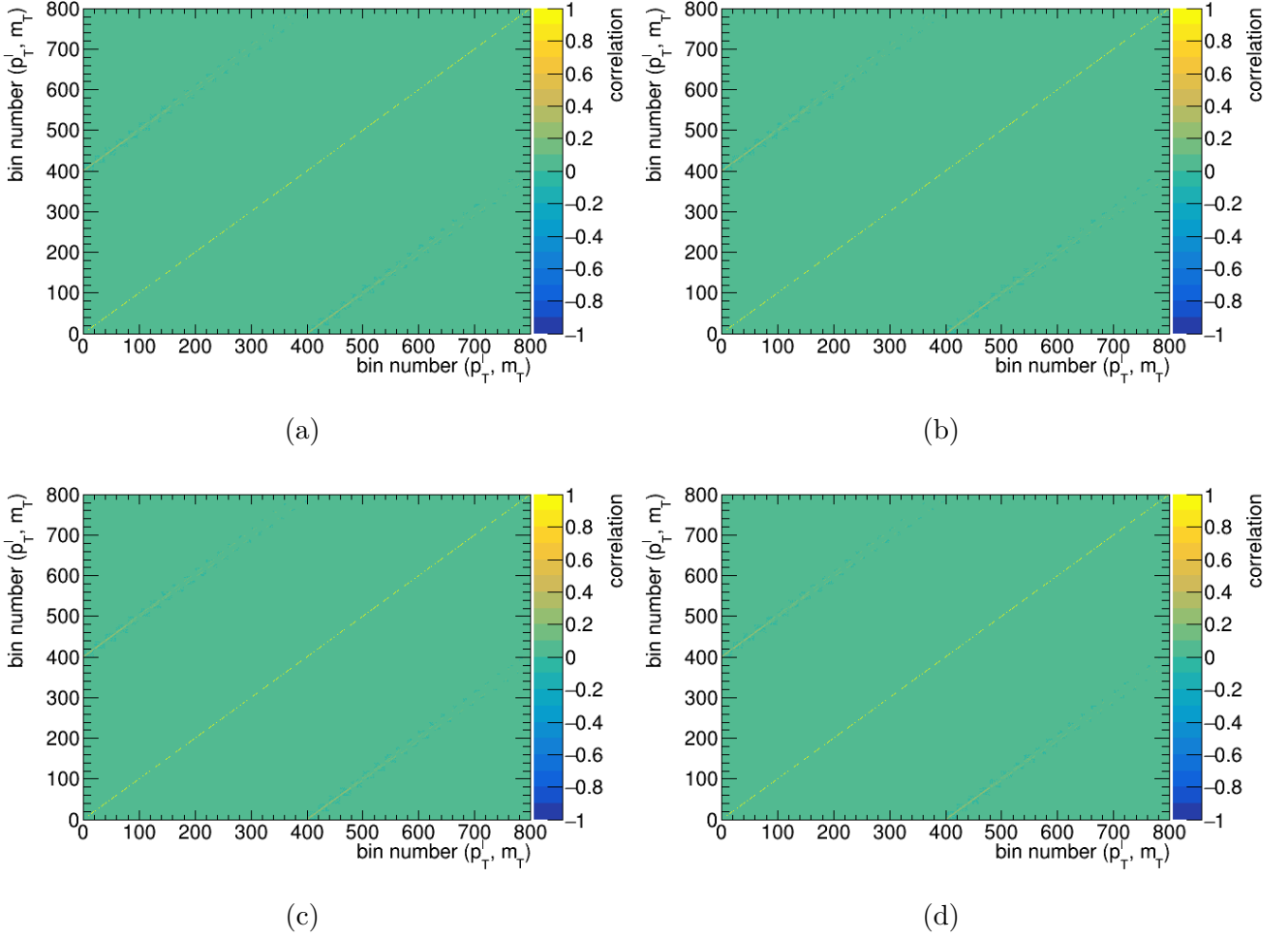
Figure 6.22: Correlation matrices generated with $N_{\text{toy}} = 5 \times 10^4$ pseudo-experiments for (a) $W^- \to e^- \bar{\nu}_e$ (b) $W^- \to \mu^- \bar{\nu}_\mu$ channels at 5.02 TeV and (c) $W^- \to e^- \bar{\nu}_e$ and (d) $W^- \to \mu^- \bar{\nu}_\mu$ channels at 13 TeV.

distribution of the 8 channels $W^{\pm} \to e^{\pm}\nu$, $W^{\pm} \to \mu^{\pm}\nu$ at 5 and 13 TeV for each observable, p_T^{ℓ} and m_T, and the joint fit taking into account the statistical correlations generated by bootstrap toys. Contrary to the 7 TeV analysis, the dataset at low pile-up is blinded and the central value of the fit is not crucial in the study. However, the interest lies in the potential precision that can be reached in the future m_W measurement. Additionally, it is important to understand the uncertainty components of each fit and the contribution of each systematic source to the total systematic uncertainty.

Results for each fit using all channels are shown in Table 6.11. The m_T fit has a total uncertainty of 16.2 MeV, precision that is comparable to the result obtained at 7 TeV. For p_T^{ℓ}, a total uncertainty of 18.2 MeV is obtained that is larger than the 7 TeV p_T^{ℓ} result but smaller than the m_T one. The total joint fit allows to potentially reduce the total uncertainty reaching a value of 14.3 MeV that is so far, the most precise value of m_W with LHC dataset. This corresponds to an improvement of 11.7% in m_T and 21.4% in p_T^{ℓ} in the low pile-up fit.

The statistical components for each observable, m_T and p_T^{ℓ}, are 13.1 MeV and 14.7 MeV, respectively. For the joint fit, the statistical component is further reduced to 12 MeV, which corresponds to an improvement of 8.4% in m_T and 18.4% in p_T^{ℓ}. Similarly, the systematic uncertainty for each observable is 9.6 MeV for m_T and 10.8 MeV for p_T^{ℓ} that is further constrained to 7.7 MeV, representing an improvement of 19.8% in m_T and 28.7% in p_T^{ℓ}. This not only shows the power of the PLH fit in constraining the systematic sources but also the statistical component. The implemented dataset is still *work in progress* and by consequence the modelling needs further work. This is reflected in the fit quality with χ^2/n.d.f of about 1.1. However, for the final fit the precision is expected to improve with a better fit quality.

The uncertainty decomposition for the systematic sources is showed in Table 6.12 for the single observable fit (p_T^{ℓ} or m_T) and the joint fit. The sources of uncertainty are highly reduced as for example the PDF, which represents about 30% and 37% reduction with respect to m_T and p_T^{ℓ}, respectively. Similarly for the muon calibration which shows a reduction of about 30% and 35% with respect to the single fits. In the case of p_T^W, the larger uncertainty comes from p_T^{ℓ} which is more sensitive to the modelling of p_T^W but the joint fit allows the m_T fit to dominate. This leads to

a final result of 1.5 MeV which represent a reduction of 44% with respect to p_T^ℓ result.

The *preliminary* ranking plots for shift induced in the POI by the NPs and the uncertainty decomposition are shown in Fig. 6.23. The shifts in the m_W showed in Fig. 6.23a are obtained using Eq. (4.43) that rely in a full analytical calculation. On the other hand, results in Fig. 6.23b are ranked by the contribution of the systematic source to the total systematic uncertainty. These contributions are obtained by fluctuating the NP global observable as described in Eq. (4.52). These plots show that some nuisance parameters as the CT18A PDF EV are pulled considerably after the fit, which is indicative of the work that remains.

Table 6.11: Fit results in MeV for m_T, p_T^ℓ and joint fit at 5.02 TeV and 13 TeV. The first columns represent the total uncertainty (σ_{total}), the statistical component (σ_{stat}) and the total systematic (σ_{syst}). The last column is the χ^2/n.d.f of each fit.

Fit	σ_{total}	σ_{stat}	σ_{syst}	χ^2/n.d.f
m_T	16.2	13.1	9.6	3469.8/3197
p_T^ℓ	18.2	14.7	10.8	3423.9/3197
Joint fit $(p_T^\ell,\, m_T)$	14.3	12.0	7.7	6974.3/6397

Table 6.12: Uncertainty components for p_T^ℓ, m_T and joint fit results for m_W measurement using the low pile-up dataset.

Unc. [MeV]	m_T	p_T^ℓ	Joint $(p_T^\ell,\, m_T)$
$e-$SF	2.3	2.2	1.3
$e-$calib.	6.5	6.7	5.3
$\mu-$SF	2.4	3.3	2.0
$\mu-$calib.	2.4	2.6	1.7
u_T	2.5	2.5	2.4
Lumi	0.6	0.7	0.5
Backg.	2.0	3.1	2.1
p_T^W	1.5	2.7	1.5
PDF	4.6	5.1	3.2
σ_{syst}	9.6	10.8	7.7

Reducing uncertainties and prospects

One of the objectives of the present work is to improve the muon calibration by implementing the calibration procedure described in chapter 5. The procedure described has for objective to reduce the uncertainty in the muon calibration as well as the sagitta bias uncertainty. Since these results
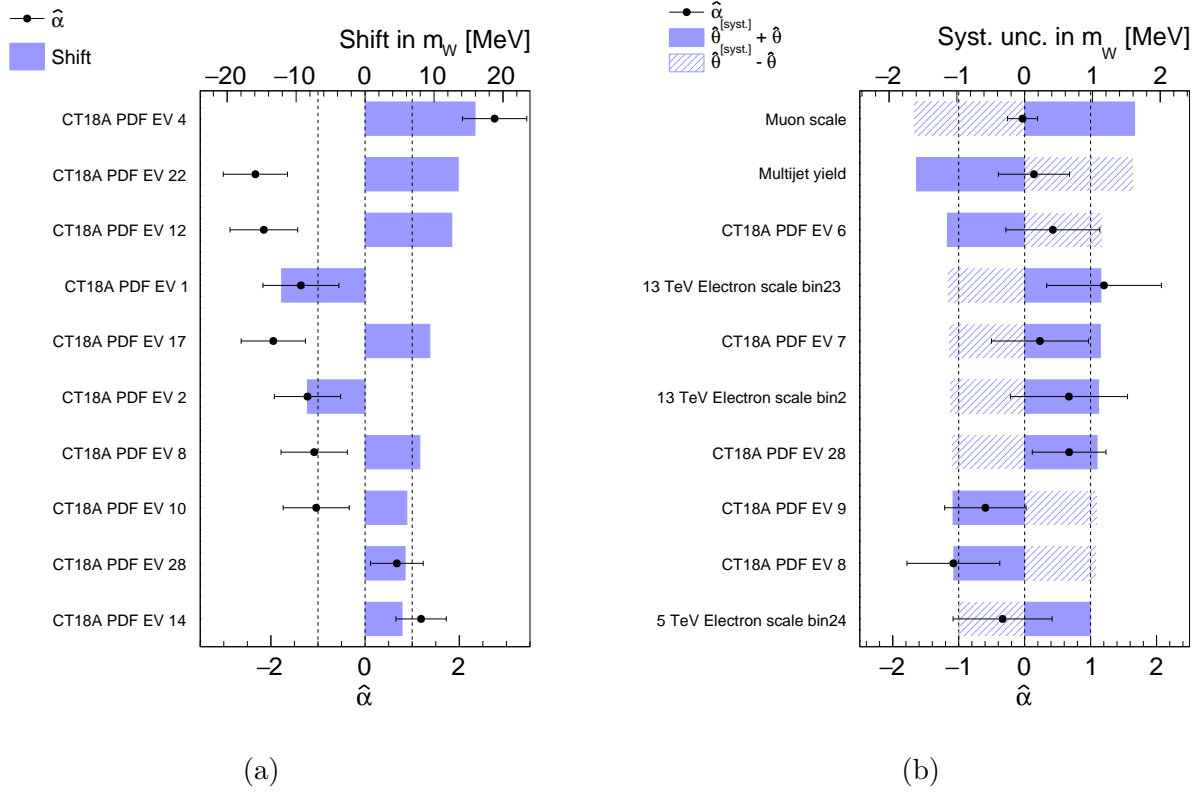
Figure 6.23: Ranking plot for (a) largest shifts induced in the POI and (b) largest systematic uncertainty component in m_W for the joint fit (p_T^ℓ, m_T) with low pile-up dataset.

are not currently applied in the presented low pile-up datasets a projection of the possible impact into the m_W uncertainty is carried out. For this, the sensitivity of these nuisance parameters to the probability model is reduced by different scale factors. This means, the uncertainty in the muon calibration and the uncertainty in the sagitta bias is reduced by factors 2, 3, 4 and 5. Results of the expected total, statistical and total systematic uncertainty are shown in Fig. 6.24. These results show a reduction in the total uncertainty of 1 MeV when the sensitivity in the muon calibration is reduced by a factor of 5 (Fig. 6.24a).

Notice that contrary to a traditional fit, reducing the systematic uncertainty has not only effect in the systematic component. Fig. 6.24b shows that the statistical component is reduced by 1.2 MeV. On the other hand, the systematic component increases when the uncertainties are reduced up to a factor 3 and then both components, σ_{stat} and σ_{syst}, start to decrease. In a traditional fit, if the systematic component is reduced by a given factor f, it might straightforwardly be expected,

$$\sigma_{\text{total}}^2 = \sigma_{\text{stat}}^2 + (\sigma_{\text{syst}}/f)^2 \,, \tag{6.29}$$

but this is not the case in PLH fits since as described in Section 4.3, there is an interplay between systematic sources. This means that each component of the POI uncertainty is directly affected by the scale factor. Therefore, reducing the uncertainty in one systematic source can affect the constraints on other correlated systematic sources. For example, if the reduced systematic uncertainty was previously providing an anti-correlation effect with another systematic source, reducing it can lead to a less constrained total systematic uncertainty. Similarly, if some sources are directly affect by a charge effect, the scale factor could has zero impact.

Results in Fig. 6.24 show an small effect in scaling the sagitta bias uncertainty. This is due to the fact that the sagitta is a charge dependent effect and by consequence when performing a joint fit, this benefits from the opposite charge cancellation. However, this cancellation is not perfect since the number of W^+ and W^- candidates are not exactly the same, and by consequence, the symmetry is broken. To know what is the effect of the scale factors in the uncertainty components a similar study is performed only with the muon channels by electric charge as shown in Fig. 6.25. In
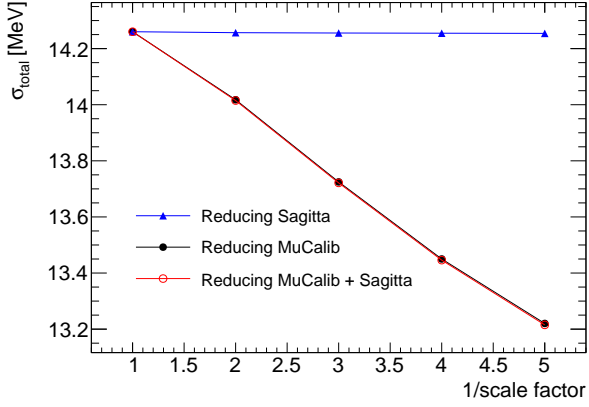
(a)
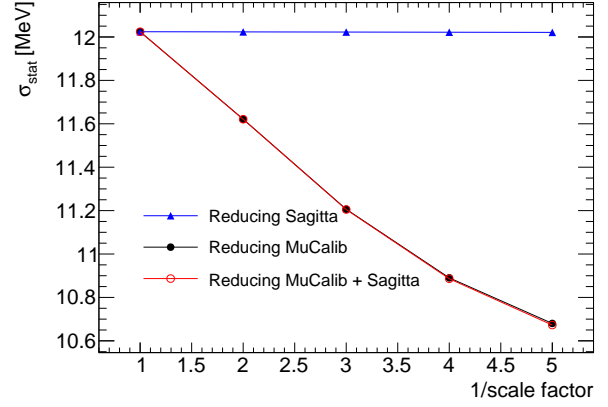
(b)
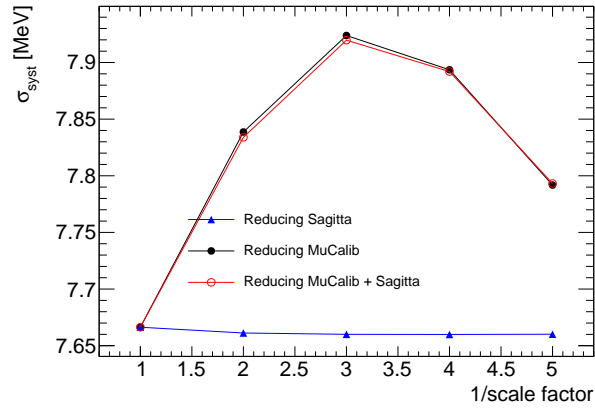
(c)

Figure 6.24: Uncertainty components in m_W for (a) total uncertainty, (b) statistical uncertainty and (c) systematic uncertainty in $W \rightarrow e\nu$ and $W \rightarrow \mu\nu$ by reducing the muon calibration and sagitta bias uncertainties in the joint fit (p_T^ℓ, m_T) at $5.02 + 13$ TeV.
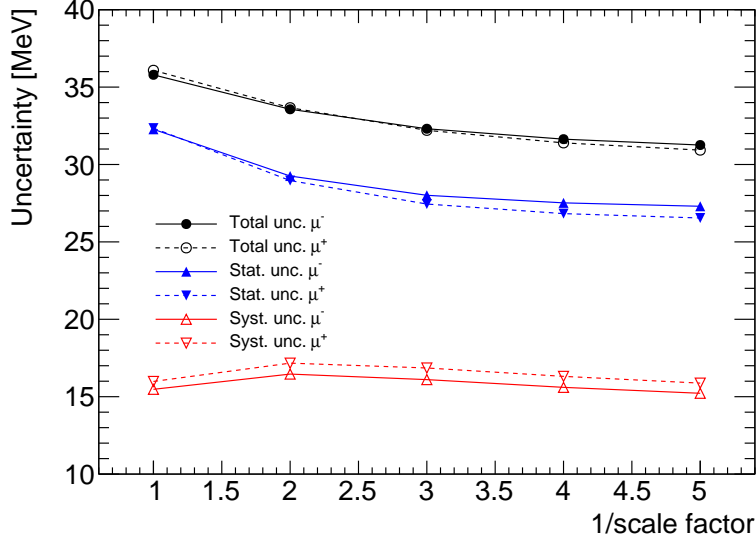
Figure 6.25: Uncertainty components in the $W^{\pm} \to \mu^{\pm}\nu$ channel by scaling the sagitta bias uncertainty for the joint $5.02 + 13$ TeV for positive and negative electric charges.

fact, reducing the sagitta uncertainty leads to a reduction of about 4.5 MeV in the total uncertainty and 5.2 MeV in the statistical component. In the case of the total systematic component, this increases when the sensitivity is reduced by two and it starts to decrease for larger factors leading to a maximum reduction of 0.25 MeV. Notice that these results also show that the effect in positive and negative muons is not the same due to the fact that W^+ and W^- number of candidates are not the same. Similar to the previous result, reducing a systematic source sensitivity produces an impact on the statistical component with an overall reduction in the total uncertainty. Taking into account that the global fit benefits from the charge cancellation this is not relevant for obtaining the global m_W value, however, it is for estimating the mass of W^+ and W^- independently in each category.

6.8 Expected precision for m_W at $\sqrt{s} = 5.02$, 7 and 13 TeV

Two independent studies have been carried out, the high pile-up at 7 TeV and the low pile-up at 5.02 TeV and 13 TeV. Results at 7 TeV benefits from a high statistics compared to the low pile-up. Meanwhile, the low pile-up benefits from a better resolution in the hadronic recoil and a new p_T^W modelling that is unbiased by construction and that allows to reduce the corresponding

uncertainties. To exploit the current ATLAS datasets, a single measurement at $5.02 + 7 + 13$ TeV is carried out through a joint fit. For this, the correlations among the datasets should be accounted properly. As discussed in section 6.6, the p_T^ℓ and m_T datasets at 7 TeV were prepared with different PCA in some systematics sources, leading to different NPs for both distributions. For this reason a joint fit is not straightforward. However, the studies showed that a $p_T^\ell - m_T$ statistical combination at 7 TeV is mainly dominated by p_T^ℓ and for that reason only this observable is considered to perform a joint fit.

Since the p_T^ℓ high pile-up dataset and low pile-up datasets are from different data-taking periods (Run 1 and Run 2), they are fully statistical uncorrelated and by consequence no bootstrap toys are required. Nevertheless, the systematics sources need to be correlated. The common systematic sources shared by the datasets are the parton distribution functions corresponding to the CT18A PDF set with 29 eigen vectors (EV). Taking this into account and correlating only the systematic sources, a joint fit in bin number $\left(p_T^\ell + m_T\right)^{5 + 13 \text{ TeV}} + p_T^{\ell,\, 7 \text{ TeV}}$ is performed.

Fit results are shown in Table 6.13 where a total uncertainty of 10.3 MeV is obtained. The main constraining power comes from the statistical component with a reduction of 4 MeV and 1.2 MeV in the total systematic uncertainty with respect to the low pile-up joint fit. This represents a reduction of 28% in the total uncertainty, 33.3% in the statistical component and 15.6% in the total systematic. Notice that the central value of the fit, m_W, at 7 TeV is unblinded while the low pile-up dataset is blinded. This leads to a bad quality fit that will be improved once all the systematic sources are completed in the low pile-up analysis and the muon calibration is improved. The present study is carried to study the prospects in precision.

Table 6.13: Fit results in MeV for m_T, p_T^ℓ and joint fit at 5.02 TeV, 7 TeV and 13 TeV. The first columns represent the m_W value, total uncertainty (σ_{total}), the statistical component σ_{stat} and the total systematic (σ_{syst}). The last column is the $\chi^2/$n.d.f of each fit.

Fit	σ_{total}	σ_{stat}	σ_{syst}	$\chi^2/$n.d.f
m_T	16.2	13.1	9.6	3469.8/3197
p_T^ℓ	18.2	14.7	10.8	3423.9/3197
Joint fit: $5.02 + 13$ TeV	14.3	12.0	7.7	6974.3/6397
Joint fit: $5.02 + 7 + 13$ TeV	10.3	8.0	6.5	7449.9/6536

6.9 Compatibility and combination of world W-boson mass measurements

Several high-precision measurements of m_W have been carried out by different experiments at the LEP (ALEPH, DELPHI, L3 and OPAL), Tevatron (CDF and D0) and the LHC (ATLAS and LHCb). However, recent results, particularly from the CDF experiment, have shown significant deviations when compared to other measurements, raising questions about the compatibility of these results. For that reason, a dedicated study of combination and compatibility is necessary to study the potential precision reached by the current results.

At hadron colliders like the LHC and Tevatron, the W-boson mass is typically measured by analyzing the kinematics of the W-boson's leptonic decay into a charged lepton and a neutrino, $W \to \ell\nu$. The major kinematic variables used in these measurements are the transverse momentum of the charged lepton (p_T^ℓ), the transverse mass (m_T) and the recoil transverse momentum (u_T). Each experiment used a large dataset and sophisticated statistical techniques to measure m_W with high precision leading to the results in Table 6.14.

Table 6.14: W-boson mass measurement by different experiments.

Facility	Experiment	m_W (MeV)
LEP	ALEPH + DELPHI + L3 + OPAL	80376.0 ± 33.0
Tevatron	CDF	80433.5 ± 9.4
	D0	80375.0 ± 23.0
LHC	LHCb	80354.0 ± 32.0
	ATLAS 2017	80370.0 ± 19.0
	ATLAS 2024 (This work)	80366.5 ± 15.9

The accuracy of m_W measurements is influenced by the choice of Parton Distribution Functions (PDFs). Different experiments have used various PDF sets, such as CT14, CT18, MMHT2014, MSHT20 NNPDF3.1 and NNPDF4.0, each offering distinct parametrizations and uncertainties. Since m_W depends on the initial-state partons, the choice of PDF set can introduce significant systematic uncertainties.

Previous work in Ref. [82] performed the compatibility and combination study of m_W using the measurement of the W-boson mass by the ATLAS collaboration in 2017 [76]. In this work, the compatibility and combination studies using the latest m_W results by ATLAS 2024 in Table 6.6 are carried out.

Combining these measurements into a single, precise value of m_W requires dedicated treatment of the systematic uncertainties and correlations. First, each measurement is reinterpreted within a common theoretical framework to compare the central values and uncertainties, ensuring that differences in the PDF sets are accounted for. This reference model includes the description of W-boson production, the Breit-Wigner lineshape, and W-boson polarization. The formalism to bring all the measurements to a common framework follows the methodology described in Ref. [82] where an exhaustive analysis is discussed.

The adjustment process involves emulating the measurement procedures using Monte Carlo event generation and simplified detector simulations. The Monte Carlo samples are produced with a reference W-boson mass and width. Events are reweighted to different W-boson mass values using a Breit-Wigner distribution. This reweighting has been validated to provide accurate mass values within a statistical uncertainty of approximately 0.2 MeV.

The uncertainties from the different experiments, which have different center-of-mass energies, initial states, and lepton pseudorapidity coverage, are evaluated to account for non-trivial correlations. The shift in the m_W resulting from a change in the generator model is estimated by creating templates accounting for the experiment's model and the same kinematics distributions of an alternate model, i.e. Pseudo-data. The impact, δm_W, of this pseudo-data is determine via the χ^2 off-set method as described in section 4.1.

A consistent set of uncertainties and correlations between experiments is established by evaluating δm_W across multiple PDF sets within the reference theoretical model. The total theoretical shift, δm_W, is obtained by summing the individual contributions. This total shift is then added to each experimental measurement to determine the adjusted value used in the final combination. Finally, for each PDF set, a final covariance matrix is constructed accounting for experimental and theoretical uncertainties. The combination of m_W is performed using the fitting strategy described

in section 4.3 that incorporates the adjusted measurements and their correlation as follows,

$$-2\ln\mathcal{L}_{\text{cmb}}(\vec{\theta}) = \sum_{i,j}\left(m_i - \sum_p U_{ip}\theta_p\right)C_{ij}^{-1}\left(m_j - \sum_q U_{jq}\theta_q\right), \tag{6.30}$$

where i, j run over the measurements and p, q over the POI. $\vec{m}$ is the measurements vector with covariance matrix C. $\vec{\theta}$ is the POI vector and U_{ip} is 1 when measurement i is an estimator of POI p, and 0 otherwise [132].

Combinations are performed in two cases. First, for each PDF set all measurements are combined while the second case consider all measurements except CDF. These results are showed in Tables 6.15 and 6.17, respectively. Where final values are in agreement with Ref. [82].

For the first case, a combination of all measurements results in uncertainties from 8.6 MeV to 10.2 MeV and χ^2 probabilities of 10^{-6} to 2×10^{-3}, respectively. This reflects the discrepancy between the measurement with respect to the CDF result. Due to the larger uncertainties, the CT18 PDF set is chosen as the baseline with a combination value of $m_W = 80388.4 \pm 10.3$ MeV with a probability of 0.2%. The relative weights in the combination are shown in Table 6.16 that for CT18 corresponds to 38.6%, 10.0%, 5.3%, 36.4% and 9.6% for ATLAS (2024), LHCb, D0, CDF and LEP respectively. This shows a larger contribution of the new m_W measurement by ATLAS, which, compared to the 2017 measurement, has a weight of 28% with total uncertainty of 11.5 MeV and PDF uncertainty of 7.7 MeV [82]. This means that the new ATLAS result improves the total uncertainty in 10% and the PDF uncertainty in 19%.

Table 6.15: Combination of all m_W measurements with all experiments. Shown for each PDF are the PDF uncertainty, χ^2, and probability of obtaining this χ^2 or larger. m_W and σ_{PDF} units are in MeV.

	All experiments			
PDF set	m_W	σ_{PDF}	χ^2	$\text{Prob}(\chi^2, \text{n.d.f})$
CT14	80389.2 ± 10.2	6.3	17.3	0.2%
CT18	80388.4 ± 10.3	6.2	16.5	0.2%
MMHT2014	80394.0 ± 8.5	4.8	18.5	0.1%
MSHT20	80389.0 ± 8.7	5.1	19.8	0.1%
NNPDF3.1	80397.7 ± 8.5	5.0	28.7	0.001%
NNPDF4.0	80397.7 ± 8.6	5.0	33.8	0.0001%

Table 6.16: Relative combination weights (in percent) for all experiments.

Measurement	CT14	CT18	MMHT2014	MSHT20	NNPDF3.1	NNPDF4.0
ATLAS 2024	38.6	40.6	28.4	32.2	25.2	29.5
LHCb	10.0	10.5	8.2	9.1	7.9	8.3
CDF	36.4	34.7	49.0	44.7	52.2	47.8
D0	5.3	4.4	7.7	7.0	8.1	7.6
LEP	9.6	9.8	6.7	7.0	6.6	6.8

In the second case, a combination excluding CDF measurement is performed with uncertainties ranging from 11.0 MeV to 11.8 MeV and χ^2 probability of 53% and 96%, respectively. This shows a good compatibility between the measurements with an increase of 1.5 MeV to 2.4 MeV with respect to the full combination. The significance (in σ units) is also quantified with respect to the CDF measurement ranging 4σ to 5.7σ. For the CT18, the final combination retrieves a value of $m_W = 80366.1 \pm 11.7$ MeV with 92% probability that differs from CDF by 3.8σ. Relative combination weights are shown in Table 6.18, with 54.2%, 13.9%, 19.3% and 12.6% for ATLAS, LHCb, D0 and LEP, respectively. The addition of the new m_W result improves considerably its contribution with respect to the 2017 result, where ATLAS weight was 42% with a total uncertainty of 13.3 MeV and PDF uncertainty of 6.2 MeV [82]. This is a reduction of 12% and 26% in the total uncertainty and the PDF uncertainty, respectively.

The 2017 and 2024 ATLAS m_W results as well as the m_W combinations for all experiments and all experiments except CDF are shown in Fig. 6.26. It is necessary to highlight the difference in the m_W values obtained in 2017 and 2024 (this work) with the various PDF sets. Since the 2024 results implemented the profile likelihood fit, a constraining power in the PDF uncertainties plays a relevant role and the results show a similar tendency for common PDF sets. This also reflects the viability of the profiling technique with respect to the χ^2 off-set method.

6.10   Summary

The current status of m_W and Γ_W has been discussed for the high pile-up at 7 TeV. Furthermore, the prospects and expected precision for m_W in low pile-up at 5.02 TeV and 13 TeV have been
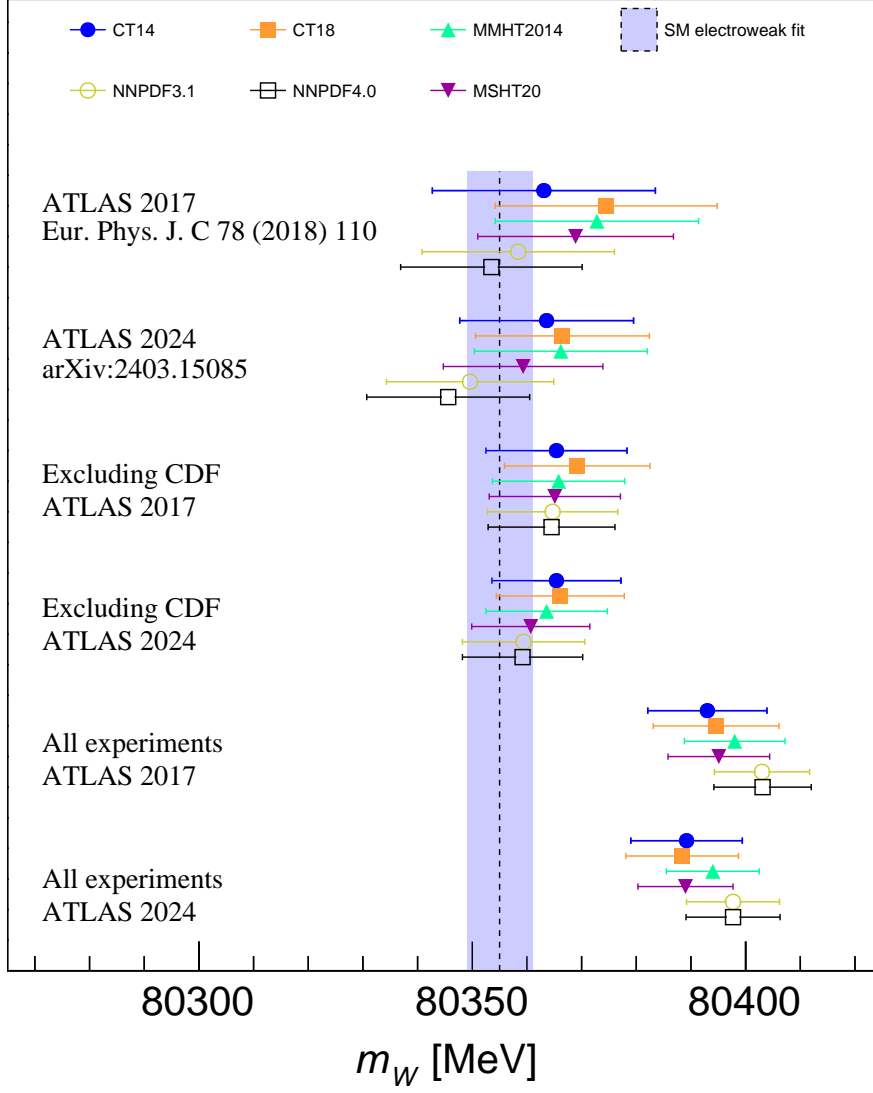
Figure 6.26: The first and new ATLAS m_W result and combined m_W values and uncertainties for all experiments and all experiments except CDF using the CT14, CT18, MMHT2014, MMHT20, NNPDF3.1, and NNPDF4.0 PDF sets.

Table 6.17: Combination of all m_W measurements except CDF. Shown for each PDF are the PDF uncertainty, χ^2, and probability of obtaining this χ^2 or larger. m_W and σ_{PDF} units are in MeV.

	All experiments except CDF				
PDF set	m_W	σ_{PDF}	χ^2	$\text{Prob}(\chi^2, \text{n.d.f})$	Significance with respect to CDF (σ units)
CT14	80365.4 ± 11.8	4.7	0.3	96%	4.0
CT18	80366.1 ± 11.7	4.6	0.5	92%	3.8
MMHT2014	80363.6 ± 11.1	3.3	0.6	89%	4.2
MSHT20	80360.7 ± 10.8	3.5	0.3	96%	4.3
NNPDF3.1	80359.4 ± 11.2	4.0	1.1	78%	5.3
NNPDF4.0	80359.2 ± 11.0	3.6	2.2	53%	5.7

Table 6.18: Relative combination weights (in percent) for all experiments except CDF.

Measurement	CT14	CT18	MMHT2014	MSHT20	NNPDF3.1	NNPDF4.0
ATLAS 2024	53.5	54.2	50.3	54.3	51.5	52.9
LHCb	13.7	13.9	13.8	13.4	13.6	13.3
D0	20.2	19.3	24.5	21.5	23.4	22.6
LEP	12.7	12.6	11.4	10.8	11.5	11.1

evaluated. For both analyses, the dataset and simulation have been largely discussed as well as the different background estimation, modelling of uncertainties and uncertainty propagation. One of the breakthroughs correspond to the p_T^W modelling at low pile-up using the Iterative Bayesian Unfolding approach. In this, a direct measurement of the W boson transverse momentum has been performed to reduce the uncertainties related to the p_T^Z extrapolation. This leads to a p_T^W spectrum that is unbiased by construction and can potentially reduce the corresponding uncertainties.

A new fitting strategy to evaluate the systematic uncertainties has been introduced. This is, the profile likelihood fit contrary, the χ^2 offset method used in previous studies. This fitting strategy has been evaluated in both scenarios numerical and analytical. The numerical approach considered uncertainties with a Poisson distribution. Meanwhile, the analytical solution assumed uncertainties that are Gaussian-distributed. The analytical solution allowed to obtain the uncertainty components such as total, statistical and systematic. To asses the uncertainty decomposition of the systematic sources, the global shifted observable method was implemented. This allowed to obtain components that recover the total systematic uncertainty when they are summed in quadrature, contrary to the

impact method.

Results at 7 TeV are revisited from the first ATLAS publication [76] showing a compatibility between the new and old measurements and an improvement in the precision from 19 MeV to 16 MeV. The PDF has been largely studied by implementing different PDF sets, showing that m_W result is driven by the pre-fit PDF uncertainties, and is strongly reduced when allowing for enlarged uncertainties. The baseline result corresponds to the one with CT18 PDF set, which is the most conservative one and leads to current value of m_W of [107],

$$m_W = 80366.5 \pm 9.8(\text{stat.}) \pm 12.5(\text{syst.}) \text{ MeV} = 80366.5 \pm 15.9 \text{ MeV}. \tag{6.31}$$

No deviation with respect to the SM was found. By a similar approach, the first W boson width (Γ_W) measurement was performed with similar studies showing no strong dependence with the PDF set. Result with CT18 PDF set correspond to,

$$\Gamma_W = 2202 \pm 32(\text{stat.}) \pm 34(\text{syst.}) \text{ MeV} = 2202 \pm 47 \text{ MeV}. \tag{6.32}$$

This is, the most precise single Γ_W measurement and it agrees with the SM within two standard deviations.

In the low pile-up scenario, the prospects in precision were studied for two observables, p_T^ℓ and m_T with CT18A PDF set. These independent fits showed a preliminary blinded result of,

$$
\begin{aligned}
m_W^{m_T} &= XYZ \pm 13.1(\text{stat.}) \pm 9.6(\text{syst.}) \text{ MeV} = XYZ \pm 16.2 \text{ MeV}. \\
m_W^{p_T^\ell} &= XYZ \pm 14.7(\text{stat.}) \pm 10.8(\text{syst.}) \text{ MeV} = XYZ \pm 18.2 \text{ MeV}.
\end{aligned}
\tag{6.33}
$$

These results were further improved by performing a joint fit of the two observables in which the statistical correlations were properly evaluated in the different u_T and η_ℓ categories for all the channels and centre-of-mass energy. Taking this into account, the expected precision obtained in the low pile-up is given by,

$$m_W^{5+13 \text{ TeV}} = XYZ \pm 12.0(\text{stat.}) \pm 7.7(\text{syst.}) \text{ MeV} = XYZ \pm 14.3 \text{ MeV}, \tag{6.34}$$

showing a reduction in the PDF uncertainties and muon calibration of about 30% with respect to the single fits and 44% in p_T^W with respect to the p_T^ℓ fit result. To determine the potential improvement in precision by improving the muon calibration and sagitta bias, different exercises by reducing the sensitivity of these nuisance parameters were carried out. Results showed an improvement of about 1 MeV in the total uncertainty when uncertainties are reduced by a factor of 5. Getting the most of the ATLAS datasets, a preliminary joint fit between the p_T^ℓ 7 TeV and the full low pile-up dataset was performed with the CT18A PDF set (common PDF set between the data), giving a final precision of,

$$m_W^{5+7+13\text{ TeV}} = XYZ \pm 8.0(\text{stat.}) \pm 6.5(\text{syst.})\text{ MeV} = XYZ \pm 10.3\text{ MeV}, \tag{6.35}$$

where a reduction of 28% in the total uncertainty, 33.3% in the statistical uncertainty and 15.6% in the total systematic was obtained with respect to the low pile-up fit.

Finally, the compatibility and combination between the new ATLAS 2024 result at 7 TeV (Table 6.6) and other experimental results, such as those from LHCb, CDF, D0, and LEP, were studied. Different PDF sets were considered in a consistent framework accounting for the different correlations. Two combinations of all measurements were performed: one including CDF (w/ CDF) and one without CDF (w/o CDF), using various PDF sets with CT18 as the baseline. Results with CDF showed uncertainties ranging from 8.6 MeV to 10.2 MeV with probabilities from 10^{-6} to 2×10^{-3}. On the other hand, when CDF is removed the total uncertainty spans values from 11 MeV to 11.8 MeV implying an increase in the uncertainty from 1.5 MeV to 2.4 MeV with respect to the full combination. However, these results shows a χ^2 probability from 53% to 96%. CT18 baseline results lead to the world averages,

$$\begin{aligned} m_W^{\text{w/ CDF}} &= 80388.4 \pm 10.3\text{ MeV}, \\ m_W^{\text{w/o CDF}} &= 80366.1 \pm 11.7\text{ MeV}. \end{aligned} \tag{6.36}$$

where a compatibility of 0.2% is obtained when CDF is included and 92% compatibility is obtained when CDF is removed differing from CDF by 3.8σ.

Conclusion

This work presents the current status of the W boson mass and width using the Run 1 dataset at 7 TeV, and the prospects of the W boson mass with the Run 2 low pile-up dataset at 5.02 TeV and 13 TeV. For this, a dedicated calibration procedure of the ATLAS Inner Detector and Muon Spectrometer was designed and implemented. A fitting strategy based on profile likelihood fits was largely explored and the analytical solution in the regime where the uncertainties are Gaussian-distributed was utilized. A consistent way to study the uncertainty components: total, statistical and systematic uncertainties was provided and a method to obtain the uncertainty decomposition based on global shifted observable was discussed. This method was also introduced for general distributions and in the Gaussian limit a consistent analytical result was described. In the same way, a method for combining profile likelihood fit results using decomposed uncertainties was also introduced and applied.

The calibration procedure considered possible charged dependent biases related to the muon track sagitta that was evaluated by minimising the variance of the invariant mass distribution. After correction, the bias was reduced from an average value of 0.05 TeV^{-1} to 2×10^{-4} TeV^{-1} improving the resolution in the invariant mass of the Z boson and J/ψ meson. To calibrate the ID for possible geometrical deformations, a large study using $J/\psi \to \mu\mu$ was performed showing a global scale bias and modulations in the invariant mass with a 0.02% deviation with respect to the simulation. To correct these deformations, different models accounting for radial, longitudinal, and magnetic field distortions were simulated to generate templates. These templates were then used to perform an analytical fit of the data with respect to the simulation. A final magnetic field-radial model was implemented with relative bias of $\langle \varepsilon_B \rangle = -1.5 \times 10^{-3}$ and $\langle \varepsilon_R \rangle = 1.0 \times 10^{-3}$ for the

magnetic field and radial distortions, respectively. After correction, the scale and modulations in the invariant mass were corrected leading to a data-to-simulation agreement at the per mille level in the scales.

In the case of the MS, the alignment residuals between the ID and MS were investigated showing a bias of about 1.5 mm in the longitudinal impact parameter and few mrad in the polar angle. To this bias, a charge dependent effect was observed with possible origin in the toroidal magnetic field in the tile calorimeter region. To mitigate this, the magnetic field in the tile calorimeter was re-evaluated, proposing an effective correction of 25% of the current field strength. Additionally, a more sophisticated approach involved computing a dedicated correction map in (η, ϕ)-space, which effectively reduced the charge-dependent effects. For the bias in the impact parameters, a dedicated map in the second coordinates, transverse impact parameter and azimuthal angle, was obtained and injected as a correction function in the tracks. After correction, the track reconstruction between the MS and ID was improved and a good agreement between data and simulation was obtained.

To complete the calibration procedure, after the pre-corrections a dedicated muon momentum calibration (MMC) was carried out. This MMC considers the scale and resolution parameters that account for magnetic field mismodelling and multiple scattering effects. The di-muon invariant mass was fitted using the template fit approach and the final calibration was retrieved by an analytical fit. The scale and resolution final maps were obtained as a function of the muon rapidity and the simulation was corrected. A final data-to-simulation agreement at the per mille level was obtained.

For the W boson mass and width, a fitting strategy based on profile likelihood fit was implemented. The particular case where the uncertainties are Gaussian-distributed was considered and the analytical solution was proposed. This approach allowed a proper decomposition of the fit uncertainties and to determine the actual contribution of each systematic source to the final measurement uncertainty. Moreover, the PDF dependency of both m_W and Γ_W was studied with different PDF sets showing that m_W result is driven by the pre-fit PDF uncertainties, and it is strongly reduced when allowing for enlarged uncertainties. For Γ_W a weak dependence with the

252

PDF set was found. The final result for the W mass measurement at 7 TeV was found to be,

$$m_W = 80366.5 \pm 9.8(\text{stat.}) \pm 12.5(\text{syst.}) \text{ MeV} = 80366.5 \pm 15.9 \text{ MeV}. \tag{6.37}$$

while for the width,

$$\Gamma_W = 2202 \pm 32(\text{stat.}) \pm 34(\text{syst.}) \text{ MeV} = 2202 \pm 47 \text{ MeV}. \tag{6.38}$$

In the case of the low pile-up, a new p_T^W modelling was largely explored by implementing the Iterative Bayesian Unfolding instead of the usual p_T^Z extrapolation. This new approach allowed to obtain a better modelling that is unbiased by construction and it allowed for a reduction in the uncertainty. For the low pile-up dataset a preliminary blinded result for m_W was obtained to be,

$$m_W^{5.02\,+\,13\text{ TeV}} = XYZ \pm 12.0(\text{stat.}) \pm 7.7(\text{syst.}) \text{ MeV} = XYZ \pm 14.3 \text{ MeV}. \tag{6.39}$$

Combining with the 7 TeV data the final result is given by,

$$m_W^{5.02\,+\,7\,+\,13\text{ TeV}} = XYZ \pm 8.0(\text{stat.}) \pm 6.5(\text{syst.}) \text{ MeV} = XYZ \pm 10.3 \text{ MeV}. \tag{6.40}$$

The presented results are still work in progress for both muon calibration and W boson mass measurement. However, this work aims to show the prospects in m_W while also highlighting areas requiring further work, which will potentially improve the precision.

Finally, the compatibility and combination of the world W-boson mass measurements were assessed by taking into account the latest results from LEP, CDF II, D0 and LHCb, with the current ATLAS 2024 result at 7 TeV in Table 6.6. This study leads to the current world average for both with CDF and without the CDF measurement,

$$
\begin{aligned}
m_W^{\text{w/ CDF}} &= 80388.4 \pm 10.3 \text{ MeV}, \\
m_W^{\text{w/o CDF}} &= 80366.1 \pm 11.7 \text{ MeV}.
\end{aligned}
\tag{6.41}
$$

where a compatibility of 0.2% is obtained when CDF is included and 92% compatibility is obtained when CDF is removed differing by 3.8σ using the CT18 PDF set.

Bibliography

[1] M. E. Peskin and D. V. Schroeder, *An Introduction to Quantum Field Theory.* Westview Press, 1995. Reading, USA: Addison-Wesley (1995) 842 p.

[2] S. Weinberg, "A Model of Leptons," *Phys. Rev. Lett.*, vol. 19, pp. 1264–1266, 1967.

[3] A. Salam and J. C. Ward, "Weak and electromagnetic interactions," *Nuovo Cim.*, vol. 11, pp. 568–577, 1959.

[4] G. 't Hooft and M. J. G. Veltman, "Regularization and Renormalization of Gauge Fields," *Nucl. Phys. B*, vol. 44, pp. 189–213, 1972.

[5] G. Aad *et al.*, "Observation of a new particle in the search for the Standard Model Higgs boson with the ATLAS detector at the LHC," *Phys. Lett. B*, vol. 716, pp. 1–29, 2012.

[6] S. Chatrchyan *et al.*, "Observation of a New Boson at a Mass of 125 GeV with the CMS Experiment at the LHC," *Phys. Lett. B*, vol. 716, pp. 30–61, 2012.

[7] A. Arbuzov, "Quantum Field Theory and the Electroweak Standard Model," *CERN Yellow Rep. School Proc.*, vol. 3, pp. 1–35, 2018.

[8] C. S. Wu, E. Ambler, R. W. Hayward, D. D. Hoppes, and R. P. Hudson, "Experimental Test of Parity Conservation in β Decay," *Phys. Rev.*, vol. 105, pp. 1413–1414, 1957.

[9] Y. Fukuda *et al.*, "Evidence for oscillation of atmospheric neutrinos," *Phys. Rev. Lett.*, vol. 81, pp. 1562–1567, 1998.

[10] P. Adamson *et al.*, "Measurement of Neutrino and Antineutrino Oscillations Using Beam and Atmospheric Data in MINOS," *Phys. Rev. Lett.*, vol. 110, no. 25, p. 251801, 2013.

[11] P. W. Higgs, "Broken Symmetries and the Masses of Gauge Bosons," *Phys. Rev. Lett.*, vol. 13, pp. 508–509, 1964.

[12] F. Englert and R. Brout, "Broken symmetry and the mass of gauge vector mesons," *Physical review letters*, vol. 13, no. 9, p. 321, 1964.

[13] A. Pich, "The Standard model of electroweak interactions," pp. 1–48, 2 2005.

[14] M. Aaboud *et al.*, "Measurement of inclusive and differential cross sections in the $H \to ZZ^* \to 4\ell$ decay channel in pp collisions at $\sqrt{s} = 13$ TeV with the ATLAS detector," *JHEP*, vol. 10, p. 132, 2017.

[15] G. Aad *et al.*, "Measurements of the Higgs boson production and decay rates and constraints on its couplings from a combined ATLAS and CMS analysis of the LHC pp collision data at $\sqrt{s} = 7$ and 8 TeV," *JHEP*, vol. 08, p. 045, 2016.

[16] R. L. Workman *et al.*, "Review of Particle Physics," *PTEP*, vol. 2022, p. 083C01, 2022.

[17] H. Spiesberger, M. Spira, and P. M. Zerwas, "The Standard model: Physical basis and scattering experiments," pp. 1505–1533, 11 2000.

[18] R. Carey, T. Gorringe, and D. Hertzog, "Mulan: a part-per-million measurement of the muon lifetime and determination of the Fermi constant," *SciPost Phys. Proc.*, p. 016, 2021.

[19] L. Morel, Z. Yao, P. Cladé, and S. Guellati-Khélifa, "Determination of the fine-structure constant with an accuracy of 81 parts per trillion," *Nature*, vol. 588, no. 7836, pp. 61–65, 2020.

[20] S. Schael *et al.*, "Precision electroweak measurements on the Z resonance," *Phys. Rept.*, vol. 427, pp. 257–454, 2006.

[21] A. Djouadi and C. Verzegnassi, "Virtual Very Heavy Top Effects in LEP / SLC Precision Measurements," *Phys. Lett. B*, vol. 195, pp. 265–271, 1987.

[22] L. Avdeev, J. Fleischer, S. Mikhailov, and O. Tarasov, "0($\alpha\alpha_s^2$) correction to the electroweak ρ parameter," *Phys. Lett. B*, vol. 336, pp. 560–566, 1994. [Erratum: Phys.Lett.B 349, 597–598 (1995)].

[23] K. G. Chetyrkin, J. H. Kuhn, and M. Steinhauser, "Three loop polarization function and O (alpha-s**2) corrections to the production of heavy quarks," *Nucl. Phys. B*, vol. 482, pp. 213–240, 1996.

[24] Y. Schroder and M. Steinhauser, "Four-loop singlet contribution to the rho parameter," *Phys. Lett. B*, vol. 622, pp. 124–130, 2005.

[25] A. Freitas, W. Hollik, W. Walter, and G. Weiglein, "Electroweak two loop corrections to the $M_W - M_Z$ mass correlation in the standard model," *Nucl. Phys. B*, vol. 632, pp. 189–218, 2002. [Erratum: Nucl.Phys.B 666, 305–307 (2003)].

[26] A. Freitas, W. Hollik, W. Walter, and G. Weiglein, "Complete fermionic two loop results for the M(W) - M(Z) interdependence," *Phys. Lett. B*, vol. 495, pp. 338–346, 2000. [Erratum: Phys.Lett.B 570, 265 (2003)].

[27] M. Awramik and M. Czakon, "Complete two loop electroweak contributions to the muon lifetime in the standard model," *Phys. Lett. B*, vol. 568, pp. 48–54, 2003.

[28] M. Awramik and M. Czakon, "Complete two loop bosonic contributions to the muon lifetime in the standard model," *Phys. Rev. Lett.*, vol. 89, p. 241801, 2002.

[29] G. Weiglein, "Results for precision observables in the electroweak standard model at two loop order and beyond," *Acta Phys. Polon. B*, vol. 29, pp. 2735–2741, 1998.

[30] M. Faisst, J. H. Kuhn, T. Seidensticker, and O. Veretin, "Three loop top quark contributions to the rho parameter," *Nucl. Phys. B*, vol. 665, pp. 649–662, 2003.

[31] J. Haller, A. Hoecker, R. Kogler, K. Mönig, T. Peiffer, and J. Stelzer, "Update of the global electroweak fit and constraints on two-Higgs-doublet models," *Eur. Phys. J. C*, vol. 78, no. 8, p. 675, 2018.

[32] M. Baak, J. Cúth, J. Haller, A. Hoecker, R. Kogler, K. Mönig, M. Schott, and J. Stelzer, "The global electroweak fit at NNLO and prospects for the LHC and ILC," *Eur. Phys. J. C*, vol. 74, p. 3046, 2014.

[33] S. Heinemeyer, W. Hollik, D. Stockinger, A. M. Weber, and G. Weiglein, "Testing the MSSM with the Mass of the W Boson," *Pramana*, vol. 69, pp. 783–788, 2007.

[34] K.-Y. Zhang and W.-Z. Feng, "Explaining the W boson mass anomaly and dark matter with a U(1) dark sector*," *Chin. Phys. C*, vol. 47, no. 2, p. 023107, 2023.

[35] M. E. Peskin and T. Takeuchi, "Estimation of oblique electroweak corrections," *Phys. Rev. D*, vol. 46, pp. 381–409, Jul 1992.

[36] G. Cacciapaglia, A. Deandrea, A. M. Iyer, and A. Pinto, "Sifting composite from elementary models at FCCee and CePC," *SciPost Phys.*, vol. 14, p. 170, 2023.

[37] D. B. Kaplan, H. Georgi, and S. Dimopoulos, "Composite Higgs Scalars," *Phys. Lett. B*, vol. 136, pp. 187–190, 1984.

[38] C. P. Burgess, M. Pospelov, and T. ter Veldhuis, "The Minimal model of nonbaryonic dark matter: A Singlet scalar," *Nucl. Phys. B*, vol. 619, pp. 709–728, 2001.

[39] A. Blondel and P. Janot, "FCC-ee overview: new opportunities create new challenges," *Eur. Phys. J. Plus*, vol. 137, no. 1, p. 92, 2022.

[40] M. Bauer, M. Heiles, M. Neubert, and A. Thamm, "Axion-Like Particles at Future Colliders," *Eur. Phys. J. C*, vol. 79, no. 1, p. 74, 2019.

[41] H. Cheng *et al.*, "The Physics potential of the CEPC. Prepared for the US Snowmass Community Planning Exercise (Snowmass 2021)," in *Snowmass 2021*, 5 2022.

[42] B. Abbott *et al.*, "Inclusive jet production in $p\bar{p}$ collisions," *Phys. Rev. Lett.*, vol. 86, pp. 1707–1712, 2001.

[43] R. E. Taylor, "Deep inelastic scattering: The Early years," *Rev. Mod. Phys.*, vol. 63, pp. 573–595, 1991.

[44] D. Adams, B. Adeva, E. Arik, A. Arvidson, B. Badelek, M. Ballintijn, G. Bardin, G. Baum, P. Berglund, L. Betev, *et al.*, "Spin structure of the proton from polarized inclusive deep-inelastic muon-proton scattering," *Physical Review D*, vol. 56, no. 9, p. 5330, 1997.

[45] H. Abramowicz and A. C. Caldwell, "Hera collider physics," *Reviews of Modern Physics*, vol. 71, no. 5, p. 1275, 1999.

[46] A. D. Martin, "Proton structure, Partons, QCD, DGLAP and beyond," *Acta Phys. Polon. B*, vol. 39, pp. 2025–2062, 2008.

[47] G. Altarelli and G. Parisi, "Asymptotic Freedom in Parton Language," *Nucl. Phys. B*, vol. 126, pp. 298–318, 1977.

[48] Y. L. Dokshitzer, "Calculation of the Structure Functions for Deep Inelastic Scattering and e+ e- Annihilation by Perturbation Theory in Quantum Chromodynamics.," *Sov. Phys. JETP*, vol. 46, pp. 641–653, 1977.

[49] V. N. Gribov and L. N. Lipatov, "Deep inelastic e p scattering in perturbation theory," *Sov. J. Nucl. Phys.*, vol. 15, pp. 438–450, 1972.

[50] V. N. Gribov and L. N. Lipatov, "e+ e- pair annihilation and deep inelastic e p scattering in perturbation theory," *Sov. J. Nucl. Phys.*, vol. 15, pp. 675–684, 1972.

[51] A. Simonelli, "Analytic Solutions of the DGLAP Evolution and Theoretical Uncertainties," 1 2024.

[52] J. Blumlein and A. Vogt, "The Evolution of unpolarized singlet structure functions at small x," *Phys. Rev. D*, vol. 58, p. 014020, 1998.

[53] A. J. Buras, "Asymptotic Freedom in Deep Inelastic Processes in the Leading Order and Beyond," *Rev. Mod. Phys.*, vol. 52, p. 199, 1980.

[54] S. Dulat, T.-J. Hou, J. Gao, M. Guzzi, J. Huston, P. Nadolsky, J. Pumplin, C. Schmidt, D. Stump, and C. P. Yuan, "New parton distribution functions from a global analysis of quantum chromodynamics," *Phys. Rev. D*, vol. 93, no. 3, p. 033006, 2016.

[55] H.-L. Lai, M. Guzzi, J. Huston, Z. Li, P. M. Nadolsky, J. Pumplin, and C. P. Yuan, "New parton distributions for collider physics," *Phys. Rev. D*, vol. 82, p. 074024, 2010.

[56] J. Pumplin, D. R. Stump, J. Huston, H. L. Lai, P. M. Nadolsky, and W. K. Tung, "New generation of parton distributions with uncertainties from global QCD analysis," *JHEP*, vol. 07, p. 012, 2002.

[57] G. Aad *et al.*, "Determination of the parton distribution functions of the proton using diverse ATLAS data from pp collisions at $\sqrt{s} = 7$, 8 and 13 TeV," *Eur. Phys. J. C*, vol. 82, no. 5, p. 438, 2022.

[58] L. A. Harland-Lang, A. D. Martin, P. Motylinski, and R. S. Thorne, "Parton distributions in the LHC era: MMHT 2014 PDFs," *Eur. Phys. J. C*, vol. 75, no. 5, p. 204, 2015.

[59] T.-J. Hou *et al.*, "New CTEQ global analysis of quantum chromodynamics with high-precision data from the LHC," *Phys. Rev. D*, vol. 103, no. 1, p. 014013, 2021.

[60] S. Bailey, T. Cridge, L. A. Harland-Lang, A. D. Martin, and R. S. Thorne, "Parton distributions from LHC, HERA, Tevatron and fixed target data: MSHT20 PDFs," *Eur. Phys. J. C*, vol. 81, no. 4, p. 341, 2021.

[61] R. D. Ball *et al.*, "Parton distributions from high-precision collider data," *Eur. Phys. J. C*, vol. 77, no. 10, p. 663, 2017.

[62] R. D. Ball *et al.*, "The path to proton structure at 1% accuracy," *Eur. Phys. J. C*, vol. 82, no. 5, p. 428, 2022.

[63] G. Heinrich, "Qcd lecture 3: Ir singularities, jets and event shapes, pdfs." Presented at the 2023 EUROPEAN SCHOOL OF HIGH-ENERGY PHYSICS, September 2023.

[64] C. Monini, *Single-top s channel cross-section measurement with the ATLAS detector.* PhD thesis, 09 2014.

[65] J. Kretzschmar, *Standard Model physics at the LHC*, pp. 153–171. 2019.

[66] J. M. Campbell, J. W. Huston, and W. J. Stirling, "Hard Interactions of Quarks and Gluons: A Primer for LHC Physics," *Rept. Prog. Phys.*, vol. 70, p. 89, 2007.

[67] C. Anastasiou, L. J. Dixon, K. Melnikov, and F. Petriello, "High precision QCD at hadron colliders: Electroweak gauge boson rapidity distributions at NNLO," *Phys. Rev. D*, vol. 69, p. 094008, 2004.

[68] J. M. Campbell, R. K. Ellis, and D. L. Rainwater, "Next-to-leading order QCD predictions for $W + 2$ jet and $Z + 2$ jet production at the CERN LHC," *Phys. Rev. D*, vol. 68, p. 094021, 2003.

[69] C. Balazs and C. P. Yuan, "Soft gluon effects on lepton pairs at hadron colliders," *Phys. Rev. D*, vol. 56, pp. 5558–5583, 1997.

[70] F. Landry, R. Brock, P. M. Nadolsky, and C. P. Yuan, "Tevatron Run-1 Z boson data and Collins-Soper-Sterman resummation formalism," *Phys. Rev. D*, vol. 67, p. 073016, 2003.

[71] S. Camarda, L. Cieri, and G. Ferrera, "Drell–Yan lepton-pair production: qT resummation at N3LL accuracy and fiducial cross sections at N3LO," *Phys. Rev. D*, vol. 104, no. 11, p. L111503, 2021.

[72] T. Sjostrand, S. Mrenna, and P. Z. Skands, "A Brief Introduction to PYTHIA 8.1," *Comput. Phys. Commun.*, vol. 178, pp. 852–867, 2008.

[73] J. Bellm *et al.*, "Herwig 7.0/Herwig++ 3.0 release note," *Eur. Phys. J. C*, vol. 76, no. 4, p. 196, 2016.

[74] E. Bothmann *et al.*, "Event Generation with Sherpa 2.2," *SciPost Phys.*, vol. 7, no. 3, p. 034, 2019.

[75] G. Aad *et al.*, "Precise measurements of W- and Z-boson transverse momentum spectra with the ATLAS detector using pp collisions at $\sqrt{s} = 5.02$ TeV and 13 TeV," 4 2024.

[76] M. Aaboud *et al.*, "Measurement of the W-boson mass in pp collisions at $\sqrt{s} = 7$ TeV with the ATLAS detector," *Eur. Phys. J. C*, vol. 78, no. 2, p. 110, 2018. [Erratum: Eur.Phys.J.C 78, 898 (2018)].

[77] R. Aaij *et al.*, "Measurement of the W boson mass," *JHEP*, vol. 01, p. 036, 2022.

[78] C. Hays, "High precision measurement of the W-boson mass with the CDF II detector," *PoS*, vol. ICHEP2022, p. 898, 2022.

[79] G. Arnison *et al.*, "Experimental Observation of Isolated Large Transverse Energy Electrons with Associated Missing Energy at $\sqrt{s} = 540$ GeV," *Phys. Lett. B*, vol. 122, pp. 103–116, 1983.

[80] S. Schael *et al.*, "Electroweak Measurements in Electron-Positron Collisions at W-Boson-Pair Energies at LEP," *Phys. Rept.*, vol. 532, pp. 119–244, 2013.

[81] T. A. Aaltonen *et al.*, "Combination of CDF and D0 W-Boson Mass Measurements," *Phys. Rev. D*, vol. 88, no. 5, p. 052018, 2013.

[82] S. Amoroso *et al.*, "Compatibility and combination of world W-boson mass measurements," *Eur. Phys. J. C*, vol. 84, no. 5, p. 451, 2024.

[83] J. de Blas, M. Ciuchini, E. Franco, A. Goncalves, S. Mishima, M. Pierini, L. Reina, and L. Silvestrini, "Global analysis of electroweak data in the Standard Model," *Phys. Rev. D*, vol. 106, no. 3, p. 033003, 2022.

[84] L. Adam, P. Bechtle, M. Boonekamp, K. Desch, A. Dimitrievska, P. D. Kennedy, O. Kivernyk, P. Konig, J. Kremer, J. Kretzschmar, A. E. Pinto Pinoargote, M. Schott, N. Vranjes, and

C. Wang, "New measurement of the W-boson mass and W-boson width at $\sqrt{s} = 7$ TeV," tech. rep., CERN, Geneva, 2022.

[85] L. Evans and P. Bryant, "LHC Machine," *JINST*, vol. 3, p. S08001, 2008.

[86] K. Aamodt *et al.*, "The ALICE experiment at the CERN LHC," *JINST*, vol. 3, p. S08002, 2008.

[87] A. A. Alves, Jr. *et al.*, "The LHCb Detector at the LHC," *JINST*, vol. 3, p. S08005, 2008.

[88] S. Chatrchyan *et al.*, "The CMS Experiment at the CERN LHC," *JINST*, vol. 3, p. S08004, 2008.

[89] G. Aad *et al.*, "*The ATLAS Experiment at the CERN Large Hadron Collider*," *JINST*, vol. 3, p. S08003, 2008.

[90] E. Lopienska, "The CERN accelerator complex, layout in 2022. Complexe des accélérateurs du CERN en janvier 2022," 2022. General Photo.

[91] M. Liberatore, *Top of the tops: Combining searches for Dark Matter with top quarks at $\sqrt{s} = 13$ TeV with the ATLAS detector*. PhD thesis, Humboldt-Universität zu Berlin, Mathematisch-Naturwissenschaftliche Fakultät, 2023.

[92] T. Kawamoto *et al.*, "*New Small Wheel Technical Design Report*," tech. rep., 2013. ATLAS New Small Wheel Technical Design Report.

[93] G. Aad *et al.*, "The ATLAS Inner Detector commissioning and calibration," *Eur. Phys. J. C*, vol. 70, pp. 787–821, 2010.

[94] S. Haywood, L. Rossi, R. Nickerson, and A. Romaniouk, *ATLAS inner detector: Technical Design Report, 2*. Technical design report. ATLAS, Geneva: CERN, 1997.

[95] J. Pequenao, "Computer generated image of the ATLAS inner detector." 2008.

[96] N. Wermes and G. Hallewel, *ATLAS pixel detector: Technical Design Report*. Technical design report. ATLAS, Geneva: CERN, 1998.

[97] G. Aad *et al.*, "Operation and performance of the ATLAS semiconductor tracker," *JINST*, vol. 9, p. P08009, 2014.

[98] M. Aaboud *et al.*, "Performance of the ATLAS Transition Radiation Tracker in Run 1 of the LHC: tracker properties," *JINST*, vol. 12, no. 05, p. P05002, 2017.

[99] ATLAS collaboration, *ATLAS muon spectrometer: Technical Design Report.* Technical design report. ATLAS, Geneva: CERN, 1997.

[100] A. Yamamoto *et al.*, "The ATLAS central solenoid," *Nucl. Instrum. Meth. A*, vol. 584, pp. 53–74, 2008.

[101] ATLAS collaboration, *ATLAS tile calorimeter: Technical Design Report.* Technical design report. ATLAS, Geneva: CERN, 1996.

[102] ATLAS collaboration, *ATLAS liquid-argon calorimeter: Technical Design Report.* Technical design report. ATLAS, Geneva: CERN, 1996.

[103] G. Aad *et al.*, "Operation of the ATLAS trigger system in Run 2," *JINST*, vol. 15, no. 10, p. P10004, 2020.

[104] G. Ciapetti, F. Pastore, E. Petrolo, S. Rosati, F. Spila, R. Vari, S. Veneziano, and L. Zanello, "The ATLAS barrel level-1 muon trigger calibration," in *12th Workshop on Electronics for LHC and Future Experiments (LECC 2006)*, pp. 323–327, 2007.

[105] E. Pasqualucci, "Application of the ATLAS DAQ and Monitoring System for MDT and RPC Commissioning," 3 2007.

[106] G. Aad *et al.*, "Improved luminosity determination in pp collisions at sqrt(s) = 7 TeV using the ATLAS detector at the LHC," *Eur. Phys. J. C*, vol. 73, no. 8, p. 2518, 2013.

[107] G. Aad *et al.*, "Measurement of the W-boson mass and width with the ATLAS detector using proton-proton collisions at $\sqrt{s}$ = 7 TeV," 3 2024.

[108] G. Aad *et al.*, "Luminosity determination in *pp* collisions at $\sqrt{s} = 13$ TeV using the ATLAS detector at the LHC," *Eur. Phys. J. C*, vol. 83, no. 10, p. 982, 2023.

[109] M. Aaboud *et al.*, "Performance of the ATLAS Trigger System in 2015," *Eur. Phys. J. C*, vol. 77, no. 5, p. 317, 2017.

[110] G. Aad *et al.*, "Performance of electron and photon triggers in ATLAS during LHC Run 2," *Eur. Phys. J. C*, vol. 80, no. 1, p. 47, 2020.

[111] ATLAS Collaboration, "Luminosity public results for run 1." https://twiki.cern.ch/twiki/bin/view/AtlasPublic/LuminosityPublicResultsRun1, 2011.

[112] ATLAS Collaboration, "Luminosity public results for run 2." https://twiki.cern.ch/twiki/bin/view/AtlasPublic/LuminosityPublicResultsRun2, 2015.

[113] ATLAS Collaboration, "Luminosity public results for run 3." https://twiki.cern.ch/twiki/bin/view/AtlasPublic/LuminosityPublicResultsRun3, 2022.

[114] ATLAS collaboration, "Software Performance of the ATLAS Track Reconstruction for LHC Run 3," tech. rep., CERN, Geneva, 2021. All figures including auxiliary figures are available at https://atlas.web.cern.ch/Atlas/GROUPS/PHYSICS/PUBNOTES/ATL-PHYS-PUB-2021-012.

[115] S. Gadatsch, *The Higgs Boson*. PhD thesis, Amsterdam U., 2015.

[116] G. Aad *et al.*, "*Muon reconstruction and identification efficiency in ATLAS using the full Run 2 pp collision data set at $\sqrt{s} = 13$ TeV*," *Eur. Phys. J. C*, vol. 81, no. 7, p. 578, 2021.

[117] G. Aad *et al.*, "*Studies of the muon momentum calibration and performance of the ATLAS detector with pp collisions at $\sqrt{s} = 13$ TeV*," *Eur. Phys. J. C*, vol. 83, no. 8, p. 686, 2023.

[118] ATLAS Collaboration, "*Muon reconstruction performance of the ATLAS detector in 2022*," 2023.

[119] ATLAS Collaboration, "*Early Run 3 muon reconstruction performance of the ATLAS detector*," 2023.

[120] A. Salzburger, "The ATLAS Track Extrapolation Package," tech. rep., CERN, Geneva, Jun 2007. All figures including auxiliary figures are available at https://atlas.web.cern.ch/Atlas/GROUPS/PHYSICS/PUBNOTES/ATL-SOFT-PUB-2007-005.

[121] S. Rettie, "Muon identification and performance in the ATLAS experiment," *PoS*, vol. DIS2018, p. 097, 2018.

[122] W. Lampl, S. Laplace, D. Lelas, P. Loch, H. Ma, S. Menke, S. Rajagopalan, D. Rousseau, S. Snyder, and G. Unal, "Calorimeter Clustering Algorithms: Description and Performance," tech. rep., CERN, Geneva, 2008. All figures including auxiliary figures are available at https://atlas.web.cern.ch/Atlas/GROUPS/PHYSICS/PUBNOTES/ATL-LARG-PUB-2008-002.

[123] M. Aaboud *et al.*, "Electron reconstruction and identification in the ATLAS experiment using the 2015 and 2016 LHC proton-proton collision data at $\sqrt{s} = 13$ TeV," *Eur. Phys. J. C*, vol. 79, no. 8, p. 639, 2019.

[124] N. Besson, M. Boonekamp, E. Klinkby, T. Petersen, and S. Mehlhase, "Re-evaluation of the LHC potential for the measurement of Mw," *Eur. Phys. J. C*, vol. 57, pp. 627–651, 2008.

[125] G. Aad *et al.*, "The ATLAS Simulation Infrastructure," *Eur. Phys. J. C*, vol. 70, pp. 823–874, 2010.

[126] S. Agostinelli *et al.*, "GEANT4–a simulation toolkit," *Nucl. Instrum. Meth. A*, vol. 506, pp. 250–303, 2003.

[127] M. Stoneking and D. Den Hartog, "Maximum-likelihood fitting of data dominated by poisson statistical uncertainties," *Review of scientific instruments*, vol. 68, no. 1, pp. 914–917, 1997.

[128] A. Pinto, Z. Wu, F. Balli, N. Berger, M. Boonekamp, E. Chapon, T. Kawamoto, and B. Malaescu, "Uncertainty components in profile likelihood fits," *Eur. Phys. J. C*, vol. 84, no. 6, p. 593, 2024.

[129] A. E. Pinto Pinoargote, E. Chapon, M. Boonekamp, F. Balli, and Z. Wu, "Analytical approach to the Profile Likelihood fit and uncertainty decomposition study," tech. rep., CERN, Geneva, 2023.

[130] W. A. Rolke, A. M. Lopez, and J. Conrad, "Limits and confidence intervals in the presence of nuisance parameters," *Nucl. Instrum. Meth. A*, vol. 551, pp. 493–503, 2005.

[131] J. Kieseler, "A method and tool for combining differential or inclusive measurements obtained with simultaneously constrained uncertainties," *Eur. Phys. J. C*, vol. 77, no. 11, p. 792, 2017.

[132] A. Valassi, "Combining correlated measurements of several different physical quantities," *Nucl. Instrum. Meth. A*, vol. 500, pp. 391–405, 2003.

[133] L. Demortier, "Equivalence of the best-fit and covariance-matrix methods for comparing binned data with a model in the presence of correlated systematic uncertainties," CDF Note 8661, 1999.

[134] G. L. Fogli, E. Lisi, A. Marrone, D. Montanino, and A. Palazzo, "Getting the most from the statistical analysis of solar neutrino oscillations," *Phys. Rev. D*, vol. 66, p. 053010, 2002.

[135] D. Stump, J. Pumplin, R. Brock, D. Casey, J. Huston, J. Kalk, H. L. Lai, and W. K. Tung, "Uncertainties of predictions from parton distribution functions. 1. The Lagrange multiplier method," *Phys. Rev. D*, vol. 65, p. 014012, 2001.

[136] R. S. Thorne, "Uncertainties in parton related quantities," *J. Phys. G*, vol. 28, pp. 2705–2716, 2002.

[137] M. Botje, "Error estimates on parton density distributions," *J. Phys. G*, vol. 28, pp. 779–790, 2002.

[138] A. Glazov, "Averaging of DIS cross section data," *AIP Conf. Proc.*, vol. 792, no. 1, pp. 237–240, 2005.

[139] R. Barlow, "Combining experiments with systematic errors," *Nucl. Instrum. Meth. A*, vol. 987, p. 164864, 2021.

[140] B. List, "Decomposition of a covariance matrix into uncorrelated and correlated errors." https://indico.desy.de/event/3009/contributions/64704/, 2010. Alliance Workshop on Unfolding and Data Correction, DESY.

[141] G. Aad *et al.*, "Measurement of dijet cross sections in *pp* collisions at 7 TeV centre-of-mass energy using the ATLAS detector," *JHEP*, vol. 05, p. 059, 2014.

[142] D. Britzger, "The Linear Template Fit," *Eur. Phys. J. C*, vol. 82, no. 8, p. 731, 2022.

[143] L. A. Goodman, "On the exact variance of products," *Journal of the American statistical association*, vol. 55, no. 292, pp. 708–713, 1960.

[144] J. Kirchner, "Data analysis toolkit# 5: uncertainty analysis and error propagation," *University of California Berkeley Seismological Laboratory. Available online at: http://seismo. berkeley. edu/˜ kirchner/eps_120/Toolkits/Toolkit_05. pdf*, 2001.

[145] H. H. Ku *et al.*, "Notes on the use of propagation of error formulas," *Journal of Research of the National Bureau of Standards*, vol. 70, no. 4, 1966.

[146] S. D. Drell and T.-M. Yan, "Massive Lepton Pair Production in Hadron-Hadron Collisions at High-Energies," *Phys. Rev. Lett.*, vol. 25, pp. 316–320, 1970. [Erratum: Phys.Rev.Lett. 25, 902 (1970)].

[147] J. Alwall, R. Frederix, S. Frixione, V. Hirschi, F. Maltoni, O. Mattelaer, H. S. Shao, T. Stelzer, P. Torrielli, and M. Zaro, "The automated computation of tree-level and next-to-leading order differential cross sections, and their matching to parton shower simulations," *JHEP*, vol. 07, p. 079, 2014.

[148] T. Sjostrand, S. Mrenna, and P. Z. Skands, "A Brief Introduction to PYTHIA 8.1," *Comput. Phys. Commun.*, vol. 178, pp. 852–867, 2008.

[149] D. Bardin, A. Leike, T. Riemann, and M. Sachwitz, "Energy-dependent width effects in e+e- annihilation near the z-boson pole," *Physics Letters B*, vol. 206, no. 3, pp. 539–542, 1988.

[150] G. Aad *et al.*, "Alignment of the ATLAS Inner Detector in Run-2," *Eur. Phys. J. C*, vol. 80, no. 12, p. 1194, 2020.

[151] ATLAS collaboration, "Performance of the muon spectrometer alignment in 2017 and 2018 data," tech. rep., CERN, Geneva, 2021. All figures including auxiliary figures are available at https://atlas.web.cern.ch/Atlas/GROUPS/PHYSICS/PUBNOTES/ATL-MUON-PUB-2021-002.

[152] G. Aad *et al.*, "Performance of the ATLAS muon triggers in Run 2," *JINST*, vol. 15, no. 09, p. P09015, 2020.

[153] P. Nason, "A New method for combining NLO QCD with shower Monte Carlo algorithms," *JHEP*, vol. 11, p. 040, 2004.

[154] S. Frixione, P. Nason, and C. Oleari, "Matching NLO QCD computations with Parton Shower simulations: the POWHEG method," *JHEP*, vol. 11, p. 070, 2007.

[155] S. Alioli, P. Nason, C. Oleari, and E. Re, "A general framework for implementing NLO calculations in shower Monte Carlo programs: the POWHEG BOX," *JHEP*, vol. 06, p. 043, 2010.

[156] P. Golonka and Z. Was, "PHOTOS Monte Carlo: A Precision tool for QED corrections in Z and W decays," *Eur. Phys. J. C*, vol. 45, pp. 97–107, 2006.

[157] A. Collaboration, "Measurement of the muon momentum reconstruction performance for the ATLAS experiment at the LHC utilising 139 fb^{-1} of pp collisions produced at $\sqrt{s} = 13$ TeV between 2015 and 2018.," tech. rep., CERN, Geneva, 2022.

[158] S. Marti i Garcia, S. Camarda, T. Golling, M. Danninger, N. A. Styles, J. Wollrath, W. K. Di Clemente, S. Henkelmann, J. Jimenez Pena, O. Estrada Pastor, A. K. Morley, H. Oide, A. T. Vermeulen, P. Butti, E. Ricci, F. M. Follega, and R. Iuppa, "Studies of radial distortions of the ATLAS Inner Detector," tech. rep., CERN, Geneva, 2018.

[159] A. Thaler, E. Kneringer, and V. Cairo, "Study of the global momentum scale bias," tech. rep., CERN, Geneva, 2021.

[160] J. R. Guerrero, N. Calace, S. Camarda, and S. Marti i Garcia, "The ϕ-dependent radial distortion of the ATLAS Inner Detector," tech. rep., CERN, Geneva, 2019.

[161] M. Aleksa *et al.*, "Measurement of the ATLAS solenoid magnetic field," *JINST*, vol. 3, p. P04003, 2008.

[162] J. C. Collins and D. E. Soper, "Angular Distribution of Dileptons in High-Energy Hadron Collisions," *Phys. Rev. D*, vol. 16, p. 2219, 1977.

[163] E. Richter-Was and Z. Was, "Separating electroweak and strong interactions in Drell–Yan processes at LHC: leptons angular distributions and reference frames," *Eur. Phys. J. C*, vol. 76, no. 8, p. 473, 2016.

[164] A. Karlberg, E. Re, and G. Zanderighi, "NNLOPS accurate Drell-Yan production," *JHEP*, vol. 09, p. 134, 2014.

[165] C. Amelung, F. Bauer, and P.-F. Giraud, "Performance of the muon spectrometer alignment in 2017 and 2018 for the R22 re-processing," tech. rep., CERN, Geneva, Oct 2020. Supporting note of ATL-COM-MUON-2020-058.

[166] A. E. Pinto Pinoargote, M. Boonekamp, P.-F. Giraud, and L. Chevalier, "Muon alignment studies for the Z and J/ψ resonances," tech. rep., CERN, Geneva, 2024.

[167] V. M. Abazov *et al.*, "Measurement of the W Boson Mass with the D0 Detector," *Phys. Rev. Lett.*, vol. 108, p. 151804, 2012.

[168] T. Aaltonen *et al.*, "High-precision measurement of the W boson mass with the CDF II detector," *Science*, vol. 376, no. 6589, pp. 170–176, 2022.

[169] F. A. Berends, G. Burgers, W. Hollik, and W. L. van Neerven, "The Standard Z Peak," *Phys. Lett. B*, vol. 203, pp. 177–182, 1988.

[170] P. A. Zyla *et al.*, "Review of Particle Physics," *PTEP*, vol. 2020, no. 8, p. 083C01, 2020.

[171] N. Andari, M. Boonekamp, R. Hanna, and S. Camarda, "Measurement of m_W at 7 TeV: Physics modeling," tech. rep., CERN, Geneva, 2014.

[172] A. M. Sirunyan *et al.*, "Measurement of the inclusive $t\bar{t}$ cross section in pp collisions at $\sqrt{s} = 5.02$ TeV using final states with at least one charged lepton," *JHEP*, vol. 03, p. 115, 2018.

[173] S. Hoche, F. Krauss, M. Schonherr, and F. Siegert, "NLO matrix elements and truncated showers," *JHEP*, vol. 08, p. 123, 2011.

[174] G. Aad *et al.*, "Measurement of $W^{\pm}$ and Z-boson production cross sections in *pp* collisions at $\sqrt{s} = 13$ TeV with the ATLAS detector," *Phys. Lett. B*, vol. 759, pp. 601–621, 2016.

[175] T. Xu, M. Boonekamp, L. Aperio Bella, C. Wang, B. R. Davis-Purcell, M. Li, Z. Wu, F. Balli, and J. Kretzschmar, "Multi-jet background in low-pile-up runs taken in 2017 and 2018," tech. rep., CERN, Geneva, 2019.

[176] K. Cranmer, G. Lewis, L. Moneta, A. Shibata, and W. Verkerke, "HistFactory: A tool for creating statistical models for use with RooFit and RooStats," 6 2012.

[177] L. Lyons, D. Gibaut, and P. Clifford, "How to Combine Correlated Estimates of a Single Physical Quantity," *Nucl. Instrum. Meth. A*, vol. 270, p. 110, 1988.

[178] A. Hayrapetyan *et al.*, "Combination of measurements of the top quark mass from data collected by the ATLAS and CMS experiments at $\sqrt{s} = 7$ and 8 TeV," 2023.

[179] T. Aaltonen *et al.*, "Precise measurement of the W-boson mass with the CDF II detector," *Phys. Rev. Lett.*, vol. 108, p. 151803, 2012.

[180] V. M. Abazov *et al.*, "Measurement of the W boson mass with the D0 detector," *Phys. Rev. D*, vol. 89, no. 1, p. 012005, 2014.

[181] G. Aad *et al.*, "Combined Measurement of the Higgs Boson Mass from the H→$\gamma\gamma$ and H→ZZ*→4ℓ Decay Channels with the ATLAS Detector Using s=7, 8, and 13 TeV pp Collision Data," *Phys. Rev. Lett.*, vol. 131, no. 25, p. 251802, 2023.

[182] The Tevatron Electroweak Working Group, "Combination of cdf and d0 results on the width of the w boson," 2010.

[183] Z. Wu, *Improvement of the muon spectrometer and precision W-boson physics in ATLAS.* Theses, Université Paris-Saclay ; University of science and technology of China, Sept. 2023.

[184] G. D'Agostini, "A Multidimensional unfolding method based on Bayes' theorem," *Nucl. Instrum. Meth. A*, vol. 362, pp. 487–498, 1995.

[185] G. D'Agostini, "Improved iterative Bayesian unfolding," in *Alliance Workshop on Unfolding and Data Correction*, 10 2010.

Appendix A

Extra results in muon muomentum calibration

A.1 Di-muon invariant mass reconstruction

This section describes the behavior of the angle between two muons in the rest frame under an infinitesimal transformation. The di-muon invariant mass in the rest frame is given by,

$$m^2 = 2p_1 p_2 (1 - \cos\theta_{12}), \tag{A.1}$$

where p_1 and p_2 are the momentum of the two muons and θ_{12} is the angle between the two particles that can be expressed as a function of the laboratory frame angles, the polar angle, θ and the azimuthal angle, ϕ, as,

$$\cos\theta_{12} = \cos\theta_1 \cos\theta_2 + \sin\theta_1 \sin\theta_2 \cos(\phi_1 - \phi_2). \tag{A.2}$$

Under an infinitesimal transformation of the angles $|\varepsilon| \ll 1$, $\cot\theta$ changes as follows,

$$\cot\theta \rightarrow \cot\theta \cdot (1 + \varepsilon), \tag{A.3}$$

which implies,

$$\cos\theta \to \cos\theta \cdot (1 + \varepsilon \sin^2\theta),$$
$$\sin\theta \to \sin\theta \cdot (1 - \varepsilon \cos^2\theta). \tag{A.4}$$

Then, $\cos\theta_{12}$ transforms as,

$$1 - \cos\theta_{12} \to (1 - \cos\theta_{12}) \cdot (1 + \varepsilon \Delta_{\theta\phi}), \tag{A.5}$$

with,

$$\Delta_{\theta\phi} = \frac{\sin^2\theta_1 + \sin^2\theta_2}{1 - \sec\theta_1 \sec\theta_2 + \tan\theta_1 \tan\theta_2 \cos(\phi_1 - \phi_2)} - \frac{(\cos^2\theta_1 + \cos^2\theta_2)\cos(\phi_1 - \phi_2)}{\cot\theta_1 \cot\theta_2 + \cos(\phi_1 - \phi_2) - \csc\theta_1 \csc\theta_2}. \tag{A.6}$$
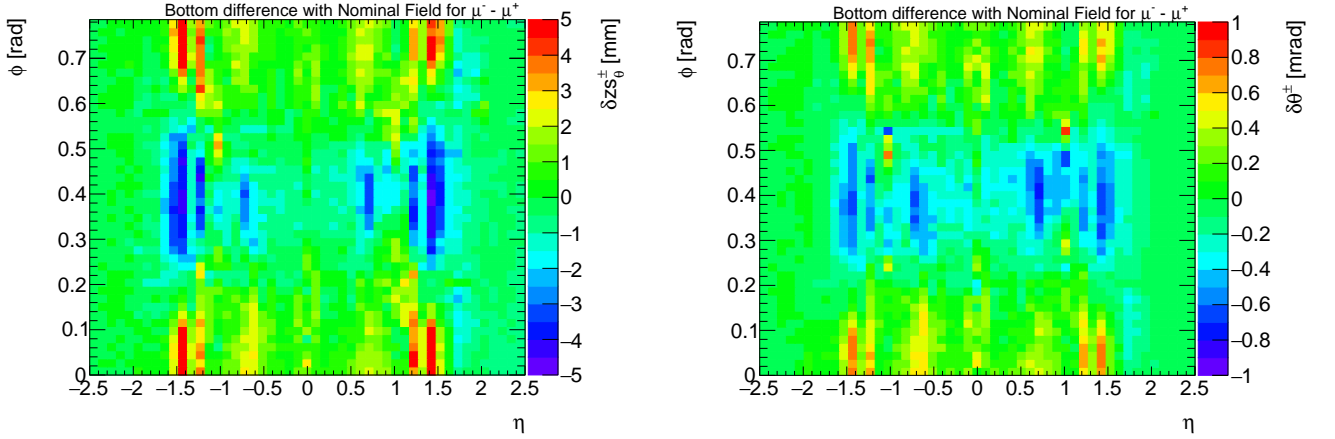
A.2 MS/ID residual biases for bottom region 2D maps

Figure A.1: Asymmetry 2D bottom region maps for (left) $\delta z s_\theta^\pm$ and (right) $\delta\theta^\pm$ for $\mu^- - \mu^+$ with nominal magnetic field at $p_T > 20$ GeV.
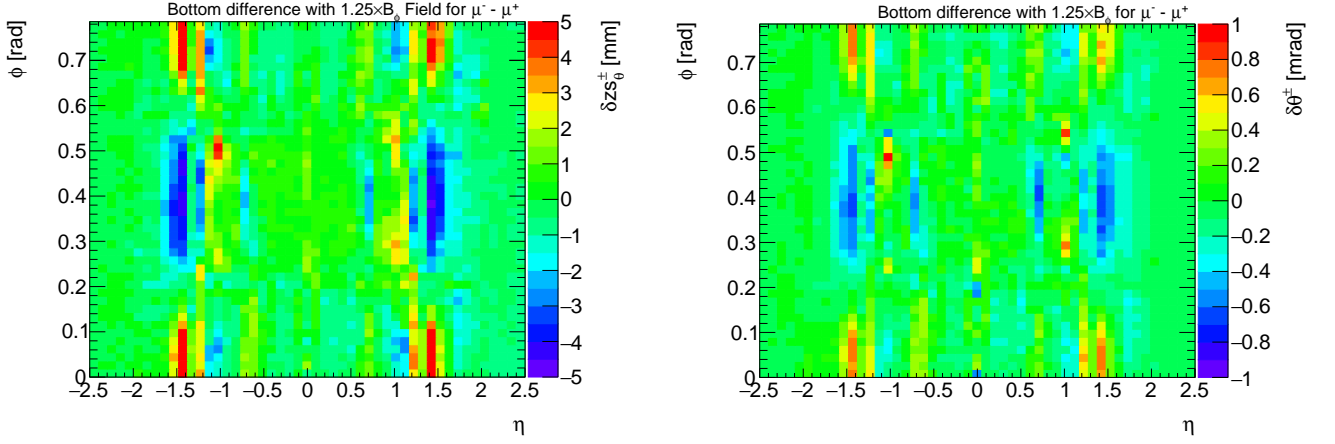
274

Figure A.2: Asymmetry 2D bottom region maps (left) $\delta z s_{\theta}^{\pm}$ and (right) $\delta\theta^{\pm}$ for $\mu^{-} - \mu^{+}$ with $1.25 \times B_{\phi}$ modified magnetic field at $p_{T} > 20$ GeV.
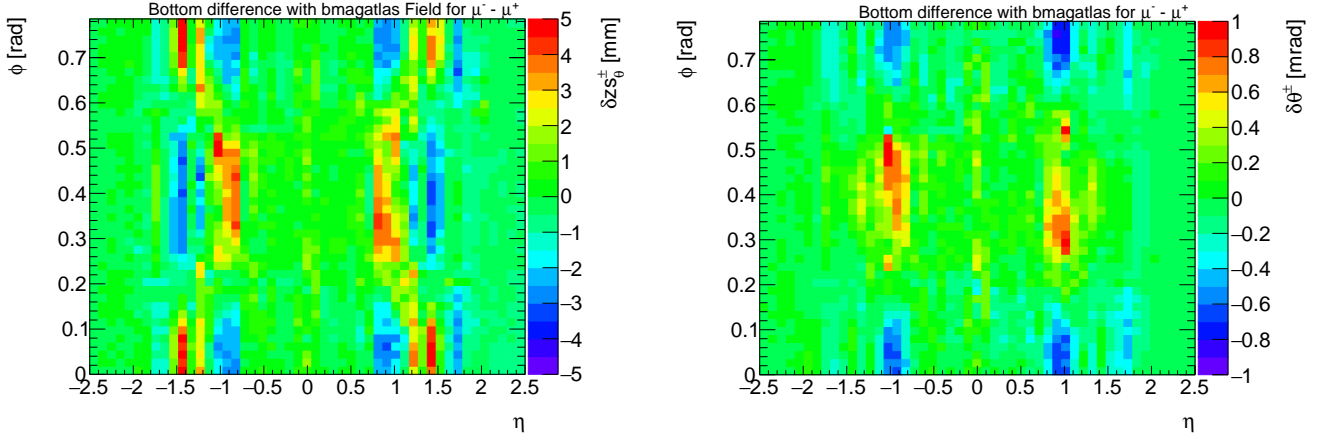

Figure A.3: Asymmetry 2D bottom region maps $\delta z s_{\theta}^{\pm}$ and $\delta\theta^{p}m$ for $\mu^{-} - \mu^{+}$ with bmagatlas field at $p_{T} > 20$ GeV.
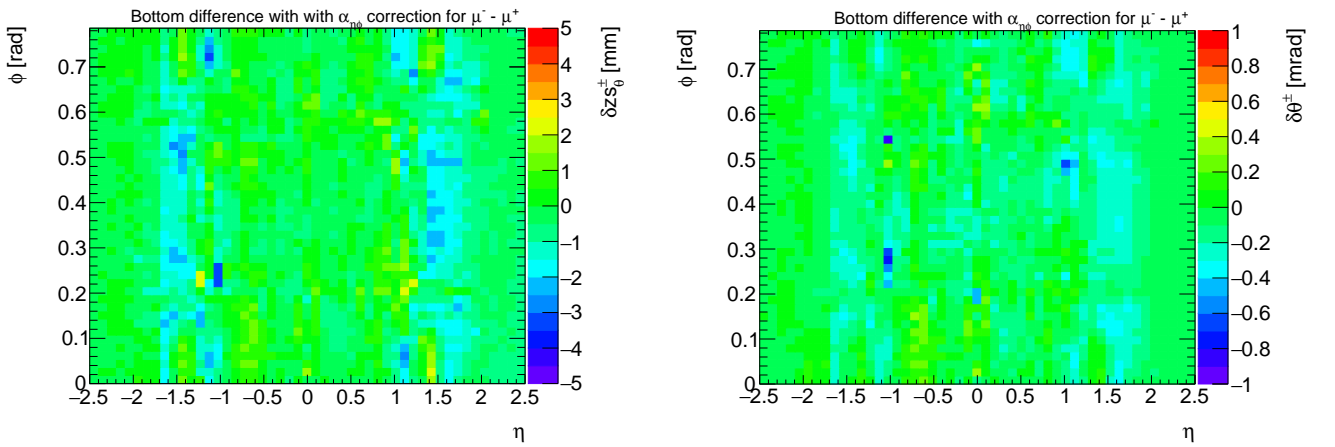

Figure A.4: Asymmetry 2D bottom region maps (left) $\delta z s_{\theta}^{\pm}$ and (right) $\delta\theta^{\pm}$ for $\mu^{-} - \mu^{+}$ after correction at $p_{T} > 20$ GeV.